



TURNkey - Towards more Earthquake-resilient Urban Societies through a Multi-sensor-based Information System enabling Earthquake Forecasting, Early Warning and Rapid Response actions

This project has received funding from the European Union's Horizon 2020 research and innovation programme under grant agreement No 821046



Towards more Earthquake-resilient Urban Societies through a Multi-sensor-based Information System enabling Earthquake Forecasting, Early Warning and Rapid Response actions

TURNkey

Deliverable D3.8

Report on improved procedures for rapid mapping of earthquake shaking, including adjustment factors for local site effects (RRE)

Authors:	<p>BRGM: Rosemary Fayjaloun, Pierre Gehl, Agathe Roullé, Anne Lemoine, Samuel Auclair</p> <p>UIce: Atefe Darzi, Benedikt Halldorsson, Sahar Rahpeyma</p> <p>EUC: Barbara Borzi, Francesca Bozzoni, Ali Guney Ozcebe, Elisa Zuccolo</p> <p>EMSC: Rémy Bossu, Matthieu Landès, Julien Roch, Frédéric Roussel</p> <p>INFP: Stefan Florin Balan, Carmen Cioflan, Bogdan Apostol</p> <p>NOA: Nicos Melis, Stratos Liadopoulos</p> <p>KNMI: Elmer Ruigrok, Pauline Kruiver</p> <p>BUW: Jochen Schwarz, Peshawa Luqman Hasan, Silke Beinersdorf, Lars Abrahamczyk</p>
Responsible Partner:	BRGM

Version:	1.0
Date:	31/07/2021
Reviewers:	Daniel Kuehn (NOR), John Douglas (UStr), Sergio Molina (UA)
Distribution level:	Public

DOCUMENT REVISION HISTORY

Date	Version	Editor	Comments
29/07/2021	1.0	Final	

LIST OF PARTNERS

Participant	Name	Country
NOR	Stiftelsen NORSAR	Norway
DEL	Stichting Deltares	Netherlands
KNMI	Koninklijk Nederlands Meteorologisch Instituut	Netherlands
BRGM	Bureau de Recherches Géologiques et Minières	France
EMSC	Euro-Mediterranean Seismological Centre	France
UIce	Haskoli Islands (University of Iceland)	Iceland
EUC	Fondazione Eucentre	Italy
UStr	University of Strathclyde	UK
BUW	Bauhaus-Universität Weimar	Germany
UA	Universidad de Alicante	Spain
ARU	Anglia Ruskin University Higher Education Corporation	UK
UNIBG	Università degli Studi di Bergamo	Italy
UCL	University College London	UK
INFP	Institutul National de Cercetare si Dezvoltare pentru Fizica Pamantului	Romania
YET	YetItMoves S.r.l.	Italy
GMP	Gempa GmbH	Germany
NOA	National Observatory of Athens	Greece
NTC	Nutcracker Research Ltd.	UK
B80	Beta 80 SpA	Italy
Sim	Siminn hf.	Iceland
UPat	Panepistimio Patron (University of Patras)	Greece

GLOSSARY

Acronym	Description
BN	Bayesian Network
DEM	Digital Elevation Model
EEW	Earthquake Early Warning
GMICE	Ground-Motion Intensity Conversion Equation
GMM	Ground Motion Model

GMPE	Ground-Motion Prediction Equation
IM	Intensity Measure
PGA	Peak Ground Acceleration
PGV	Peak Ground Velocity
RRE	Rapid Response to Earthquakes
SA	Spectral Acceleration
TB	Test-Bed
Vs30	Averaged shear wave velocity in the first 30 meters

INDEX OF CONTENTS

Document revision history	2
List of partners.....	2
Glossary.....	2
Index of contents	1
Index of figures.....	3
Index of tables	9
1 EXECUTIVE SUMMARY	1
2 INTRODUCTION	2
3 STATE-OF-THE-ART OF RAPID MAPPING PROCEDURES (SHAKE-MAPS).....	4
3.1 Shake-map algorithms	4
3.1.1 USGS ShakeMap® algorithm	5
3.1.2 Bayesian Network algorithm.....	7
3.1.3 Alternative ground-motion inference methods.....	8
3.2 Shake-maps based on an experience-based approach for areas with sparse seismic networks	10
3.2.1 Overview	10
3.2.2 General Procedure	10
4 RANKING OF GROUND-MOTION MODELS	13
4.1 Introduction	13
4.2 Pre-selection of GMMs	15
4.3 Screening of database	15
4.4 Scoring methods	16
4.4.1 Log-likelihood	16
4.4.2 Pari-mutuel gambling score.....	17
4.4.3 Quantile score.....	17
4.4.4 Euclidean metric distance.....	17
4.4.5 Deviance Information Criterion.....	18
4.5 Ranking.....	18
4.6 Application examples: ranking of GMMs for TB-4 and TB-6.....	18
4.6.1 GMM ranking for TB-4.....	20
4.6.2 GMM ranking for TB-6.....	21
5 UPDATING OF GROUND-MOTION and intensity attenuation MODELS.....	24
5.1 Direct updating of GMM coefficients	24
5.1.1 Methodology.....	25
5.1.2 Dataset	27

5.1.3	Overview of the analysis	28
5.1.4	Example of the calibration of GMM coefficients for a single event	28
5.1.5	Small earthquakes subsequent to the Ussita M5.9 event.....	34
5.1.6	Conclusive remarks	37
5.2	Derivation of shake-maps using uncertain GMM coefficients.....	37
5.2.1	Methodology.....	38
5.2.2	Data and models	40
5.2.3	Preliminary results.....	41
5.3	Verification of conversion equations between intensity and peak ground motion.....	48
5.3.1	Ground motion intensity conversion equations (GMICE).....	48
5.3.2	Observed intensity and recorded ground motion.....	51
5.4	Verification and updating of intensity attenuation	54
5.4.1	Preselection of intensity attenuation relations	54
5.4.2	Basics steps of an updating procedure.....	56
5.4.3	Model curves (including scatter)	57
5.4.4	Examples	60
6	ADJUSTMENT FACTORS FOR LOCAL SITE CONDITIONS	62
6.1	Knowledge-based framework for the generation of site-specific shake-maps	62
6.2	Site-specific refinement of shaking effects.....	66
6.2.1	Classification based on shear-wave velocity Vs30 parameters	66
6.2.1.1	Calculation of average shear-wave velocity values.....	66
6.2.1.2	NEHRP classification.....	67
6.2.1.3	Eurocode site classification (first generation)	67
6.2.1.4	Eurocode site classification (second generation).....	68
6.2.1.5	German site classification scheme DIN 4149:2005.....	69
6.2.2	Code-related soil factors (second generation of Eurocode 8).....	70
6.2.3	Site amplification using earthquake data.....	71
6.2.4	Soil Factors in ground motion prediction equations.....	76
6.2.5	Site response analysis (SRA).....	80
6.2.6	Instrumental site classification	80
6.2.7	Refinement of shaking effects via intensity increments for local site conditions.....	82
6.3	Harmonized Vs30 maps at European level.....	86
6.4	Collection of site amplification factors at local level	94
6.4.1	TB1: Bucharest, Romania.....	94
6.4.1.1	Elements of geology and layout of Bucharest	94
6.4.1.2	Recent subsoil studies in Bucharest.....	95
6.4.1.3	Spectral amplification factor (local amplification and nonlinear behaviour of soil strata) .	97

6.4.1.4	Amplification models for shake-maps.....	100
6.4.2	TB2: Pyrenees mountain range, France.....	100
6.4.3	TB3: Hveragerði and Húsavík, Iceland	104
6.4.3.1	Localized site amplification and station terms	104
6.4.3.2	The geology of Hveragerdi and Husavik, TB3 Iceland.....	106
6.4.3.3	Proxies of site amplification	110
6.4.3.4	Predicting site effects in GMMs for Iceland.....	114
6.4.4	TB-5: Gioia Tauro port, Italy.....	116
6.4.5	TB6: Groningen area, Netherlands.....	123
6.4.5.1	Vs30 for Groningen	123
6.4.5.2	Amplification model for Groningen	127
6.4.5.3	Testing site-amplification proxies	130
6.5	Recommendations for TBs	137
7	SOCIAL SENSORS AS SOURCES OF OBSERVATION.....	140
7.1	Felt reports.....	140
7.1.1	Introduction	140
7.1.2	A rapid data collection.....	140
7.1.3	Felt reports and shaking estimates.....	141
7.1.4	Spatial clustering of felt reports.....	143
7.1.5	Current and future developments.....	144
7.2	Information from social media (Twitter).....	144
7.2.1	A global social network to monitor earthquakes around the world.....	144
7.2.2	Analysis of Twitter feeds with agnostic extraction of the raw felt area	146
7.2.3	Generation of Twitter-enhanced shake-maps	148
8	CONCLUDING REMARKS	153
9	REFERENCES	155
10	APPENDIX I.....	178

INDEX OF FIGURES

Figure 2-1: The locations of the six geographically-based TURNkey Testbeds (TB-1 to TB-6, ellipses), plotted on the SHARE European Seismic Hazard of Giardini et al. (2013).....	3
Figure 3-1: Schematic main principles of ShakeMap® v3.5 and the Bayesian inference shake-map procedures. ShakeMap® v4 does not correct to rock conditions before interpolation.	4
Figure 3-2: Illustration of a BN structure for the generation of a shake-map, with nine grid points $Y(.)$ and two observations Y_{obs}	7
Figure 3-3: (a) Example of a 4-point grid with one instrumental observation (Y_{obs1}) and one macroseismic observation (Z_{obs2}); (b) corresponding BN, where the evidenced nodes are displayed in red.	8

Figure 3-4: Shake-map generated with the Bayesian updating approach for the M 4.3 Lourdes (France) earthquake of December 30th, 2012. Left: contour of PGA (in %g); Right: field of associated uncertainty $\sigma \ln PGA$. Triangles represent ground-motion measurements and circles are macroseismic observations. 10

Figure 3-5: Shake-map generation procedures (Schwarz et al., 2006, 2008a; Beinersdorf, 2016) – example shown here: 2004 Waldkirch earthquake Germany $M_w 4.6$; * denotes a corresponding macroseismic intensity map. 11

Figure 3-6: Usability of shake-maps for loss assessment (Schwarz et al., 2006, 2008a; Beinersdorf, 2016): radial scenario with ΔI (SRA) of 2004 Waldkirch earthquake with an hypothetical intensity $I_0 = VIII$ 12

Figure 4-1: Graph showing the number of GMMs published each year (columns) and their cumulative total number (lines) [https://www.gmpe.org.uk. Last updated: 14 January 2021]. 14

Figure 4-2: Magnitude-distance distribution of the 5790 recordings (from 273 events) used to rank GMMs for TB-4..... 19

Figure 4-3: (a) Map showing events within the PGV database for $M > 1.5$. 103 events (black circles) are related to the Groningen gas field, the remaining 11 events (red circles) are related to other gas fields. From Ruigrok and Dost (2020). (b) Magnitude-distance distribution of the 3260 PGV values used to rank GMMs for TB-6. 19

Figure 5-1. Flowchart followed in this study for updating the GMM coefficients during the ongoing propagation of earthquake waves. Indices j and k are for station j and analysis time k , $PGA_{GMM,A,T1,m-2s}$ is the geometric mean minus 2 standard deviations of PGA predicted by the original GMM considering A site class and T1 topography, $PGAr_{A,T1,m}$ is the geometric mean of the recorded PGA considering A site class and T1 topography. R and R_{max} are distance metric (in our case epicentral) and its maximum allowable value. 27

Figure 5-2. Black lines: lower 2.5-percentile limit of the original GMM ($PGAp_{A,\mu-2\sigma}$), continuous blue lines: mean prediction of the updated GMM, dashed blue lines: $\mu-1s$ and $\mu+1s$ predictions of the updated GMM, grey markers: geometric means of recorded and normalized PGA values at the end of the shaking, red markers: geometric means of the recorded and normalized PGA values at timestep k ($PGAr_{A,T1}(k_j)$). (a), (b), (c) provide the summary for the initial guess, intermediate guess (at time step=15s after the initiation of the rupture), and final guess, respectively. The analysis was carried out by using the M6.5 Norcia event..... 30

Figure 5-3. Site condition and topography normalized PGA maps in comparison with the corresponding (final) recorded values. (a), (b), (c) represent initial, intermediate, and final guesses. The analysis was carried out by using the single event of M6.5 Norcia..... 30

Figure 5-4. Time dependent change in (a): standard deviation (s), (b) pari-mutuel gambling (PGM) score, (c) log-likelihood (LLH) score. The analysis was made by using a single event of M6.5 (Norcia event). The time $t=0$ s represents the rupture initiation, magnitude is considered to be known from the beginning. 32

Figure 5-5. Time-dependent change of prediction of normalized PGA ($PGA_{A,T1}$) for (a) T1214, (b) AQF, (c) MMP1 stations. The analysis is made by using a single event of M6.5 (Norcia). 33

Figure 5-6 (a and d): $PGA_{A,T1}-R_{epi}$ predictions of the original (black) GMM and GMM updated at 0s (blue) versus the scatter of recorded values. (b and e): initial $PGA_{A,T1}$ maps (i.e. at the theoretical timestep when the M estimate is stable) versus final observations. (c and f): Final $PGA_{A,T1}$ map versus observations. For the initial guess, GMM coefficients are set according to their final values obtained employing the M5.9 Ussita event. (a to c) are for event ID 4 and (d to f) are for event ID 5 (see Table 5-1). 35

Figure 5-7 (a and d): $PGA_{A,T1}-R_{epi}$ predictions of the original (black) and updated at 0s (blue) GMMs versus the scatter of recorded values. (b and e): Initial $PGA_{A,T1}$ maps (i.e. at the theoretical time instant when M estimate is relatively stabilized) versus final observations. (c and f): Final $PGA_{A,T1}$ map versus observations. For the initial guess, GMM coefficients are set according to their final values obtained in the M5.9 Ussita event. (a to c) are for event ID 6 and (d to f) are for event ID 7 (see Table 5-2)..... 36

Figure 5-8: Adapted BN structure for the updating of GMM coefficients (three uncertain coefficients θ_1 , θ_2 , and θ_3 are assumed here). Three grid points $Y(\cdot)$ and two observations Y_{obs} are considered. 39

Figure 5-9: Polynomial site amplification function dependent on Vs_{30} (m/s) used for the Italian earthquakes, from Kotha et al. (2020) GMM. 41

Figure 5-10: PGA estimates for the Norcia earthquake, on rock conditions..... 44

Figure 5-11: SA(1s) estimates for the Norcia earthquake, on rock conditions..... 44

Figure 5-12: PGA estimates for the Lourdes earthquake, on rock conditions. The model “KO20 - posterior” is overlapping with the model “KO20 - shake-map” 45

Figure 5-13: SA(1s) estimates for the Lourdes earthquake, on rock conditions. The model “KO20 - posterior” is overlapping with the model “KO20 - shake-map” 45

Figure 5-14. Comparison of measurements with assigned macroseismic intensity of the earthquakes a) 1978 Albstadt (Wieck and Schneider 1980), 2011 Virginia (CEMSD 2011), and 2020 Croatia (EMSC 2020) with the dataset used by (Faenza and Michelini 2010) and b) 1992 Roermond (Ahorner 1993), 2004 Waldkirch (EW- and NS- Component, (LED 2005) checked against the relationships acc. to (Medvedev and Sponheuer 1969; Tselentis and Danciu 2008; Faenza and Michelini 2010; Caprio *et al.* 2015) 50

Figure 5-15. Measurements of the peak ground acceleration (PGA) in [cm/s²] named with station code [measured PGA] (LED, 2005, red triangle) and (RAP, 2005, purple triangle) of the Dec. 5, 2004 Waldkirch earthquake (black star indicates the epicentre). 52

Figure 5-16. Comparison of spectral accelerations S_a of the ground motion measurements acc. to (LED (2005, 2013) with the GMPE (Schwarz et al., 2007) of the assumed subsoil class (classification acc. to German code) based on the geological map of (LRGB (1998) and additional rock spectra for non-rock-type stations. 53

Figure 5-17. Influence of earthquake parameters a) local magnitude M_L , b) epicentral intensity I_0 , c) attenuation coefficient α , d) focal depth h_0 on the intensity attenuation using the relationships a) (Ahorner, 1983a), and b) to d) (Sponheuer, 1960), cf. (Beinersdorf, 2016). 54

Figure 5-18. Selected evaluation forms of a) intensity attenuation relationship and point source, b) intensity attenuation relationship and line source with orientation from seismic moment or moment tensor solution (example Figure 6-12b), c) radii with defined distance from the epicentre (grouping macroseismic observations according to distance from the epicentre or hypocentre of the earthquake and used for individual attenuation functions) of the attenuation in individual intensity based on attenuation relationships and macroseismic intensity observations, cf. (Beinersdorf, 2016). 55

Figure 5-19. Shaking effects of the induced earthquakes within the gas production fields 1997 Roswinkel (M_L 3.4, (Dost et al., 1997)) and 2012 Huizinge (M_L 3.5, (Dost and Kraaijpoel, 2013)) compared to variations of the respective intensity attenuations which are shown here as intensity increments ΔI (cf. Schwarz et al., 2019b). 56

Figure 5-20. Example for the intensity attenuation derived from macroseismic observations for the 1911 Ebingen earthquake of epicentral intensity $I_0 = VIII$ (8.0) and focal depth $h_0 = 10$ km for the relations acc. to (Sponheuer, 1960; Ahorner et al., 1986; Rosenhauer, 1999) 57

Figure 5-21. Comparison of intensity attenuations with macroseismic observations for the earthquakes 1978 Albstadt, 1997 Roswinkel, and 2012 Huizinge compared to the intensity attenuations acc. to (Sponheuer, 1960; Rosenhauer, 1999) for the corresponding earthquake 57

Figure 5-22. Magnitude-based intensity attenuation (M_L) acc. to (Ahorner and Rosenhauer 1993; Rosenhauer 1999) in comparison to the macroseismic observations for the corresponding earthquake; here 1978 Albstadt, thick red line – baseline of the intensity attenuation, scatter range: minimum and maximum values of the equally distributed parameters 58

Figure 5-23. Variations acc. to Table 5-10 of the magnitude-based intensity attenuation (M_L) acc. to Rosenhauer (1999) in comparison to the macroseismic observations for the corresponding earthquake; here 1978 Albstadt, thick red line - baseline of the intensity attenuation, scatter range: minimum and maximum values of the equally distributed parameters 60

Figure 6-1: Knowledge-based framework for the generation of site-specific shake-maps 63

Figure 6-2: Soil factors according to Eurocode second generation (European Committee for Standardization, 2021) for all six soil classes A through F at different seismicity levels. 71

Figure 6-3. Short-period amplification factors with respect to ground condition SC-Ib from the study of Borchardt (1994) for input ground motion 0.1, 0.2, 0.3 and 0.4g. 73

Figure 6-4. Mid-period amplification factors with respect to ground condition SC-Ib from the study of Borchardt (1994) for input ground motion 0.1, 0.2, 0.3 and 0.4g. 74

Figure 6-5: Variation of soil factors at different ranges of V_{s30} according to site amplifications using single EQ data (Borcherdt, 1994) and soil factors from second generation of Eurocode (European Committee for Standardization, 2021).....	75
Figure 6-6: Variation in soil amplification factors for selected ground motion prediction equations Akkar and Bommer (2010); Darzi et al. (2019); Bindi et al. (2014) as a function of shear wave velocity at 30 m depth for periods $T=0.4s$ and $T=1s$	79
Figure 6-7: Shake-map computed for the 2020 Croatia earthquake using the ground motion prediction equation of Bindi et al. (2014): a) without consideration of soil factors, b) with consideration of soil factors.	80
Figure 6-8: Method of an experimental seismic site assessment: classification scheme for relevant site categories. Qualitative ranges of possible peak frequencies of one-dimensional transfer functions for site classification schemes: (a) site-specific subsoil classes according to DIN 4149:2005 (2005); (b) refined NEHRP site classes by Rodriguez-Marek and Bray (1997); graphs are taken from Land and Schwarz (2006).	81
Figure 6-9: Spectral H/V-ratios of microtremors overlain with the classification scheme based on (a) DIN 4149:2005 (2005) site classes; “Central European scheme” referring to DIN 4149:2005 (2005); and (b) refined NEHRP site classes by Rodriguez-Marek and Bray (1997); graphs are taken from Land and Schwarz (2006); “U.S. classification scheme” referring to Rodriguez-Marek et al. (2001).....	82
Figure 6-10. Number of underlying data sets (a) and mean value of the intensity increments (b, red – intensity increase, green intensity decrease, yellow – as predicted by intensity attenuation relationship) prepared via a raster according to information from Ahorner (pers. com.) and combined with districts of the respective study area (based on the preliminary work by Ahorner and Budny (1985)).....	83
Figure 6-11. Example for the evaluation of a grid element with macroseismic observations for the 1911 Ebingen earthquake of epicentral intensity $I_0 = VIII$ (8.0) and focal depth $h_0 = 10$ km for the relations according to Ahorner et al. (1986) and Sponheuer (1960).	84
Figure 6-12. Scenarios (Intensity EMS-98) of the Dec. 5, 2004 Waldkirch earthquake (epicentre ★) based on the attenuation model from Sponheuer (1960) for the epicentral intensity $I_0 = VI$ (6.0)	86
Figure 6-13: Geology-based V_{s30} model for TB1.	88
Figure 6-14: DEM-based V_{s30} model for TB1.	88
Figure 6-15: Geology-based V_{s30} model for TB2 (left: Luchon area; right: Perpignan-Figueras area).	89
Figure 6-16: DEM-based V_{s30} model for TB2 (left: Luchon area; right: Perpignan-Figueras area).	89
Figure 6-17: Geology-based V_{s30} model for TB3 (left: town of Hveragerði; right: town of Húsavík).	90
Figure 6-18: DEM-based V_{s30} model for TB3 (left: town of Hveragerði; right: town of Húsavík).	90
Figure 6-19: Geology-based V_{s30} model for TB4.	91
Figure 6-20: DEM-based V_{s30} model for TB4.	91
Figure 6-21: Geology-based V_{s30} model for TB5.	92
Figure 6-22: DEM-based V_{s30} model for TB5.	92
Figure 6-23: Geology-based V_{s30} model for TB6.	93
Figure 6-24: DEM-based V_{s30} model for TB6.	93
Figure 6-25: Romania map with location of Bucharest and Vrancea (main seismic source).....	94
Figure 6-26: Improved V_{s30} map for Bucharest City. (Project NATO SFP/981882).	96
Figure 6-27: Response spectra for the site INCERC-Bucharest obtained from recordings during the three most destructive earthquakes of the last century (Bălan et al. 2016).	100
Figure 6-28: Left: map of the Luchon area and the 53 municipalities. Right: location of the Luchon area overlaid with the French seismic zonation map.	101
Figure 6-29: Comparison of soil characterization maps at different scales, expressed as amplification factors, for the Luchon area. Left: geology-based model presented in Section 6.2; right: regional model.....	102
Figure 6-30: Comparison of soil characterization maps at different scales, expressed as amplification factors, for the Luchon area. Left: geology-based model presented in section 6.2; right: local model.....	103
Figure 6-31: Pie charts of the distribution of soil characterization classes in urbanized areas for the three defined scale scenarios.	103

Figure 6-32 Geological maps of the towns of Hveragerði (top) and Húsavík (bottom) in TB3 Iceland that are of the highest detail and spatial resolution, shown along with the recording stations of the Icelandic strong-motion arrays (ICEARRAY I at top, ICEARRAY II at bottom) (Rahpeyma et al. 2019).	104
Figure 6-33 Mean station terms at ICEARRAY I stations in Hveragerdi relative to a reference station on bedrock.	105
Figure 6-34 Posterior distributions of station terms at ICEARRAY II stations in Husavik relative to the array average.	106
Figure 6-35 Geological maps for TB3-Hveragerdi and TB3-Husavik with lower resolution, obtained from ÍSOR database (http://jardfraedikort.is/).	107
Figure 6-36 Geological maps for TB3-Husavik of yet coarser resolution.	108
Figure 6-37 Geological and slope maps of Iceland along with the locations of the strong-motion (ICEARRAY I and II and IceSMN) and seismic (SIL) stations.	109
Figure 6-38 Near-surface geology of Iceland showing the categories of estimated Vs30 velocities, listed in Table 6-23.	111
Figure 6-39 Map of VS30-based site classes for Iceland (top right panel), North Iceland (top left panel) and SW-Iceland (bottom left panel), classified by the topographic slope proxy according to slope-Vs30 ranges proposed by Wald and Allen (2007) for active tectonic regions. DEM 20m-by-20m (2/3 arcsec) resolution is used to generate the inferred Vs30 map (Darzi et al. 2022)	112
Figure 6-40. Map of VS30-based site classes for TB3-Hveragerdi (left) and TB3-Husavik (right), classified by the topographic slope proxy according to slope-Vs30 ranges proposed by Wald and Allen (2007) for active tectonic regions. DEM 20m-by-20m (2/3 arcsec) resolution is used to generate the inferred Vs30 map (Darzi et al., 2022).	113
Figure 6-41. European VS30 maps based on (left) DEM topographic slope according to Wald and Allen (2007a) based on a 30 arc-second DEM model (~ 1000 m resolution).	113
Figure 6-42. European geology-based site class model for the Hveragerdi (left) and Husavik (right) testbeds, according to Vilanova et al. (2018).	114
Figure 6-43 The six new Bayesian GMMs for Iceland predicting PGA and PSA vs. oscillator period (Kowsari et al. 2020a).	115
Figure 6-44: Seismic geotechnical soil modelling for the Northern part of Gioia Tauro port (Bozzoni et al., 2014): a) available data; b) 1D soil stratigraphy.	118
Figure 6-45: Seismic geotechnical soil modelling for the Southern part of Gioia Tauro port (Bozzoni et al., 2014): a) available data; b) 1D soil stratigraphy.	119
Figure 6-46: Stochastic ground response analysis for the Northern part of Gioia Tauro port (475-years return period): a) 1000 random Vs profiles generated by Bozzoni et al. (2014); the red line represents the mean profile; b) acceleration response spectra computed out of 1000 numerical simulations (black lines) and mean spectrum (red line).	121
Figure 6-47: Comparison among acceleration response spectra with associated uncertainties ($\mu \pm \sigma$), computed by using linear-equivalent (red lines) and non-linear (blue lines) 1D ground response analysis for the Northern part of the port and the return period of 100 years.	122
Figure 6-48: Geological cross section from south (left) to north (right). Different colours and codes denote different geological formations. The wedge of Holocene deposits consists of geological formations coded by NA (Naaldwijk), NAWO (Naaldwijk, Wormer Member), NAWA (Naaldwijk, Walcheren member), NIHO (Nieuwkoop, Holland Peat) and NIBA (Nieuwkoop, Basal Peat) (from Kruiver et al., 2017a). The position of the cross-section is shown in Figure 6-49.	123
Figure 6-49: GeoTOP lithoclasses, showing a dominant outcropping of clay in the northern part and sand in the southern part (from Kruiver et al. 2017a). The dashed line shows the outline of the Groningen gas field with a 5 km buffer zone added.	124
Figure 6-50: Example of Vs observations in the SCPT data set, for clays from the Peelo Formation. The observations of Vs are plotted versus the confining stress σ'_0 normalised by atmospheric pressure p_a . The solid line describes a regression, while dotted lines indicate 95% confidence intervals (from Kruiver et al., 2017b).	125

Figure 6-51: Examples of mean V_S profiles (red lines, using the mean regression parameters) and sampled V_S profiles (black lines, using random samples of V_S from the confidence interval and a correlation of 0.5 between successive layers of varying soil type). The column on the left of each panel shows layers of constant soil type (from Kruiver et al., 2017b)..... 125

Figure 6-52: Mean (left) and standard deviation (right) of V_{S30} for the Groningen region for the most recent Ground Motion Model version 6 (after Kruiver et al., 2017b)..... 126

Figure 6-53: Mean V_{S30} map of Groningen using the symbology of Section 6.3. Left: classes F2 and F3 from Vilanova et al. (2018). Right: classes using Table 6-15 based on DEM. 127

Figure 6-54: Weak motion AFs for the zones in the Groningen region. The AFs are shown for an M 4.5, R 5 km scenario and selected periods (from Bommer et al., 2019b). 129

Figure 6-55: (Left) cross-plot of the largest Peak Ground Velocity (PGV) being observed at 200 m depth (x-axis) and at 0 m depth (y-axis), for borehole station G01. (Right) a distribution of extracted amplification factors (circles), their mean (solid line) and 68% confidence zone delimited with the dashed lines. 131

Figure 6-56: A plot of Vilanova V_{S30} versus measured AF data points at 61 stations of the G-network and the fitted function through the data points using Equation (6-2)..... 132

Figure 6-57: A plot of DEM V_{S30} versus measured AF data points at 61 stations of the G-network and the fitted function through the data points using Equation (6-12)..... 133

Figure 6-58: A plot of GeoTOP V_{S30} versus measured AF data points at 61 stations of the G-network and the fitted function through the data points using Equation (6-12)..... 134

Figure 6-59: A plot of SCPT V_{S30} versus measured AF data points at 51 stations of the G-network and the fitted function through the data points using Equation (6-12)..... 135

Figure 6-60: A plot of SCPT V_{S30} versus measured AF data points at 51 stations of the G-network and the fitted function through the data points using Equation (6-12)..... 135

Figure 6-61: A plot of SCPT V_{S30} versus measured AF data points at 51 stations of the G-network and the fitted function through the data points using Equation (6-12). The AF is determined in the 1-4 Hz frequency band, whereas the previous figures plot AFs in the 1-10 Hz band. 136

Figure 7-1: Map of felt reports for M6.4 Petrinja Croatia Dec. 29th 2020 earthquake through the app, website for mobile devices and website for desktop. 141

Figure 7-2: Comparison between intensity vs distance (top) and shake-map with EMSC felt reports (left) and DYFI data (right) for the M5.7 Western Turkey earthquake of Sept. 26th 2019. 142

Figure 7-3: Estimated standard deviation for EMSC felt reports (red curve) and DYFI data (black curve) as a function of the number of observations in 1km² grid cells..... 143

Figure 7-4: Examples of felt reports spatially averaged into different grid cells. 144

Figure 7-5: (a) A priori estimation of the MI and the contour lines defining the “felt area” from Twitter data, example of a location inside the felt area; (b) Truncated normal distribution of the macroseismic intensities at two locations shown in (a) by purple and blue dots, after considering the information from the felt area, and the expected values to be entered as evidence observations (red dotted vertical lines) and implemented to generate map (c). (c) A posteriori estimation of the MI when considering the “felt area” from Twitter data. Coordinate of epicenter in (a) and (b) are from RéNaSS (example from the M5.2 Barcelonnette earthquake in 2014)..... 149

Figure 7-6: Successive steps and datasets involved in the generation of shake-maps that include Twitter data. GMPE stands for Ground-Motion Prediction Equation, GMICE for Ground-Motion Intensity Conversion Equation, BN for Bayesian Network, E(MMI) for the expected value of macroseismic intensity. 150

Figure 7-7: Shake-maps for the Barcelonnette earthquake, taking into account the information from: (a) the seismic stations recording PGA (shown as red squares), (b) the Twitter data (the felt zone is bordered by black lines), and (c) both seismic stations and Twitter data. The contour lines represent the reference isoseismal areas defined by the French Central Seismological Office (BCSF). 151

Figure 7-8: Same as Figure 6-7, for the Le Teil earthquake..... 151

INDEX OF TABLES

Table 4-1: List of pre-selected GMMs for TB-4, along with their main characteristics, namely: region of data used for the development of the model, horizontal component, magnitude range, distance range, distance metric and site characterization	20
Table 4-2: Ranking of GMMs for TB-4 considered in this study. The five GMMs with highest final ranking are highlighted in bold.....	20
Table 4-3: List of pre-selected GMMs for TB-6, along with their main characteristics, namely: region of data used for the development of the model, horizontal component, magnitude range, distance range, distance metric and site characterization.	21
Table 4-4: Ranking of GMMs for TB-6 considered in this study. In bold are highlighted the four GMMs with highest final ranking.	22
Table 5-1: Earthquake events considered in this study with corresponding IDs. EMSC: European-Mediterranean Seismological Centre. Latitude, longitude, depth refer to the hypocentral location. M: moment magnitude. Abbr: abbreviations used in the text. Note: * in the M column represents the local magnitude. .	27
Table 5-2: Log standard deviation (s) of the updated GMMs, pari-mutuel gambling score (PGMS) and log-likelihood score (LLHS) of updated (u) and original (o) GMMs for their initial and final guesses by employing the M5.9 Ussita event for pre-calibration and subsequent events for evaluation. Positive PGMS and lower LLHS indicate the better performing GMM. Value in parentheses show the corresponding PGMS and LLHS when considering the sigma of the original GMM. See Table 5-1 for the flat file information of the events under consideration.	37
Table 5-3: Role of the GMM coefficients c_1 and c_3 considered in the updating process. In KO20, $H_d = 4$ and $R_{ref} = 30$; in BI11, $R_{ref} = 1$ and h is set at 10 for shallow earthquakes.	42
Table 5-4: Results of the BN updating for the Norcia earthquake, for PGA and SA(1s). “Prior” stands for the direct application of the GMM without any updating or use of observations. “Posterior” represents the updated model with uncertain coefficients. “Shake-map” represents the shake-map approach presented in Section 3, without any updating of coefficients. * KO20 coefficients and error terms are in $\ln(\cdot)$ space; ** BI11 coefficients and error terms are in $\log_{10}(\cdot)$ space.....	42
Table 5-5: Results of the BN updating for the Lourdes earthquake, for PGA and SA(1s). “Prior” stands for the direct application of the GMM without any updating or use of observations. “Posterior” represents the updated model with uncertain coefficients. “Shake-map” represents the shake-map approach presented in Section 3, without any updating of coefficients. * KO20 coefficients and error terms are in $\ln(\cdot)$ space; ** AB10 coefficients and error terms are in $\log_{10}(\cdot)$ space.....	43
Table 5-6: Scores and ranking of the various models predicting PGA for the studied earthquakes.	46
Table 5-7: Scores and ranking of the various models predicting SA(1s), for the studied earthquakes.	47
Table 5-8: Compared ground motion intensity conversion equations (GMICE) in Figure 5-14.....	49
Table 5-9: Parameters of the earthquakes 1911 Ebingen, 1978 Albstadt, 1997 Roswinkel, and 2012 Huizinge taken for the intensity attenuations in Section 5 (Schwarz et al., 2019a, pt. B and C of EKDAG).....	55
Table 5-10: Modifications in PSSAEL acc. to Schwarz et al. (2014) (Figure 5-22 and Figure 5-23).....	59
Table 6-1: Examples of site-specific level of data availability.....	65
Table 6-2: Sub-soil classes as a function of v_s , 30 based on NEHRP site classification guidelines (Building Seismic Safety Council, 2004)	67
Table 6-3: Ground types according to Eurocode 8 (European Committee for Standardization, 2004).....	67
Table 6-4: Standard combination site type classification scheme (Schwarz, 2018); recommended definition of depth values $H_{vsh} = 5m$; $H_{st} = 30m$; $H_d = 60$ to $100m$; $H_{vd} = 200m$	68
Table 6-5: Ground classes according to DIN 4149:2005, 2005; R for areasominantlypredominantly characterised by rock; T for transition zones between R and S; S sedimentary basins; A for firm to medium firm soil; B for loose soil (gravel to coarse sands, marls); C fine grained soil (fine sands) (Schwarz, 2018). 69	69
Table 6-6: Standard site categorization according to (European Committee for Standardization, 2021; Schwarz, 2018).....	70
Table 6-7: Site amplification factors $F \propto$ and $F\beta$ for the standard site categories.	70

Table 6-8: Subsoil classification based on shear wave velocity according to (Borcherdt, 1994)	72
Table 6-9: Short and mid-period amplification factors with respect to reference ground conditions SC-Ib (firm to hard rock).	73
Table 6-10: Site amplification factors for the second generation of Eurocode 8, using equations of Borcherdt (1994).	74
Table 6-11: List of ground motion prediction equations with implemented site scaling models; GMPE coefficients are taken as written in original author documents	77
Table 6-12: Site categorization based on v_s , H and f_0	81
Table 6-13: Relative Intensity increment ΔI (Ahorner et al., 1986; Bossu et al., 2000).....	85
Table 6-14. Data fields describing the Vs30 model based on geology.....	87
Table 6-15. Raster codes expressed in Vs30 ranges, for the model based on DEM.	87
Table 6-16: Bucharest- INCERC seismic station (Mărmureanu Gh. et al. 2014, Bălan et al. 2016).	98
Table 6-17: Bucharest- Panduri seismic station (Mărmureanu Gh. et al. 2014, Bălan et al. 2016).	98
Table 6-18: Bucharest- Metalurgiei seismic station (Mărmureanu Gh. et al. 2014, Bălan et al. 2016).	98
Table 6-19: Bucharest- Branesti seismic station (Mărmureanu Gh. et al. 2014, Bălan et al. 2016).....	98
Table 6-20: Mean values of spectral amplification factors for three strong earthquakes from the 20th century (Mărmureanu et al., 1996).	99
Table 6-21. Station terms at ICEARRAY I stations in Hveragerdi relative to a reference station on bedrock	105
Table 6-22. Station terms at ICEARRAY II stations in Husavik relative to a reference station on bedrock	106
Table 6-23. Nine different categories used to describe the geological units of Iceland for USGS ShakeMap's implementation at the IMO in association with the SAFER project, along with their corresponding shear-wave velocity estimates. Velocities of underwater geological units (lakes, oceans) are estimated.....	111
Table 6-24. Estimates of the average shear-wave velocities of the geological units in Hveragerdi and Husavik	112
Table 6-25. Geology-based Vs30 classes (Vilanova et al., 2018).....	114
Table 6-26: Mean values of geotechnical parameters and corresponding uncertainties assumed for the stratigraphic profile of the subsoil for the Northern area of the Gioia Tauro port.....	120
Table 6-27: Amplified peak ground acceleration (PGA_{amp}) predicted from stochastic ground response analysis for the Northern and the Southern part of Gioia Tauro harbour and PGA on rock outcropping provided by the current Italian building code.....	121
Table 6-28: Summary of local site condition maps in each TB	137
Table 10-1: Recordings from the Norcia earthquake: coordinates of the stations (Long, Lat), Vs30, distance from the source (Rjb) and PGA and SA at 1s (in m/s^2), as the maximum of the two horizontal components and corrected for site effects following Kotha et al. (2020) amplification factors based on Vs30.	178
Table 10-2: Recordings from the Lourdes earthquake: coordinates of the stations (Long, Lat), distance from the source (Rjb), amplification factor based on EC8 classes, and corrected PGA on rock conditions (in m/s^2).	183

1 EXECUTIVE SUMMARY

This report details the procedures that have been applied, developed or improved in Task 3.4 for the rapid generation of ground shaking maps (i.e., shake-maps). The report revolves around several actions and technical results, which are organized as follows:

- Section 3 summarizes the state-of-the-art of current shake-map algorithms and systems, based on a review by Guérin-Marthe et al. (2021). The USGS ShakeMap v4 approach is compared to a method based on Bayesian updating, which is put forward as one of the technical solutions to be implemented in the TURNkey platform.
- Section 4 is based on previous work carried out in Task 3.3.2: in each TB, various GMMs (Ground-Motion Models) are evaluated and ranked, via different scoring metrics. The selected GMMs may then be used for the generation of shake-maps in each TB.
- Section 5 details novel research efforts, where the GMM coefficients are updated in order to match the observations. This approach is useful to rapidly update a GMM in a given area for a given earthquake, so that the updated GMM may be reused for subsequent events (e.g., in a seismic sequence) in order to improve the accuracy of ground-shaking estimates. Two parallel and complementary methods are presented, namely a direct calibration of the coefficients (EUC) and a Bayesian updating of the uncertain coefficients in the shake-map (BRGM).
- Section 6 discusses site amplification models that are available in each TB: besides local models, Vs30 maps generated at the European level (in the European project SERA) are extracted for each TB. Recommendations are given for each TB on which model should be applied, and whether the SERA model represents a satisfying approximation.
- Section 7 explores additional sources of observations that may be used to characterise shake-maps: collection and aggregation of felt reports by EMSC; and extraction of Twitter data and integration as soft evidence in the shake-maps by BRGM.

The Bayesian approach for the derivation of shake-maps has been implemented in a Python code, which is briefly described in the companion deliverable report D3.9.

2 INTRODUCTION

While earthquakes remain unpredictable, their impact on populations can be significantly reduced by taking appropriate and timely actions following strong ground motions. Updated damage and loss assessment can be performed in near-real time by using recordings from seismic stations, by using felt intensity observations such as “Did You Feel It” (DYFI) reports (Wald et al., 2011), or even by using large amounts of data from social media such as Twitter in order to refine areas of felt intensity (Fayjaloun et al., 2021a). The updated spatial field of ground-motion parameters is in turn used as an input to damage and loss assessment software developed in WP4.

The literature review by Guérin-Marthe et al. (2021), which focused on the analysis of state-of-the-art approaches for rapid mapping (or shake-maps), has investigated existing shake-map systems, in terms of the different algorithms used, as well as their respective input data. Several algorithms used to compute shake-maps have been discussed in detail (see Azarbakht et al., 2020): the U.S. Geological Survey (USGS) ShakeMap® version 3.5 (Wald et al., 2006) and version 4 (Worden et al., 2018), and a Bayesian inference method (Gehl et al., 2017). While straightforward in theory, most shake-map processes require an accurate knowledge of several parameters and models in practice:

- The selected GMM and GMICE (Ground-Motion Intensity Conversion Equations) have an influence on the distribution of the ground-motion field, and the chosen models should be adapted to the specific area of interest.
- Knowledge of the epicentral parameters of the earthquake (location, depth and magnitude). In particular, the epicentral depth is often poorly constrained within the first automatic notifications immediately available after the event, while it critically affects the assessment of ground motions in the near field.
- The knowledge of the fault mechanism and dimension is an essential factor as well: in the case of large earthquakes, a fault-source model (instead of a point-source) is required in order to better constrain near-field ground motions. However, such models may not be defined until several hours following the earthquake, leading to substantial uncertainties in the early versions of the shake-map.
- An accurate map of soil classes, associated to Vs30 values or site amplification factors, is also crucial in order to properly estimate the expected level of ground shaking. This is an important source of uncertainty for ShakeMap® 3.5 and the Bayesian inference methods that should not be overlooked, since the amplification coefficients associated with some soil classes can be large. A microzonation of these soil types incorporating a calibration of the amplification factors via geophysical measurements is therefore to be preferred, when possible, over global approaches such as that proposed by Wald and Allen (2007).
- Both the GMICE and the site amplification factors that together enable conversion of rock accelerations to felt intensities come at the cost of significant additional uncertainties (e.g. the standard deviation related to the GMICE).
- Finally, other parameters of the algorithms pertain to the seismic stations that are to be considered for the computation of the bias (i.e., global level of the shake-map): a selection is usually made based on a cut-off distance from the epicentre

(i.e. distant stations are screened out), or on a significant deviation of the observation from the initially GMM estimate. Although already configurable in the ShakeMap® system, the calibration of such choices deserves further investigations.

Therefore, the present report aims at addressing and investigating some of the identified shortcomings, namely:

- the selection of suitable GMMs to use in each TB, through some ranking metrics (Section 4);
- the rapid updating of GMM coefficients, via recorded strong motions, in order to improve the accuracy of shake-maps and potentially update the models to be used for subsequent aftershocks (Section 5);
- the evaluation of suitable site amplification models for each TB area, in addition to the European-level Vs30 model recently developed in the SERA project (Section 6). The locations of the TBs are shown in Figure 2-1;
- the use of alternative sources of field observations, such as felt reports collected from mobile apps or the analysis of Twitter feeds in order to identify broad ranges of intensity (Section 7).

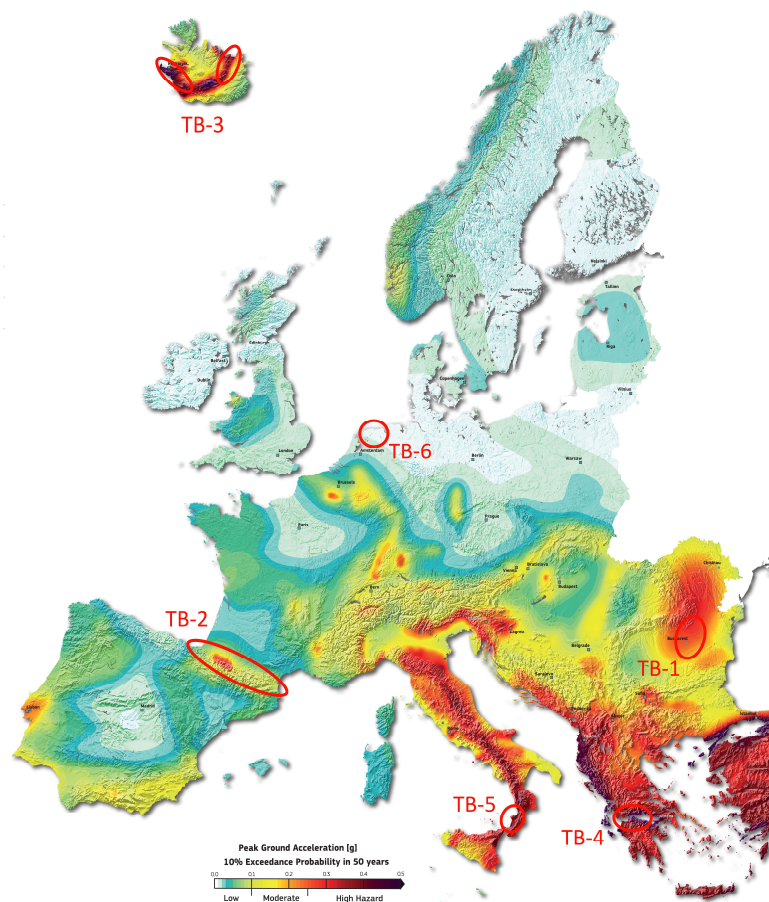


Figure 2-1: The locations of the six geographically-based TURNkey Testbeds (TB-1 to TB-6, ellipses), plotted on the SHARE European Seismic Hazard of [Giardini et al. \(2013\)](#).

3 STATE-OF-THE-ART OF RAPID MAPPING PROCEDURES (SHAKE-MAPS)

When an earthquake is detected, the magnitude and the location of the hypocenter are estimated. A Ground Motion Model (GMM), also called Ground Motion Prediction Equation (GMPE), is then applied in order to estimate ground-motion parameters around the hypocenter (each GMM having specific validity criteria such as magnitude range, fault mechanism and dimension, distance to the source, geodynamical context). The observations recorded during the event (i.e., ground-motion measurements and macroseismic intensities when available) are collected, sometimes corrected by site amplification factors (in order to adjust the measurements from soil conditions to rock conditions) and used to update the distribution of the ground-motion field (Figure 3-1). The latter result is called a shake-map, which is an estimate of the ground motion usually in the form of intensity measures (IMs) such as PGA (Peak Ground Acceleration), SA (Spectral Acceleration), PGV (Peak Ground Velocity) or macroseismic intensity. In the case macroseismic intensities are exploited as observations, a Ground-Motion-Intensity Conversion Equation (GMICE) is used in order to obtain ground-motion estimates. At the end, if the observations have initially been corrected for site amplification, the amplification factors are applied at each grid point (Figure 3-1) in order to adjust the ground-motion parameters from rock conditions to the actual soil conditions of the area.

3.1 Shake-map algorithms

The following section presents the main algorithms used to generate shake-maps, taking observations and uncertainties into account: the USGS ShakeMap® algorithms (Wald et al., 2006; Worden et al., 2018) and the Bayesian inference method (Gehl et al., 2017).

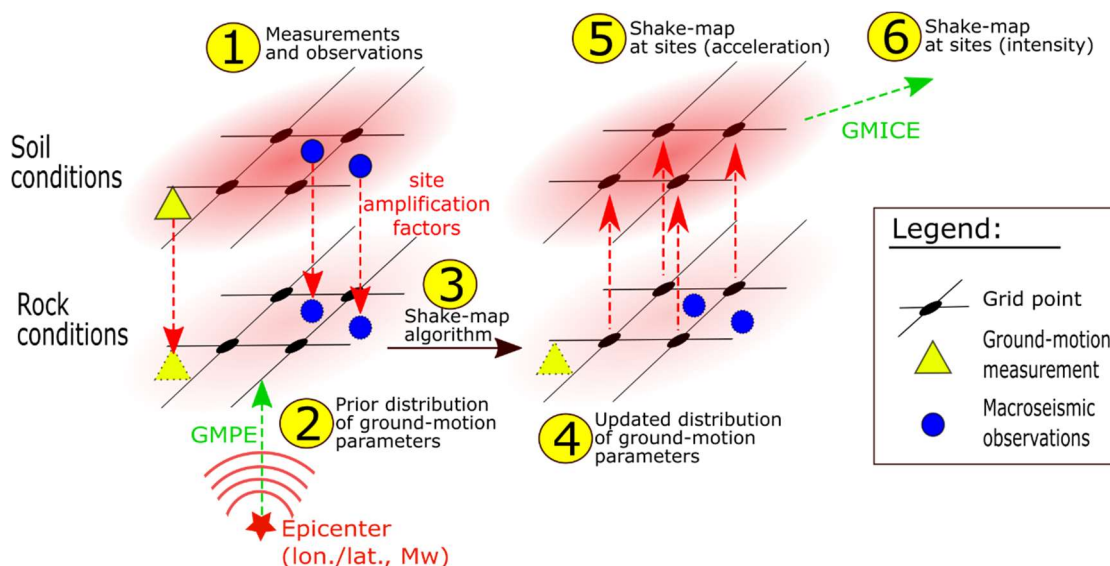


Figure 3-1: Schematic main principles of ShakeMap® v3.5 and the Bayesian inference shake-map procedures. ShakeMap® v4 does not correct to rock conditions before interpolation.

3.1.1 USGS ShakeMap® algorithm

The most widespread and elaborate shake-map system is the one operated by the USGS, thanks to developments by Wald et al. (1999; 2006). The still widely used version 3.5 is based on a weighted interpolation algorithm (Worden et al., 2010). At the locations of observations, the global bias introduced by the observations with respect to the initial GMM estimates is computed: the bias is corrected by finding the magnitude that reduces the errors between the observed and the predicted ground motions, when the GMM is evaluated for the adjusted magnitude. The bias-adjusted GMM is applied in order to estimate corrected ground parameters over a spatial grid. At each grid point, the ground-motion parameter of interest is updated through a weighted average between the bias-adjusted GMM estimate and the interpolated observations: the GMM estimate is weighted by the inverse of the variance provided by the GMM, while each observation is weighted by the term $1/\sigma_{obs}^2$ (i.e., σ_{obs} is the standard deviation assigned to the observation - it increases with distance between the observation and the grid point, based on a ground-motion spatial correlation model). Based on the interpolation scheme proposed by Worden et al. (2010), the mean updated ground-motion parameter Y at grid point (x,y) is expressed as:

$$\overline{Y}_{xy} = \frac{\frac{Y_{GMM,xy}}{\sigma_{GMM}^2} + \sum_{i=1}^n \frac{Y_{obs,xy,i}}{\sigma_{obs,xy,i}^2} + \sum_{j=1}^m \frac{Y_{convobs,xy,j}}{\sigma_{convobs,xy,j}^2}}{\frac{1}{\sigma_{GMM}^2} + \sum_{i=1}^n \frac{1}{\sigma_{obs,xy,i}^2} + \sum_{j=1}^m \frac{1}{\sigma_{convobs,xy,j}^2}} \quad (3-1)$$

where $Y_{GMM,xy}$ is the bias-corrected GMM estimate at the point (x,y) , and $Y_{obs,xy,i}$ (resp. $Y_{convobs,xy,j}$) is the i th ground-motion measurement out of n (resp. the j th macroseismic observation out of m) scaled to the point (x,y) . The scaling from the observation's location to each grid point (x,y) is performed using the relative source-to-distance factors provided by the GMM:

$$\begin{cases} Y_{obs,xy,i} = Y_{obs,i} \times \left(\frac{Y_{GMM,xy}}{Y_{GMM,obs,i}} \right) \\ Y_{convobs,xy,j} = Y_{convobs,j} \times \left(\frac{Y_{GMM,xy}}{Y_{GMM,convobs,j}} \right) \end{cases} \quad (3-2)$$

Similarly, the total variance of the updated ground-motion parameter Y at grid point (x,y) is expressed as:

$$\sigma_{Y,xy}^2 = \frac{1}{\frac{1}{\sigma_{GMM}^2} + \sum_{i=1}^n \frac{1}{\sigma_{obs,xy,i}^2} + \sum_{j=1}^m \frac{1}{\sigma_{convobs,xy,j}^2}} \quad (3-3)$$

where σ_{GMM} is the standard deviation of the intra-event error term associated with the GMM: when sufficient observations are present, it is assumed that the inter-event error term is well enough constrained by the bias correction. $\sigma_{obs,xy,i}$ is the standard deviation associated with an observation location at a given distance d from the grid point (x,y) : for instance, $\sigma_{obs,xy,i} = \sigma_{GMM} \cdot f(d)$, where f is decreasing with distance d . Usually, if d tends towards zero, $\sigma_{obs,xy,i}$ tends towards zero (i. e., the observed value becomes the dominant term in near field); and if d tends towards infinity, $\sigma_{obs,xy,i}$ tends towards infinity (i.e., the GMM estimate becomes the dominant in far

field). The functional form and values taken by f depend on the spatial correlation model that is associated with the ground-motion parameter of interest. By default, [Worden et al. \(2010\)](#) propose a radius of 10 km, within which we have $\sigma_{obs,xy,i} < \sigma_{GMM}$; another radius of 15 km is defined, beyond which it is assumed that $\sigma_{obs,xy,i} = \infty$. The radius of influence of observations has a strong influence on the local shape of the shake-map and further sensitivity studies should be performed in order to assess its link with the spatial correlation of the ground-motion parameters. On the other hand, the standard deviation $\sigma_{convobs,xy,j}$ related to the uncertainty associated with macroseismic observations is decomposed into the distance-based standard deviation $\sigma_{obs,xy,j}$ (as detailed above), and the standard deviation of the GMICE (i.e. uncertainty from converting the macroseismic intensity into a ground-motion parameter):

$$\sigma_{convobs,xy,j}^2 = \sigma_{obs,xy,j}^2 + \sigma_{conv}^2 \quad (3-4)$$

The simple equations used by the algorithm prevent the build-up of computational complexity, since the optimization of Eq. (3-1) allows the computation time to remain linearly proportional to the number of grid points ([Worden et al., 2010](#)). This shake-map system is flexible enough to produce updated maps of various types of ground-motion parameters (e.g., PGA, PGV, SA at different periods), as long as the ad-hoc GMMs are available. Shake-maps in terms of macroseismic intensity are also provided, thus making a direct use of the macroseismic testimonies that are collected after the earthquake event. It should be noted that the recent version change of ShakeMap® (from version 3.5 to 4) has introduced a different interpolation scheme, namely the use of the multi-variate normal (MVN) distribution ([Vanmarcke, 1983](#); [Stafford, 2012](#)). The vector of ground-motion parameters \mathbf{Y} (assumed to be normally distributed) is divided into \mathbf{Y}_1 (m prediction sites or grid points) and \mathbf{Y}_2 (n observations sites), with the following expressions for the mean μ and variance Σ :

$$\mu_{\mathbf{Y}} = \begin{bmatrix} \mu_{\mathbf{Y}_1} \\ \mu_{\mathbf{Y}_2} \end{bmatrix} \quad \Sigma_{\mathbf{Y}} = \begin{bmatrix} \Sigma_{\mathbf{Y}_1\mathbf{Y}_1} & \Sigma_{\mathbf{Y}_1\mathbf{Y}_2} \\ \Sigma_{\mathbf{Y}_2\mathbf{Y}_1} & \Sigma_{\mathbf{Y}_2\mathbf{Y}_2} \end{bmatrix} \quad (3-5)$$

Then, given a set of observations $\mathbf{Y}_2 = \mathbf{y}_2$, a vector of residuals is defined as $\square = \mathbf{y}_2 - \mu_{\mathbf{Y}_2}$. Thanks to the MVN, it is possible to express the mean and variance of the set of predictions \mathbf{Y}_1 as follows:

$$\mu_{\mathbf{Y}_1|\mathbf{y}_2} = \mu_{\mathbf{Y}_1} + \Sigma_{\mathbf{Y}_1\mathbf{Y}_2} \cdot \Sigma_{\mathbf{Y}_2\mathbf{Y}_2}^{-1} \cdot \zeta \quad (3-6)$$

$$\Sigma_{\mathbf{Y}_1\mathbf{Y}_2|\mathbf{y}_2} = \Sigma_{\mathbf{Y}_1\mathbf{Y}_1} - \Sigma_{\mathbf{Y}_1\mathbf{Y}_2} \cdot \Sigma_{\mathbf{Y}_2\mathbf{Y}_2}^{-1} \cdot \Sigma_{\mathbf{Y}_2\mathbf{Y}_1} \quad (3-7)$$

The initial mean values of \mathbf{Y}_1 are obtained from a GMM, and the variance-covariance matrix is assembled from the standard deviations associated with the GMM and from the spatial correlation structure of the ground-motion parameter(s) of interest. Therefore, the results from equations (3-6) and (3-7) may be directly used as the updated ground-motion distribution for the generation of the shake-map. [Worden et al. \(2018\)](#) also show that this approach enables the consideration of multiple types of ground-motion parameters (e.g., PGA, SA at different periods) simultaneously: thanks to the cross-correlation structure between some ground-motion parameters (especially spectral responses), it is possible to gain knowledge and constrain shake-maps when only parameters of a given type have been recorded, for instance.

3.1.2 Bayesian Network algorithm

In parallel, [Gehl et al. \(2017\)](#) have proposed an approach based on Bayesian updating of correlated Gaussian fields: the prior distribution of the ground-motion field, consisting of a simple predictive scenario of the earthquake event with a GMM, is updated with the observations in order to generate a posterior distribution of the ground motion at each grid point. To this end, a Gaussian Bayesian Network (BN) models the distribution of a given ground-motion parameter Y at each grid point i (Figure 3-2). Thanks to the lognormal assumption used in most GMMs, a lognormal-normal conversion is able to express the conditional probability of Y_i as a normal distribution, with the mean expressed as:

$$\mu(Y_i|\mathbf{U}, W) = X_i + \sigma_\zeta \cdot \sum_{j=i}^n t_{ij} \cdot U_j + \sigma_\eta \cdot W \quad (3-8)$$

where X_i is the mean estimate of the ground-motion parameter from the GMM, σ_ζ is the standard-deviation of the intra-event term, and σ_η is the standard-deviation of the inter-event term. The matrix of elements t_{ij} results from the Cholesky decomposition of the correlation matrix between the intra-event terms: spatial correlation models such as the one from [Jayaram and Baker \(2009\)](#) may be used to compute this correlation, based on the distances between all grid points and observations. The variables U_j and W follow a standard normal distribution and they are essential to model the statistical dependence between the Y_i , and consequently the updating process: W is related to the inter-event error terms (perfectly correlated across all sites, for a given earthquake), while U_j are related to the intra-event error terms (partially correlated, depending on the inter-site distances).

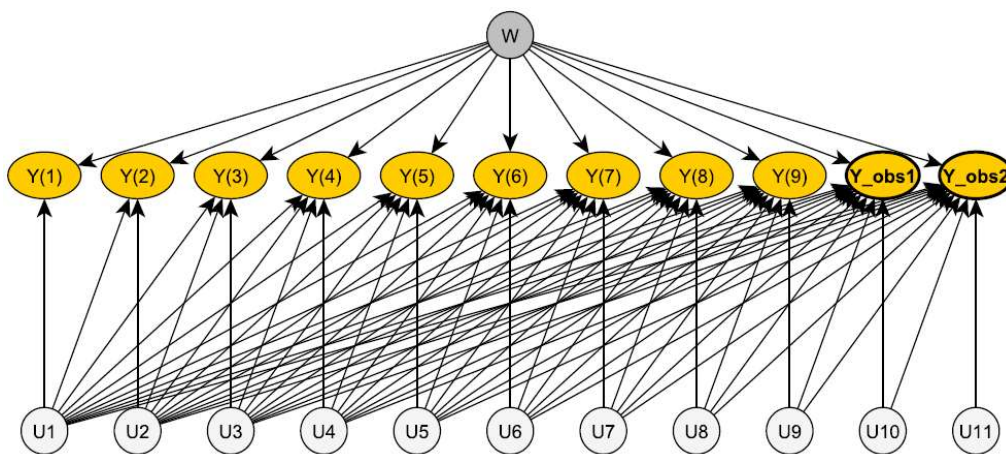


Figure 3-2: Illustration of a BN structure for the generation of a shake-map, with nine grid points $Y(\cdot)$ and two observations Y_{obs} .

Observations, either in the form of ground-motion measurements or macroseismic intensities (with the associated uncertainties), are added to the BN as evidence, and then the posterior distribution of the ground-motion parameters is collected at the variables representing the grid points. In the case the observation results from macroseismic data, the uncertain link between the MI and the reference ground-motion parameter Y_i (e.g., log PGA) is taken into account by

adding an extra node Z_i in the BN, as shown in Figure 3-3. The variable Z_i is assumed to follow a normal distribution conditioned on Y_i , quantified as follows:

$$\begin{cases} \mu(Z_i|Y_i) = f(Y_i) \\ \sigma(Z_i|Y_i) = \sigma_{GMICE,Y_i} \end{cases} \quad (3-9)$$

where f is a function referring to a GMICE, such as the model proposed by [Caprio et al. \(2015\)](#); and σ_{GMICE,Y_i} is the standard deviation related to the GMICE function.

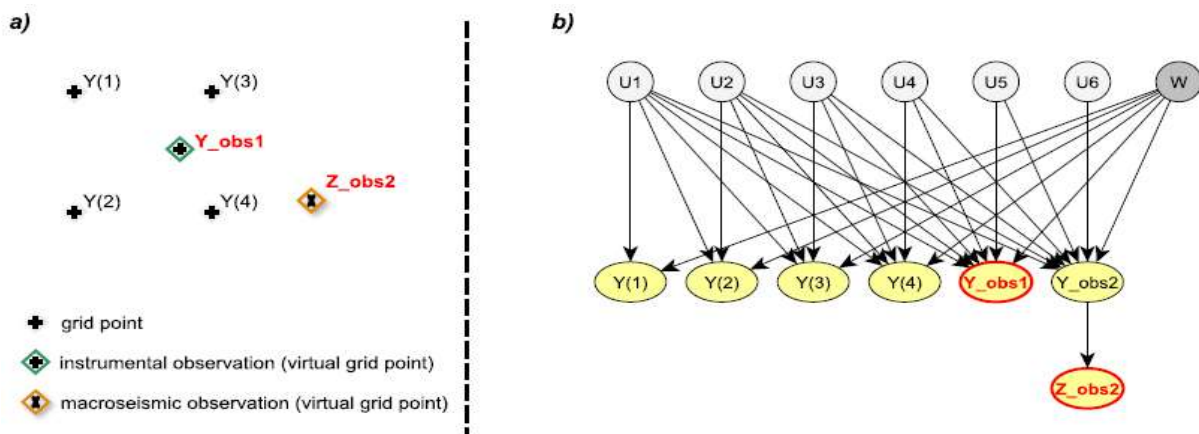


Figure 3-3: (a) Example of a 4-point grid with one instrumental observation (Y_{obs1}) and one macroseismic observation (Z_{obs2}); (b) corresponding BN, where the evidenced nodes are displayed in red.

This approach is able to generate updated maps for the usual ground-motion parameters (i.e., PGA, PGV, SA) as well as macroseismic intensity (Figure 3-4). The Bayesian updating method has been validated by [Gehl et al. \(2017\)](#) on a synthetic case, where the updated ground-motion parameters are shown to be identical to the 'analytical solution' (i.e., resolution of a conditional multivariate normal distribution ([Stafford, 2012](#))). This alternative approach has the merit of generating an exact solution for the uncertainty field associated with the shake-map, and of being transparent about the treatment of spatial correlation (i.e., direct use of correlation models from the literature). To some extent, it is able to model fields of different ground-motion parameters within the same BN, thus taking advantage of cross-correlation between parameters and potentially improving the precision of the shake-map (similarly to ShakeMap® v4). However, the significant epistemic uncertainties related to the choice of GMM and GMICE remain, and the flexibility of BN comes at a higher computational cost than the ShakeMap® v3.5 and v4 methods. Solutions such as the division of the BN into sub-grids have been proposed by [Gehl et al. \(2017\)](#): currently, shake-maps can be processed within a couple of minutes, on the condition that the number of observations to integrate as evidence is not too large (i.e., less than one hundred data points).

3.1.3 Alternative ground-motion inference methods

Apart from the above-detailed updating methods, other ways of generating shake-maps have been investigated by [Douglas \(2007\)](#). The methods are classified according to whether they

take account of the spatial correlation of the ground-motion field. Among the methods ignoring the spatial correlation of shaking, the following ones are mentioned:

- *Unadjusted GMM accounting for site effects*: it merely consists in the application of a GMM to the parameters of the earthquake, while adding amplification factors to the soil conditions.
- *Bias-corrected GMM accounting for site effects*: based on the ground-motion measurements, a global bias adjustment is performed on the GMM, in order to account for the actual inter-event variation. This approach is similar to the bias adjustment performed in the ShakeMap® v3.5 algorithm.
- *Derivation of an event-specific GMM*: if there are sufficient ground-motion measurements, a specific GMM with a simple functional form may be regressed from the data, in order to account for both the rate of decay and the inter-event bias.

Two methods accounting for the spatial correction of shaking are also detailed by [Douglas \(2007\)](#):

- *Universal kriging*: it is a geostatistical method that consists of kriging with a drift model, which accounts for data (i.e., the ground-motion measurements) and an underlying trend (i.e., decay with the epicentral distance). An exponential semi-variogram, with a distance parameter a (which needs to be defined), is used in order to model the spatial correlation between the observations and the sites of interest.
- *Adapted method of King et al. (2004)*: observations are weighted with respect to their distance to the sites of interest, and a GMM is used for correcting differences in epicentral distance (between the sites and the observations).

In [Douglas \(2007\)](#), all these methods are tested on ground-motion data from the 2004 Les Saintes earthquake (Guadeloupe, France) and the results are compared to the ones obtained using the ShakeMap® approach. It is found that the more elaborate methods accounting for spatial correlation are associated with lower aleatory variability and provide similar results in the vicinity of observations. However, at locations that are more than 10 km away from the nearest observation, much larger uncertainties (both aleatory and epistemic) are observed, with little leeway to better constrain the ground-motion field.

Various geostatistical interpolation techniques (e.g., kriging and cokriging methods) have also been benchmarked by [Costanzo \(2018\)](#) in order to derive shake-maps in terms of Arias Intensity and Cumulative Absolute Velocity for the M_w 6.0 Amatrice and the M_w 6.5 Norcia earthquakes in 2016. A comparison of the author's maps – based on various modelling assumptions – with the official shake-maps published after the two events has led to the identification of current needs for the further improvement of shake-maps: extended regression models between macroseismic intensity and ground-motion parameters, introduction of local site effects, and integration of near-source effects when converting ground-motion parameters to macroseismic intensity.

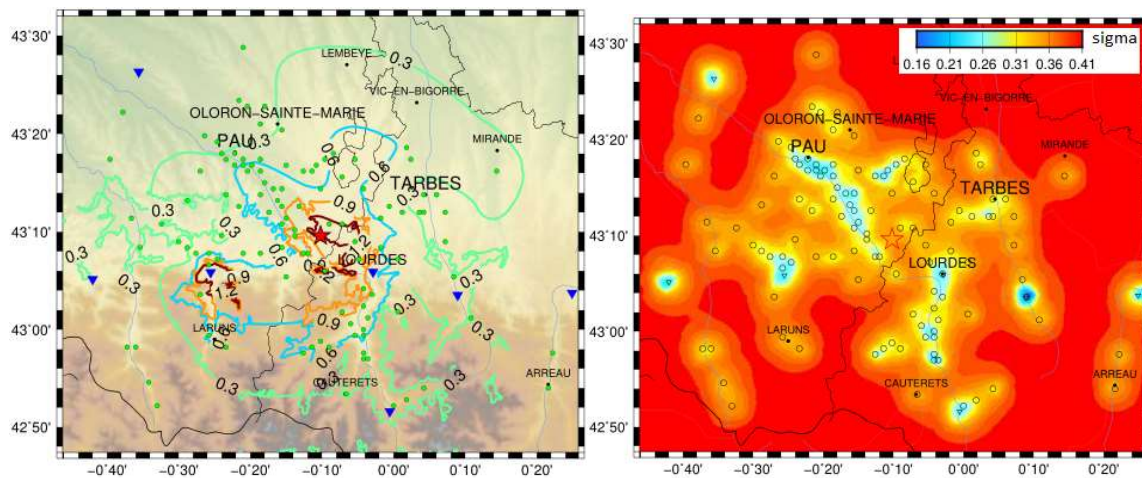


Figure 3-4: Shake-map generated with the Bayesian updating approach for the M 4.3 Lourdes (France) earthquake of December 30th, 2012. Left: contour of PGA (in %g); Right: field of associated uncertainty $\sigma_{\ln PGA}$. Triangles represent ground-motion measurements and circles are macroseismic observations.

3.2 Shake-maps based on an experience-based approach for areas with sparse seismic networks

3.2.1 Overview

Shake-maps refer to concepts of web-based intensity assignments and the use of recorded ground motions (in case of the existence of a refined seismic network) to correlate the instrumental data with the reported observations and to derive initial estimates of the consequences. For earthquake regions with low to medium seismicity the required comprehensive seismic instrumentation is normally not available and damage-related registrations are still missing, experience of historical earthquakes and macroseismic observations (in terms of intensities) could be still taken as primary input.

This section gives an overview of how to generate macroseismic shaking maps based on macroseismic observations and their systematic evaluation, and how local or regional characteristics of site amplification (anomalies) could be inserted (see also section 6.1, Figure 6-1). An evaluation of available information on the existing building stock, the construction types and building categories provides the basis to describe the grade of "impact" in different fields of interest. The relevant tools use databases and damage models which are related to the European Macroseismic Scale EMS-98 and the empirical intensity concept (cf. WP4).

3.2.2 General Procedure

The generation of macroseismic maps has a long tradition in engineering seismology. Especially in the times before instrumental measurements were available, they were the only information about the location (epicentre) and the strength of an earthquake. Traditionally, questionnaires with the descriptions of observable effects regarding objects, damage to buildings and the impact on humans were used to determine the intensity (related to the used macroseismic scale) and to create a map of shaking effects (shake-map) based on the locations. They are the main source to estimate the magnitude of an earthquake in pre-instrumental times (see Figure

3-5: section “Macroseismic observations / Felt reports” and “SM1: Traditional”). The abbreviation “SM” stands for shake-map and is used in the following. Nowadays, on the basis of such surveys and related ground motion prediction equations (GMPE), these data are used to generate shake-maps automatically (e.g. Wald et al., 1999a,b, see Figure 3-5: SM3 and SM4+SM6 = hybrid shake-map HSM46*). The ground-motion related procedure was developed for the high seismicity region of California, and later applied in other regions in the Central and Eastern United States as well. It is used system worldwide via the shake-map-system with partially local adjustments. It is an efficient tool to get a first idea about extent and severity of shaking in terms of ground motions and therefore instrumental intensity assignments. The calculated intensity maps may provide the institutions responsible for disaster management with decision criteria to organize rescue teams and technique in the most affected regions, where higher damage has to be expected. To create the shake-maps within minutes, it is necessary to have sufficient data (a dense mesh of instrumentation) and appropriate ground-motion models. These are the principle limitations in case of low to moderate seismic regions as e.g. Germany.

Figure 3-5 displays approaches that can be implemented in Central Europe to obtain a shake-map.

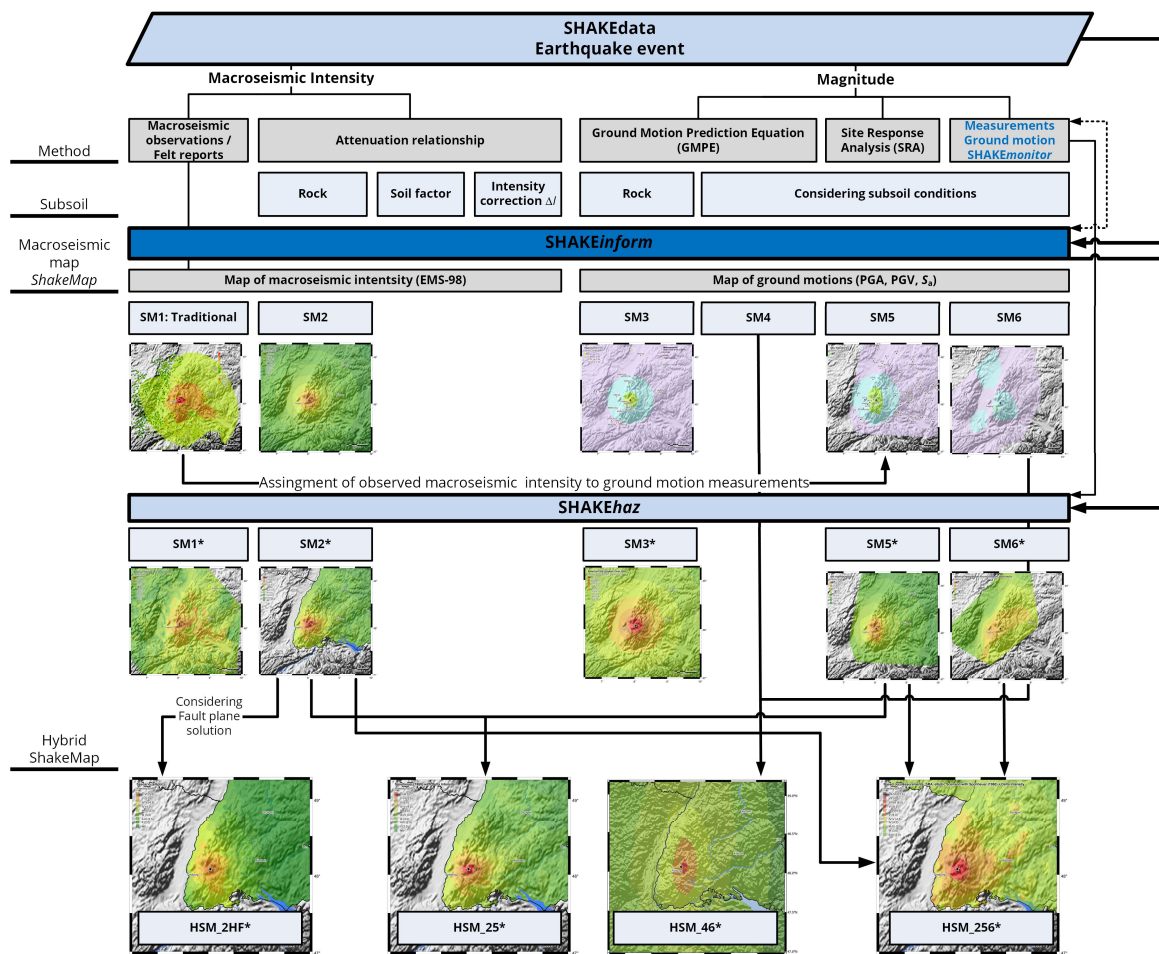


Figure 3-5: Shake-map generation procedures (Schwarz et al., 2006, 2008a; Beinersdorf, 2016) – example shown here: 2004 Waldkirch earthquake Germany M_w 4.6; * denotes a corresponding macroseismic intensity map.

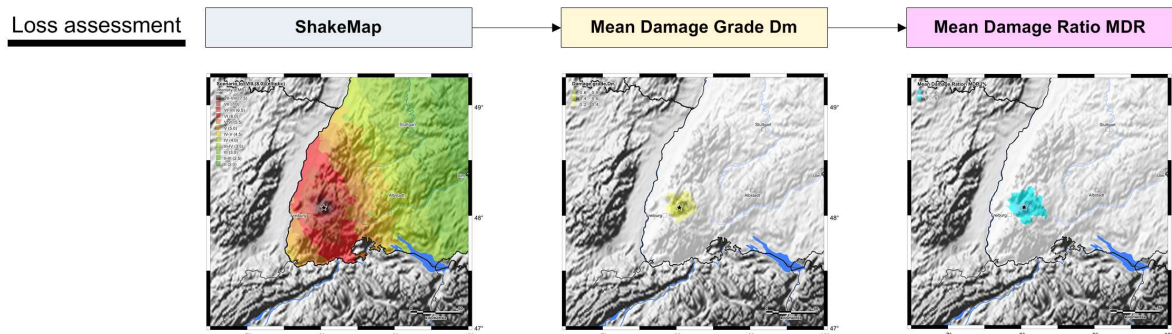


Figure 3-6: Usability of shake-maps for loss assessment (Schwarz et al., 2006, 2008a; Beinersdorf, 2016): radial scenario with ΔI (SRA) of 2004 Waldkirch earthquake with an hypothetical intensity $I_0 = VIII$

SHAKEdata (s. Figure 3-5: top section) includes the collection of data, whether by questionnaire, internet query or interactive web services. It includes aerial photography and the processing of spatial data (especially also after the event itself), as well as on-site surveys or the evaluation of damage surveys. SHAKEinform processes the status of data collection and derives information for various user groups from it. The aim is to provide information at short notice, such that the processing of empirical values (e. g. historical earthquakes) is useful in advance. Maps of shaking effects (SHAKEhaz) can be generated based on the regional characteristics with regard to the impact models (e. g. by taking into account amplification effects due to the subsoil conditions).

In general, only a few strong motion recordings are available in low to medium seismic regions (SM6, SM6*). Therefore, it is necessary to replace the missing input data (at fictive supporting points) by appropriate functions. These functions can be attenuation relationships based on the physical decrease of the wave energy (e. g. radial, elliptic – direction-dependent, taking into account subsoil or rock conditions. Directly after detection of an event it is possible to an attenuation of macroseismic intensity (SM2) or a ground motion prediction equation (GMPE) (SM3). SM3 can be transferred to a macroseismic intensity map (SM3*) using ground motion intensity conversion equation (GMICE, cf. section 5.3). To consider the deep geology, a site response analysis (SRA) can be performed on the basis of soil profiles or by using H/V spectral ratios from noise measurements (SM5, SM5*). The topography can also be considered by slope-related modification factors (SM4). Depending on the knowledge level and the density of points, combinations of these data can be used to generate hybrid shake-maps.

Shake-maps as presented in Figure 3-5 can be used to assign mean damage grade D_m and the mean damage ratio MDR on the basis of statistical data concerning the building stock composition, vulnerability functions of building types, and assets (see Figure 3-6, Schwarz et al., 2006, 2008a, 2016). They provide the direct entry to Rapid Response and Loss Estimates.

Figure 3-5 and Figure 3-6 present a stepwise approach to calculate shake-maps. Depending on the state of knowledge in the respective region, simplified procedures with only one input variable such as magnitude or comprehensive procedures with knowledge of 3D geology as well as specific ground motion models can be applied. This can be adapted in a modular way, depending on the level of knowledge. The conversion to macroseismic intensity is given at any time.

4 RANKING OF GROUND-MOTION MODELS

Subtask 3.3.2 of the TURNkey project aims at improving estimates of ground motion (and uncertainty estimates) at sites of interest in the time between earthquake occurrence and the arrival of the strong shaking, particularly in the aftershock period for emergency response purposes. Thus, this subtask:

- 1) selected the optimal ground motion model for the TBs,
- 2) improved estimates of ground motion parameters for EEW, particularly in the aftershock period and for emergency response purposes in RRE applications,
- 3) assessed the uncertainties associated with EEW estimates,
- 4) performed a noise study with the aim of assessing the performance of the low-cost sensors used in TURNkey alongside with reference instrumentation for its use in EEW applications.

Objective (3) has been already addressed in the Deliverable D3.1 – Part 2, while the activities related with objective (4) will be included in the Deliverable D2.9. Therefore, the focus of both this section and Section 5.1 is to describe the activities aimed at a fast and accurate prediction of ground shaking. These are achieved through objectives (1) and (2). Specifically, concerning objective (1), a Python code for ranking Ground Motion Models (GMMs) was developed, while objective (2) was addressed with a Python code for updating of GMM coefficients.

4.1 Introduction

GMMs, also known as Ground Motion Prediction Equations (GMPEs) or attenuation relationships, are empirical models, which allow estimation of the earthquake ground motion expected at a given site (i.e. a ground motion intensity measure) from a set of explanatory variables describing the source, wave propagation path and site response (Akkar et al., 2012). Over the last decades, the functional forms that have been proposed for the ground motion models vary in the level of complexity of their parameters and their derivation techniques. The first ground motion model was magnitude- and distance-dependent and no standard deviation was reported for the equation (Esteva and Rosenblueth, 1964). Since then, the number of empirical prediction equations that have been published has exceeded 400 (Figure 4-1). Significant effort has been made to address the variability associated with the models and its components, as well as to define more precisely the epistemic uncertainties involved (Douglas and Edwards, 2016).

Nowadays, the models are usually (but not only) given in terms of PGA (Peak Ground Acceleration), PGV (Peak Ground Velocity) and pseudo-SA (Spectral Acceleration) for 5% of critical damping and they are commonly based on the geometrical mean of the two horizontal components (GM) or the RotD50 component (Boore, 2010). The standard practice uses the random-effect model proposed by Abrahamson and Youngs (1992) or the maximum likelihood regression method (Joyner and Boore, 1993) to estimate the coefficients of the model. The principal parameters in the GMMs include the magnitude, style-of-faulting, source-to-site distance and the site characteristics. Besides, there have been multiple attempts to include additional independent variables that model the ground motion behaviour in a more realistic manner such as the hanging wall effect or the dip angle.

The main source variable is the magnitude and it is usually included through a nonlinear scaling. The moment magnitude (M_w) is often preferred because, unlike other magnitudes (e.g.

M_L , M_d), it does not saturate. The style-of-fault defines the fault mechanism as normal, reverse or strike-slip. In addition, some recent models account for the impact that the top of the rupture plane (Z_{TOR}) can make on the ground motion (e.g. Boore et al., 2014; Campbell and Bozorgnia, 2014) or a variable considering the directivity of the earthquake ground motion field (Spudich et al., 2014).

The wave propagation path parameters are incorporated in the functional form by using source-to-site distance measurements (e.g. epicentral distance R_{epi} , hypocentral distance R_{hyp} , Joyner-Boore distance R_{JB} , or rupture distance R_{rup}). Although the point-sources distance metrics (R_{epi} and R_{hyp}) were the most common measurements in the past but the extended-sources distance metrics (R_{JB} and R_{rup}) have become more popular, because they present a more appropriate variation of the ground motion amplitude at the sites close to the source. Recent models derive the coefficients of their functional forms for different types of distance, providing simultaneously ground motion predictions for several distance types (e.g. Akkar et al., 2014; Ameri et al., 2017). Furthermore, regional effects are sometimes available in the GMMs, capturing the suggested regional dependence of the ground motion (e.g. Abrahamson et al., 2014; Chiou and Youngs, 2014).

The site response is incorporated in the ground motion model by the site characterisation variable, which is expressed either in terms of V_{s30} (average shear-wave velocity in the top 30 m) or defined by the site class. The latter can be categorised based on the NEHRP (BSSC - Building Seismic Safety Council, 2001) or the EC8 (CEN, 2003), for example. Both types of site characterisation represent near-surface conditions. In addition, some GMMs consider either the depth to the 1 km/s ($Z_{1.0}$) or 2.5 km/s ($Z_{2.5}$) velocity horizons (Boore et al., 2014; Campbell and Bozorgnia, 2014), since they capture the effect of deeper structures on the ground motion. Despite the great advances in recent investigations, ground motion characterisation is still a topic of research. Therefore, the ground motion derivation techniques are expected to be improved and models that are now available are likely to be updated.

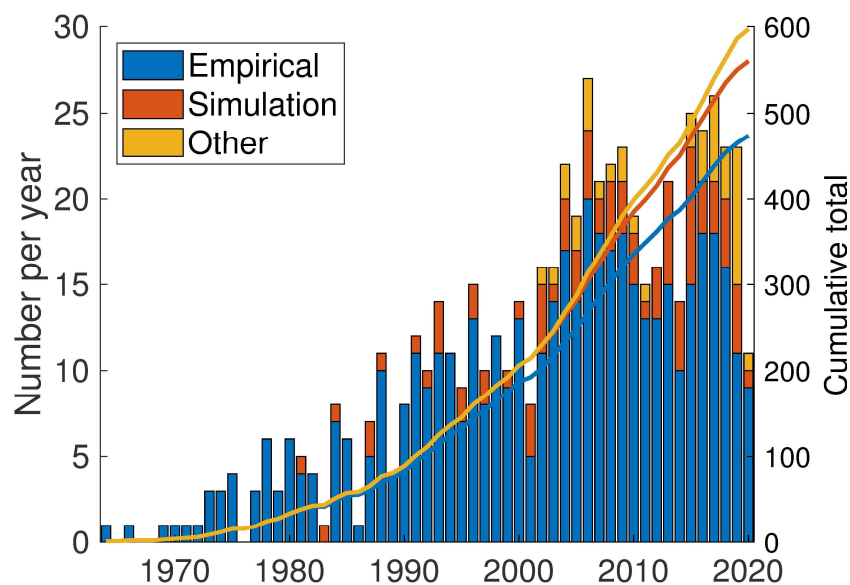


Figure 4-1: Graph showing the number of GMMs published each year (columns) and their cumulative total number (lines) [<https://www.gmpe.org.uk>. Last updated: 14 January 2021].

The rapidly increasing number of GMMs has led to two main procedures to identify the GMMs that are most suitable for the site under investigation: admittance criteria and rejection criteria. The former is based on the analyst's knowledge to determine the most appropriate GMMs, which is often based on familiarity with specific models.

The rejection criteria approach is recommended to avoid this subjectivity by initially considering all the published ground motion models (i.e. those included in the comprehensive summary of available GMMs worldwide compiled by Douglas, <https://www.gmpe.org.uk>) and then rejecting those that do not satisfy the conditions of the state-of-art. The candidate models obtained in this pre-selection phase are then used as input for data-driven selection methods capable to assign a score to each candidate GMM, thus ranking the GMMs according to their performance with respect to a common dataset.

The methodology adopted in the tool developed in Subtask 3.3.2 is described in the following sections.

4.2 Pre-selection of GMMs

One of the most commonly adopted rejection criteria are the so-called exclusion method proposed by Cotton et al. (2006) and updated by Bommer et al. (2010). This method consists in reducing the complete list of published ground motion models found in the literature to the possible smallest set of independent models that would be appropriate to represent the particular target area. The method suggested to reject models: (1) derived for an inappropriate tectonic regime; (2) not published in a peer-reviewed journal; (3) with insufficient documentation on the calibration dataset; (4) superseded by a more recent publication; (5) with the period range not appropriate for engineering applications; (6) with inappropriate functional form (i.e. lacking either non-linear magnitude dependence or magnitude-dependent decay with distance); (7) obtained with inappropriate regression method. Besides these general criteria, target-specific pre-selection criteria can also be defined.

The tool for ranking GMMs uses the GMMs library included in OpenQuake engine (<https://github.com/gem/oq-engine/#openquake-engine>). This library, which is open-source and continuously updated with newly published GMMs, was enriched by test-bed specific GMMs, which were purposely coded in Python language. They include the GMMs by (Sokolov et al., 2008) for TB-1, (Tapia, 2006) for TB-2, (Kowsari et al., 2020b) for TB-3, (Boore et al., 2020) for TB-4, (Lanzano et al., 2020) for TB-5, (Bommer et al., 2019) and the GMM included in Ruigrok and Dost (2020) for TB-6.

The tool requires a list of candidate GMMs as input, which have to be selected a priori using, for example, the exclusion method proposed by Cotton et al. (2006) and updated by Bommer et al. (2010).

4.3 Screening of database

The tool for ranking GMMs is shipped with the European Strong Motion flatfile (Lanzano, 2018), but custom databases can also be used (i.e. local database).

The tool allows defining a subset of the catalogue to be used for ranking GMMs, in order to satisfy pre-defined requisites specified by the user in terms of:

- range of magnitudes to be considered;
- range of Joyner-Boore distances to be considered;

- range of event depths to be considered;
- list of focal mechanisms to be considered;
- list of EC8 soil classes to be considered;
- range of Vs30 to be considered;
- list of proximity codes to be considered;
- range of sensor depths to be considered;
- list of nations to be considered, in which events are located;
- list of nations to be considered, in which stations are located;
- list of structural periods to be considered.

In order to apply complex GMMs, which requires an accurate characterization of the fault rupture plane, missing parameters from the earthquake catalogue are computed through the (Kaklamanos et al., 2011) relationships, which allows estimating R_{rup} and R_X (horizontal distance to top edge of rupture measured perpendicular to the strike (site coordinate) from M_W , R_{JB} , source-to-site azimuth (assumed to be $\alpha=50^\circ$ if not known) and geometry of the fault plane. Kaklamanos et al., (2011) suggest also standard methods useful to estimate the parameters characterizing the fault plane (width, *dip*, Z_{TOR}), if not known, along with useful relationships to estimate $Z_{1.0}$ and $Z_{2.5}$. If the *rake* angle is unknown, the following values are assumed in the tool according to the focal mechanism: *rake*= -90° for normal faults, *rake*= 90° for reverse faults and *rake*= 0° for strike-slip faults. Similarly, if Vs30 is unknown, the following values are considered: Vs30=150 m/s for EC8 soil category 'D', Vs30=250 m/s for EC8 soil category 'C', Vs30=500 m/s for EC8 soil category 'B' and Vs30=1000 m/s for EC8 soil category 'A'.

4.4 Scoring methods

Scoring methods used for ranking GMMs selection may have limitations (Arroyo et al., 2014; Roselli et al., 2016). Therefore, it has been decided to adopt multiple scoring techniques to measure the performance of the models. In the specific, we have considered 5 methods: the log-likelihood (LLH), the pari-mutuel gambling score, the quantile score, the Euclidean metric distance (EMD) and the Deviance Information Criterion (DIC).

4.4.1 Log-likelihood

This is one of the most common algorithms to score GMMs. Initially proposed by Scherbaum et al. (2009), it allows assessing the relative performance of various GMMs against a ground-motion dataset. The algorithm is based on the probability that an observed ground motion is actually realized under the hypothesis that a model is true (Beauval et al., 2012). The negative average LLH (Delavaud et al., 2012) measures the distance between a model and the data-generating distribution as:

$$LLH = -\frac{1}{N} \sum_{i=1}^N \log_2(g(x_i)) \quad (4-1)$$

in which N is the number of observations x_i , g is the probability density function (assumed to have a normal distribution) predicted by the GMM, and \log_2 is the logarithm with base 2. A small

LLH indicates that the candidate model is close to the model that has generated the data, while a large LLH corresponds to a model that is less likely of having generated the data.

The quality of LLH depends on the relationship between the model g and the set of observations x . If x has been used for the derivation of the model, the model will appear better than it really is, by an amount that depends on the degrees of freedom of the model.

4.4.2 Pari-mutuel gambling score

The original method by [Zechar and Zhuang \(2014\)](#) has been adapted by [Lanzano et al. \(2020\)](#) for scoring GMMs. The comparison of the performance of several GMMs is considered in terms of gambling or betting. Let us assume we have m bettors (or m models) that at the end of every game split the total sum of the bets in a way that reflects their forecast skill. The return of each bettor is the ratio of the amount that the bettor wagered on the outcome to the total amount wagered on the outcome, multiplied by the size of the 'pot'; hence the net return for the j -th forecast/model is denoted as the pari-mutuel gambling score:

$$G_j = \frac{1}{N} \sum_{i=1}^N \left(-1 + m p_{ij} \frac{1}{\sum_{j=1}^m p_{ij}} \right) \quad (4-2)$$

where N is the number of observations, $p_{ij} = 2(1 - \Phi)$ is the probability of the normalized residual of being exceeded and it is evaluated from the cumulative normal distribution function (Φ) [i are the observations and j the models]. The gambling scores can be positive or negative and they sum to 0. The best performance is reached for the largest positive value.

4.4.3 Quantile score

In this method, probabilistic forecasts of a continuous quantity (e.g. strong motion variable) take the form of predictive quantiles. If we assume that α is the desired quantile, r is the forecaster quantile (obtained through the normal inverse cumulative distribution function of a quantity related to the desired quantile) and ω is the observed value (assumed to be the normalized residual), the scoring rule is:

$$S(r; \omega) = (\omega - r)(1\{\omega \leq r\} - \alpha) \quad (4-3)$$

As in the case of the pari-mutuel gambling score, the original quantile method (Gneiting and Raftery 2007) has been adapted by [Lanzano et al. \(2020\)](#) for scoring GMMs. This method penalizes the residuals on the tails of the distribution by a greater extent than those in the body of the distribution, which are rewarded. It was introduced by (Lanzano et al. 2020) to overcome the limitation of the LLH method, which seems to assign a better artificial performance to models with larger standard deviations if the observed data differ from the median estimations.

4.4.4 Euclidean metric distance

The method proposed by [Cremen et al. \(2020\)](#) leverages a statistical tool from sensitivity analysis to quantitatively compare the distribution of residuals from a GMM with the

distribution expected for an exact fit of the model to the underlying observations. The Euclidean metric distance can be calculated as:

$$EMD_x = \sqrt{(\mu_x - \mu_0)^2 + (\sigma_x - \sigma_0)^2} \quad (4-4)$$

in which x refers to the normalized inter-event or intra-event residuals, μ_x and σ_x are the maximum-likelihood estimates of the mean and standard deviation (observed case), respectively, and μ_0 and σ_0 are the mean and standard deviation of the standard normal distribution (perfect case), respectively. The final score for the proposed evaluation procedure is a combination of the inter-event and intra-event EMDs. The smaller the score, the closer the residuals are to the ideal distribution and the better the model.

4.4.5 Deviance Information Criterion

The DIC (Kowsari et al., 2019) is a Bayesian generalization of the well-known Akaike information criterion (AIC). It is used within Bayesian statistical models and is adjusted for posterior inference based on Markov chain Monte Carlo (MCMC) algorithms.

In the method two assumptions that include the prior and posterior standard deviations are made in the context of Bayesian statistical analysis. The DIC value with the prior sigma, i.e., when ranking a GMM using its published sigma, is basically the same as in the LLH, but with different score values. The novelty of this method is the posterior distribution of sigma, which is obtained for a GMM based on the observed ground motions. In this case, the DIC shows the deviance of predicted values from the observed ground motions that is representative of the aleatory variability in the region under study. The DIC with a posterior sigma ranks models more favourably when they are associated with smaller bias between median GMM predictions and the observed ground motions, and the corresponding posterior standard deviation is close to the aleatory variability of the ground motions in the region under study, for the given dataset.

4.5 Ranking

The scoring methods are applied in the tool separately for each considered intensity measure (IM), namely the PGV, PGA or SA at selected structural periods.

In order to combine the different scores and produce a global ranking, the following procedure is adopted:

- 1) computation of the average score for each method and GMM, by averaging across the considered IMs;
- 2) computation of the ranking for each method, by assigning a cardinal number to each GMM (0 corresponds to the worst-performing GMM);
- 3) computation of final ranking by summing the ranking for each GMM (across the five considered methods).

4.6 Application examples: ranking of GMMs for TB-4 and TB-6

The tool has been applied for TB-4 and TB-6 considering local catalogues. The magnitude-distance distribution of the recordings from TB-4 adopted to rank GMMs is provided in Figure

4-2. The catalogue for TB-6 is described in [Ruigrok and Dost \(2020\)](#). It contains 3289 PGV values from 114 events obtained from recordings of induced seismicity in the Netherlands. The magnitudes of the events vary between 1.5 and 3.6. The location of the events and the magnitude-distance distribution of the recordings is shown in Figure 4-3. The catalogue is dominated by events related to the Groningen gas field, where hypocentral depths are approximately 3 km.

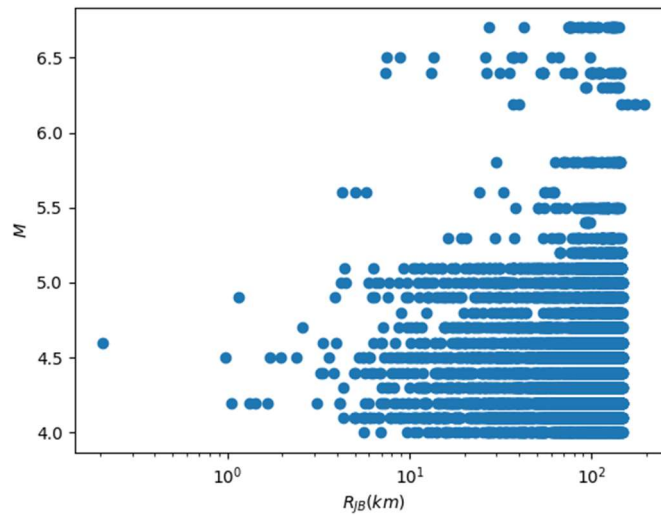


Figure 4-2: Magnitude-distance distribution of the 5790 recordings (from 273 events) used to rank GMMs for TB-4.

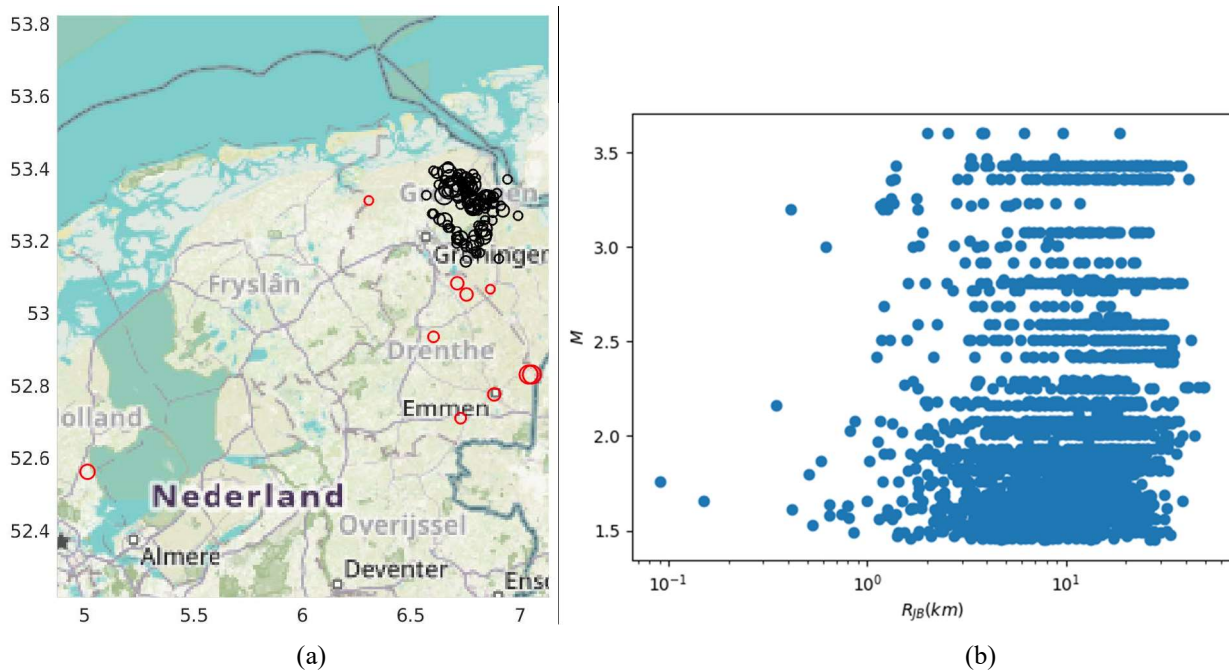


Figure 4-3: (a) Map showing events within the PGV database for $M > 1.5$. 103 events (black circles) are related to the Groningen gas field, the remaining 11 events (red circles) are related to other gas fields. From [Ruigrok and Dost \(2020\)](#). (b) Magnitude-distance distribution of the 3260 PGV values used to rank GMMs for TB-6.

4.6.1 GMM ranking for TB-4

Table 4-1 lists the 14 pre-selected GMMs for TB-4.

Table 4-1: List of pre-selected GMMs for TB-4, along with their main characteristics, namely: region of data used for the development of the model, horizontal component, magnitude range, distance range, distance metric and site characterization

ID	Reference	Region	Horizontal component	Magnitude (Mw)	Distance (km)	Distance metric	Site characterization
ASK14	Abrahamson et al. (2014)	World	RotD50	3.0-7.9	0-300	R_{rup}	Vs30
ASB14	Akkar et al. (2014)	Europe and Middle East	GM	4.0-7.6	0-200	R_{JB} , R_{epi} , R_{hyp}	Vs30
AM17	Ameri et al. (2017)	Europe and Middle East	GM	3-7.6	0-200	R_{JB} , R_{epi}	4 EC8 Classes
ITA10	Bindi et al. (2011)	Italy	GM	4.1-6.9	0-200	R_{JB}	5 EC8 Classes
BND14	Bindi et al. (2014)	Europe and Middle East	GM	4.0-7.6	0-300	R_{JB} , R_{hyp}	4 EC8 Classes, Vs30
BSSA14	Boore et al. (2014)	World	RotD50	3.0-7.9	0-400	R_{JB}	Vs30
BSSA21	Boore et al. (2021)	Greece	RotD50	4.0-7.0	0-300	R_{JB}	Vs30
CB14	Campbell and Bozorgnia (2014)	World	RotD50	3.0-7.9	0-300	R_{rup}	Vs30
CZ15	Cauzzi et al. (2015)	World	GM	4.5-7.9	0-150	R_{rup}	4 EC8 Classes, Vs30
CY14	Chiou and Youngs (2014)	World	RotD50	3.1-7.9	0-400	R_{rup}	Vs30
DBC14	Derras et al. (2014)	Europe and Middle East	GM	3.0-7.6	0-550	R_{JB}	Vs30
HG20	Huang and Galasso (2019)	Italy	RotD50	4.0-6.9*	0-250	R_{JB}	3 Classes (soft soil, stiff soil, rock)
KS15	Kuehn and Scherbaum (2015)	Europe and Middle East	GM	4.0-7.6	0-200	R_{JB}	Vs30
ITA18	Lanzano et al. (2019)	Italy	RotD50	4.0-8.0	0-200	R_{JB} , R_{rup}	Vs30

In case of models developed for several distance metrics (ASB14, AM17, BND14, ITA18) or different parameters for site characterization (BND14, CZ15), the performances for all possible combinations have been evaluated.

In order to test the GMMs listed in Table 4-1, the GMMs by KS15 was also implemented into OpenQuake, while HG20 was kindly provided in OpenQuake format by Kenneth Otárola (UCL). The tool for ranking GMMs was applied considering the PGA as intensity measure. The results are provided in Table 4-2. The best five GMMs turned out to be: ITA18- R_{JB} (score 106), ITA10 (score 102), HG20 and ITA18- R_{rup} (score 101), BSSA21 (score 87). For TURNkey, both ITA18 and the Greek BSSA21 will be adopted, thus replacing BSSA14, which was used for computations in TB-4 until now.

Table 4-2: Ranking of GMMs for TB-4 considered in this study. The five GMMs with highest final ranking are highlighted in bold.

GMM	LLH		G		Q		EMD		DIC		FINAL ranking
	score	ranking	Score	ranking	score	ranking	score	ranking	score	ranking	
ASK14	2.72	4	-0.21	6	0.82	4	1.48	4	18938.74	4	22
ASB14- R_{JB}	2.57	5	-0.27	3	0.83	5	1.37	5	17569.45	7	25
ASB14- R_{epi}	2.32	14	-0.16	12	0.92	13	1.09	14	16817.33	17	70
ASB14- R_{hyp}	2.42	12	-0.19	9	0.89	11	1.20	10	17237.79	14	56
AM17- R_{JB}	2.23	16	0.06	17	1.01	16	0.92	15	17322.17	12	76

AM17-R _{epi}	2.18	17	0.13	18	1.05	18	0.86	17	17073.71	15	85
ITA10	1.95	21	0.46	20	1.10	19	0.18	21	15347.01	21	102
BND14-R _{JB} -Vs30	2.44	9	-0.22	5	0.88	8	1.26	8	17344.33	11	41
BND14-R _{hyp} -Vs30	2.49	8	-0.21	7	0.87	7	1.32	6	17660.38	6	34
BND14-R _{JB} -EC8	2.39	13	-0.18	11	0.90	12	1.12	12	17351.79	9	57
BND14-R _{hyp} -EC8	2.24	15	-0.05	15	0.97	15	0.89	16	16944.24	16	77
BSSA14	2.42	11	-0.08	14	0.93	14	1.12	13	17308.48	13	65
BSSA21	2.14	18	0.05	16	1.02	17	0.76	18	16320.69	18	87
CB14	3.04	2	-0.26	4	0.76	3	1.87	1	19591.06	2	12
CZ15-Vs30	2.99	3	-0.36	2	0.72	2	1.54	3	19485.10	3	13
CZ15-EC8	3.11	1	-0.38	1	0.68	1	1.61	2	19814.48	1	6
CY14	2.57	6	-0.10	13	0.89	10	1.29	7	17829.46	5	41
DBC14	2.51	7	-0.18	10	0.84	6	1.16	11	17348.35	10	44
HG20	2.00	19	1.43	22	1.21	22	0.71	19	16047.66	19	101
KS15	2.43	10	-0.21	8	0.88	9	1.23	9	17374.23	8	44
ITA18-R_{JB}	1.94	22	0.45	19	1.10	21	0.17	22	15287.64	22	106
ITA18-R_{rup}	1.97	20	0.48	21	1.10	20	0.20	20	15474.40	20	101

4.6.2 GMM ranking for TB-6

Table 4-3 lists the 8 pre-selected GMMs for TB-6 (selected from the list of available GMMs in OpenQuake).

Table 4-3: List of pre-selected GMMs for TB-6, along with their main characteristics, namely: region of data used for the development of the model, horizontal component, magnitude range, distance range, distance metric and site characterization.

ID	Reference	Region	Horizontal component	Magnitude	Distance (km)	Distance metric	Site characterization
ASB14	Akkar et al. (2014)	Europe and Middle East	GM	4.0-7.6 (Mw)	0-200	R _{epi} , R _{hyp}	Vs30 ₀
Atkinson2015	Atkinson (2015)	World	RotD50	3.0-6.0 (Mw)	<40	R _{hyp}	-
BindiEtAl2014RhypEC8NoSOF	Bindi et al. (2014)	Europe and Middle East	GM	4.0-7.6 (Mw)	0-300	R _{hyp}	4 EC8 Classes
DostEtAl2004	Dost et al. (2004)	Netherlands	GMRotD100	0.8-4.9 (ML)	<25	R _{hyp}	-
BOM19GM	Bommer et al. (2019a)	Netherlands	GM	1.8-3.6 (ML)	<35(50)	R _{epi}	-
BMR2GM	Ruigrok and Dost (2020)	Netherlands	GM	1.5-3.6 (ML)	<150 km	R _{hyp}	-
DouglasEtAl2013Stochastic	Douglas et al. (2013)	Mainly geothermally related (stochastic simulations)	GM	1*-4*(Mw)	<20	R _{hyp}	-
ZalachorisRathje2019	Zalachoris and Rathje (2019)	Texas, Oklahoma, and Kansas	RotD50	3.-5.8 (Mw)	4-500	R _{hyp}	Vs30

In case of models developed for several distance metrics (ASB14) or different parameters corresponding to several values of stress drop (1 bar, 10 bar, 100 bar), attenuation quality factor Q (200, 600, 1800) and high-frequency kappa (0.005, 0.02, 0.04, 0.05 s) (DouglasEtAl2013Stochastic), the performances for all possible combinations have been evaluated.

The tool for ranking GMMs was applied considering the PGV as intensity measure. The results are provided in Table 4-4. The best four GMMs turned out to be:

DouglasEtAl2013StochasticSD010Q600K005 (score 173), BMR2GM (score 164), DouglasEtAl2013StochasticSD100Q200K005 (score 163), DouglasEtAl2013StochasticSD100Q1800K020 (score 162). Currently, the BOM19GM has been implemented in the operational process by gas field operator NAM. Within Groningen, KNMI uses the GMM V6 model (Bommer et al., 2019b) for shake maps. This model is rather complex and has not been implemented in OpenQuake within TURNkey. Outside of Groningen, KNMI uses BMR2GM to produce PGV shake maps for $M > 1.9$ events.

Table 4-4: Ranking of GMMs for TB-6 considered in this study. In bold are highlighted the four GMMs with highest final ranking.

GMM	LLH		G		Q		DIC		FINAL ranking
	score	ranking	Score	ranking	score	ranking	score	ranking	
ASB14-Repi	3.87	16	-	25	0.35	14	11783.66	18	73
ASB14-Rhyp	5.67	7	0.16	-	0.19	6	13344.92	8	35
Atkinson2015	3.02	22	0.54	14	0.60	23	11029.24	23	89
BindiEtAl2014RhypEC8NoSOF	1.77	33	-	21	1.10	35	8077.96	33	142
DostEtAl2004	6.22	3	0.29	41	0.15	5	14081.18	6	25
BOM19GM	1.49	41	0.68	11	0.98	32	6545.69	41	149
BMR2GM	1.1	44	0.9	39	1.1	37	5236.19	44	164
DouglasEtAl2013StochasticSD001Q200K005	3.04	21	0.6	35	0.54	19	11341.76	21	80
DouglasEtAl2013StochasticSD001Q200K020	4.25	13	0.37	19	0.27	9	12883.74	13	42
DouglasEtAl2013StochasticSD001Q200K040	5.84	5	0.70	7	0.13	3	14197.18	4	15
DouglasEtAl2013StochasticSD001Q200K060	7.39	1	0.87	3	0.09	1	15114.88	1	4
DouglasEtAl2013StochasticSD001Q600K005	2.03	31	0.94	1	0.98	31	9059.06	31	123
DouglasEtAl2013StochasticSD001Q600K020	3.14	19	0.37	30	0.54	21	11485.78	19	77
DouglasEtAl2013StochasticSD001Q600K040	4.69	9	-	18	0.24	8	13299.51	9	32
DouglasEtAl2013StochasticSD001Q600K060	6.25	2	0.75	6	0.13	2	14465.32	2	8
DouglasEtAl2013StochasticSD001Q1800K005	1.75	34	0.89	2	1.15	39	7997.95	34	140
DouglasEtAl2013StochasticSD001Q1800K020	2.77	25	0.76	33	0.68	24	10862.73	25	97
DouglasEtAl2013StochasticSD001Q1800K040	4.30	11	0.17	23	0.30	11	12928.96	11	43
DouglasEtAl2013StochasticSD001Q1800K060	5.86	4	-	10	0.15	4	14209.34	3	15
DouglasEtAl2013StochasticSD010Q200K005	1.74	35	0.68	4	1.11	36	7926.36	35	138
DouglasEtAl2013StochasticSD010Q200K020	2.69	26	0.86	2	0.68	25	10710.88	26	99
DouglasEtAl2013StochasticSD010Q200K040	4.20	14	0.59	22	0.34	13	12825.87	14	53
DouglasEtAl2013StochasticSD010Q200K060	5.77	6	-	12	0.19	7	14148.39	5	23
DouglasEtAl2013StochasticSD010Q600K005	1.4	42	0.82	5	1.3	44	5844.43	43	173
DouglasEtAl2013StochasticSD010Q600K020	1.83	32	1.3	44	1.08	33	8331.11	32	128
DouglasEtAl2013StochasticSD010Q600K040	3.13	20	1	1	0.58	22	11478.64	20	82
DouglasEtAl2013StochasticSD010Q600K060			0.33	20					

GMM	LLH		G		Q		DIC		FINAL ranking
	score	ranking	Score	ranking	score	ranking	score	ranking	
DouglasEtAl2013StochasticSD010Q600K060	4.65	10	-	9	0.30	12	13265.70	10	41
DouglasEtAl2013StochasticSD010Q1800K005	1.62	37	0.68	43	1.14	38	7335.38	37	155
DouglasEtAl2013StochasticSD010Q1800K020	1.62	36	0.83	36	1.20	40	7354.14	36	148
DouglasEtAl2013StochasticSD010Q1800K040	2.78	24	0.17	24	0.69	26	10888.50	24	98
DouglasEtAl2013StochasticSD010Q1800K060	4.27	12	0.61	13	0.36	15	12901.72	12	52
DouglasEtAl2013StochasticSD100Q200K005	1.50	40	1.08	40	1.25	43	6598.17	40	163
DouglasEtAl2013StochasticSD100Q200K020	2.13	29	0.22	29	0.91	29	9371.35	29	116
DouglasEtAl2013StochasticSD100Q200K040	3.54	18	0.43	17	0.49	18	12061.01	17	70
DouglasEtAl2013StochasticSD100Q200K060	5.11	8	0.70	8	0.28	10	13659.12	7	33
DouglasEtAl2013StochasticSD100Q600K005	2.03	30	0.89	37	0.93	30	9061.58	30	127
DouglasEtAl2013StochasticSD100Q600K020	1.56	38	0.95	38	1.22	41	6997.63	38	155
DouglasEtAl2013StochasticSD100Q600K040	2.58	27	0.04	26	0.77	27	10477.27	27	107
DouglasEtAl2013StochasticSD100Q600K060	4.06	15	0.53	15	0.43	16	12674.33	15	61
DouglasEtAl2013StochasticSD100Q1800K005	2.99	23	0.22	28	0.54	20	11248.27	22	93
DouglasEtAl2013StochasticSD100Q1800K020	1.54	39	1.12	42	1.23	42	6874.52	39	162
DouglasEtAl2013StochasticSD100Q1800K040	2.29	28	0.15	27	0.88	28	9793.94	28	111
DouglasEtAl2013StochasticSD100Q1800K060	3.70	17	0.44	16	0.49	17	12263.90	16	66

5 UPDATING OF GROUND-MOTION AND INTENSITY ATTENUATION MODELS

5.1 Direct updating of GMM coefficients

Timely estimation and even prediction of the impact distribution of an earthquake and also of a seismic sequence are of fundamental importance to mitigate the seismic risk and increase the resilience to seismic hazard within the TURNkey project. In this framework, it is proposed to investigate the benefit of implementing an approach based on updating of ground motion prediction coefficients to make initial estimations of ground shaking intensities immediately after the earthquake wave propagation. Originally proposed by [De Matteis and Convertito \(2015\)](#), the method is able to infer new values of the coefficients of a parent ground motion prediction equation by using the ground motion data recorded during an earthquake. In the original approach, the coefficients are continuously updated based on the actual information gathered by the regional accelerometric network installed in the geographical area under consideration. Although the results of the real-time applications of the [De Matteis and Convertito \(2015\)](#) approach appear promising, further analysis employing a larger number of earthquakes is recommended by the authors themselves.

Following the implementation of the approach, its capabilities were rigorously evaluated by using data from earthquakes ($M > 4.0$) recorded by the Italian seismic network operating during the seismic sequence that affected Central Italy in 2016, particularly within the timeframe between 16 October and 14 November 2016. The selected temporal frame, which has been selected because of the relevance of their induced impacts (e.g. [Stewart et al., 2018](#)) and the huge amount of reliable and available data (e.g. site characterization and topography classification for many recording stations.), includes also the two large events belonging to the 2016 seismic sequence (i.e. $M 5.9$ October, 26 Ussita and $M 6.5$ October 30, 2016 Norcia). A data-driven assessment of the performance of the near real-time updated ground motion model has been carried out by scoring instant-by-instant calculations performed using both the parent and the updated ground motion models. The predictions of the near real-time updated GMMs are tested against ground-motion data recorded in real earthquakes and compared with the parent GMM. The performance of the GMMs is measured by using two approaches: the well-established log-likelihood (LLH) method ([Scherbaum et al., 2009](#)) and the innovative pari-mutuel gambling score ([Zechar and Zhuang, 2014](#)). The latter is adopted in recent studies in the literature (e.g. [Lanzano et al., 2020](#)) to assess the performance of GMMs.

Based on the obtained results, it is concluded that the approach can improve the accuracy of rapid ground shaking estimates, which is useful for rapid response applications. When one considers aftershocks or further major events occurring within a limited time-space window, it is shown that the use of coefficients calibrated using data from a previous major event ($M > 5$) provides more accurate, event and region-specific prediction equations, thus encouraging its use also for earthquake early warning purposes.

5.1.1 Methodology

Similar to the original article, we are applying the GMM proposed by [Bindi et al. \(2011\)](#), ITA10, not only because it was the national GMM during the 2016 sequence, but also since it is based on epicentral distance, which does not require a rupture plane. Such choice is obviously fundamental when it comes to the determination of shaking intensities within a few seconds after the fault rupture begins, as the inversion of the geometry of the fault plane geometry and other seismological quantities (slip, rupture velocity, strike, dip, rake angles) requires more computation time.

For the sake of clarity, the original equation provided by ITA10 is reported in Eq. (5-1) for Peak Ground Acceleration (PGA), which has been chosen for its popularity in earthquake hazard and risk assessment.

$$Y = e_1 + [c_1 + c_2(M - M_{ref})] \left(\frac{(\sqrt{R^2 + h^2})}{R_{ref}} \right) - c_3 \left[(\sqrt{R^2 + h^2}) - R_{ref} \right] \quad (5-1)$$

$$+ \{b_1(M - M_h) + b_2(M - M_h)^2; M \leq M_h \ 0; otherwise \} + F_S$$

$$+ F_{SOF}$$

In Eq (5-1), e_1 is the static term (= 3.672), c_1 (= -1.94) and c_2 (= 0.413) are magnitude and distance terms, c_3 (= 1.34e-4) is the distance term, b_1 (= -0.262) and b_2 (= -0.0707) are magnitude terms for magnitudes (M) smaller than maximum magnitude, M_h (= 6.75). R is the (epicentral) distance, h is a constant (= 10.322 km), R_{ref} is the reference distance (= 1 km). F_S is the site-effect factor based on Eurocode 8 (CEN, 2004) site classification (= 0, 0.162, 0.240, 0.105, 0.570 for A, B, C, D, E sites respectively). M_{ref} is the reference magnitude (= 5) and F_{SOF} is a factor based on the type of the fault rupture (= -5.03e-2, 1.05e-1, -5.44e-2, 0 for “normal”, “reverse”, “strike-slip”, and “unknown” rupture types, respectively). For the logarithmic standard deviation (s), we consider the value of within-event variability to be 0.29.

In our case, the problem we would like to solve includes only the unknown of distance, which reduces the indeterminacy of the equation to single unknown. As a matter of fact, for a given magnitude M , the impact of the coefficients b_1 and b_2 will not depend any other parameter, hence their effect would be same of e_1 . Likewise, parameter c_2 will behave similar to c_1 . Once we consider also the unknown fault rupture style FOS , and already known site conditions S , the number of independent variables drops to three which are e_1 , c_1 , and c_3 . We observe that proper variability on three parameters (e_1 , c_1 , c_3) will provide sufficient flexibility of the GMM.

For PGA predictions, [Bindi et al. \(2011\)](#) report the standard deviations of e_1 , c_1 , and c_3 as 0.316, 0.257, and 1.57e-3, respectively. The best combination of three varied parameters is found through a discrete value searching algorithm at each analysis time step following the initiation of the fault rupture (for fast calculation purposes, we considered equal time intervals with $\Delta t=3s$) by minimizing the sum of squared errors between logarithms of observed and predicted geometric mean of PGAs. Near real-time fitting of the GMM is made by taking into consideration different criteria, summarized below:

1. Stations with epicentral distance larger than a certain predefined epicentral distance, R_{max} , are not considered in the computations (in our case $R_{max}=200$ km).
2. In order to start the updating procedure, it is expected that the number of stations (n_{min}) satisfying criterion (1) should be greater than the number of parameters being varied (i.e. in our case, 3). Until this condition is satisfied, initial GMM coefficients are kept.
3. For any station j and time k , in order to be considered within the updating scheme, site class and topography normalized maximum acceleration at any time t_j ($PGA_{r,A,T1}$) should be greater or equal to -2 standard deviation prediction of the parent GMM ($PGA_{GMM,A,T1,\mu-2\sigma}$). The stations not satisfying this condition are excluded from the updating procedure at time t_i ;

It is important to note that parameter fitting of the GMM is carried out under homogeneous site and topography conditions. Therefore, first the soil amplification effect is removed by dividing the recorded PGA values by (10^{F_s}) . Consequently, we normalize also according to the topographic amplification effects by dividing the soil-effect normalized PGA values by 1.0, 1.2, and 1.4 corresponding to T1, T2-T3, and T4 classes according to the Italian Building Code (NTC18, 2018), which is consistent with Eurocode 8 (2003; EC8). After the normalization, the final value is denominated as $PGA_{r,A,T1}$ representing the recorded geometric mean PGA at rock (site class A) and flat topography (topography class T1) conditions.

The flowchart of the updating operation is illustrated in **Erreur! Source du renvoi introuvable.**, which is slightly different to its original form (i.e. [De Matteis and Converito, 2015](#)). In a single forward run, we start with initial values for c_1 , e_1 , c_3 coefficients and event sigma s , which may be defined either by the default values of ITA10 or through region and time specific pre-calibrated values. As first step, the lower bound ($\mu-2\sigma$) predictions of $PGA_{A,T1}$ are made at every station with epicentral distance smaller than the maximum threshold value (R_{max}). In the second step, the actual geometric means of the horizontal peak component accelerations are recovered and normalized according to uniform site and topography conditions. In the third step, if the total number of exceedances of lower bound PGA predictions is greater than a certain threshold (for instance three stations for the determination of three coefficients as defined in Criterion 2), new values of e_1 , c_1 , and c_3 are obtained through the minimization of the sum of error squares by only using the data acquired by the stations with peak intensity exceeding the lower bound threshold (Criterion 3). In the final step, based on the new median prediction, sigma (σ) of the seismic station observations and GMM scores (PGMS and LLH) are computed. Note that in case Criterion 2 is not satisfied, the initial values for e_1 , c_1 , c_3 , and σ are kept.

Based on the desire of the user, the procedure defined in the paragraph above may be repeated several times during an event or calculated once immediately following the event. Furthermore, the procedure may be applied for a single event (in this case the initial values of e_1 , c_1 , c_3 , and s are controlled by ITA10) or during a seismic sequence or aftershock swarm (in this case, the initial values may be set as pre-calibrated).

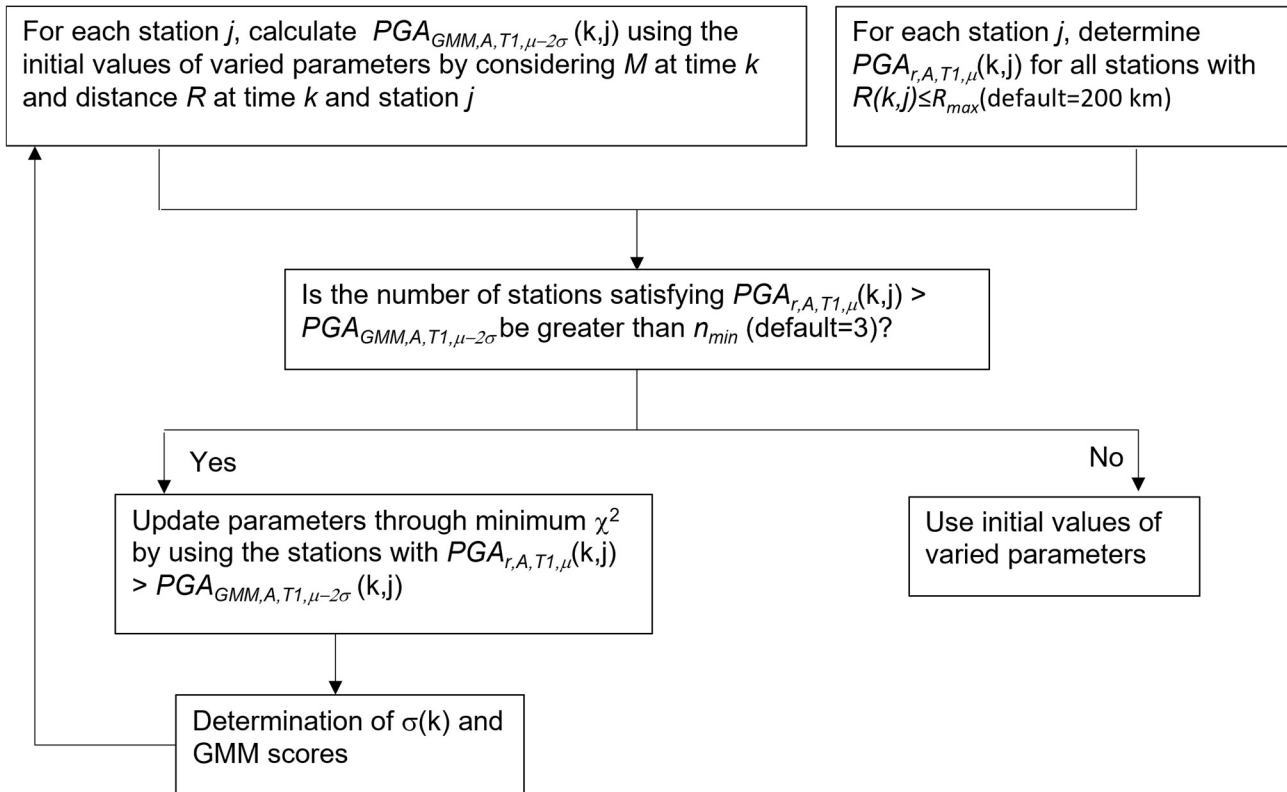


Figure 5-1. Flowchart followed in this study for updating the GMM coefficients during the ongoing propagation of earthquake waves. Indices j and k are for station j and analysis time k , $PGA_{GMM,A,T1,m-2s}$ is the geometric mean minus 2 standard deviations of PGA predicted by the original GMM considering A site class and T1 topography, $PGA_{r,A,T1,m}$ is the geometric mean of the recorded PGA considering A site class and T1 topography. R and R_{max} are distance metric (in our case epicentral) and its maximum allowable value.

5.1.2 Dataset

In order to evaluate the performance of the method described, we compiled a dataset which contains a total of 20 events (Table 5-1), which) that occurred between 16 October and 14 November 2016, belonging to the 2016 Central Italy seismic sequence, with magnitudes greater or equal to 4.0 registered by 405 seismic stations installed in the nearby regions of Umbria, Marche, Lazio, and Abruzzo. The data were downloaded using the current version of ITACA (Italian Accelerometric Archive) v3.1 through the website of INGV (Italian National Institute of Geophysics and Volcanology). Far away stations ($R_{epi} > 200$ km) and bad quality data, highlighted by INGV, are excluded from the dataset. In the final set, approximately 100-150 corrected two horizontal component signals remain available for each event.

Table 5-1: Earthquake events considered in this study with corresponding IDs. EMSC: European-Mediterranean Seismological Centre. Latitude, longitude, depth refer to the hypocentral location. M: moment magnitude. Abbr: abbreviations used in the text. Note: * in the M column represents the local magnitude.

ID	Time (UTC)	Latitude (°)	Longitude (°)	Depth (km)	M	EMSC ID	Abb.
1	2016-10-16 09:32:35	42.74770	13.17570	9.2	4.0	20161016_0000047	

2	2016-10-26 17:10:36	42.87470	13.12430	8.1	5.4	20161026_0000077	
3	2016-10-26 19:18:06	42.90870	13.12880	7.5	5.9	20161026_0000142	Ussita
4	2016-10-26 21:42:01	42.86400	13.12230	9.9	4.5	20161026_0000133	
5	2016-10-27 03:19:27	42.84270	13.14270	9.2	4.0	20161027_0000016	
6	2016-10-27 03:50:25	42.98470	13.12050	8.7	4.1	20161027_0000018	
7	2016-10-27 08:21:47	42.87470	13.09900	9.4	4.3	20161027_0000072	
8	2016-10-30 06:40:18	42.83220	13.11070	9.2	6.5	20161030_0000029	Norcia
9	2016-10-30 07:07:54	42.71500	13.18820	10.2	4.1*	20161030_0000037	
10	2016-10-30 07:34:47	42.92730	13.13280	9.5	4.0*	20161030_0000039	
11	2016-10-30 11:58:17	42.84480	13.05650	9.8	4.0	20161030_0000130	
12	2016-10-30 12:07:00	42.84180	13.07570	9.7	4.5	20161030_0000135	
13	2016-10-30 13:34:54	42.6716	13.16580	9.6	4.1	20161030_0000170	
14	2016-10-30 18:21:09	42.78230	13.15030	8.5	4.0	20161030_0000281	
15	2016-10-31 03:27:40	42.76120	13.08580	10.6	4.0	20161031_0000053	
16	2016-10-31 07:05:45	42.83880	13.12630	9.5	4.0	20161031_0000097	
17	2016-11-01 07:56:39	42.99020	13.13450	8.3	4.8	20161101_0000060	
18	2016-11-03 00:35:01	43.02770	13.04930	8.1	4.7	20161103_0000003	
19	2016-11-12 14:43:33	42.71870	13.20570	9.8	4.1	20161112_0000066	
20	2016-11-14 01:33:43	42.85870	13.15620	10.9	4.1*	20161114_0000010	

5.1.3 Overview of the analysis

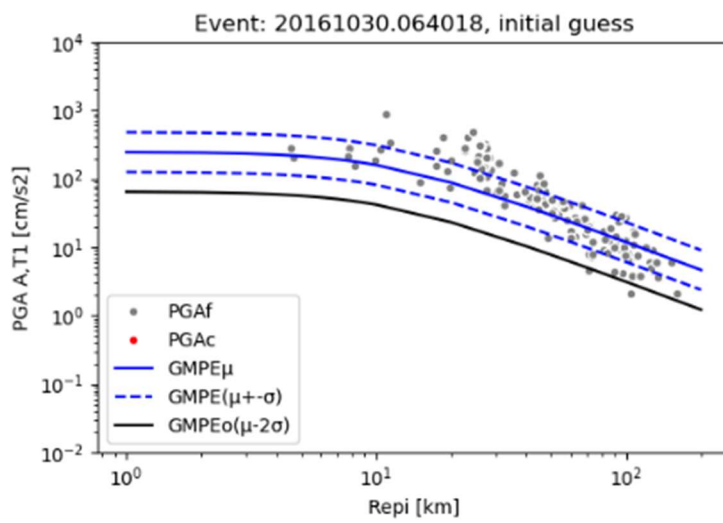
The implemented algorithm is tested against recordings from real earthquakes (i.e. the dataset described in Section 5.1.2) in terms of two different perspectives: (i) for a single event by considering the October 30, 2016 M6.5 (Norcia) mainshock, (ii) for the seismic sequence by considering the entire 20 events shown in Table 5-1. The performance of the GMMs, i.e. the near real-time updated GMM and the parent GMM, are assessed by using the widely-used log-likelihood (LLH) method (Scherbaum et al., 2009) and the more recent pari-mutuel gambling score (Zechar and Zhuang, 2014). The following sections present examples of analyses carried out at EUC.

5.1.4 Example of the calibration of GMM coefficients for a single event

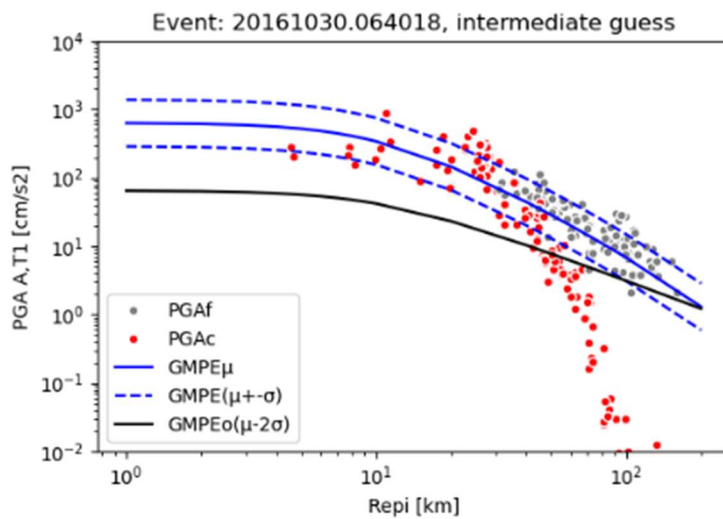
In Figure 5-2, the effect of GMM updating is illustrated in terms of the shape of the GMM by considering the M6.5 Norcia event. As noted previously, the updating is handled by making use

of actual values of the geometric means of the peak ground acceleration values (normalized in terms of soil classification and topography) at time t provided that they are greater than the lower limit defined by $\mu - 2\sigma$ estimates of the original GMM (where μ stands for the mean value and σ stands for the standard deviation).

The updating scheme is initiated by using the original μ (and σ), once the number of stations exceeds 3 (the value set for the minimum station threshold). Consequently, as the propagation of the waves further continues, further stations exceeding the lower limit enter in the algorithm to find the best combination from the discrete values of $c1$, $e1$, and $c3$.



(a)



(b)

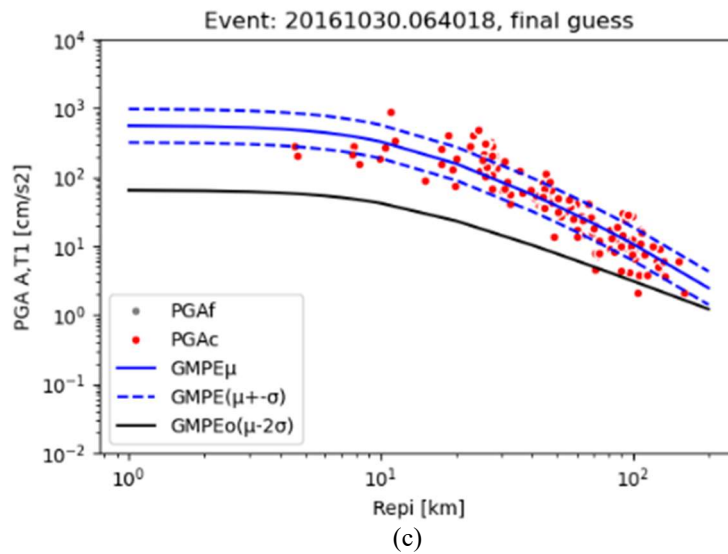


Figure 5-2. Black lines: lower 2.5-percentile limit of the original GMM ($PGA_{A,T1}(\mu-2\sigma)$), continuous blue lines: mean prediction of the updated GMM, dashed blue lines: $\mu-1\sigma$ and $\mu+1\sigma$ predictions of the updated GMM, grey markers: geometric means of recorded and normalized PGA values at the end of the shaking, red markers: geometric means of the recorded and normalized PGA values at timestep k ($PGA_{A,T1}(k,j)$). (a), (b), (c) provide the summary for the initial guess, intermediate guess (at time step=15s after the initiation of the rupture), and final guess, respectively. The analysis was carried out by using the M6.5 Norcia event.

In Figure 5-3, on the other hand, normalized PGA maps ($PGA_{A,T1}$) at the same timesteps are illustrated and compared with the corresponding maximum recorded values at the end of the shaking. Apart from a few points at which the shaking was underestimated, the final prediction is observed to be well in line with the recorded values. Moreover, in spite of being slightly more intense, at 15 s after the rupture initiates, a sufficiently good distribution of intensities is noted up to $R_{epi} = 100$ km. Yet, it should be kept in mind that the original GMM was already able to provide good estimates for the mid- and far-field distance range.

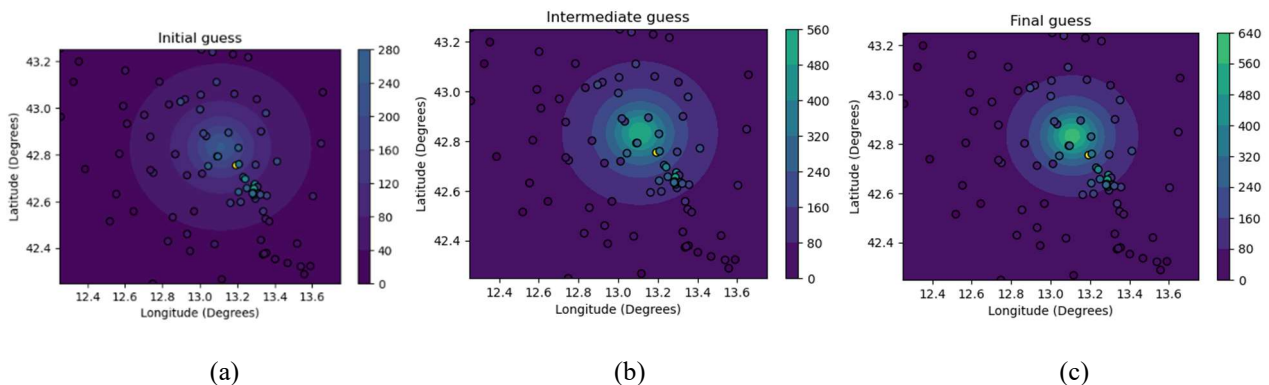
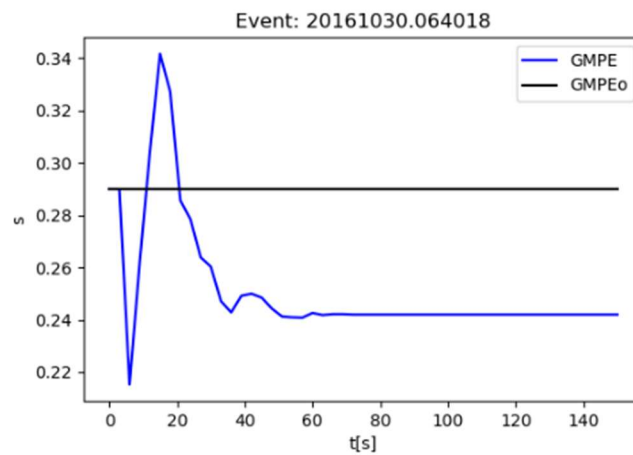
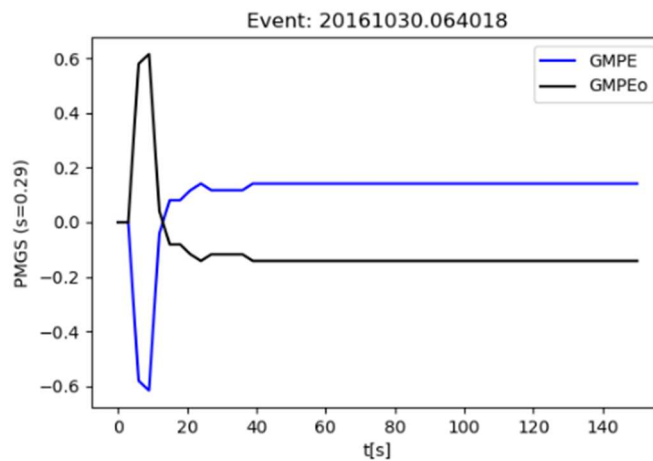


Figure 5-3. Site condition and topography normalized PGA maps in comparison with the corresponding (final) recorded values. (a), (b), (c) represent initial, intermediate, and final guesses. The analysis was carried out by using the single event of M6.5 Norcia.

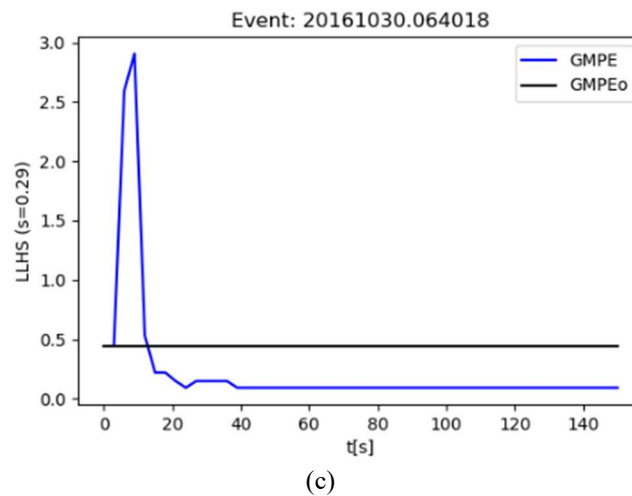
In Figure 5-4, temporal dependence of GMM uncertainty, PGM and LLH scores are represented. It can be observed that the uncertainty (s) deviates around the original value and becomes smaller in the end. In terms of the comparative scores, for the updated GMM we start seeing positive (win) conditions and smaller LLH values after around 20 seconds, hence it could be underlined that the updated GMM predicts better values than the parent GMM. The comparisons are provided by using the sigma of the original GMM ($s=0.29$), since a dependency on sigma is noted in the calculation of the scores.



(a)



(b)



(c)

Figure 5-4. Time dependent change in (a): standard deviation (s), (b) pari-mutuel gambling (PGM) score, (c) log-likelihood (LLH) score. The analysis was made by using a single event of M6.5 (Norcia event). The time $t=0$ s represents the rupture initiation, magnitude is considered to be known from the beginning.

Similarly good performance is observed for the entire set of events under study. It is confirmed that the updated GMM provides estimations of ground motion intensity parameter distributions at the end of the earthquake wave propagation at least with the same precision and accuracy with respect to the parent GMM.

In Figure 5-5, we display a representative set of the time-dependent prediction and recorded normalized PGA values. Here, it is underlined that for nearby stations, the lead times are generally short (e.g. AQF with $R_{epi} = 43$ km) and unstable, and may even be negative (e.g. T1214 with $R_{epi} = 11$ km). Once the distance gets larger, lead times get longer. Overall, the predictions made by the updated GMM are better, yet there exist cases, in which the original GMM performs better and/or earlier (e.g. MMP1 with $R_{epi}=71$ km). In this analysis, time $t=0$ s, the start of the fault rupture, for the purpose of synchronization of the ground motions, although such $t=0$ s time is impossible to determine in advance since at the initiation of the fault rupture magnitude will remain uncertain.

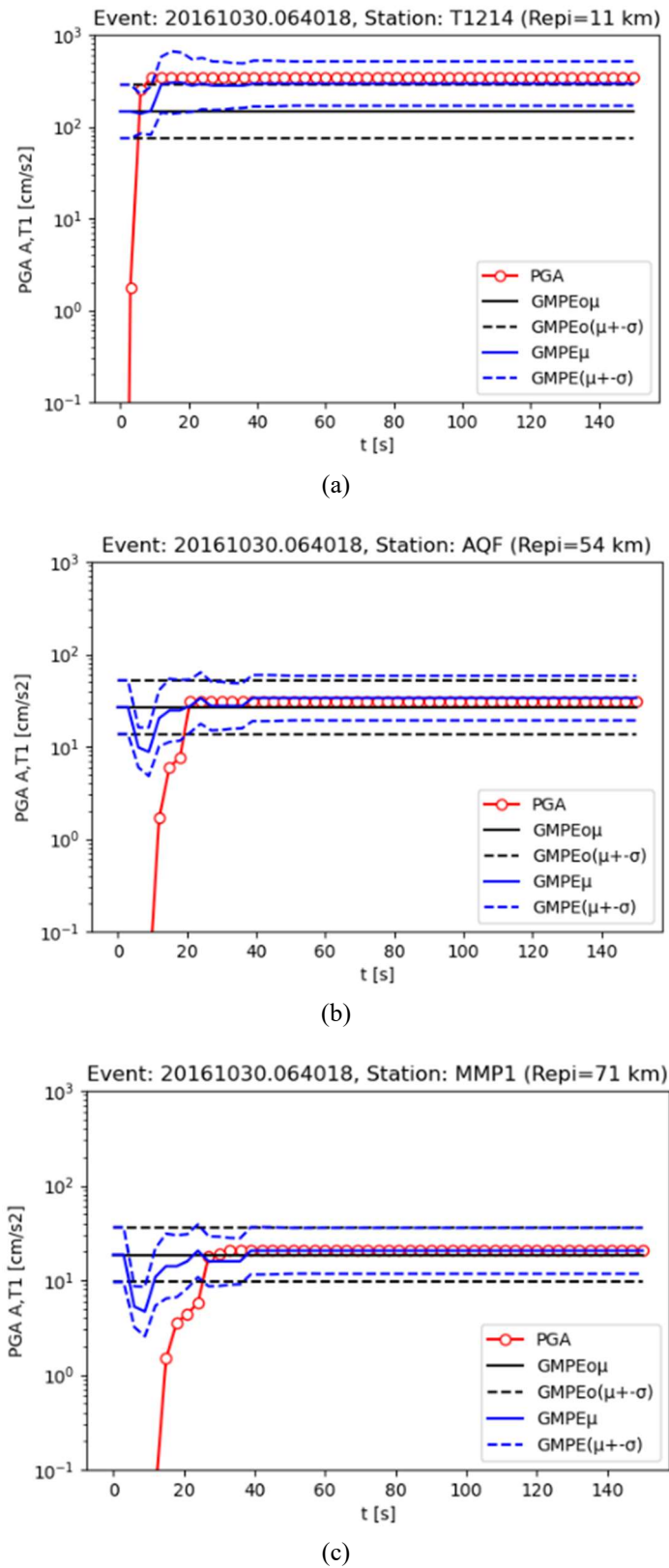


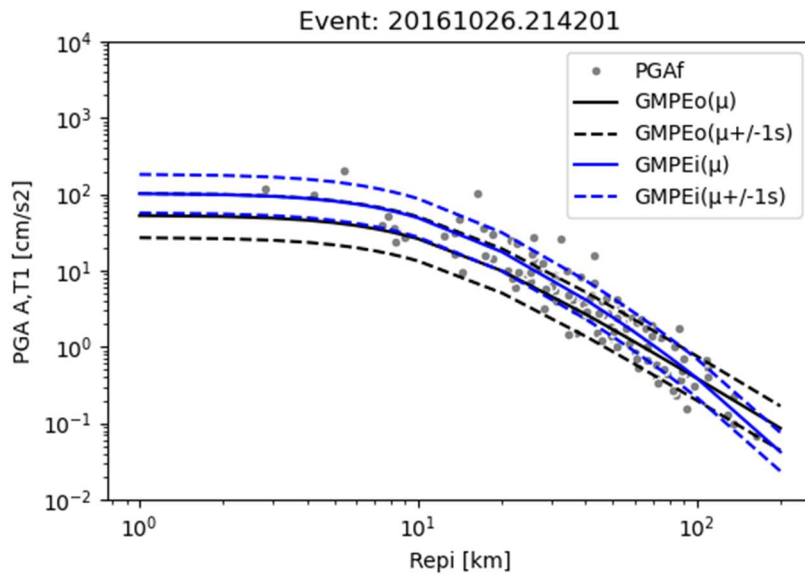
Figure 5-5. Time-dependent change of prediction of normalized PGA ($PGA_{A,Tl}$) for (a) T1214, (b) AQF, (c) MMP1 stations. The analysis is made by using a single event of M6.5 (Norcia).

Despite its superior performance as a tool for post-earthquake intensity estimation, the real-time performance of the updating methodology is found rather limited. While the lead times for far-field stations may be sufficiently long, coefficients for stations close to the epicentral region can most likely not be estimated in time.

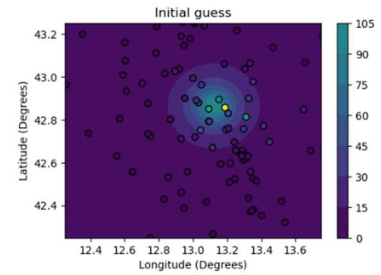
5.1.5 Small earthquakes subsequent to the Ussita M5.9 event

The second analysis concerns the use of pre-initialized GMMs instead of the parent GMMs. The focus will be given to specific cases, in which the events will be evaluated in groups. During each evaluation, the initial conditions of GMM parameters ($c1$, $e1$, $c3$, s) will be readjusted based on the selected criteria under consideration. We will focus only on the initial (which may be considered as the time when the magnitude estimation is stable) and final predictions (when the peak values of PGAs are stable). The results are discussed in terms of $PGA_{A,T1}$ maps, PGM and LLH score values. According to the results of our extensive analysis, pre-initialization increases the accuracy of the input GMM for both aftershocks and main shocks of the same seismic sequence. In order to demonstrate its performance, we provide an example of 4 minor shocks that occurred following the Ussita M5.9 event.

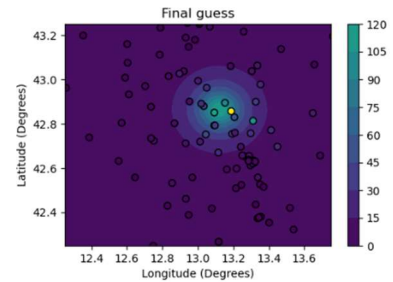
As an illustration, we calibrate the parameters based on the Ussita M5.9 main event. Subsequently, we use the calibrated GMM as starting point for subsequent events with IDs 4, 5, 6, and 7 (see Table 5-1). The results are presented in Figure 5-6 and Figure 5-7 in terms of $PGA_{A,T1}$ maps as well as initial and final $PGA_{A,T1}-R_{epi}$ relations. Initial and final scores are reported in Table 5-2, by providing the sigma (s) = 0.29.



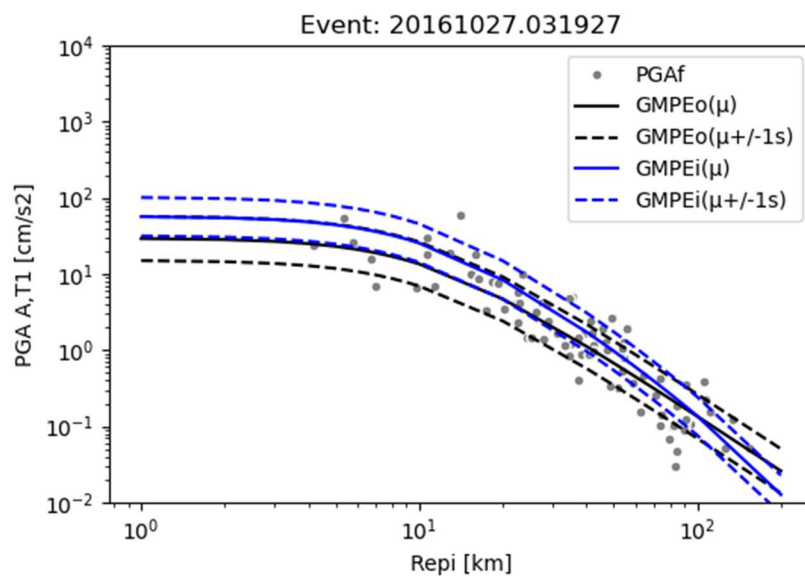
(a)



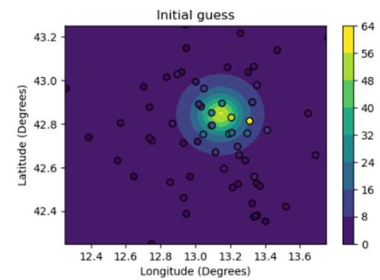
(b)



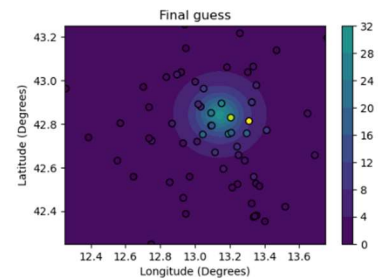
(c)



(d)

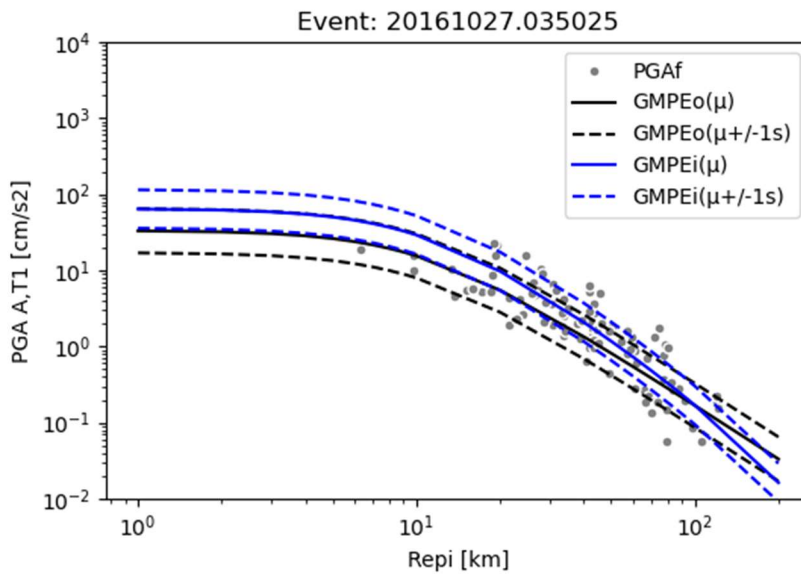


(e)

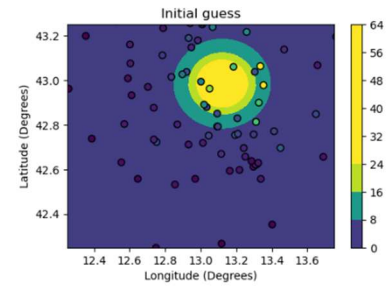


(f)

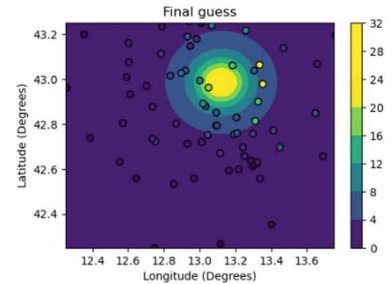
Figure 5-6 (a and d): $PGA_{A,T1}$ - R_{epi} predictions of the original (black) GMM and GMM updated at 0s (blue) versus the scatter of recorded values. (b and e): initial $PGA_{A,T1}$ maps (i.e. at the theoretical timestep when the M estimate is stable) versus final observations. (c and f): Final $PGA_{A,T1}$ map versus observations. For the initial guess, GMM coefficients are set according to their final values obtained employing the M5.9 Ussita event. (a to c) are for event ID 4 and (d to f) are for event ID 5 (see Table 5-1).



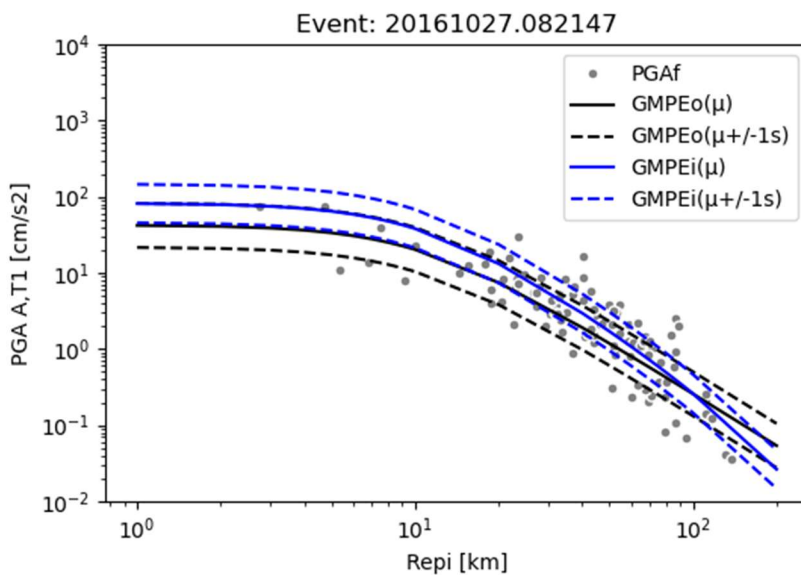
(a)



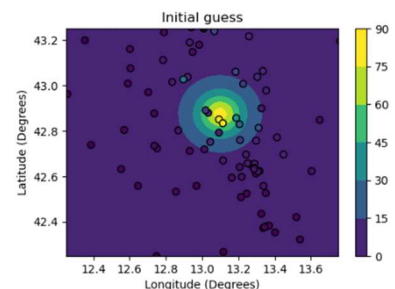
(b)



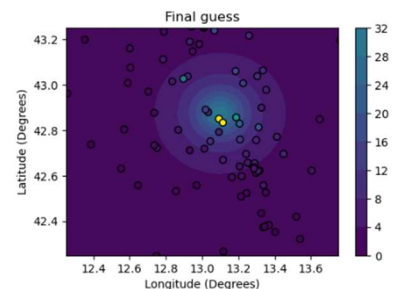
(c)



(d)



(e)



(f)

Figure 5-7 (a and d): $PGA_{A,T1}$ - R_{epi} predictions of the original (black) and updated at 0s (blue) GMMs versus the scatter of recorded values. (b and e): Initial $PGA_{A,T1}$ maps (i.e. at the theoretical time instant when M estimate is relatively stabilized) versus final observations. (c and f): Final $PGA_{A,T1}$ map versus observations. For the initial guess, GMM coefficients are set according to their final values obtained in the M5.9 Ussita event. (a to c) are for event ID 6 and (d to f) are for event ID 7 (see Table 5-2).

Table 5-2: Log standard deviation (s) of the updated GMMs, pari-mutuel gambling score (PGMS) and log-likelihood score (LLHS) of updated (u) and original (o) GMMs for their initial and final guesses by employing the M5.9 Ussita event for pre-calibration and subsequent events for evaluation. Positive PGMS and lower LLHS indicate the better performing GMM. Value in parentheses show the corresponding PGMS and LLHS when considering the sigma of the original GMM. See Table 5-1 for the flat file information of the events under consideration.

Event ID	Initial GMM vs GMM original				Final GMM vs GMM original			
	s	PGMS	LLHSu	LLHSo	s	PGMS	LLHSu	LLHSo
4	0.252	0.060	0.080	0.248	0.249	0.066	0.073	0.248
5	0.252	-0.077	0.519	0.337	0.283	0.000	0.337	0.337
6	0.252	0.030	0.349	0.419	0.289	0.056	0.321	0.419
7	0.252	0.021	0.554	0.578	0.318	0.033	0.506	0.578

We conclude that for event IDs 4, 6, and 7, the initial estimates of shaking based on the previously calibrated GMM are better than the ones provided by the parent GMM ITA10. This may be observed by comparing scores for the initial guess. On the other hand, for the event ID 5, the original GMM provides better initial predictions. In all of cases, the upper bound of near-fault predictions provided by the previously calibrated GMM is better. This is because the previously calibrated GMM has higher accelerations due to the finite fault nature of the M5.9 event, hence the epicentral distance becomes less important.

Finally, it should be underlined that similarly encouraging results are obtained when considering (i) the Norcia mainshock and the following small events, (ii) the Ussita and Norcia events in a sequence, (iii) the M5.4 earthquake before the Ussita event (ID 2) and the Ussita sequence, and (iv) two moderate events with M4.7-4.8 (IDs 17 and 18) occurring after the Norcia event.

5.1.6 Conclusive remarks

Based on the analysis made, it may be stated that the GMM coefficient updating method is apt for RRE purposes by providing a consistent performance greater or equal to the parent GMM and, once it is calibrated by using the results of a close-by $M > 5$ event, it is also able to provide better GMMs for EEW applications for subsequent main- or aftershocks. We do not recommend its use for time-dependent updating of the coefficients during the seismic wave propagation process as it requires sufficiently long lead times and provides only unstable predictions during the initial seconds. We demonstrated the results using a regional GMPE and we expect a similar performance employing a global GMM.

5.2 Derivation of shake-maps using uncertain GMM coefficients

GMMs typically used in seismic hazard and risk applications predict a probability distribution of values of a specific ground motion parameter, such as PGA or SA at a particular oscillator period. GMMs are empirically calibrated models with functional forms depending on

explanatory variables that characterize the earthquake source (magnitude, depth, and style of faulting), the travel path (distance), and the site (V_{s30} and depth of sediments). However, GMMs derived through regression analysis are associated with large epistemic uncertainties due to insufficient data to constrain median predictions, especially for applications in regions with relatively few recordings. To tackle this issue, it is beneficial to make regional adjustments to the GMMs to render them more applicable to the target region and site. Recently, [Kowsari et al. \(2019, 2020\)](#) recalibrated the GMMs used in Iceland to Icelandic data using Bayesian regression and Markov Chain Monte Carlo simulations. The new GMMs thus form a suite of models that can be used with confidence in predicting PGA and SA for regional earthquakes, and thereby can serve for reassessing the seismic hazard in these regions. [Kotha et al. \(2020\)](#) proposed a new regionally adaptable GMM for Europe calibrated from the European Strong-Motion dataset.

If recent recordings are available, a continuously adjusted GMM being up to date with new data should be more accurate. The purpose of this work is to outline a new paradigm in shake-map development, in which the underlying GMM is continuously updated as new data becomes available. This is in contrast to the current approach, in which every few years databases are consolidated and revisions to existing models are released ([Stafford, 2019](#)). The approach proposed here consists in the continuous adjustment of both GMM coefficients and shake-map terms (i.e., inter- and intra-event error terms) in parallel. To this end, the Bayesian updating framework detailed in Section 3.1.2 is used in order to account for the uncertainty in some GMM coefficients, which are updated in the same time as the inter- and intra-event error terms of the GMM. This novel approach is under study; the methodology is described in Section 5.2.1, and it is tested with several GMMs and earthquakes in Sections 5.2.2 and 5.2.3.

5.2.1 Methodology

Most GMMs estimate a given ground-motion parameter Y through the following functional form:

$$\log Y = f(\boldsymbol{\theta}, \mathbf{X}) + \zeta + \eta \quad (5-2)$$

where $\boldsymbol{\theta}$ represents the coefficients of the GMM and \mathbf{X} the input variables to the GMM (e.g., characteristics of the earthquake, source-site distance, characteristics of the site, etc.). The intra-event error ζ and the inter-event error η are assumed to follow a normal distribution of zero mean and standard-deviation σ_ζ and σ_η , respectively.

While common shake-map approaches (see Section 3) rely on updating solely the ζ and η error terms through field observations, the proposed approach considers in addition that the coefficients $\boldsymbol{\theta}$ are partly uncertain and may be updated by the observations as well: this is especially the case for distance terms in the GMM, which can be adjusted in order to reflect changes in decay rates (e.g., over- or underestimation of observations in near- and far-field, as will be seen at the end of Section 7). Most recent GMMs are published with information on the covariance of coefficients $\boldsymbol{\theta}$, which corresponds to the epistemic uncertainty due to the regression process. The covariance of these coefficients is considered as a prior distribution, and it will be updated based on observations. To this end, the BN for the derivation of shake-

maps, detailed in Figure 3-2, is adapted in order to account for additional uncertain variables (see Figure 5-8).

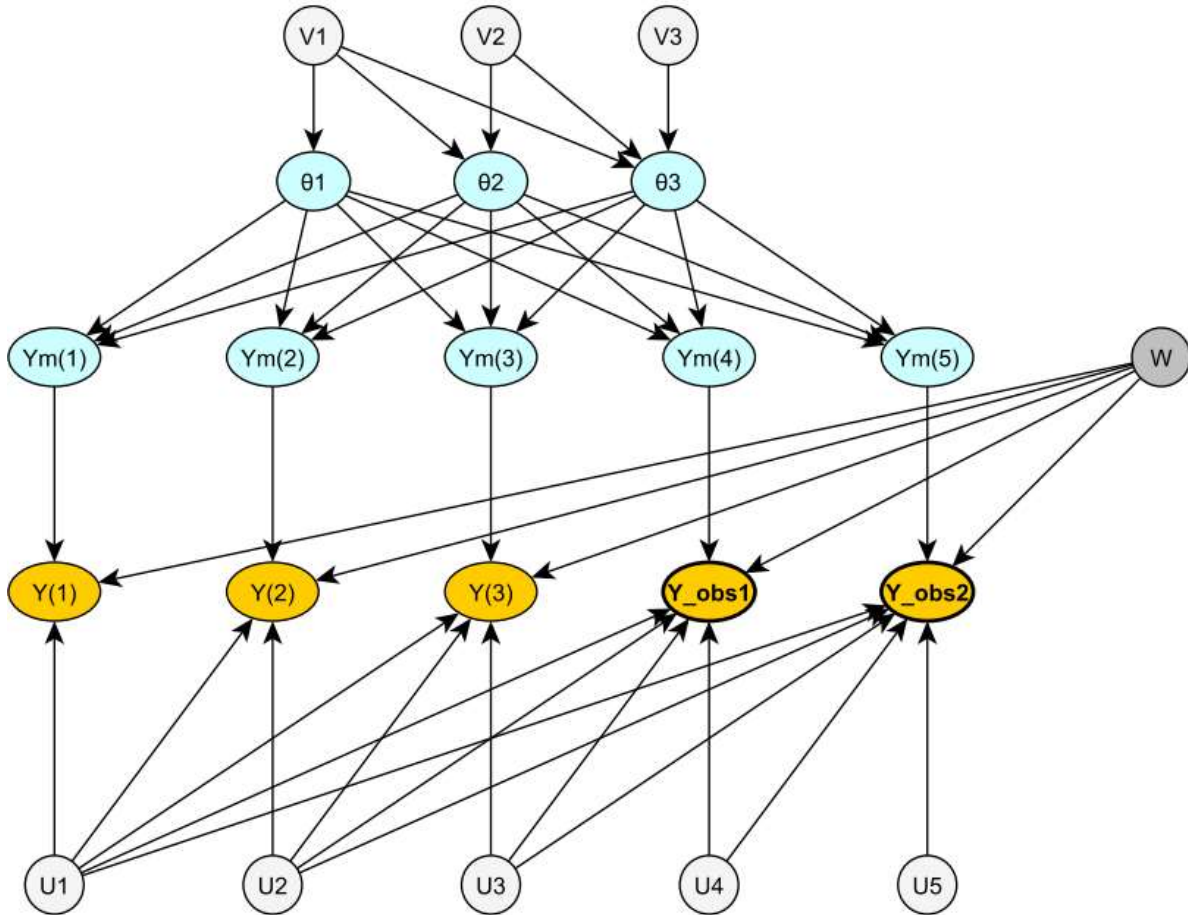


Figure 5-8: Adapted BN structure for the updating of GMM coefficients (three uncertain coefficients θ_1 , θ_2 , and θ_3 are assumed here). Three grid points $Y(\cdot)$ and two observations Y_{obs} are considered.

In Figure 5-8, the variables U and W represent the distribution of intra- and inter-event error terms, as in Section 3. The variables $Y_m(\cdot)$ represent estimates of the ground-motion parameter with the aleatory uncertainty terms: they are dependent on the epistemic uncertainty related to the distribution of GMM coefficients θ . Finally, the variables V are standard normal variables, similar to U and they are added in order to represent the correlation between the θ_i terms: they are obtained through the Cholesky decomposition of the covariance matrix of the GMM coefficients.

Provided that all variables follow normal distributions, the BN is implemented as a Gaussian Bayesian Network in the Bayes Net Toolbox (Murphy, 2002), which enables the generation of exact posterior distributions on continuous Gaussian variables. Given the input of field observations as evidence, the Bayesian inference provides multiple outcomes:

- The posterior distributions of the ground-motion parameters Y_i on a set of predefined grid points i , in the same fashion as the shake-map outputs described in Section 3.

- The posterior distributions of the GMM coefficients θ , which results in an updated GMM that may be potentially reused in further applications (e.g., mainshock-aftershock sequence).

5.2.2 Data and models

The proposed approach is tested on five past earthquake events in Europe, for which ground-motion recordings are available for the derivation of shake-maps:

- **M4.3 Lourdes earthquake** in France, December 30th 2012 (longitude = 0.17°; latitude = 43.16°). The stations' characteristics and recordings are collected from the SISPYR website (<http://www.sispyr.eu/shakemap/1356910603/products.html>).
- **M6.5 Norcia earthquake** in Italy, October 30th 2016 (longitude = 13.11°; latitude = 42.83°). The seismic stations' characteristics and recordings are collected from the INGV website (<http://shakemap.rm.ingv.it/shake4/data/8863681/current/products/stationlist.json>)
- **M6.1 Aquila earthquake** in Italy, April 6th 2009 (longitude = 13.38°; latitude = 42.34°). The seismic stations' characteristics and recordings are collected from the INGV website (<http://shakemap.rm.ingv.it/shake4/data/1895389/current/products/stationlist.json>)
- **M5.8 Emilia I earthquake** in Italy, May 20th 2012 (longitude = 11.26°; latitude = 44.9°). The seismic stations' characteristics and recordings are collected from the INGV website (<http://shakemap.ingv.it/shake4/data/772691/current/products/stationlist.json>)
- **M5.6 Emilia II earthquake** in Italy, May 29th 2012 (longitude = 11.07°; latitude = 44.84°). The seismic stations' characteristics and recordings are collected from the INGV website (<http://shakemap.ingv.it/shake4/data/841091/current/products/stationlist.json>).

Three GMMs are implemented and tested for the shake-map and coefficient updating:

- **AB10**: GMM by Akkar and Bommer (2010). It is the GMM used by default for shake-map applications in mainland France, due to the lack of robust local models. It is applied to the Lourdes earthquake only. There is no information on the variances of GMM coefficients, therefore, this GMM is only used in a conventional shake-map approach (i.e., no updating of GMM coefficients).
- **BI11**: GMM by Bindi et al. (2011), based on the Italian strong-motion database ITACA. It is applied to the Italian earthquakes. Since information on the full covariance of GMM coefficients (only diagonal terms are specified) is unavailable, it is assumed that the studied GMM coefficients are uncorrelated in the prior distribution: such assumption is probably incorrect, however it correspond to a non-informative prior, which will converge towards more realistic correlation values after the updating.
- **KO20**: recent GMM for Europe by Kotha et al. (2020). It provides regional adjustments for the Pyrenees (Lourdes) and Apennines (Norcia and L'Aquila) areas, in terms of coefficients c_3 (anelastic attenuation) and $\Delta L2L$ (source variability). The model comes with a full covariance matrix of GMM coefficients. As the most complete and adaptable model, it is applied to all earthquakes.

The recordings of the Norcia earthquake are listed in Table 10-1 of Appendix I, in terms of PGA and SA at 1s, along with the coordinates of each station. Similarly, the recordings of the Lourdes earthquake are listed in Table 10-2.

The Joyner-Boore distance (R_{jb}) is used as the distance term, i.e. the closest distance to the horizontal projection of the earthquake rupture plane. For the Italian earthquakes, this distance measure is already specified in the database of the seismic recordings. For the Lourdes earthquake, R_{jb} in km is estimated as follows (Leonard, 2010):

$$L = 10^{(-2.59 + 0.60M)} \quad (5-3)$$

$$R_{jb} = \max\{R_{epicentral} - 0.3L, 0.1\} \quad (5-4)$$

For the Italian recordings, the site correction from Kotha et al. (2020), based on V_{s30} (Figure 5-9), is used to correct recordings from site effects and to estimate ground-motion parameters at rock conditions. For Lourdes recordings, ground-motion parameters are corrected to rock conditions by using a local map of EC8 classes, which are converted to amplification factors.

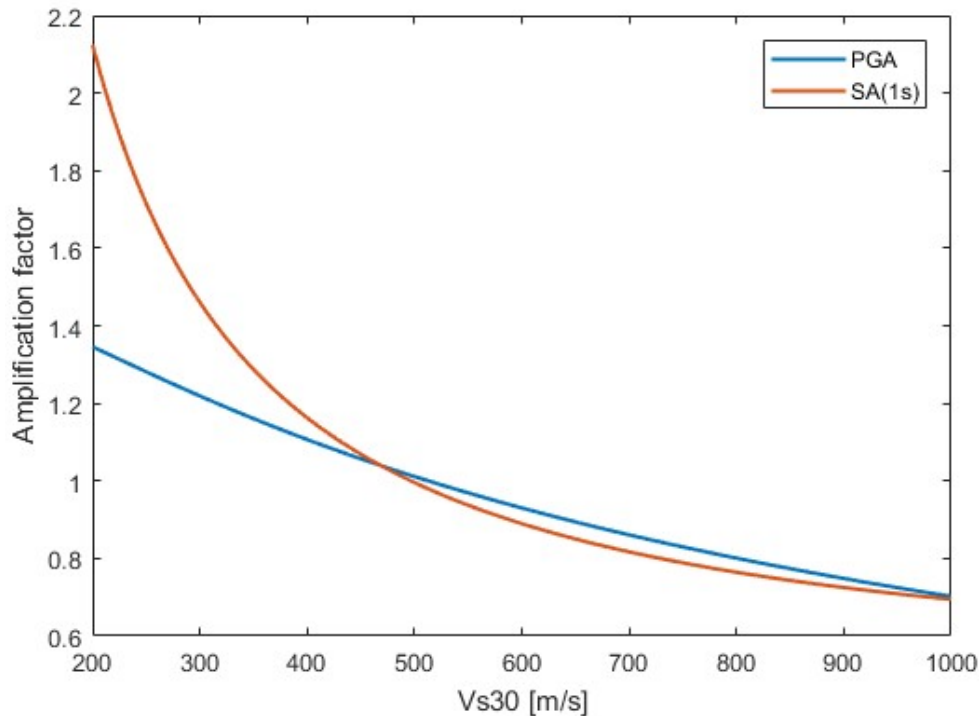


Figure 5-9: Polynomial site amplification function dependent on V_{s30} (m/s) used for the Italian earthquakes, from Kotha et al. (2020) GMM.

5.2.3 Preliminary results

As discussed in the previous sub-section, only for the **KO20** and **BI11** GMMs, coefficients will be partly updated with the BN approach. For both models, only the coefficients related to

distance terms are updated, since these are the coefficients that have an effect on the spatial distribution of ground-motion parameters (which is controlled to some extent by the seismic recordings in the affected area). The updating of other coefficients — for instance those related to magnitude terms — would require the use of multiple earthquake events in the Bayesian process. However, in the present shake-map application, only one earthquake is considered at a time, therefore there is no point in updating such coefficients. The updating of the inter-event error term already serves the purpose of adjusting the global level of the ground-motion field: adding other uncertain variables that have a similar role in the GMM would break the uniqueness of the solution and create convergence issues in the BN inference. As a result, two coefficients are updated in the BN: they are referred to as c_1 and c_3 in both **KO20** and **BI11** GMMs (Table 5-3).

Table 5-3: Role of the GMM coefficients c_1 and c_3 considered in the updating process. In KO20, $H_d = 4$ and $R_{ref} = 30$; in BI11, $R_{ref} = 1$ and h is set at 10 for shallow earthquakes.

Uncertain coefficients	Multiplicative parameters in the GMM	
	KO20	BI11
c_1	$\log \sqrt{\frac{R_{jb}^2 + H_d^2}{R_{ref}^2 + H_d^2}}$	$\log_{10} \sqrt{\frac{R_{jb}^2 + h^2}{R_{ref}^2}}$
c_3	$\frac{1}{100} \left[\sqrt{R_{jb}^2 + H_d^2} - \sqrt{R_{ref}^2 + H_d^2} \right]$	$- \left[\sqrt{R_{jb}^2 + h^2} - R_{ref} \right]$

The preliminary results at this stage of the study are presented here: the updated distributions of the GMM coefficients are detailed in Table 5-4 for the Norcia earthquake, and in Table 5-5 for the Lourdes earthquake. Figure 5-10 to Figure 5-13 represent the updated backbone GMMs, on rock conditions, for the different earthquakes and assumptions.

Table 5-4: Results of the BN updating for the Norcia earthquake, for PGA and SA(1s). “Prior” stands for the direct application of the GMM without any updating or use of observations. “Posterior” represents the updated model with uncertain coefficients. “Shake-map” represents the shake-map approach presented in Section 3, without any updating of coefficients. * KO20 coefficients and error terms are in $\ln(\cdot)$ space; ** BI11 coefficients and error terms are in $\log_{10}(\cdot)$ space.

	PGA					
	KO20*			BI11**		
	Prior	Posterior	shake-map	Prior	Posterior	shake-map
$E[c_1]$	-1.4979	-1.5042	-	-1.9400	-1.8946	-
$\sigma[c_1]$	0.0136	0.0135	-	0.2580	0.0945	-
$E[c_3]$	-0.6099	-0.7448	-	1.34E-4	0.0032	-
$\sigma[c_3]$	0.0453	0.0399	-	0.0016	7.22E-4	-
$\rho_{c_1c_3}$	-0.2704	-0.3538	-	0	0.8032	-
$E[\eta]$	0	0.2333	0.1530	0	0.2047	0.0242
$\sigma[\eta]$	0.4419	0.0444	0.0391	0.1720	0.1288	0.0241
	SA(1s)					

	KO20*			BI11**		
	Prior	Posterior	shake-map	Prior	Posterior	shake-map
$E[c_1]$	-1.1244	-1.1196	-	-1.1140	-1.1813	-
$\sigma[c_1]$	0.0126	0.0124	-	0.1410	0.0755	-
$E[c_3]$	-0.6049	-0.5852	-	2.54E-4	0.0016	-
$\sigma[c_3]$	0.0327	0.0305	-	8.63E-4	5.61E-4	-
$\rho_{c_1c_3}$	-0.3429	-0.4044	-	0	0.7206	-
$E[\eta]$	0	0.5091	0.5238	0	0.1420	-0.0956
$\sigma[\eta]$	0.4442	0.0391	0.0357	0.2220	0.1093	0.0236

Table 5-5: Results of the BN updating for the Lourdes earthquake, for PGA and SA(1s). “Prior” stands for the direct application of the GMM without any updating or use of observations. “Posterior” represents the updated model with uncertain coefficients. “Shake-map” represents the shake-map approach presented in Section 3, without any updating of coefficients. * KO20 coefficients and error terms are in $\ln(\cdot)$ space; ** AB10 coefficients and error terms are in $\log_{10}(\cdot)$ space.

	PGA				
	KO20*			AB10**	
	Prior	Posterior	shake-map	Prior	shake-map
$E[c_1]$	-1.4979	-1.4975	-	-	-
$\sigma[c_1]$	0.0136	0.0136	-	-	-
$E[c_3]$	-0.0146	-0.0143	-	-	-
$\sigma[c_3]$	0.0453	0.0448	-	-	-
$\rho_{c_1c_3}$	-0.2704	-0.2785	-	-	-
$E[\eta]$	0	-0.4895	-0.4891	0	-0.2290
$\sigma[\eta]$	0.4419	0.1145	0.1127	0.0994	0.0545
	SA(1s)				
	KO20*			AB10**	
	Prior	Posterior	shake-map	Prior	shake-map
$E[c_1]$	-1.1244	-1.1242	-	-	-
$\sigma[c_1]$	0.0126	0.0126	-	-	-
$E[c_3]$	0.4141	0.4170	-	-	-
$\sigma[c_3]$	0.0327	0.0325	-	-	-
$\rho_{c_1c_3}$	-0.3429	-0.3485	-	-	-
$E[\eta]$	0	-1.5441	-1.5426	0	-0.3028
$\sigma[\eta]$	0.4442	0.1046	0.1035	0.1483	0.0649

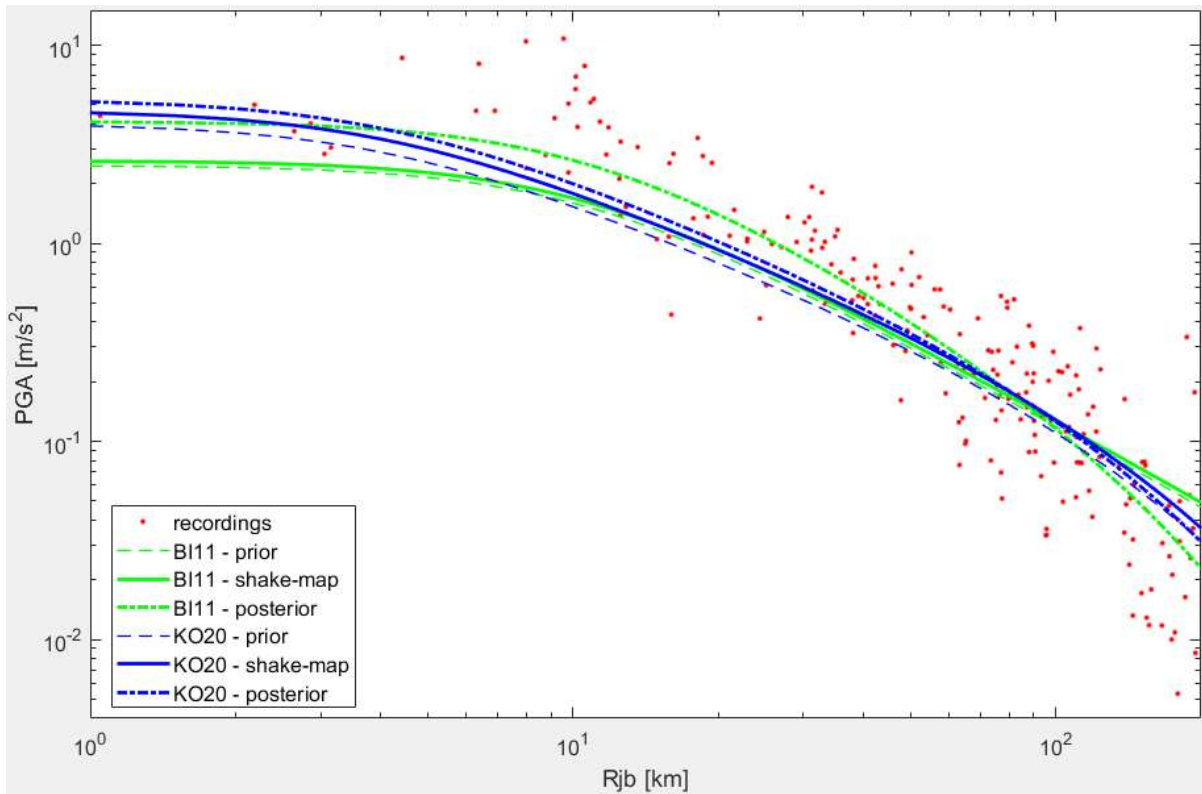


Figure 5-10: PGA estimates for the Norcia earthquake, on rock conditions.

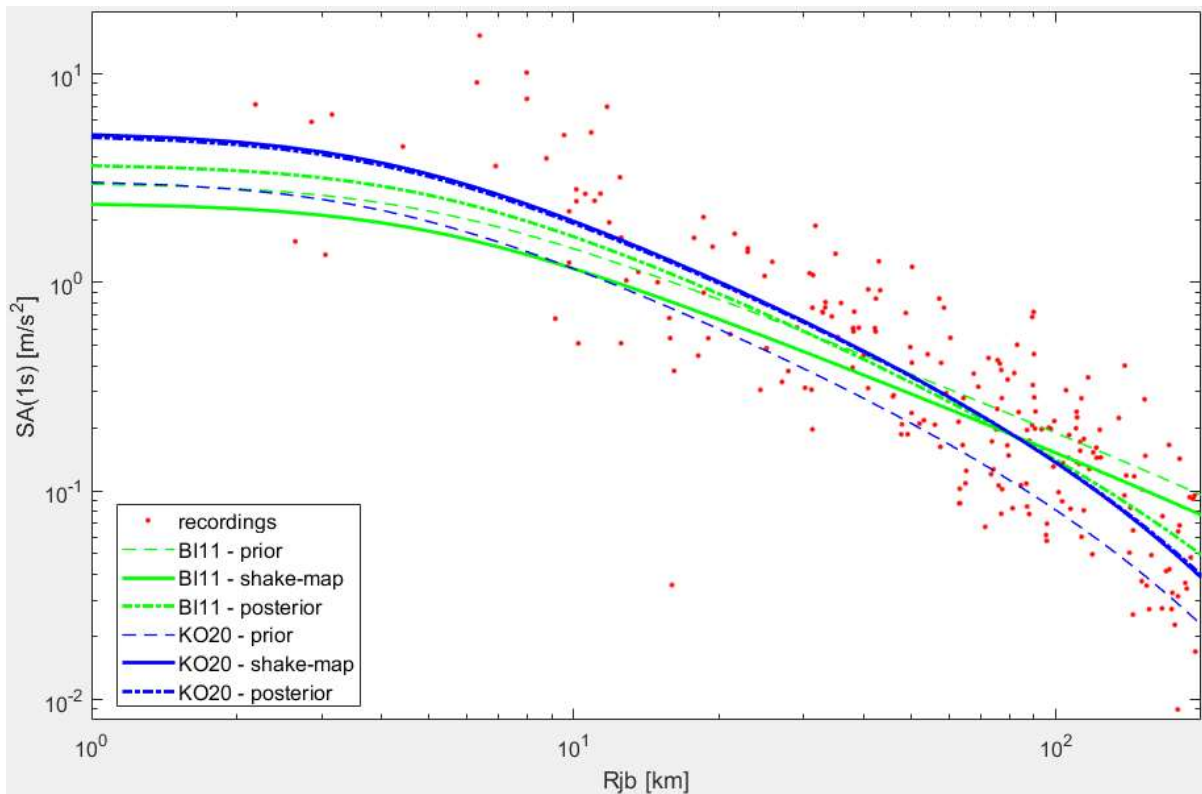


Figure 5-11: SA(1s) estimates for the Norcia earthquake, on rock conditions.

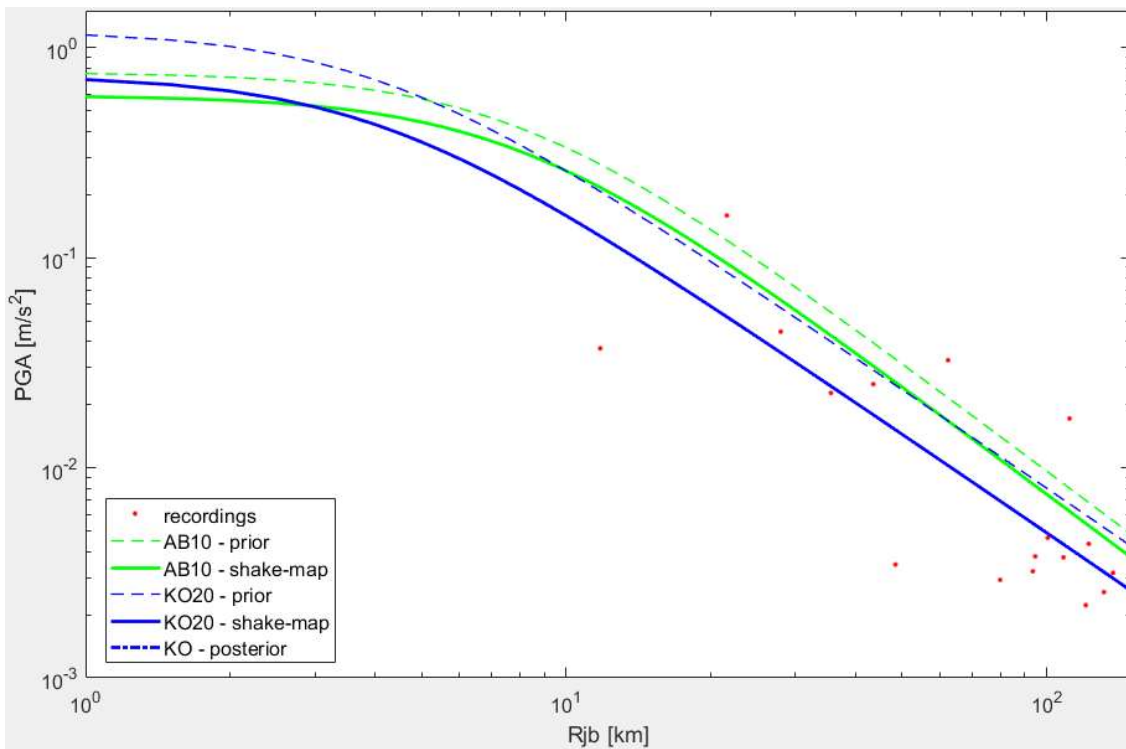


Figure 5-12: PGA estimates for the Lourdes earthquake, on rock conditions. The model “KO20 - posterior” is overlapping with the model “KO20 - shake-map”.

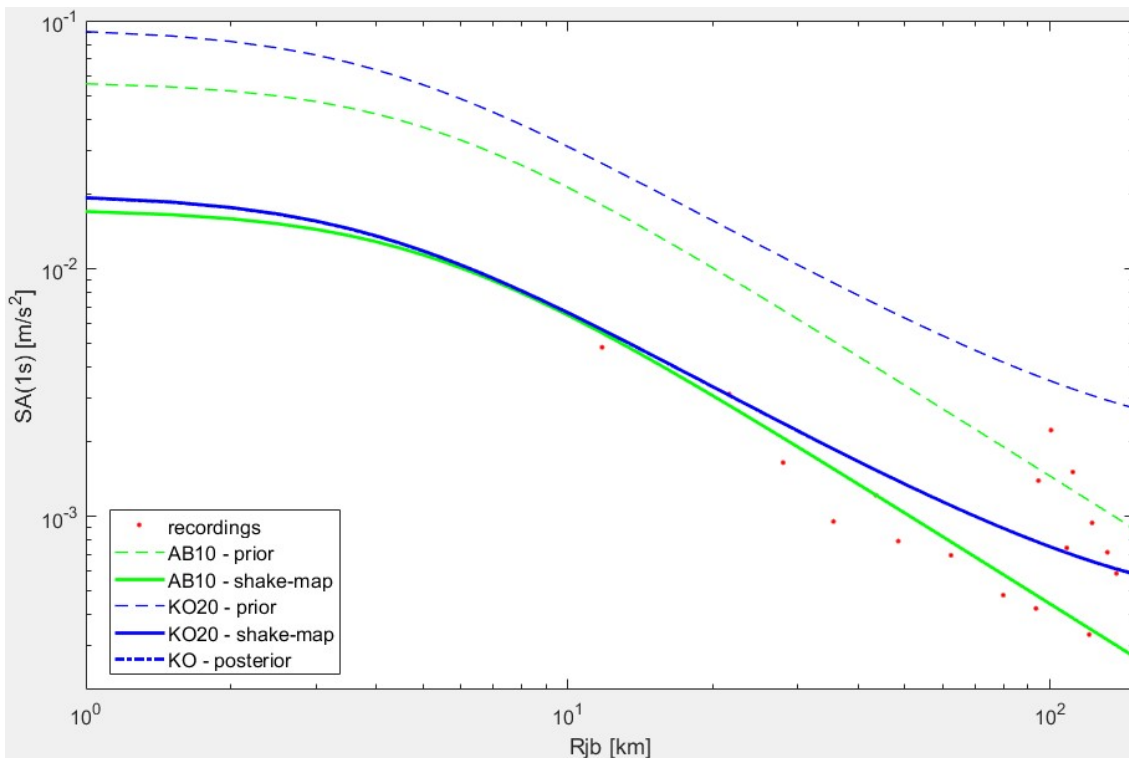


Figure 5-13: SA(1s) estimates for the Lourdes earthquake, on rock conditions. The model “KO20 - posterior” is overlapping with the model “KO20 - shake-map”.

The performance of the various models is evaluated through a set of scoring metrics, which are defined as follows:

- **LLH**: log-likelihood measure, as defined in Section 4
- **PMG**: Pari-Mutuel Gambling score, as defined in Section 4.
- **Q**: quantile score, as defined in Section 4.
- **EMD**: Euclidean Metric Distance, as defined in Section 4.
- **MSE**: Mean Squared Error, which is expressed as:

$$MSE = \sqrt{\frac{1}{N} \sum_{i=1}^N (\log Y_{obs,i} - \log Y_{pred,i})^2} \quad (5-5)$$

where N is the number of observations (recorded data for each earthquake), $Y_{obs,i}$ is the observed value and $Y_{pred,i}$ the value predicted by the model.

The score values are detailed in Table 5-6 and Table 5-7, for PGA and SA(1s) predictions, respectively. For each model, the suffixes are defined as follows:

- ***_pr**: prior estimates, i.e. the GMM is applied without using the observations.
- ***_sm**: shake-map estimates, without updating the GMM coefficients.
- ***_pt**: shake-map estimates, including the update of GMM coefficients c_1 and c_3 .

In the tables, the green cells indicate the best performing model for each metric. A global ranking is proposed (last column of the tables), where the ranking of each model is added across all metrics (#1 being the best): the model with the lowest ranking value corresponds to the best performing model.

Table 5-6: Scores and ranking of the various models predicting PGA for the studied earthquakes.

		PGA					
Earthquake	Model	LLH	PMG	Q	EMD	MSE	Ranking
Lourdes	KO20_pr	1.01778	-0.17780	-0.01911	0.69014	0.40700	18
	KO20_sm	0.89701	0.30074	0.03044	0.07475	0.33257	8
	KO20_pt	0.89493	0.30076	0.03044	0.07480	0.33256	7
	AB10_pr	1.54447	-0.27896	-0.06669	0.98066	0.47184	25
	AB10_sm	1.08228	-0.14473	-0.02348	0.65904	0.40113	17
Norcia	KO20_pr	0.52026	-0.07340	0.00904	0.38711	0.33447	22
	KO20_sm	0.77343	-0.01699	0.00983	0.17452	0.31656	16
	KO20_pt	0.67017	0.05175	0.00454	0.03506	0.30741	16
	BI11_pr	0.49490	-0.04545	0.00899	0.27182	0.34095	21
	BI11_sm	0.50315	-0.01820	0.00831	0.19854	0.33541	20
	BI11_pt	0.22805	0.10229	0.00720	0.11746	0.27917	10
Aquila	KO20_pr	0.06498	-0.02171	0.00828	0.33377	0.25032	24
	KO20_sm	0.00432	0.00238	0.01247	0.02745	0.23730	15
	KO20_pt	0.00117	-0.00327	0.01334	0.01213	0.23682	13
	BI11_pr	0.17822	0.00155	0.02090	0.04739	0.25756	21
	BI11_sm	0.11186	0.00989	0.02018	0.00992	0.25728	14
	BI11_pt	0.15209	0.01115	0.01846	0.06251	0.25686	18

Emilia I	KO20_pr	0.38641	0.05978	0.00439	0.48355	0.31209	20
	KO20_sm	0.43142	-0.01802	0.01266	0.15239	0.28407	22
	KO20_pt	0.35083	-0.02240	0.01429	0.01250	0.27589	13
	BI11_pr	0.42278	-0.01218	-0.01365	0.61521	0.32385	26
	BI11_sm	0.19920	-0.02632	0.01271	0.10438	0.27711	16
	BI11_pt	0.20310	0.01914	0.01297	0.00698	0.27000	8
Emilia II	KO20_pr	0.47420	0.02156	-0.01323	0.50325	0.32694	19
	KO20_sm	0.51101	-0.00989	0.00292	0.01694	0.29194	20
	KO20_pt	0.49176	-0.01225	0.00297	0.03431	0.29010	18
	BI11_pr	0.48639	0.00002	-0.01660	0.60015	0.33898	25
	BI11_sm	0.26357	0.00205	0.00132	0.01099	0.29047	10
	BI11_pt	0.27778	-0.00150	0.00367	0.01807	0.29120	13

Table 5-7: Scores and ranking of the various models predicting SA(1s), for the studied earthquakes.

Earthquake	Model	SA(1s)					Ranking
		LLH	PMG	Q	EMD	MSE	
Lourdes	KO20_pr	4.97584	-0.82979	-1.15804	3.04644	0.74208	40
	KO20_sm	-0.03140	0.19945	0.02460	0.16359	0.22826	13
	KO20_pt	-0.03357	0.19994	0.02458	0.16392	0.22806	13
	AB10_pr	1.16001	-0.15856	-0.07234	1.32092	0.46189	32
	AB10_sm	0.35631	0.58896	-0.00845	0.50912	0.30871	22
Norcia	KO20_pr	1.01138	-0.12677	-0.03550	0.82216	0.39687	48
	KO20_sm	0.86858	0.03242	0.00851	0.08132	0.30730	12
	KO20_pt	0.90952	-0.00831	0.00598	0.17466	0.31089	29
	BI11_pr	0.49839	0.10617	0.00681	0.09600	0.34087	19
	BI11_sm	0.57481	0.02437	0.00457	0.18514	0.34509	36
	BI11_pt	0.37059	-0.02788	0.00652	0.12661	0.31256	24
Aquila	KO20_pr	1.72702	-0.19697	-0.08074	1.07997	0.47800	48
	KO20_sm	1.09021	0.04884	0.00163	0.14349	0.32639	33
	KO20_pt	0.95029	0.09320	0.00707	0.02283	0.31529	23
	BI11_pr	0.48005	-0.16251	-0.02608	0.65521	0.33601	38
	BI11_sm	0.21262	0.10950	0.00913	0.01584	0.28024	10
	BI11_pt	0.23613	0.10794	0.01027	0.04174	0.28211	16
Emilia I	KO20_pr	0.39185	0.01877	0.00810	0.00709	0.30995	24
	KO20_sm	0.90702	0.00430	0.00871	0.06709	0.31064	38
	KO20_pt	0.88876	0.00618	0.00907	0.03095	0.30924	26
	BI11_pr	0.63903	-0.04242	-0.01593	0.70331	0.37605	46
	BI11_sm	0.35418	0.01650	0.01277	0.02216	0.30736	14
	BI11_pt	0.34678	-0.00333	0.01331	0.03870	0.30742	20
Emilia II	KO20_pr	0.07466	0.03452	0.00805	0.04653	0.25418	21
	KO20_sm	0.24819	0.02713	0.00845	0.06664	0.25447	31
	KO20_pt	0.23666	0.04008	0.00797	0.00948	0.25337	19

BI11_pr	0.68947	-0.13965	-0.07192	1.08837	0.38789	48
BI11_sm	0.12449	0.03153	0.01606	0.02178	0.26214	22
BI11_pt	0.12278	0.00639	0.01375	0.06077	0.25652	27

From the results obtained over several recent earthquakes, several points are worth noting:

- Globally, the updating of the GMM coefficients is in competition with the updating of the GMM intra-/inter-event terms: as a result, the updated GMM does not deviate much from the original one, since in most cases the updating of error terms is sufficient to fit the recorded data.
- Recorded data over wide ranges of distance (e.g., Norcia earthquake) lead to a greater updating, as opposed to earthquakes where only a few data points are used (e.g., Lourdes earthquake).
- The scoring metrics and associated rankings show that shake-maps with updated GMMs (models “*_pt”) are more stable and that they globally rank the best.
- To some extent, the updating of GMM coefficients seems to reduce some of the biases introduced by different initial GMMs (e.g., differences between BI1 and K020 for the Norcia earthquake): at the end of the updating process, the posterior models are much closer to each other, which makes the GMM selection step less critical when deriving such shake-maps.

This approach has only been tested on a few recent earthquakes with a couple of underlying GMMs: further investigations are required before a systematic use in operational systems can be recommended.

5.3 Verification of conversion equations between intensity and peak ground motion

5.3.1 Ground motion intensity conversion equations (GMICE)

In engineering seismology, a distinction must be made between instrumental and macroseismic intensity. With the possibility of carrying out extensive instrumental measurements of the ground motion parameters, it is feasible to correlate the intensity with these measurements. The qualitative description is replaced by the measured quantity (cf. [Musson, 2002](#); [Lee, 2009](#)). Mercalli-Cancani-Sieberg-Scale ([Sieberg, 1923](#)) already gives estimate of ground motion parameters for the corresponding period $T = 1s$.

The problem lies in the compatibility of instrumental ground motion quantities and the intensities derived from them with the observed macroseismic intensities. In high seismicity regions such as California and Japan, it is possible to assign intensities on an instrumental basis due to the existing and steadily growing amount of data. Relationships are available as well for Italy ([Faenza and Michelini, 2010, 2011](#)), Greece ([Tselentis and Danciu, 2008](#)), among others. In the lower seismicity areas of Central Europe, the data basis is lacking due to few damaging earthquakes and the lack of dense seismic networks.

In Figure 5-14, peak ground acceleration (PGA) is compared with intensity *I*. For Central Europe, measurements of the PGA for the earthquakes 1978 Albstadt, 1992 Roermond and 2004 Waldkirch are processed, and, as a current example, the earthquake of 29.12.2020 Croatia. For comparison, the database for Italian earthquakes and associated intensities according to [Faenza and Michelini \(2010\)](#) as well as data of the 2011 Virginia earthquake (Eastern USA) ([USGS 2011](#)) are used. The colouring of the points indicates the employed macroseismic scale. From the graph, the large spread of the acceleration for the respective intensity levels can be seen, independent of the macroseismic scale. For intensities with potential damage (VI (6.0) to VIII (8.0)), there is a clear decrease in the available data sets. The datasets for 2020 Croatia are based on citizen data and show a wide range, which can be reduced when reviewed by qualified personnel.

Figure 5-14 compares ground motion-intensity relationships ([Tselentis and Danciu, 2008](#); [Faenza and Michelini, 2010](#); [Caprio et al., 2015](#); see equations given in Table 5-8) that are valid for individual areas of Europe. The relationship by [Faenza and Michelini \(2010\)](#) provides on average the best predictions for ground acceleration (PGA) for the earthquakes 1978 Albstadt and 2004 Waldkirch:

- Intensity V – VI (5.5): 30 cm/s²,
- Intensity VI (6.0): 45 cm/s²,
- Intensity VI – VII (6.5): 75 cm/s²,
- Intensity VII (7.0): 120 cm/s²,
- Intensity VII – VIII (7.5): 180 cm/s², and
- Intensity VIII (8.0): 270 cm/s².

Table 5-8: Compared ground motion intensity conversion equations (GMICE) in Figure 5-14

Reference	Scope of application	Equation	Data range*
(Tselentis and Danciu 2008)	Greece	$MMI = (-0.946 \pm 0.266) + (3,563 \pm 0.153) \log PGA$	MMI: IV - VIII 3.5 ≤ M ≤ 6.9 1 ≤ D _{Epi} ≤ ~ 120 km D _{PGM-Int} < 5 km
(Faenza and Michelini 2010, 2011)	Italy	$I_{MCS} = (1.68 \pm 0.22) + (2.58 \pm 0.14) \log PGA, \sigma = 0.35$	MCS: II - VIII 3.0 ≤ M ≤ 6.9 1 ≤ D _{Epi} ≤ ~ 490 km D _{PGM-Int} < 3 km Orthogonal regression
(Caprio et al. 2015)	Global active crust	$INT = 2.270 + 1.647 \log PGA$ if log PGA ≤ 1.58	DYFI (MMI): II - IX 2.5 ≤ M ≤ 7.3 < 1km ≤ D _{Epi} ≤ ~ 200 km D _{PGM-Int} < 2 km Orthogonal regression
	California	$INT = 2.270 + 1.647 \log PGA - 0.6 \pm 0.7$ if log PGA ≤ 1.58	
	Greece	$INT = 2.270 + 1.647 \log PGA - 0.0 \pm 0.8$ if log PGA ≤ 1.58	
	Italy	$INT = 2.270 + 1.647 \log PGA + 0.3 \pm 0.9$ if log PGA ≤ 1.58	

* MCS ... Mercalli-Cancani-Sieberg

MMI ... Modified Mercalli Intensity

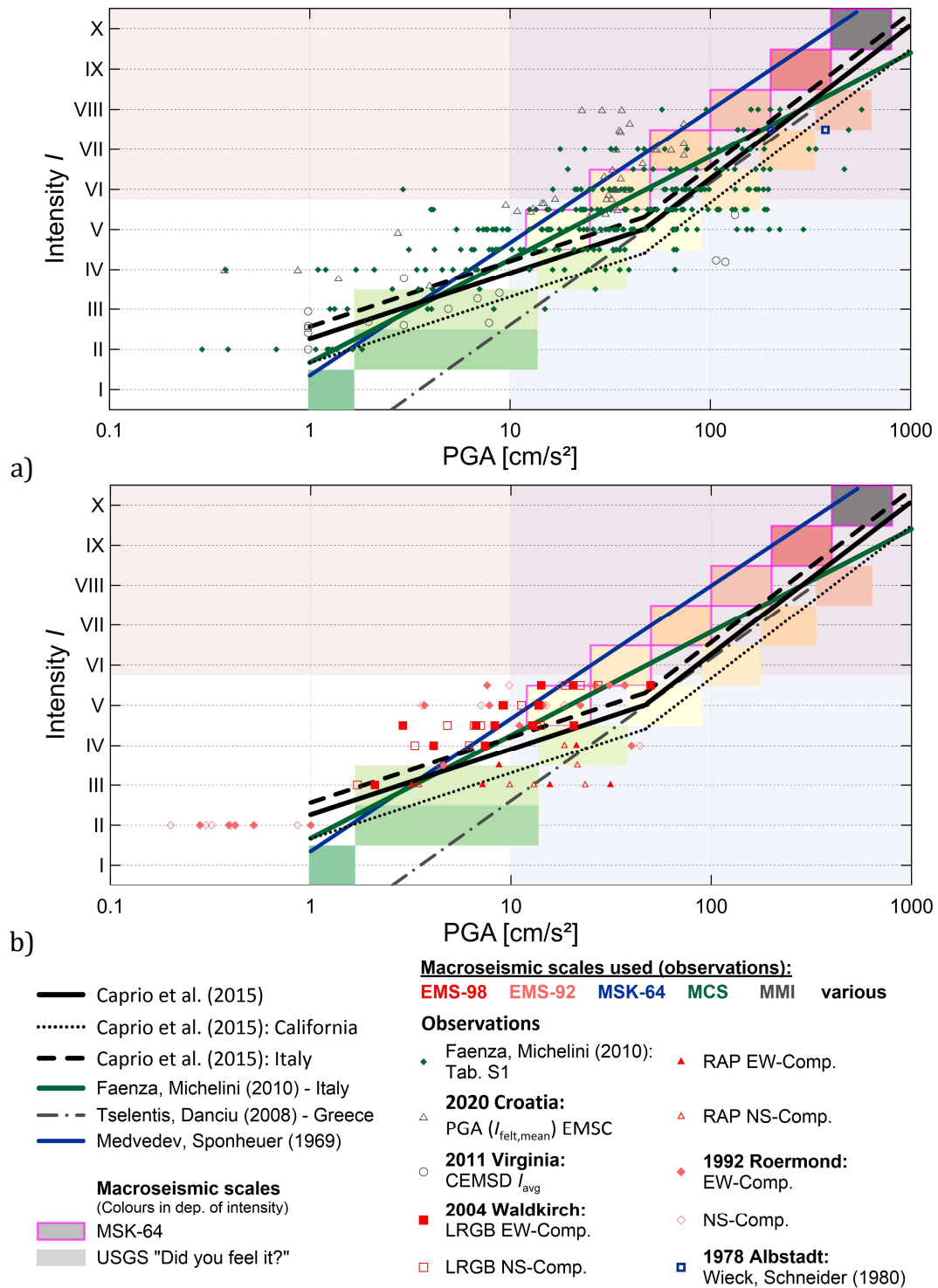


Figure 5-14. Comparison of measurements with assigned macroseismic intensity of the earthquakes a) 1978 Albstadt (Wieck and Schneider 1980), 2011 Virginia (CEMSD 2011), and 2020 Croatia (EMSC 2020) with the dataset used by (Faenza and Michelini 2010) and b) 1992 Roermond (Ahorner 1993), 2004 Waldkirch (EW- and NS- Component, (LED 2005) checked against the relationships acc. to (Medvedev and Sponheuer 1969; Tselentis and Danciu 2008; Faenza and Michelini 2010; Caprio et al. 2015)

* EMS-98 ... (Grünthal et al. 1998)
 MCS ... (Sieberg 1923, 1937)

EMS-92 ... (Grünthal et al. 1993)
 MMI ... (Wood and Neumann 1931)

MSK-64 ... (Medvedev et al. 1965)
 various ... no explicitly determined scale

The extent to which this forecast can be applied to low to medium seismicity regions with regard to macroseismic intensities from VII (7.0) will only be shown by strong earthquakes measured.

In Figure 5-14, the shaded areas of the MSK-64, given in [Medvedev and Sponheuer \(1969\)](#) intensity scale are compared with those of the MMI scale ([Wald et al., 2001](#)), which forms the basis of the USGS shake-maps. It can be clearly seen that the MMI scale underestimates the intensities in Europe (MSK scale (Figure 5-14a) as well as data sets, especially Waldkirch 2004 (Figure 5-14b) by one intensity level, especially for the range of magnitudes from 5 to 6 for the lower intensity ranges.

5.3.2 Observed intensity and recorded ground motion

For the 2004 Waldkirch earthquake, a limited number of strong motion records are available ([LED, 2005](#); [RAP, 2005](#)). In Figure 5-16, spectra of the horizontal components of near source measurements of [LED \(2005\)](#) are compared with results using the ground motion prediction equation (GMPE) proposed by [Schwarz et al. \(2007\)](#), SLKE07. The GMPEs are applied to each station on basis of the most probable subsoil class. The basis for this assumption is the geological map of ([LRGB, 1998](#)), additionally the GMPE of rock is given for the non-rock-type stations for the check of the selected geological subsoil class. The stations are sorted by distance from the epicentre D in km and the corresponding macroseismic intensity.

The macroseismic observations ([Benn et al., 2006](#)) located near the strong motion measurements were used to assign an intensity value (EMS-98) to the stations and their measurements. Buffers were created around the stations (3km, 5km, and 7km) to find valid data for these measurements.

For the majority of the measurements, the 3km-buffer is sufficient. For the intensity assessment, the obtained intensity points were used directly for gridding without creating a ground motion map in a previous step. The relation of intensity values and peak ground accelerations (PGA) of measurements are shown also in Figure 5-14. The spectra calculated for the moment magnitude M_w of 4.6 and respectively 5.1 offer in tendency an acceptable prognosis compared to the recorded component spectra (see Figure 5-16).

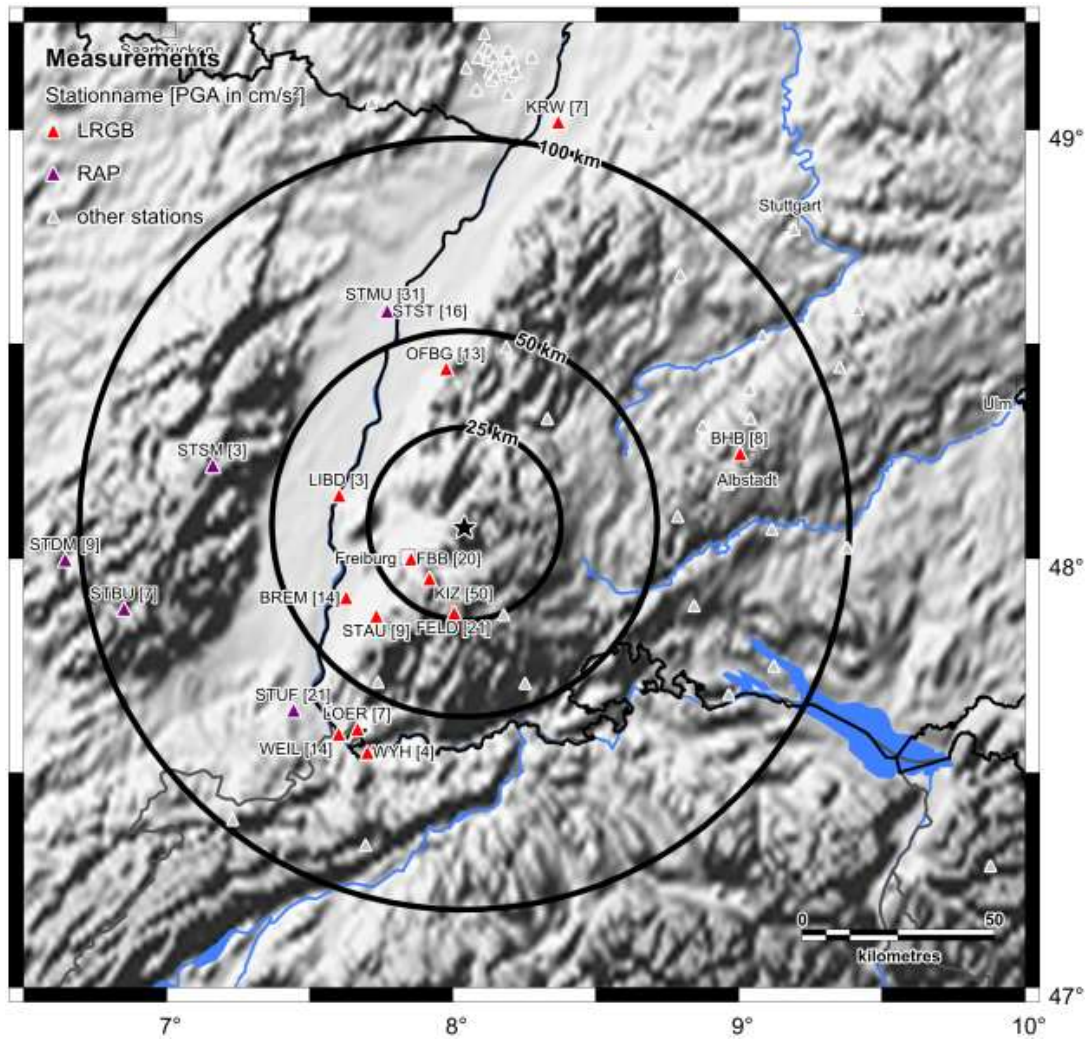


Figure 5-15. Measurements of the peak ground acceleration (PGA) in cm/s^2 named with station code [measured PGA] (LED, 2005, red triangle) and (RAP, 2005, purple triangle) of the Dec. 5, 2004 Waldkirch earthquake (black star indicates the epicentre).

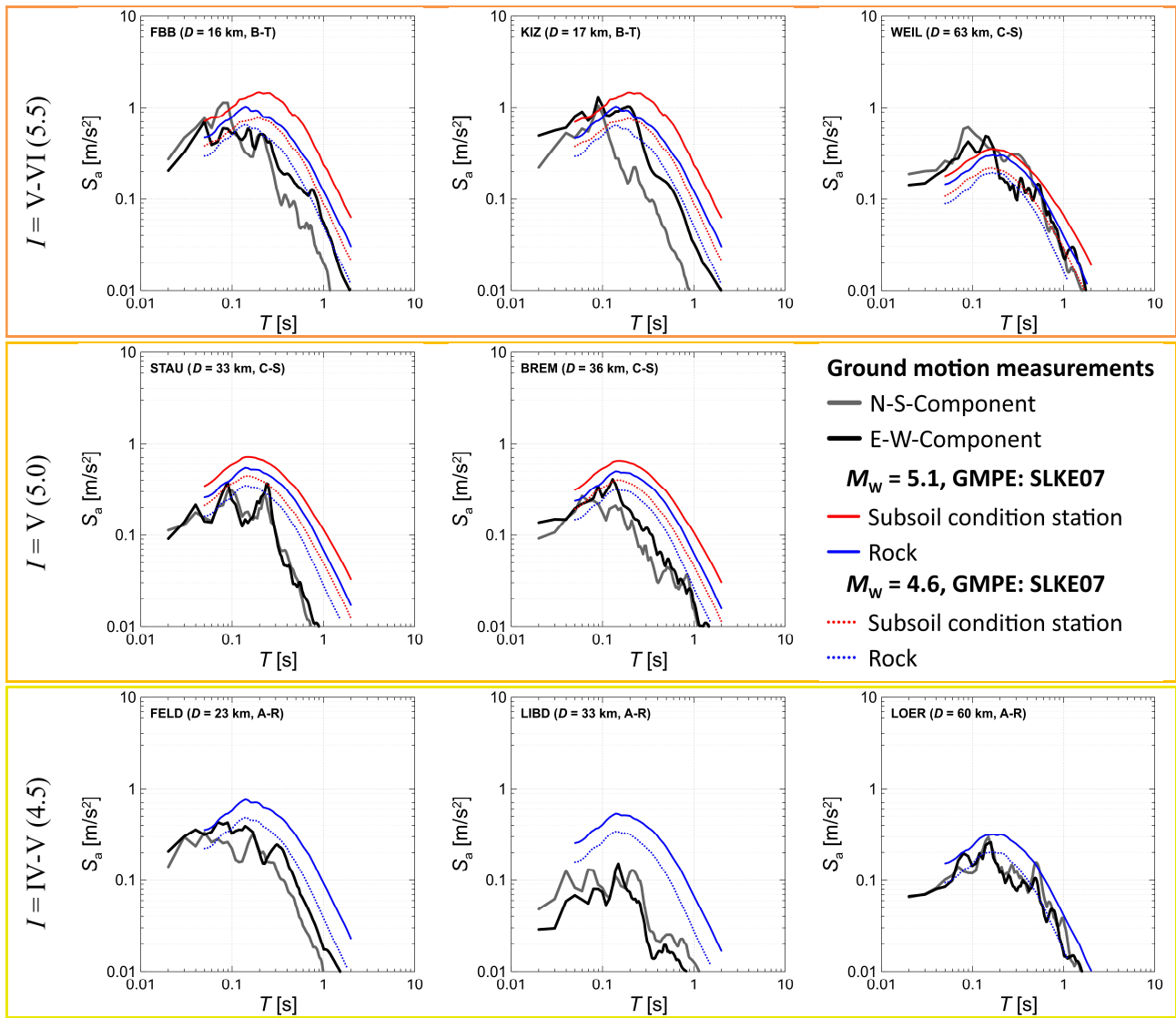


Figure 5-16. Comparison of spectral accelerations S_a of the ground motion measurements acc. to (LED (2005, 2013) with the GMPE (Schwarz et al., 2007) of the assumed subsoil class (classification acc. to German code) based on the geological map of (LRGB (1998) and additional rock spectra for non-rock-type stations.

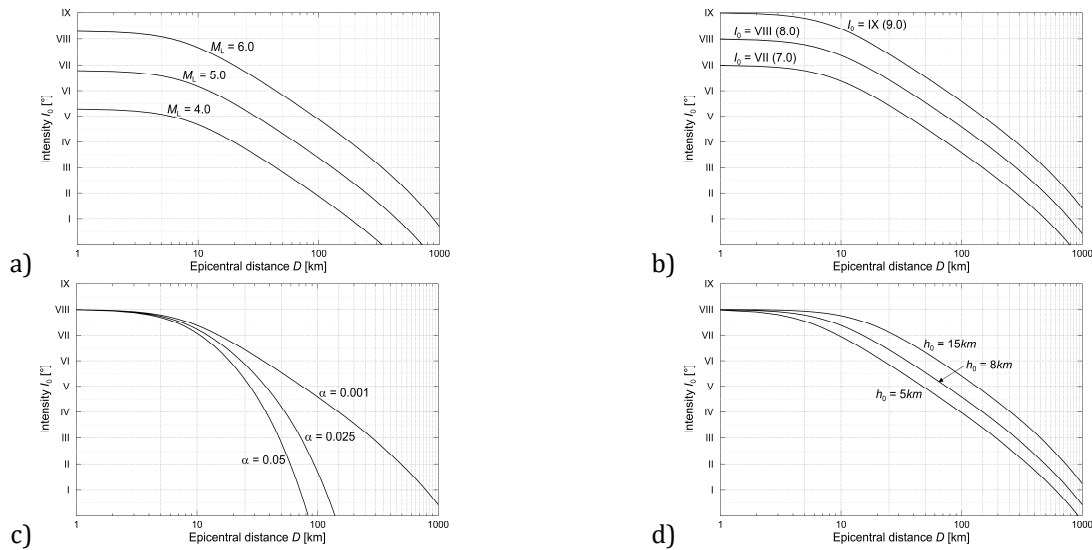


Figure 5-17. Influence of earthquake parameters a) local magnitude M_L , b) epicentral intensity I_0 , c) attenuation coefficient α , d) focal depth h_0 on the intensity attenuation using the relationships a) (Ahorner, 1983a), and b) to d) (Sponheuer, 1960), cf. (Beinersdorf, 2016).

5.4 Verification and updating of intensity attenuation

Intensity attenuations relationship are valuable method to predict the possible shaking effects for an event in time in case strong motion measurements are missing especially in sparse monitored regions, most with low to medium seismicity. With only the knowledge of magnitude or epicentral intensity the shaking effects in form of macroseismic intensity can be predicted and related to possible observed damage grades of the existing building inventory (see Section 3.2, Figure 3-5 and Figure 3-6). This is especially interesting for regions where applicable for the local conditions GMPEs based on strong earthquake measurements collected in that regions are missing.

5.4.1 Preselection of intensity attenuation relations

Various parameters have an influence on the macroseismic intensity occurring at a site. This is shown schematically in Figure 5-17. Figure 5-17a shows the influence of the increase in magnitude. It can be seen that in the relationship shown here according to Ahorner (1983a), if the magnitude increases by 1.0, the degree of intensity increases by about 1.5 in the epicentral region.

Figure 5-17b shows that with the increase of the epicentral intensity by 1.0, the curve of the attenuation relationship is shifted accordingly on the Y-axis. The variation of the intensity attenuation coefficient α and the focal depth h_0 are presented in Figure 5-17c and Figure 5-17d. The influence of the intensity attenuation coefficient α on the intensity attenuation can be clearly seen. The greater the intensity attenuation coefficient α , the faster the intensity decreases. The variation of the focal depth h_0 leads to a faster decrease in intensity over the entire curve as the focal depth h_0 decreases. The attenuation is greater with decreasing focal depth h_0 .

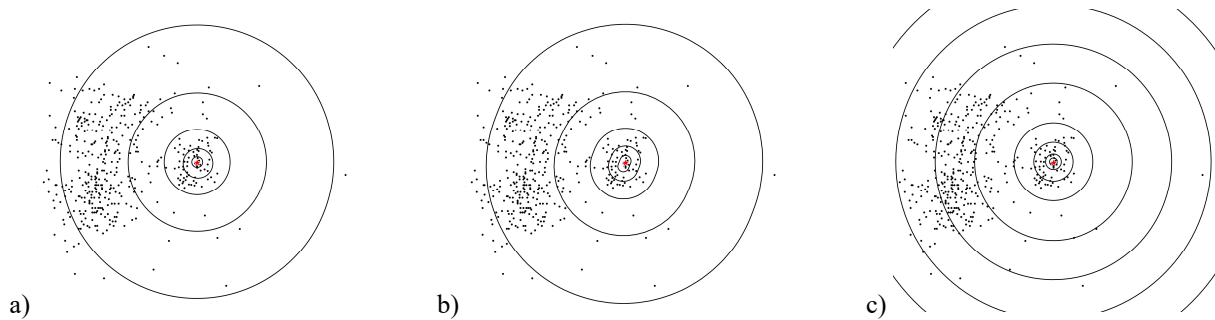


Figure 5-18. Selected evaluation forms of a) intensity attenuation relationship and point source, b) intensity attenuation relationship and line source with orientation from seismic moment or moment tensor solution (example Figure 6-12b), c) radii with defined distance from the epicentre (grouping macroseismic observations according to distance from the epicentre or hypocentre of the earthquake and used for individual attenuation functions) of the attenuation in individual intensity based on attenuation relationships and macroseismic intensity observations, cf. (Beinersdorf, 2016).

Sponheuer (1960) is used as the reference attenuation relationship. The intensity attenuation relation (Sponheuer, 1960) was developed on the basis of the method by Kövesligethy (1907) in order to determine the focal depth and the intensity attenuation coefficient using macroseismic observations of an earthquake. The following assumptions about the earthquake are made for the determination of the focal depth by Sponheuer (1960, pp. 10–11):

- the earthquake is represented as a point source,
- plane surface in the macroseismic shaking area,
- homogeneous and isotropic propagation medium (straight-line wave dispersion),
- period of the earthquake waves constant with increasing distance as well as
- radial isoseismal contour line of the each intensity level.

In Figure 5-19, macroseismic observations of the induced earthquake events 1997 Roswinkel (NL) and 2012 Huizinge (NL) are compared to the intensity attenuation according to Sponheuer (1960). The influence of the intensity attenuation coefficient α regarding the decay as well as the shift due to the focal depth h_0 is clearly seen. The finally used parameters for the intensity attenuation are given in Table 5-9.

Table 5-9: Parameters of the earthquakes 1911 Ebingen, 1978 Albstadt, 1997 Roswinkel, and 2012 Huizinge taken for the intensity attenuations in Section 5 (Schwarz et al., 2019a, pt. B and C of EK DAG)

Earthquake	M_L	M_w	I_0	α	h_0 [km]
1911 Ebingen	6.1	5.7	VIII	0.001	10.0
1978 Albstadt	5.7	5.1	VII - VIII	0.001	6.5
1997 Roswinkel	3.4	3.4	VI	0.022	2.0
2012 Huizinge	3.3	3.6	VI	0.014	3.0

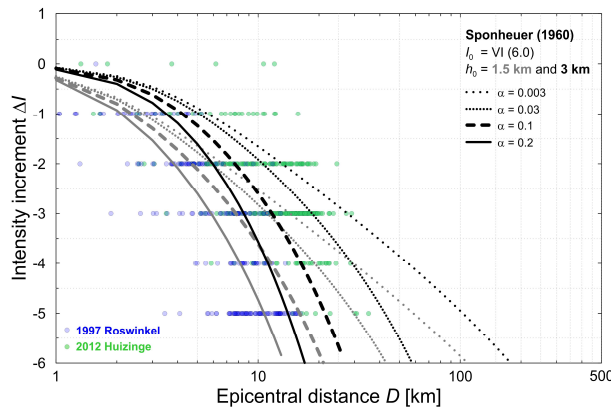


Figure 5-19. Shaking effects of the induced earthquakes within the gas production fields 1997 Roswinkel ($M_L 3.4$, (Dost et al., 1997)) and 2012 Huizinge ($M_L 3.5$, (Dost and Kraaijpoel, 2013)) compared to variations of the respective intensity attenuations which are shown here as intensity increments ΔI (cf. Schwarz et al., 2019b).

5.4.2 Basics steps of an updating procedure

An example of the intensity attenuation compared to the observed macroseismic intensities for an historic event is shown in **Erreur ! Source du renvoi introuvable.**. The investigated dataset of macroseismic points is shown as grey points. These points are grouped on the basis of equivalent radii (s. a. Figure 5-18c) and mean, standard deviation as well 95% fractile is calculated, which are shown in **Erreur ! Source du renvoi introuvable.**. Different intensity attenuations fitting to the study region are compared to the macroseismic observations (EMS-98-based). The attenuation of the intensity of the macroseismic observations evaluated according to equivalent radii with defined distance from the epicentre shows a good fit in comparison to the various intensity attenuation relationships used, even if the dataset shows a larger variety of observed intensities.

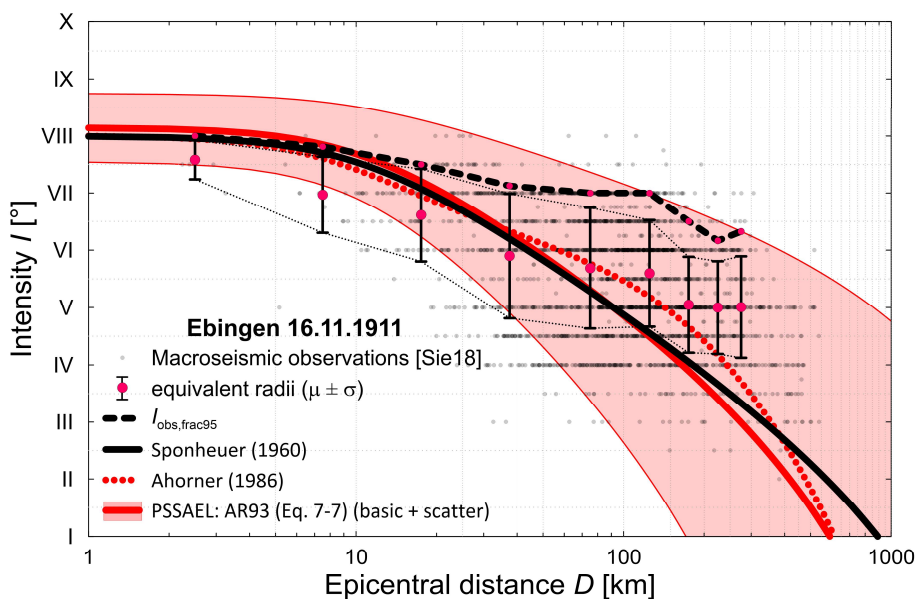


Figure 5-20. Example for the intensity attenuation derived from macroseismic observations for the 1911 Ebingen earthquake of epicentral intensity $I_0 = \text{VIII}$ (8.0) and focal depth $h_0 = 10$ km for the relations acc. to (Sponheuer, 1960; Ahorner et al., 1986; Rosenhauer, 1999)

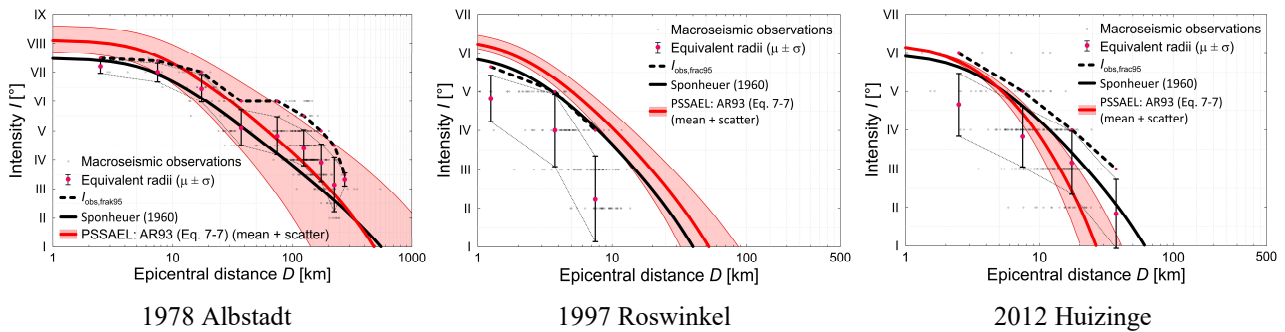


Figure 5-21. Comparison of intensity attenuations with macroseismic observations for the earthquakes 1978 Albstadt, 1997 Roswinkel, and 2012 Huizinge compared to the intensity attenuations acc. to (Sponheuer, 1960; Rosenhauer, 1999) for the corresponding earthquake

Depending on the availability of data, different procedures can be applied to create in a one-step approach (Method 2), where the macroseismic intensity is taken as input parameter. Also, the conversion of the magnitude of an earthquake event to the macroseismic intensity is possible. The macroseismic intensity shake-maps are directly calculated without using GMPEs and GMICEs (cf. Figure 6-1 and section 6.1). The starting point is the location of the epicentre and the intensity in terms of macroseismic intensity (examples: attenuation Sponheuer (1960) in Figure 5-21) or magnitude (examples: attenuation Rosenhauer (1999) in Figure 5-21). An appropriate attenuation relationship is selected, and a point source assumed (Figure 5-18a, Figure 6-12a). In case the fault, which produced the earthquake, is known then the initial source can be a line and consequentially, an elliptic attenuation of the intensity (Figure 5-18b, Figure 6-12b). Depending on the region where the earthquake is occurring, information regarding typical attenuation (Figure 5-17c) and focal depths (Figure 5-17d) can be used until the event related data are determined.

As soon as more information is available, as e.g. the fault plane, the fault plane solution or the moment tensor solution, updates can be performed. The adjustment of the attenuation relationship can be achieved as well by equivalent radii with defined distance from the epicentre by grouping macroseismic observations according to distance from the epicentre or hypocentre of the earthquake. The growing knowledge of the individual intensity attenuation is used to calculate individual attenuation functions (s. Figure 5-18c, Figure 5-21 and **Erreur ! Source du renvoi introuvable.**). Community-based observations like the ones collected by EMSC can be used here, knowing that the range of variation can be very large since evaluation by experts has not yet been carried out.

5.4.3 Model curves (including scatter)

Magnitude-based intensity attenuations valid for Central Europe have been developed by various authors (Ambraseys, 1985; Ahorner and Rosenhauer, 1986, 1993; Hinzen and Oemisch, 2001; Bakun and Scotti, 2006).

As an example, the attenuation relationship according to [Ahorner and Rosenhauer \(1986\)](#) for the intensity at a distance of 10 km I_{10} , the equation can be set up as follows:

$$I_0(R) = I_{10} + 3.0 - 3.0 \lg R - 1.3 \cdot \alpha \cdot (R - 10) \text{ with } R = \sqrt{h_0^2 + D^2} \quad (5-6)$$

with the parameters

- I_{10} ... intensity with the hypocentral distance of 10km,
- h_0 ... focal depth in km,
- D, R ... epicentre distance and hypocentre distance in km and
- α ... attenuation coefficient α in km^{-1} (usually 0.001 to 0.005).

The intensity at a distance of 10 km I_{10} can be described with the following hypothesis (valid for Central Europe) according to (Gutenberg and Richter 1956, eq. (14)) and is also used in [Ahorner \(1983b\)](#).

$$I_{10} = 1.5M_L - 1.0 \quad (5-7)$$

with the parameters

- I_{10} ... intensity at the hypocentral distance of 10 km,
- M_L ... local magnitude.

By substituting the relationship results in:

$$I(R, M_L) = 1.5M_L + 2.0 - 3 \lg R - 1.3 \cdot \alpha \cdot (R - 10) \quad (5-8).$$

Furthermore, the following mean attenuation function was determined by [Ahorner and Rosenhauer \(1986\)](#) on the basis of macroseismic observations, which is valid for the Lower Rhine Bay:

$$I - I_{10} = 10.6 - 19.05 \lg R + 10.4(\lg R)^2 - 2.1(\lg R)^3 \quad (5-9)$$

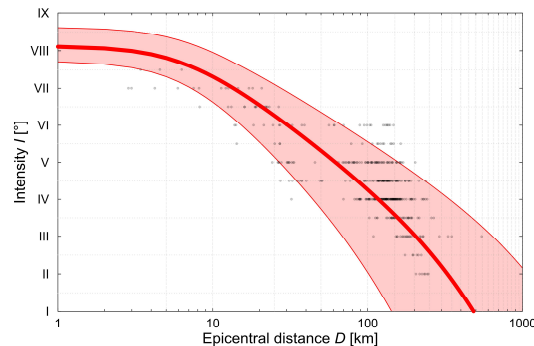


Figure 5-22. Magnitude-based intensity attenuation (M_L) acc. to ([Ahorner and Rosenhauer 1993](#); [Rosenhauer 1999](#)) in comparison to the macroseismic observations for the corresponding earthquake; here 1978 Albstadt, thick red line – baseline of the intensity attenuation, scatter range: minimum and maximum values of the equally distributed parameters

The methodology, database and derived correlations are described in more detail in [Ahorner and Rosenhauer \(1993\)](#) and [Rosenhauer and Ahorner \(1994\)](#). The application in engineering design practice leading became of relevance while linking the regional observations and earthquake parameters with the Monte-Carlo simulation techniques being introduced as **Probabilistic Seismic Site Analysis with Earthquake Libraries PSSAEL** ([Rosenhauer, 1999](#)). The principle is unique and enables the adaption of the intensity attenuation with respect to magnitude and distance (see Figures 5-21 and 5-22), i.e., intensities at the site are calculated on the basis of the local magnitude M_L , focal depth h_0 , and epicentral distance D with the help of Eq. (5-8). For the simulation of the uncertainties and attenuation characteristics Eq. (5-10) is proposed:

$$I(M, R) = AM \cdot M_L - BM - AKH \cdot \lg(R/10km) - AKOF \cdot (R/10km - 10) \quad (5-10)$$

with the coefficients

- AM ... according to [Gutenberg and Richter \(1956\)](#); base value 1.5
- BM ... magnitude range, base value 1.0 (0.4 ... 1.6) [equally distributed]
- AKH \triangleq k ... slope factor of the intensity assignments base value 3.0 (2.5 ... 4.0; [Rosenhauer, 2005](#)) [equally distributed] base value 3.0 (1.5 ... 4.0; [Ahorner and Rosenhauer, 1993](#)) [equally distributed]
- AKOF \triangleq α ... 0.003 (0.001 ... 0.01) [-2,5 (-3.0 ... -2.0)] [logarithmically equally distributed]

Table 5-10 is providing an overview of parameter variations (*variants PSSAEL*) and corresponding ranges of the coefficients which might be selected to match the observations. This might be of importance to distinguish between the types of tectonic earthquakes (TB1 to TB4) and the induced earthquakes (TB-6). The objective of Eqs. (5-8) and (5-10) is to represent the reality of the intensity attenuation of earthquakes with knowledge of magnitude and focal depth as well as the allowance of variation ranges (see Figure 5-22 and Table 5-10).

Table 5-10: Modifications in PSSAEL acc. to [Schwarz et al. \(2014\)](#) (Figure 5-22 and Figure 5-23)

Variants PSSAEL	Abbr.	AKH			BM			AKOF (α)		
		Min	—	Max	Min	—	Max	Min	—	Max
Ahorner, Rosenhauer (1993) PSSAEL*	AR93	1.50	3.00	4.00	0.40	1.00	1.60	-3.0	-2.5	-2.0
Rosenhauer (2005) PSSAEL	Ros05	2.50	3.00	4.00	0.40	1.00	1.60	-3.0	-2.5	-2.0
Vextended	Vext	2.00	3.00	4.50	0.20	1.00	1.75	-3.0	-2.5	-2.0
Vshortened	Vshort	2.75	3.00	3.50	0.75	1.00	1.25	-3.0	-2.5	-2.0
Normal [high]	Norm +	3.00		4.00	1.00		1.60	-3.0	-2.5	-2.0
Normal [low]	Norm -	2.50		3.00	0.40		1.00	-3.0	-2.5	-2.0
Normal [lower]	Norm --	1.50		3.00	0.40		1.00	-3.0	-2.5	-2.0

5.4.4 Examples

In the probabilistic hazard analyses carried out described in detail in [Rosenhauer \(1999\)](#), a correlation between intensity, magnitude and distance is used for the calculation of the site intensity in order to correctly capture the large ranges of variation that exist from earthquake to earthquake with the determined intensity occurrence rates $\lambda (> I)$.

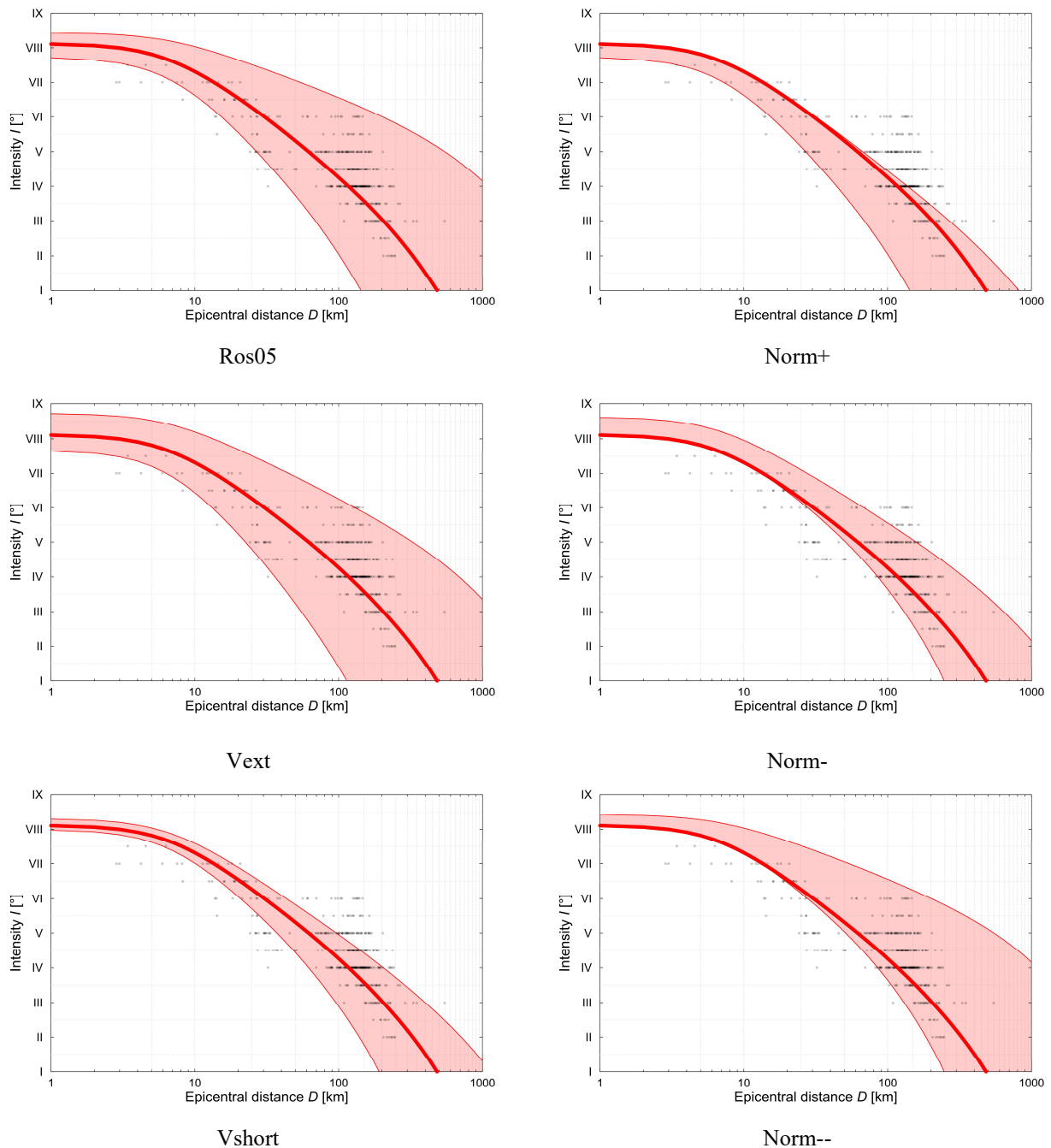


Figure 5-23. Variations acc. to Table 5-10 of the magnitude-based intensity attenuation (M_L) acc. to [Rosenhauer \(1999\)](#) in comparison to the macroseismic observations for the corresponding earthquake; here 1978 Albstadt, thick red line - baseline of the intensity attenuation, scatter range: minimum and maximum values of the equally distributed parameters

Depending on the objective of the probabilistic analysis, different variants can be included in the analysis and given a corresponding weighting (see Figure 5-23). The parameters used for this can be found in Table 5-10. The simulation of the earthquake databases for probabilistic investigations is oriented towards covering the observed shaking effect via the light red shaded area.

Employing Monte Carlo simulation, the coefficients BM, AKH and AKOF (Eq. 5-10, Table 5-10) are determined within the scope of their possible fluctuations with respect to M_L by random numbers for each simulated event. Trend analyses to show the results due to an updated intensity assignment can be calculated for all the potentially considered modelling variants.

6 ADJUSTMENT FACTORS FOR LOCAL SITE CONDITIONS

6.1 Knowledge-based framework for the generation of site-specific shake-maps

For seismic risk modelling purposes, site effects due to surface geology are generally mapped at large scales, using either the EC8 soil classes or the $v_{s,30}$ proxy parameter. These site condition maps can be computed: 1) using geological parameters (Wills and Clahan, 2006; Lee and Tsai, 2008; McPherson et al., 2013; Di Capua et al., 2016); 2) using morphological parameters (e.g., slope) (Wald and Allen, 2007a; Allen and Wald, 2009); or 3) using hybrid methods combining both geological and DEM information (Stewart et al., 2014).

Section 6.2 presents methods to take into account the site-specific geology to determine intensity and ground motion for a site as a basis for creating intensity-based spectra or scenarios and shake-maps.

In Figure 6-1, a framework for the generation of site-specific shake-maps is presented considering decisions on the procedures, level of data availability as well as the selection of the scale as an essential prerequisite for the assessment of the level of uncertainties and their applicability for RRE.

Consideration of soil factors is an important criterion that can be used for quantifying soil-specific uncertainties in ground motion measurements and the refinement of predicted shaking effects especially in regions with sparse seismic networks. The framework distinguishes two different methods (Platforms), where the first one is applicable for calibration of ground motion measurements, while the latter one can be used for the incorporation of observed shaking effects (in terms of macroseismic intensity).

At the first level of the proposed framework for site-specific shake-map generation, input datasets (Data) that can be used as criteria for soil categorization are listed. The preliminary step for the calculation of site-specific soil factors is defined through the categorization of a site into its subsoil and deep geology profile (e.g. using a Digital Elevation Model (DEM) based on shear wave velocity). Input proxies are ranked based on their level of availability (see Table 6-1). The type of parameter used to identify the soil directly affects the uncertainties in soil factors, since some parameters, e.g. deep geological studies give a better representation of soil parameters than elevation-based subsoil models.

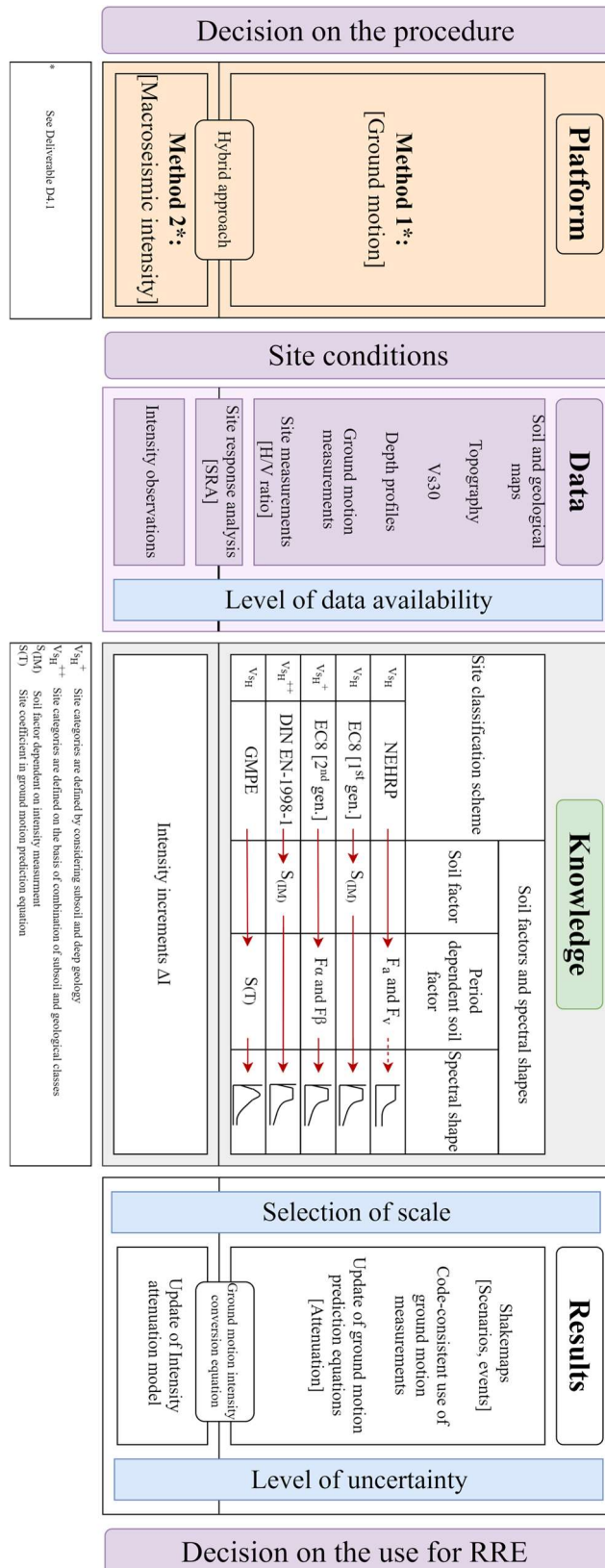


Figure 6-1: Knowledge-based framework for the generation of site-specific shake-maps

In Table 6-1, the level of data availability, following the concept introduced in Schwarz et al., 2021) for site-specific knowledge levels, these levels is introduced as a “guideline” for the TURNkey testbeds. Based on the level of data availability, different site classification schemes can be selected to determine site-dependent soil factors and spectral shapes or intensity correction factors. Accessibility to more refined knowledge for site classification (e.g. in scales 2, 3 and 4), increases the certainty of analytical assessments in shake-map calculations, vulnerability and damage grade evaluation as well as simulation of loss functions.

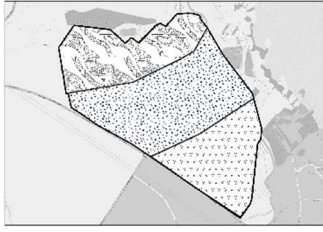
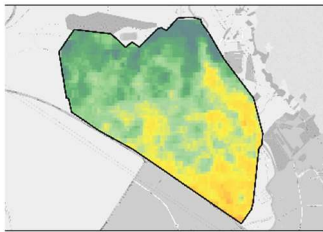
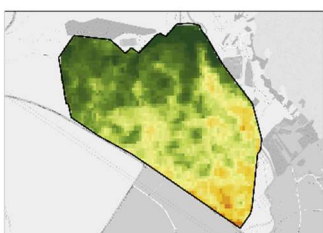
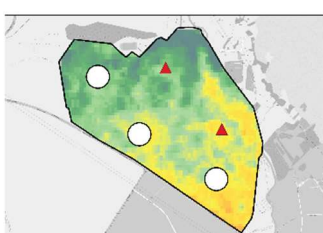
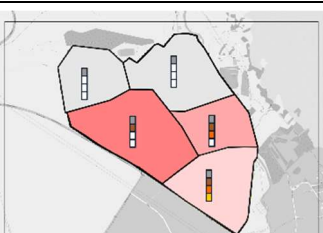
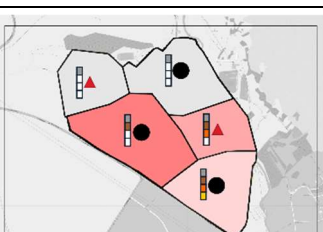
The proposed procedure lists different code-provided or regionally accepted site classification schemes that use shear wave velocity or geological profiles to categorize soil into different classes and subsequently provide soil factors or period-dependent amplification factors (Knowledge). Detailed descriptions of the listed subsoil classification schemes are provided in section 6.2:

- In section 6.2.1 the different subsoil classification schemes (NEHRP, EC 8 1st and 2nd generation, as well as DIN 4149) are presented.
- The code-related soil factors as well as site amplification factors using single earthquake data are elaborated in section 6.2.1 and section 0, respectively.
- Ground motion prediction equations that take shear wave velocity as a parameter for representing linear and nonlinear soil effects are also included in the framework (see section 6.2.4).
- Further refinement by site response studies (SRA) and instrumental site classification are introduced in sections 6.2.5 and 6.2.6.
- The second method uses intensity increments to calculate intensity attenuation models with consideration of soil profiles, topography and vulnerability of the building stock (see section 6.2.7).

Thus, in dependence of the selected scale, the site-specific information can be used for refined shake-maps (Results). Additionally, the framework allows introduction of the level of uncertainties based on available data and achievable knowledge level.

For further refinement and fulfilling RRE requirements, item-by-item data can be elaborated by the TURNkey partners in parallel to these activities to acquire detailed information provided by local authorities or decision makers.

Table 6-1: Examples of site-specific level of data availability

No	Level of data availability (LoDA)		Scale	Testbed					
	Scheme	Indicator		1	2	3	4	5	6
0		Rough geological and soil data	Macro	X ^o	X	X		X	X
1a		Subsoil data, e.g. DEM-based v_{s30} from U.S. Geological Survey	Meso	X	X	X		X	X
1b		Subsoil data, e.g. DEM-based v_{s30} from different sources	Meso	X ^{oo}	X*				X
2		Validated subsoil data, e.g. DEM-based v_{s30} validated with measurements from seismic station (▲) or soil profiles (○)	Meso						X
3		Model profile including subsoil and deep geology data	Micro	X ^{ooo}					X
4		Subsoil and deep geology data verified with measurements from seismic stations (▲), deep geology data, verified soil profiles (●), e.g. H/V method	Micro		X	X**		X	X

Legend: see next page

Legend of Table 6-1:

* based on geological logs, not DEM

** site factors obtained from earthquake recordings at stations verified with detailed geological units

° Mandrescu et al. (2007)

°° measurements in boreholes

°°° models compiled from available data (up to 2006) for previous works (e.g. Marmureanu et al., 2010)

The following sub-sections describe the modes that are available for the TBs: harmonized amplification models at the European level in Section 6.3 and more specific models at a local level in Section 6.4. Recommendations on which models to use in each TB are provided in Section 6.5.

6.2 Site-specific refinement of shaking effects

The following sections describe methods that are used as site-specific refinement of shaking based on the proposed knowledge-based framework for the generation of site-specific shake-maps (Figure 6-1) for both method 1 and method 2.

6.2.1 Classification based on shear-wave velocity Vs30 parameters

6.2.1.1 Calculation of average shear-wave velocity values

The stiffness-related classification scheme, in which the average shear-wave velocity (Vs30) is derived from the measured shear-wave velocity profile from the ground surface to a depth of 30 m at a particular site, is a well-accepted and robust parameter used to characterize local soils. The [European Committee for Standardization \(2004\)](#) and the [Building Seismic Safety Council \(2004\)](#) utilize Vs30 to categorize sites into different ground classes. The application of Vs30 can also be found in empirical ground-motion prediction equations as a parameter for modelling site-specific amplifications. Several methods are available to calculate or estimate the near-surface shear wave velocity. The Eurocode ([European Committee for Standardization, 2004](#)) calculates Vs30 using the following equation:

$$v_{S,H} = \frac{H}{\sum_{i=1,N} \frac{h_i}{v_i}} \quad (6-1)$$

Where:

- h_i is the thickness of the i -th soil layer,
- v_i is the shear-wave velocity of the i -th soil layer,
- H is the total number of soil layers from the ground surface down to the depth H ,
- $v_{S,H}$ is the equivalent value of v_s down to the reference depth H

6.2.1.2 NEHRP classification

According to the National Earthquake Hazards Reduction Program (NEHRP) (Building Seismic Safety Council, 2004), subsoil classes are classified into six different soil categories based on measured shear wave velocity up to 30 m depth. The soil at a certain site is classified into its respective class (A, B, C, D, E, and F) in accordance with Table 6-2.

Table 6-2: Sub-soil classes as a function of $v_{s,30}$ based on NEHRP site classification guidelines (Building Seismic Safety Council, 2004)

NEHRP site class	Soil description	$v_{s,30}$ (m/s)
A	Hard rock	>1500
B	Rock	760-1500
C	Very dense soil and soft rock	360-760
D	Stiff soil	18-360
E	Soft soil	<180
F	Soil requiring site specific evaluation	-

6.2.1.3 Eurocode site classification (first generation)

The first Eurocode (European Committee for Standardization, 2004) organises site classes into five typical ground types (A, B, C, D, and E) and two specific ground types (S_1 and S_2) to account for the influence of local ground conditions on seismic action. If the value of V_{s30} is not available, standard penetration test results N_{SPT} or the undrained cohesion C_u can be used instead. Table 6-3 presents the description of ground types and their related definitions according to the Eurocode 8 (European Committee for Standardization, 2004).

Table 6-3: Ground types according to Eurocode 8 (European Committee for Standardization, 2004)

Ground Type	Soil description	$v_{s,30}$ (m/s)	N_{SPT}	C_u
A	Rock or other rock-like geological formation, including at most 5 m of weaker material at the surface.	>800	-	
B	Deposits of very dense sand, gravel, or very stiff clay, at least several tens of metres in thickness, characterized by a gradual increase of mechanical properties with depth.	360-800	>50	>250
C	Deep deposits of dense or medium dense sand, gravel or stiff clay with thickness from several tens to many hundreds of meters.	180-360	15-50	70-250
D	Deposits of loose-to-medium cohesionless soil (with or without some soft cohesive layers), or of predominantly soft-to-firm cohesive soil.	<180	<15	<70
E	A soil profile consisting of a surface alluvium layer with v_s values of type C or D and thickness varying between about 5 m and	-		

	20 m, underlain by stiffer material with $v_s > 800$ m/s.			
S_1	Deposits consisting of or containing a layer at least 10 m thick of soft clays/silts with a high plasticity index ($PI > 40$) and high-water content	<100	-	10-20
S_2	Deposits of liquefiable soils of sensitive clays or any other soil profile not included in types A – E or S_1			

6.2.1.4 Eurocode site classification (second generation)

The Eurocode is periodically updated to keep up with changing knowledge. The newest draft of the Eurocode redefines the soil classification criteria, introducing new geotechnical parameters. Moreover, a new standardized approach is introduced to characterize the profiles in upper and deeper layers in combination (Schwarz, 2018).

In order to characterize a subsoil profile, both subsoil classes (SC) and geological classes (GC) are used. A ground type and site class or type is regarded as the combination of a subsoil class (SC) and a geological class (GC). The combination SC-GC follows a logical system (see concept in Table 6-4). The following ground or site types are defined:

- standard (shallow soil) site types: A-st, B-st, C-st;
- standard (deep soil) site types: B-t, C-t, C-d (C-vd).

For both types, combinations are recommendable, if amplification effects are of similar size. Very soft soil types (D) are considered in general as “difficult/problematic sites” requiring specific site investigations and foundation solutions (e.g. piles).

The standard definition of a ground type (site category) is based on the standard depth H_{st} (30 m) and the site's (soil profile's) total depth H (allowing a continuous increase of V_s within certain limits) in order to either cover the effects or to allow the profile below the reference depth H_{st} to be neglected.

Table 6-4: Standard combination site type classification scheme (Schwarz, 2018); recommended definition of depth values $H_{vs} = 5m$; $H_{st} = 30m$; $H_d = 60$ to $100m$; $H_{vd} = 200m$

Geological Class		Total Depth	Ground Types			
			A	B	C	D
			$v_{s,H_{st}} > v_{s,A}$	$v_{s,B} < v_{s,H_{st}} < v_{s,A}$	$v_{s,C} < v_{s,H_{st}} < v_{s,B}$	$v_{s,H_{st}} < v_{s,C}$
rock-like	r		A-r			
very shallow	vsh	$H < H_{vsh}$	A-vsh	B-vsh		D-vsh
shallow (standard)	sh (st)	$H < H_{st}$	A-st	B-st	C-st	D-st
transition	t	$H_{st} < H < H_d$	-	B-t	C-t	D-t
deep	d	$H_d < H < H_{vd}$	-	B-d	C-d	D-d
very deep	vd	$H > H_{vd}$	-	B-vd	C-vd	D-vd

Types of deep geology should be differentiated. The relevant ground types and site categories in European seismic regions have to be identified. Other combinations are recommendable if amplification effects are similar. Further sub-division of this classification is permitted on the basis of special instrumental and/or analytical site-classification studies.

The applied classification should represent the dominant characteristics and distinguish between those combinations which can be linked with a significant difference in amplification (soil factor, control periods). If not otherwise elaborated or specified, the classification scheme of Table 6-4 may provide the basis for application and further simplification (see Table 6-6). The user has to decide upon the combination and the effort involved to obtain more detailed information. In any case, the “easy use” option is given by the ability to consider a reduced number of basic types or utilizing “standard types”. Their amplification potential should be conservative and cover the effect of neglecting the deeper profile. The combination SC-GC follows a logical system shown in Table 6-4.

Finally, for sites where the range of shear wave velocity is $v_{s,H} < 800$ m/s site categories are characterized by the depth of the seismic bedrock formation H_{800} identified by shear wave velocity with a minimum of 800 m/s. The suggested ranges for standard site categorization for the second generation of the Eurocode (European Committee for Standardization, 2021) are shown in Table 6-6.

6.2.1.5 German site classification scheme DIN 4149:2005

The German code provision (DIN 4149:2005, 2005) determines another scheme for classifying soil based on a stiffness-related parameters in the form of shear wave velocity, and depth-related parameters considering the thickness of sedimentary soil layers above geological bedrock. The new proposed site classification scheme divides ground conditions into three possible soil classes A, B and C that can be combined with three geological subclasses R, T and S based on the average shear wave velocity up to 30 m depth combined with H_{st} at 30 m and H_d at 100 m depth (cf. Table 6-5).

Table 6-5: Ground classes according to DIN 4149:2005, 2005; R for areasominantlypredominantly characterised by rock; T for transition zones between R and S; S sedimentary basins; A for firm to medium firm soil; B for loose soil (gravel to coarse sands, marls); C fine grained soil (fine sands) (Schwarz, 2018).

Geological Class		Total Depth	Ground classes			
			A	B	C	D
			$v_{s,30} > 800$ m/s	350 m/s $< v_{s,30} < 800$ m/s	180 m/s $< v_{s,30} < 350$ m/s	Not defined
rock-like	R		A-R	B-R	C-R	
very shallow		$H < 5$ m [H_{vsh}]				
shallow (standard)		$H < 30$ m [H_{st}]				
transition	T	$H_{st} < H < H_d$		B-T	C-T	
deep	S	$H_d < H < H_{vd}$		B-S	C-S	
very deep		$H > [H_{vd}]$				

6.2.2 Code-related soil factors (second generation of Eurocode 8)

Within the scope of Eurocode, the earthquake motion at a given point on the surface is represented by an elastic ground acceleration response spectrum, henceforth called an “elastic response spectrum”. The shape of the elastic spectrum depends on the values of: T_B , the lower limit of the period of the constant spectral acceleration branch; T_C , the upper limit of the period of the constant spectral acceleration branch; T_D , the value defining the beginning of the constant displacement response range of the spectrum; and S , the soil factor for each ground type.

Table 6-6: Standard site categorization according to (European Committee for Standardization, 2021; Schwarz, 2018).

	Ground class	stiff	Medium stiff	Soft
Depth class	$H_{800}(m)$ $v_{s,H} \left(\frac{m}{s}\right)$	$400 \leq v_{s,H} < 800$	$250 \leq v_{s,H} < 400$	$150 \leq v_{s,H} < 250$
Very shallow	$H_{800} \leq 5$	A	A	E
Shallow	$5 < H_{800} \leq 30$	B	E	E
Intermediate	$30 < H_{800} \leq 100$	B	C	D
Deep	$H_{800} > 100 m$	B	F	F

For the standard site categorization in Table 6-6, values of the site amplification factors for F_α short-period (0.1-0.5 s) and F_β mid-period (0.4-2.0 s) ranges are calculated based on equations from Table 6-7. Equations for default values should be used at sites where detailed information regarding the depth of the seismic bedrock formation H_{800} and shear wave velocity $v_{s,H}$ is not known.

The corresponding values of the spectral parameter $S_{\alpha,RP}$ are calculated based on the product of the performance factor $\gamma_{LS,CC}$ and referenced spectral acceleration $S_{\alpha,ref}$ calculated for a return period of 475 years. While $S_{\beta,RP}$ is calculated based on the product of $\gamma_{LS,CC}$ and $S_{\beta,ref}$, where $S_{\beta,ref} = f_h S_{\alpha,ref}$ with values of f_h equal to 0.2, 0.3 and 0.4 for low, moderate and high seismicity areas, respectively, cf. (European Committee for Standardization, 2021). Figure 6-2 demonstrates the calculated soil amplification factors F_α and F_β for different seismicity levels according to the equations for soil factors given in Table 6-7.

Table 6-7: Site amplification factors F_α and F_β for the standard site categories.

Site category	F_α		F_β	
	c and $v_{s,H}$ available	Default value	H_{800} and $v_{s,H}$ available	Default value
A	1,0	1.0	1.0	1.0
B	$\left(\frac{v_{s,H}}{800}\right)^{-0.4r_\alpha}$	$1.3(1 - 0.1S_{\alpha,RP}/g)$	$\left(\frac{v_{s,H}}{800}\right)^{-0.7r_\beta}$	$1.6(1 - 0.2S_{\alpha,RP}/g)$
C		$1.6(1 - 0.2S_{\alpha,RP}/g)$		$2.3(1 - 0.3S_{\alpha,RP}/g)$

D		$1.8(1 - 0.3S_{\alpha,RP}/g)$		$3.2(1 - S_{\alpha,RP}/g)$
E	$\left(\frac{v_{s,H}}{800}\right)^{-0.4r_{\alpha}}\frac{H}{30}\left(4-\frac{H}{10}\right)$	$2.2(1 - 0.5S_{\alpha,RP}/g)$	$\left(\frac{v_{s,H}}{800}\right)^{-0.7r_{\beta}}\frac{H}{30}$	$3.2(1 - S_{\alpha,RP}/g)$
F	$0.90\left(\frac{v_{s,H}}{800}\right)^{-0.4r_{\alpha}}$	$1.7(1 - 0.3S_{\alpha,RP}/g)$	$1.25\left(\frac{v_{s,H}}{800}\right)^{-0.7r_{\beta}}$	$4.0(1 - S_{\alpha,RP}/g)$

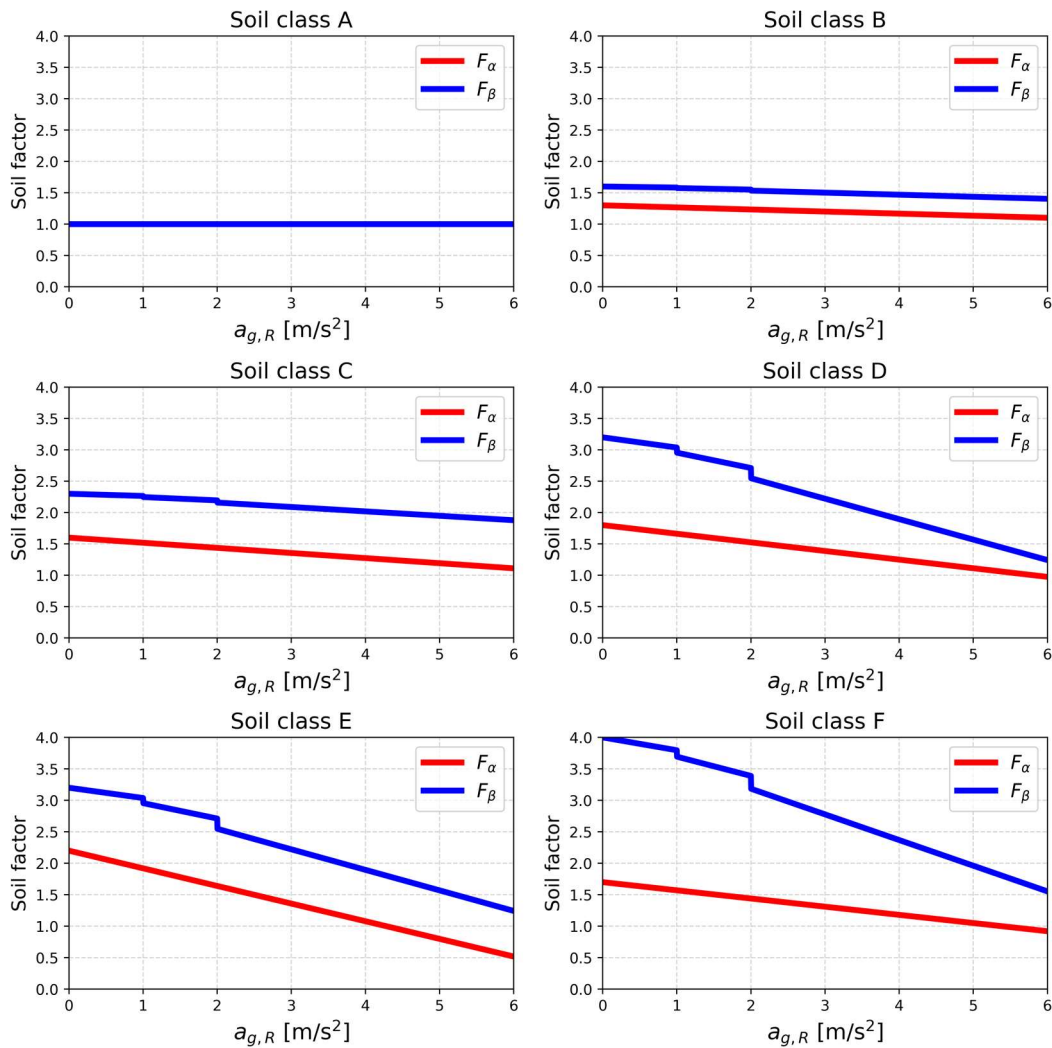


Figure 6-2: Soil factors according to Eurocode second generation (European Committee for Standardization, 2021) for all six soil classes A through F at different seismicity levels.

6.2.3 Site amplification using earthquake data

Borcherdt (1994) developed a procedure for estimating site amplification factors and the categories of subsoil classes as a function of shear wave velocity. The framework for the empirical equations is based on borehole-geotechnical data and strong motion records from the Loma Prieta, California, earthquake of 18 October 1989. The scheme for calculating site amplification factors follows three steps:

- **Step 1:** Determine input ground-motion spectral levels I_a and I_v for short and mid-period bands, respectively, from maps showing effective peak ground motion values.
- **Step 2:** Characterize local site conditions in terms of mean shear wave velocity (V_{s30}), classification of sub-soil conditions into ground classes. [Borcherdt \(1994\)](#) categorizes site soil into six different classes (see Table 6-8).
- **Step 3:** Infer site-dependent amplification factors for short-period (F_a) and mid-period (F_v) ranges specified with respect to referenced ground conditions.

Table 6-8: Subsoil classification based on shear wave velocity according to (Borcherdt, 1994)

Site Class	Site class letter	Class description	Minimum Vs30 (m/s)	Maximum Vs30 (m/s)	Average Vs30 (m/s)
SC-Ia	Ao	Hard rocks	1400	-	1620
SC-Ib	A	Firm to hard rocks	700	1400	1050
SC-II	B	Gravelly soils and soft to firm rocks	375	700	540
SC-III	C	Stiff clays and sandy soil	200	375	290
SC-IVa	D1	Non-special-study soft soils	100	200	150
SC-IVb	E	Special-study soft soils	-	-	-

Amplification factors in Table 6-9, which are also displayed in Figure 6-3 and Figure 6-4 for both short- and mid-period amplification factors, respectively, are predicted as a function of mean shear wave velocity for various input ground motion levels, with respect to reference ground class (SC-Ib). From shear wave velocity (V_{s30}), amplification factors are calculated for F_a short-period (0.1-0.5 s) and F_v mid-period (0.4-2.0 s) ranges using the procedure introduced by equations 7a and 7b derived in [Borcherdt \(1994\)](#):

$$F_a = \left(\frac{v_o}{v}\right)^{m_a} \quad (6-2)$$

$$F_v = \left(\frac{v_o}{v}\right)^{m_v} \quad (6-3)$$

$$m_a = \text{Log}[F_a(v_{SC-IV}, I)] / \text{Log}\left[\frac{v_o}{v_{SC-IV}}\right] \quad (6-4)$$

$$m_v = \text{Log}[F_v(v_{SC-IV}, I)] / \text{Log}\left[\frac{v_o}{v_{SC-IV}}\right] \quad (6-5)$$

Where:

v Shear wave velocity at 30 meters

v_o Mean shear wave velocity for the site class used as the referenced ground condition

v_{SC-IV} is mean shear wave velocity for the soft soil class (SC-IV)

$F_a(v_{SC-IV}, I)$ and $F_v(v_{SC-IV}, I)$ are short- and mid-period amplification factors for site class SC-IV specified with respect to referenced ground conditions.

Table 6-9: Short and mid-period amplification factors with respect to reference ground conditions SC-Ib (firm to hard rock).

Input ground motion (g)	m_a	Site class mean shear wave velocity (m/s)				
		SC-Ia	SC-Ib	SC-II	SC-III	SC-IV
		1620	1050	540	290	150
Short-period F_a Site Amplification with respect to class SC-Ib						
0.1	0.35	0.9	1.0	1.3	1.6	2.0
0.2	0.25	0.9	1.0	1.2	1.4	1.6
0.3	0.10	1.0	1.0	1.1	1.1	1.2
0.4	-0.05	1.0	1.0	1.0	0.9	0.9
Input ground motion (g)	m_v	Mid-period F_v Site Amplification with respect to class SC-Ib				
0.1	0.65	0.8	1.0	1.5	2.3	3.5
0.2	0.60	0.8	1.0	1.5	2.2	3.2
0.3	0.53	0.8	1.0	1.4	2.0	2.8
0.4	0.45	0.8	1.0	1.4	1.8	2.4

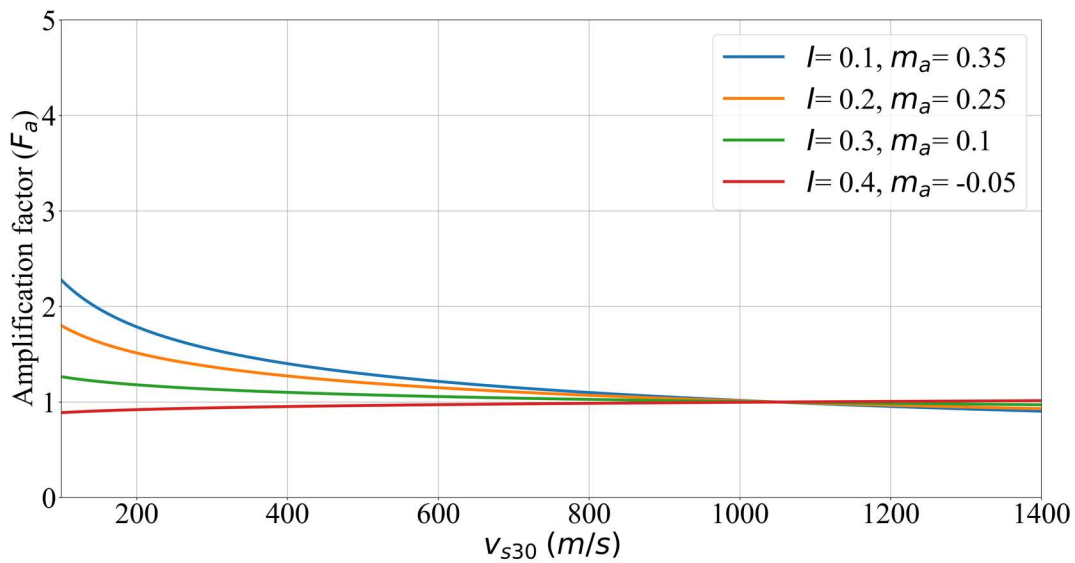


Figure 6-3. Short-period amplification factors with respect to ground condition SC-Ib from the study of Borchardt (1994) for input ground motion 0.1, 0.2, 0.3 and 0.4g.

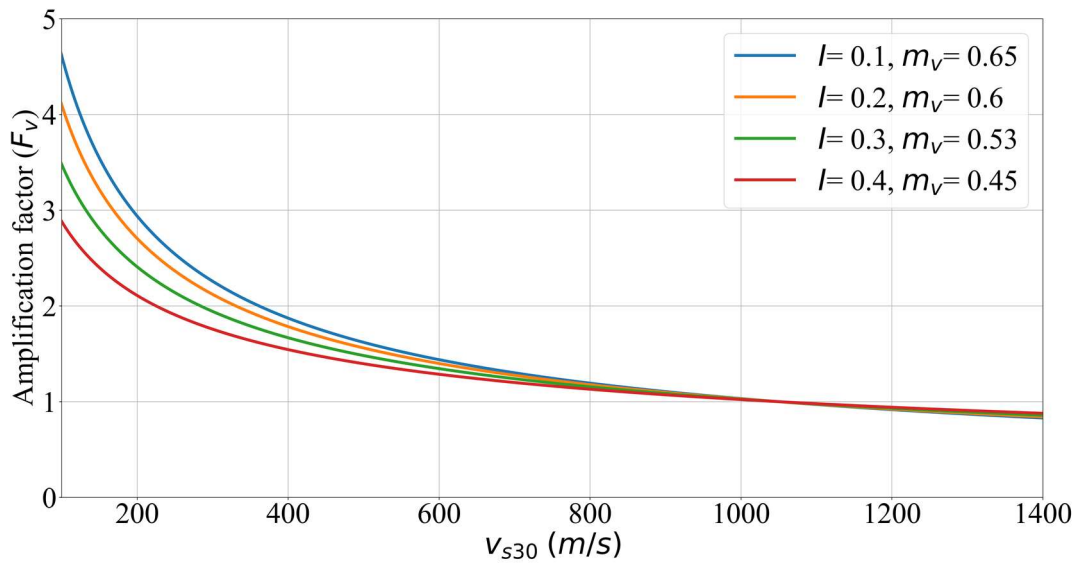


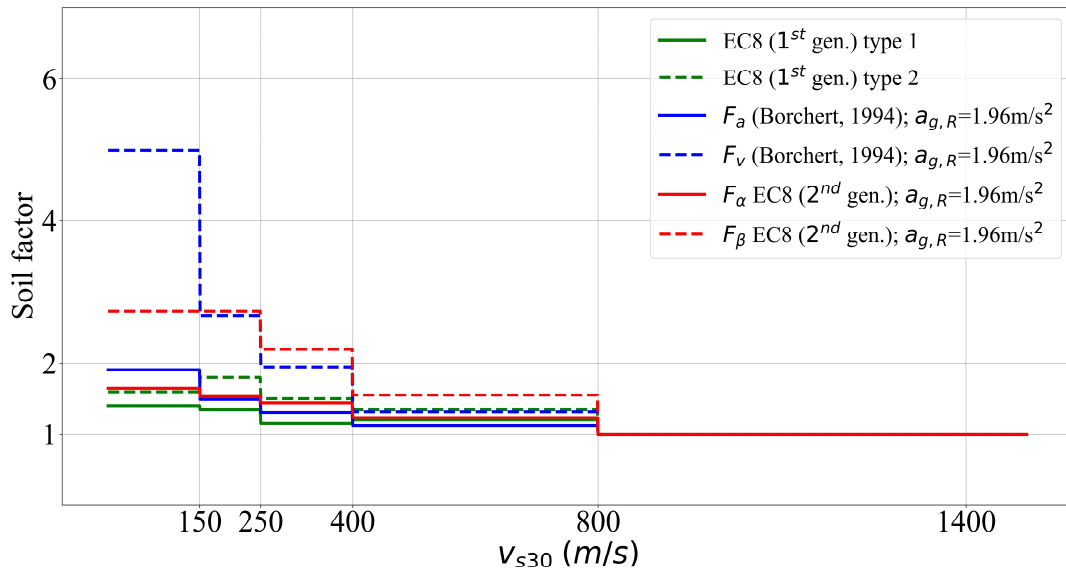
Figure 6-4. Mid-period amplification factors with respect to ground condition SC-Ib from the study of [Borcherdt \(1994\)](#) for input ground motion 0.1, 0.2, 0.3 and 0.4g.

Table 6-10: Site amplification factors for the second generation of Eurocode 8, using equations of [Borcherdt \(1994\)](#).

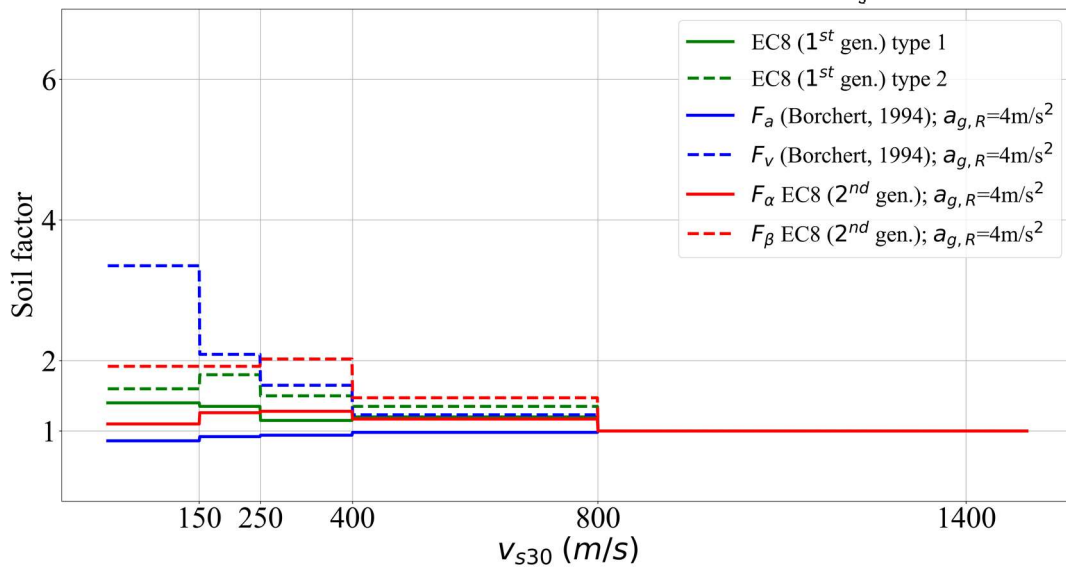
Input ground motion (g)	m_a	Site class mean shear wave velocity (m/s)						
		A	B	C	D	E		
		920	600	325	200	75		
Short period Fa Site Amplification with respect to site class A								
0.1	0.38	1.00	1.18	1.49	1.79	2.61		
0.2	0.26	1.00	1.12	1.31	1.49	1.91		
0.3	0.10	1.00	1.04	1.11	1.17	1.29		
0.4	-0.06	1.00	0.98	0.94	0.92	0.86		
Input ground motion (g)	m_v	Mid-period Site Fv Amplification with respect to site class A						
		0.1	0.69	1.00	1.34	2.05	2.87	5.65
		0.2	0.64	1.00	1.32	1.95	2.66	4.99
		0.3	0.57	1.00	1.27	1.81	2.38	4.15
		0.4	0.48	1.00	1.23	1.65	2.09	3.35

The procedure for calculating site amplification factors developed by [Borcherdt \(1994\)](#) can be adapted by other sub-soil classification schemes that use shear wave velocity as the main parameter for site categorization. First, the mean shear wave velocity for each subsoil class according to [European Committee for Standardization \(2021\)](#) is derived. Subsequently, soil amplification factors for short- and mid-periods are calculated for different seismicity levels using the scheme suggested by [Borcherdt \(1994\)](#).

Table 6-10 summarizes calculated amplification factors for short and mid-period ranges for the site classification scheme of the second generation of Eurocode ([European Committee for Standardization, 2021](#)) with reference site class A.



(a) Soil factors for moderate seismicity levels $a_{g,R} = 1.96 \frac{m}{s^2}$



(b) Soil factors for high seismicity levels $a_{g,R} = 4.0 \frac{m}{s^2}$.

Figure 6-5: Variation of soil factors at different ranges of Vs30 according to site amplifications using single EQ data (Borchert, 1994) and soil factors from second generation of Eurocode (European Committee for Standardization, 2021)

Finally, site amplification factors calculated using different techniques discussed in section 6.5 are represented in Figure 6-5, where default short- and mid-period amplification factors according to the second generation of the Eurocode (cf. Table 6-7) are plotted with calculated amplification factors using the method of Borchert (1994) (cf.

Table 6-10). Soil factors are calculated for moderate and high levels of seismicity ($a_{g,R} = 1.96 \frac{m}{s^2}$ and $a_{g,R} = 4.0 \frac{m}{s^2}$), respectively. These soil factors show that in general amplification factors tend to increase with decreasing average shear wave velocity and that the increase in amplification factors with increase of shear wave velocity is distinctly less for short-

period motion than for mid-period ranges. Also, for both short- and mid-period ranges, soil amplification factors tend to decrease with increasing input ground motion for every soil class. Both methods provide similar amplification factors for soil classes A, B, C and D, particularly for moderate seismicity levels $a_{g,R} = 1.96 \text{ m/s}^2$ however, significant differences between mid-period amplification factors for soil class E are observed. This is because the mean average shear wave velocity for soil class E according to subsoil classification of the second-generation Eurocode (European Committee for Standardization, 2021) is calculated as $V_{s30} = 75 \text{ m/s}$, which significantly increases the amplification factors in mid-period ranges.

Furthermore, for high levels of seismicity (Figure 6-5b), while both methods provide a similar trend in amplification factors for mid-period ranges F_{β} and F_v , at short period ranges, the amplification factors using single earthquake data are significantly smaller and tending toward reduction of the input ground motion, since the amplification factors derived from the Loma Prieta strong motion data (Borcherdt, 1994) are derived for low level input ground motion $a_{g,R} \cong 1 \text{ m/s}^2$, such that soil factors for high level of ground motions are derived based on extrapolation and theoretical modeling.

6.2.4 Soil Factors in ground motion prediction equations

Site amplification has been partly considered in ground-motion models for several decades. The initial site amplification models simply distinguish between rock and soil sites and incorporate the site amplification as a scaling parameter. The scaling of ground motion models using shear wave velocity (V_{s30}) generally consists of two parts, a nonlinear elastic term that is only a function of V_{s30} and a nonlinear term that accounts for nonlinear soil effects usually represented as a function of V_{s30} and input rock motion. The linear term represents site amplification for small intensities, at which the soil response is essentially linear elastic. The nonlinear term incorporates the effect of soil nonlinearity for larger intensities. Nonlinear effects represent the influence of soil nonlinearity, where the stiffness of the soil decreases and the damping increases as larger shear strains are induced in the soil. The general form of a ground motion model is:

$$\ln(S_a) = f_m + f_R + f_{site} \quad (6-6)$$

where S_a is the spectral acceleration at a given period, f_m is function scaling with magnitude, f_R represents the site-to-source distance scaling and the function f_{site} is considered as the “site amplification model” or “site response model”.

The model of Boore et al. (1997) was one of the first ground motion model to use shear wave velocity as a scaling factor to predict site amplification, but their model did not include soil nonlinearity:

$$\ln(AF) = f_{site} = a \times \ln\left(\frac{v_{s30}}{v_{ref}}\right) \quad (6-7)$$

Choi and Stewart (2005) extended the site amplification model to consider nonlinearity in the models:

$$\ln(AF) = f_{site} = a \times \ln\left(\frac{v_{S30}}{v_{ref}}\right) + b \times \ln\left(\frac{PGA_{rock}}{0.1}\right) \quad (6-8)$$

Walling et al. (2008) proposed a more complex site response model including the nonlinear effect:

$$\ln(AF) = \begin{cases} a \times \ln\left(\frac{V_{S30}}{V_{lin}}\right) + b \times \ln\left(PGA_{rock} + c \times \left(\frac{V_{S30}}{V_{lin}}\right)^n\right) & \text{for } V_{S30} < V_{lin} \\ a \times \ln\left(\frac{V_{S30}}{V_{lin}}\right) & \text{for } V_{S30} \geq V_{lin} \end{cases} \quad (6-9)$$

Table 6-11 summarizes a number of existing ground motion prediction equations along with the corresponding implemented site scaling models, either considering nonlinear soil effects or modelling amplification factors without consideration of nonlinear site effects.

Table 6-11: List of ground motion prediction equations with implemented site scaling models; GMPE coefficients are taken as written in original author documents

Ground motion model	Site scaling model
(Campbell & Bozorgnia, 2008)	$f_{site} = \begin{cases} c_{10} \ln\left(\frac{V_{S30}}{k_1}\right) + k_2 \left\{ \ln\left[A_{1100} + c \left(\frac{V_{S30}}{k_1}\right)^n\right] - \ln(A_{1100} + c) \right\} & \text{for } V_{S30} < k_1 \\ (c_{10} + k_2 n) \ln\left(\frac{V_{S30}}{k_1}\right) & \text{for } k_1 \leq V_{S30} < 1100 \\ (c_{10} + k_2 n) \ln\left(\frac{1100}{k_1}\right) & \text{for } V_{S30} \geq 1100 \end{cases}$
(Boore & Atkinson, 2008)	$F_S = F_{LIN} + F_{NL}$ $F_{LIN} = b_{lin} \ln(V_{S30}/V_{ref})$ $F_{NL} = \begin{cases} b_{nl} \ln(pga_{low}/0.1) & \text{for } pga_{4nl} \leq a_1 \\ b_{nl} \ln(pga_{low}/0.1) + c[\ln(pga_{4nl}/a_1)]^2 + d[\ln(pga_{4nl}/a_1)]^3 & \text{for } a_1 < pga_{4nl} \leq a_2 \\ b_{nl} \ln(pga_{low}/0.1) & \text{for } a_2 < pga_{4nl} \end{cases}$
(Akkar & Bommer, 2010)	$F_{site} = b_7 S_s + b_8 S_A$ <p>soft soil $S_s = 1, S_A = 0$ stiff soil $S_s = 1, S_A = 0$ Rock $S_s = 0, S_A = 0$</p>
(Montalva G., 2010)	$f_{site} = b_{lin} \ln(V_{S30}/V_{ref}) + bh800 \ln(h800/h_{ref})$ $F_{100} = a_{100} + b_{100} \ln(V_{S30}/V_{ref}) + c_{100} \ln(V_{shole}/V_{shole_{ref}})$ $F_{200} = a_{200} + b_{200} \ln(V_{S30}/V_{ref}) + c_{200} \ln(V_{shole}/V_{shole_{ref}})$
(Montalva & Rodriguez-Marek, 2010)	$\ln(\bar{y}) = F_m + F_d + F_{site}(S_{surface}) + [F_{100}(S_{100}) + F_{200}(S_{200})](1 - S_{surface})$ $F_{site} = b_{lin} \ln(V_{S30}/V_{ref})$ $F_{100} = a_{100} + b_{100} \ln(V_{S30}/V_{ref}) + c_{100} \ln(V_{s,hole}/3000)$ $F_{200} = a_{200} + b_{200} \ln(V_{S30}/V_{ref}) + c_{200} \ln(V_{s,hole}/3000)$
(Campbell & Bozorgnia, Campbell-bozorgnia NGA-West2 horizontal ground motion)	$f_{site} = f_{site,G} + S_f f_{site,J}$ $f_{site,J} = \begin{cases} (c_{12} + k_2 n) \left[\ln\left(\frac{V_{S30}}{k_1}\right) - \ln\left(\frac{200}{k_1}\right) \right] & \text{for } V_{S30} \leq 200 \\ (c_{13} + k_2 n) \ln\left(\frac{V_{S30}}{k_1}\right) & \text{for All } V_{S30} \end{cases}$

model for active tectonic domains, 2014)	$f_{site,G} = \begin{cases} c_{11} \ln\left(\frac{VS_{30}}{k_1}\right) + k_2 \left\{ \ln \left[A_{1100} + c \left(\frac{VS_{30}}{k_1} \right)^n \right] - \ln(A_{1100} + c) \right\} & \text{for } VS_{30} \leq k_1 \\ (c_{11} + k_2 n) \ln\left(\frac{VS_{30}}{k_1}\right) & \text{for } VS_{30} > k_1 \end{cases}$
(Bindi, Massa, Luzi, & Ameri, 2014)	$f_{site} = \gamma \log_{10}\left(\frac{VS_{30}}{VS_{REF}}\right)$
(Kale, Akkar, Ansari, & Hamzehloo, 2015)	$f_{site} = \begin{cases} sb_1 \ln\left(\frac{VS_{30}}{V_{REF}}\right) + sb_2 \ln\left[\frac{PGA_{REF} + c(VS_{30}/V_{ref})^n}{(PGA_{REF} + c)(VS_{30}/V_{ref})^n}\right] & \text{for } VS_{30} < V_{ref} \\ sb_1 \ln\left[\frac{\min(VS_{30}, VS_{CON})}{V_{REF}}\right] & \text{for } VS_{30} \geq V_{ref} \end{cases}$
(Abrahamson, Gregor, & Addo, 2016)	$f_{site} = \begin{cases} \theta_{12} \ln\left(\frac{V_s^*}{V_{lin}}\right) - b \ln\left[PGA_{1000} + c\left(\frac{V_s^*}{V_{lin}}\right)^n\right] & \text{for } VS_{30} < V_{lin} \\ \theta_{12} \ln\left(\frac{V_s^*}{V_{lin}}\right) + bn \ln\left(\frac{V_s^*}{V_{lin}}\right) & \text{for } VS_{30} \geq V_{lin} \end{cases}$ $V_s^* = \begin{cases} 1000 & \text{for } VS_{30} > 1000 \\ VS_{30} & \text{for } VS_{30} \leq 1000 \end{cases}$
(Sedaghati & Pezeshk, 2017)	$f_{site} = c_1 + c_2 \ln VS_{30}$
(Darzi, Zolfaghari, Cauzzi, & Donat, 2019)	$f_{site} = s_{II}II + s_{III}III$ $\begin{cases} II = III = 0 & \text{for } VS_{30} > 750 \\ II = 1, III = 0 & \text{for } 375 < VS_{30} < 750 \\ III = 1, II = 0 & \text{for } VS_{30} < 375 \end{cases}$
(Farajpour, Pezeshk, & Zare, 2019)	$f_{site} = \begin{cases} z_{14} \ln\left(\frac{VS_{30}}{k_1}\right) + k_2 \left\{ \ln \left[PGA_{Rock} + c \left(\frac{VS_{30}}{k_1} \right)^n \right] - \ln(PGA_{Rock} + c) \right\} & \text{for } VS_{30} \leq k_1 \\ (z_{14} + k_2 n) \ln\left(\frac{VS_{30}}{k_1}\right) & \text{or } VS_{30} > k_1 \end{cases}$
(Li, Zhai, Wen, & Xie, 2020)	$f_{site} = \begin{cases} s \ln\left(\frac{2V_2 - VS_{30}}{V_{ref}}\right) & \text{for } VS_{30} \leq V_2 \\ s \ln\left(\frac{VS_{30}}{V_{ref}}\right) & \text{for } V_2 < VS_{30} \leq V_1 \\ s \ln\left(\frac{V_1}{V_{ref}}\right) & \text{for } VS_{30} > V_1 \end{cases}$
(Phung, Loh, Chao, & Abrahamson, 2020)	$f_{site} = \begin{cases} a_{12} \ln\left(\frac{V_s^*}{V_{lin}}\right) - b \ln(PGA_{1000} + c) + b \ln\left[PGA_{1000} + c\left(\frac{V_s^*}{V_{lin}}\right)^n\right] & \text{for } VS_{30} < V_{lin} \\ a_{12} \ln\left(\frac{V_s^*}{V_{lin}}\right) + bn \ln\left(\frac{V_s^*}{V_{lin}}\right) & \text{for } VS_{30} \geq V_{lin} \end{cases}$
(Tusa, Horst, & Raffaele, 2020)	$f_{site} = e_i S_i$

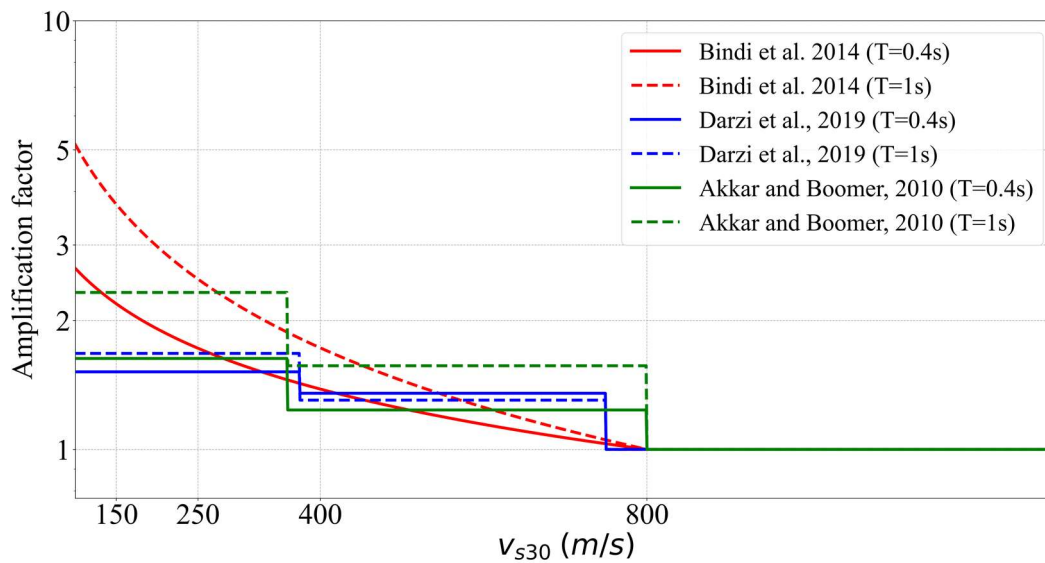


Figure 6-6: Variation in soil amplification factors for selected ground motion prediction equations [Akkar and Bommer \(2010\)](#); [Darzi et al. \(2019\)](#); [Bindi et al. \(2014\)](#) as a function of shear wave velocity at 30 m depth for periods $T=0.4s$ and $T=1s$.

Figure 6-6 shows the dependence of site amplification factors on shear wave velocity predicted by the ground motion models of [Akkar and Bommer \(2010\)](#); [Darzi et al. \(2019\)](#) compared with predicted site amplification by the ground motion model of [Bindi et al. \(2014\)](#) at spectral periods of $T=0.4s$ and $T=1s$. The ranges of shear wave velocity are set according to the [European Committee for Standardization \(2021\)](#) subsoil classes. The reason for selecting these two periods is that they correspond to the soil factors derived for short- and mid-period ranges using code-related soil factors (cf. section 6.5.3). Also, these periods are the most relevant parameters with respect to the scheme, which defines the constant acceleration and the constant velocity regions of the demand spectrum. The advantage of employing ground motion prediction equations for calculation of site amplification factors is that only one parameter (shear wave velocity V_{s30}) is required for the calculation of soil factors. On the other hand, their calculation depends on the coefficients assigned by the regression analysis according to the dataset of each GMPE at each period, while code-dependent soil factors are assigned based on analysis for short- and mid-period ranges, therefore providing better quality with less uncertainty.

The effects of site amplification on shake-maps calculated using estimated peak ground accelerations predicted from ground motion models is demonstrated in Figure 6-7. The ground motion model of [Bindi et al. \(2014\)](#) is utilized to compute a shakemap of estimated peak ground motion values for the M6.4 Petrinja Croatia Dec. 29th 2020 earthquake. In Figure 6-7(a) the shake-map is calculated without consideration of site amplification, which results in a radial attenuation of ground motion waves. However, when site amplifications are considered (see figure Figure 6-7 (b)), changes in predicted PGA values at different site classes are observed, and the final shakemap is refined based on specific site soil conditions according to values of shear wave velocity. Especially at areas close to the epicenter, where the ground motion attenuation is faster (in absolute terms).

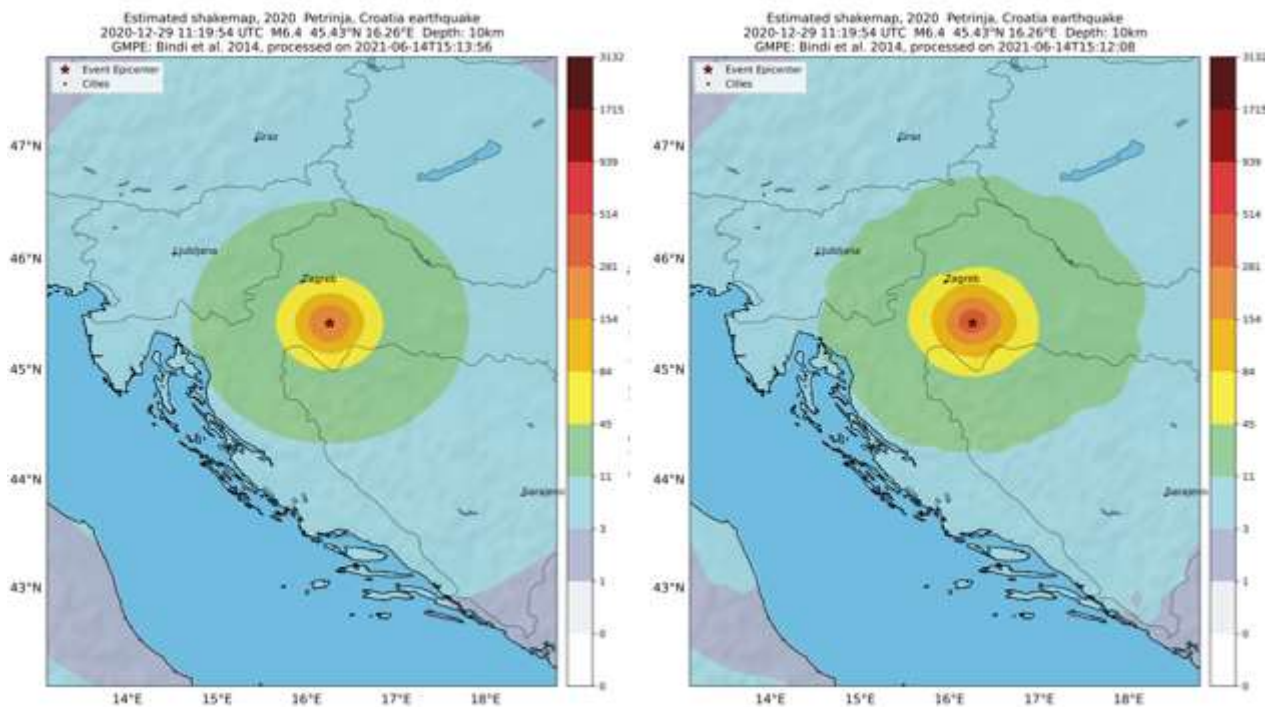


Figure 6-7: Shake-map computed for the 2020 Croatia earthquake using the ground motion prediction equation of [Bindi et al. \(2014\)](#): a) without consideration of soil factors, b) with consideration of soil factors.

6.2.5 Site response analysis (SRA)

Besides calculation of soil factors using available information regarding the subsoil conditions, e.g. shear wave velocity up to 30 m depth, ..., it is also possible to undertake a site response analysis. If the soil profile at a site is available, which includes information on deep geology, (cf. Table 6-1 level of data availability #3 3), a site response analysis can be performed for a better prediction of site amplification factors. In most cases, a 1D site response analysis is performed, using frequency-domain equivalent-linear ([Schnabel et al., 1972](#)) or time-domain nonlinear analysis ([Park and Hashash, 2004](#)). A site response analysis requires information on dynamic soil properties, which include the shear wave velocity and the modulus reduction and damping curves. The German seismic code provision DIN 4149:2005 ([DIN 4149:2005, 2005](#)) uses the soil profiles and site response analysis for the prediction of spectral values.

6.2.6 Instrumental site classification

A reliable site assessment can only be performed if sufficient information on the local subsoil conditions is available, e. g. subsoils and deep geology data verified with measurements from seismic stations (cf. Table 6-1 level of data availability # 4). For this reason, hybrid site categorization methods have been developed that consider the predominant site frequency f_0 as an additional differentiating factor. Instrumental site response studies can be used to decide on the most probable site category or ground type.

The site classification method proposed hereafter is based on the spectral H/V-ratio of microtremor data recorded at the ground surface. It is hypothesized that the H/V-ratio represents the quasi-transfer function of the underlying soil profile. Therefore, a rapid site classification can be carried out by comparing the shape of the site-specific H/V-ratio either to the transfer function of a complying theoretical model profile or by employing the predominant peak frequency f_0 of the H/V- as well as the total thickness of the sedimentary layers over geological bedrock as decision criteria (Table 6-12). Spectral H/V-ratios are determined from records of weak ground motion (ambient noise) data. The H/V technique may typically be used at locations with a horizontally layered soil profile.

Table 6-12: Site categorization based on $v_{s,H}$ and f_0

Combination of f_0 (Hz) and $v_{s,H}$ (m/s)	Site category
$f_0 > 12$ and $v_{s,H} \geq 250$	A
$f_0 < 12$ and $800 > v_{s,H} \geq 400$	B
$v_{s,H} / 250 < f_0 < v_{s,H} / 120$ and $400 > v_{s,H} \geq 250$	C
$v_{s,H} / 250 < f_0 < v_{s,H} / 120$ and $250 > v_{s,H} > 150$	D
$v_{s,H} / 120 < f_0 < 12$ and $400 > v_{s,H} > 150$ or $f_0 > 12$ and $250 > v_{s,H} \geq 150$	E
$f_0 < v_{s,H} / 250$ and $400 > v_{s,H} > 150$	F

Typical H/V-ratios and ranges of site frequencies can be taken from Figure 6-8.

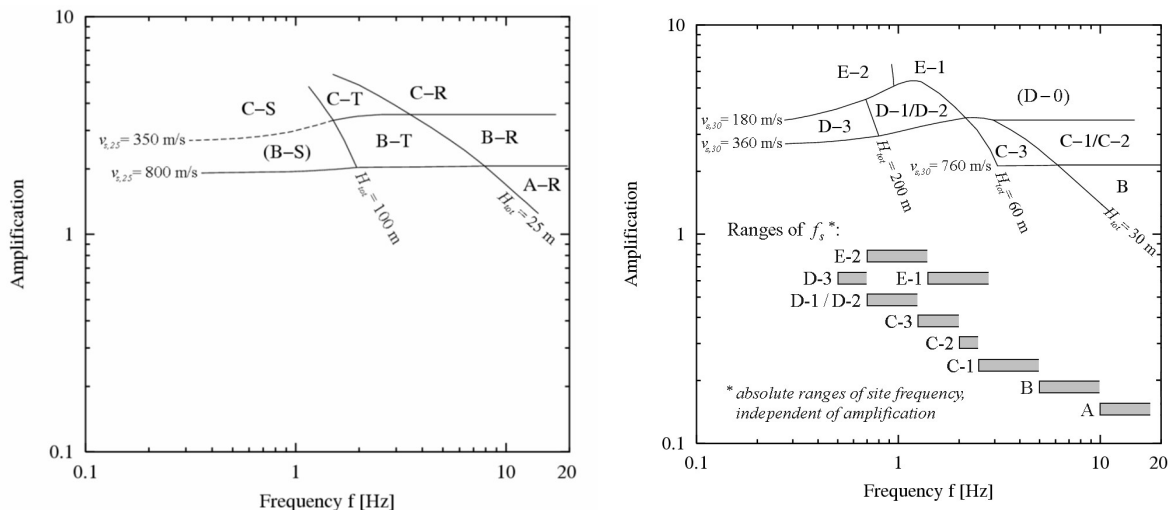


Figure 6-8: Method of an experimental seismic site assessment: classification scheme for relevant site categories. Qualitative ranges of possible peak frequencies of one-dimensional transfer functions for site classification schemes: (a) site-specific subsoil classes according to DIN 4149:2005 (2005); (b) refined NEHRP site classes by Rodriguez-Marek and Bray (1997); graphs are taken from Land and Schwarz (2006).

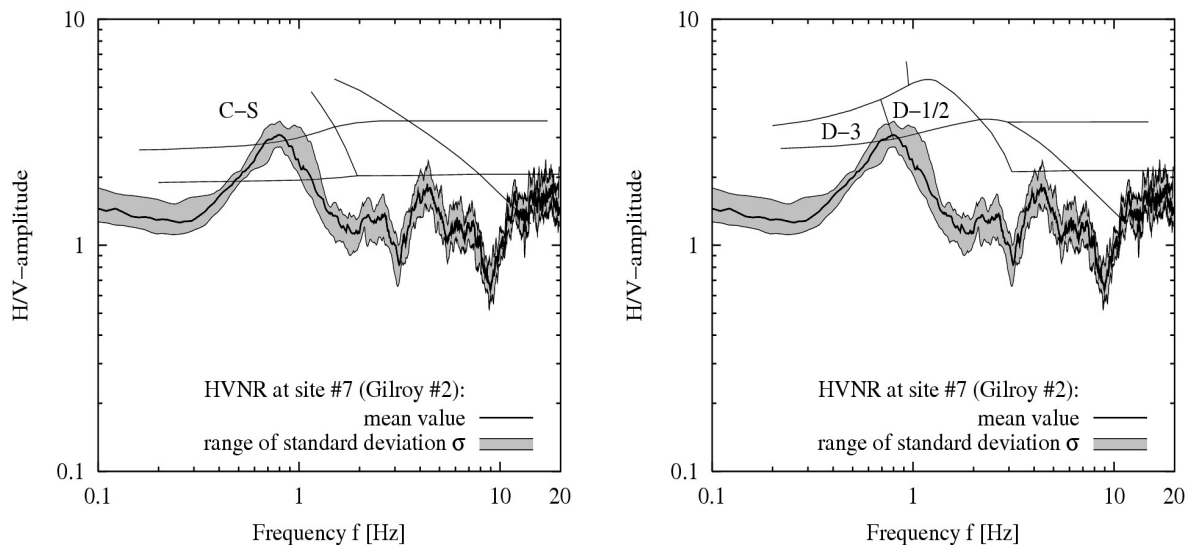


Figure 6-9: Spectral H/V-ratios of microtremors overlain with the classification scheme based on (a) DIN 4149:2005 (2005) site classes; “Central European scheme” referring to DIN 4149:2005 (2005); and (b) refined NEHRP site classes by Rodriguez-Marek and Bray (1997); graphs are taken from Land and Schwarz (2006); “U.S. classification scheme” referring to Rodriguez-Marek et al. (2001).

The average shear wave velocity is in the range of $V_{s30} = 280$ m/s, indicating NEHRP site class D. Wave velocity depth profiles are derived from USGS-Open File Report 92-287 (Gibbs et al., 1992). The total depth H_{tot} is reaching down to a depth of 165 m (Stewart et al., 2001) or 180 m (Joyner & Boore, 1981). The predominant peak frequency yields a classification of the site as C-S for DIN4149:2005 (Figure 6-9a) or D-1/2 and D-3 for NEHRP classes (Figure 6-9b).

6.2.7 Refinement of shaking effects via intensity increments for local site conditions

Whereas the previously described site classification schemes are linked to method 1, the current section discusses the concept of intensity increments for local site conditions explicitly applied in method 2 (see Figure 6-1).

If information of the soil profile of the individual seismic stations is available, the influence of the subsoil can be taken into account. If the evaluation of the data set is very extensive, it is possible to generalise the influence of the geological conditions on the observed intensity and the measured soil parameters or to determine mean soil parameters and their scatter.

Due to the different earthquake characteristics in various regions, sufficient data recordings are required for including region-specific conditions. The transfer of data from highly active seismic regions to medium to low seismic activity regions should always be viewed with caution and usually leads to a false estimation of ground motion parameters. Therefore, it should always be accompanied by a region-specific investigation, see also Kaka and Atkinson (2004).

Ahorner et al. (1986) investigated the possibility of determining intensity increments ΔI from observations of historical earthquakes in the Lower Rhine Bay in order to use them for the

adjustment of probabilistic hazard maps. The basic idea is that regionally observed intensities can provide a more differentiated picture of the hazard. For this purpose, [Ahorner et al. \(1986\)](#) used macroseismic observations of 26 Central European earthquakes in the period from 1692 to 1983. Figure 6-10 presents the results for the example region of Lower Rhine Bay, the number of underlying macroseismic observations per grid cell is displayed Figure 6-10a. The earthquakes used for the evaluation are included in the data set of the earthquake catalogue EKDAG – Part C ([Schwarz et al. 2019a](#)). The investigated earthquakes cover a range of local magnitudes $M_L = 4.2$ to 6.1 and a range of epicentral intensities $I_0 = VI-VII$ (6.5) to VIII (8.0).

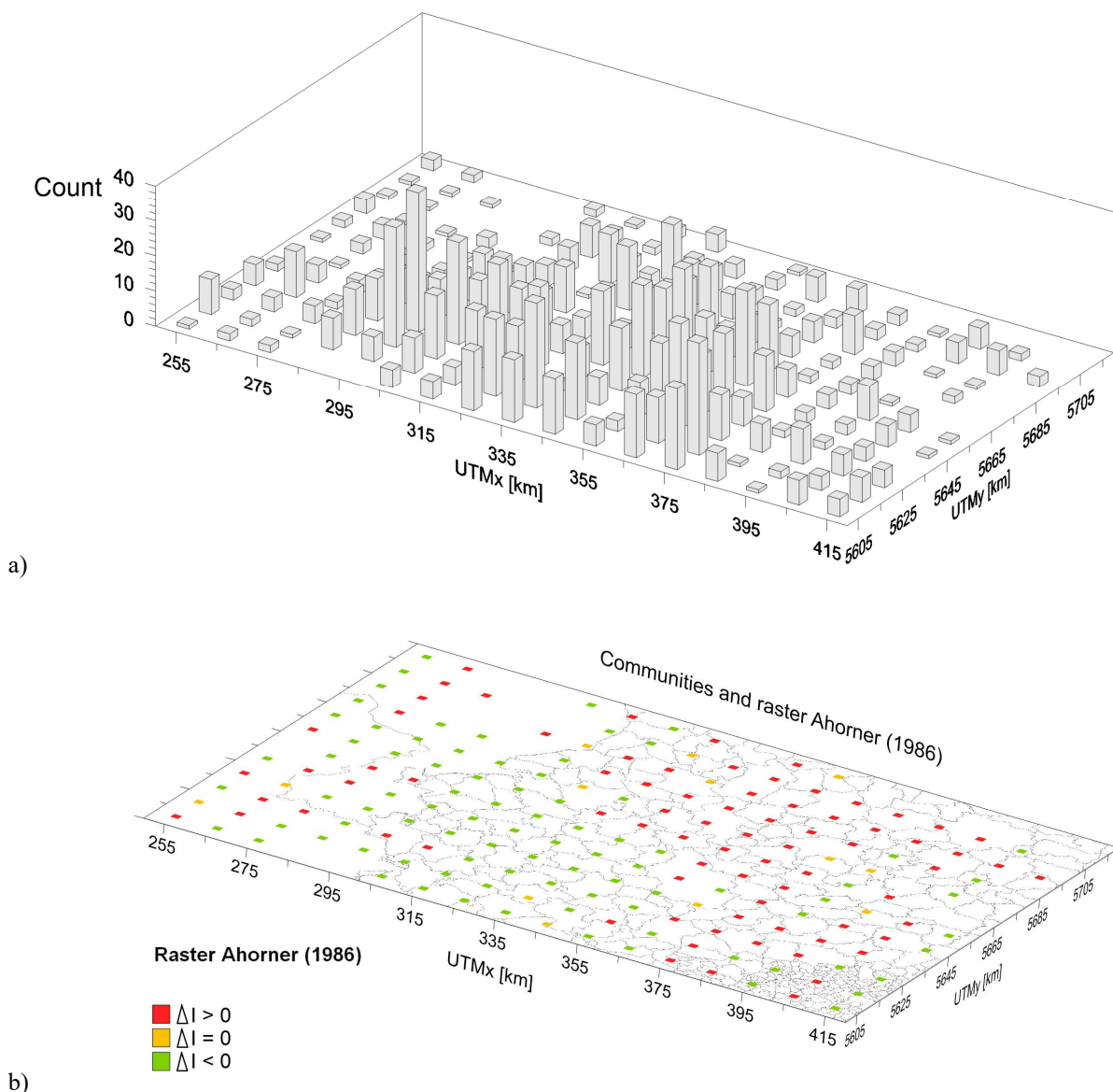


Figure 6-10. Number of underlying data sets (a) and mean value of the intensity increments (b, red – intensity increase, green intensity decrease, yellow – as predicted by intensity attenuation relationship) prepared via a raster according to information from Ahorner (pers. com.) and combined with districts of the respective study area (based on the preliminary work by [Ahorner and Budny \(1985\)](#))

For each earthquake, the attenuation of macroseismic intensity with hypocentral distance was investigated. The determination of the intensity attenuation is based on individual observations of the intensity and the corresponding focal distances (Figure 6-11). Figure 6-11 shows a sample for a selected grid element in a certain distance from the epicentre. The attenuation curves for the mean values of the intensity and their standard deviations at the respective distances is calculated. The obtained mean attenuation curves are more informative for engineering seismology than the attenuation curves derived from isoseismic gradients.

The mean intensity attenuation correlations derived by [Ahorner and Budny \(1985\)](#) mainly for the area of the Lower Rhine Bay do not show a continuous decrease in intensity, but fine structures that recur in a similar manner for many earthquakes (example in Figure 6-10b). An important result of this study is the specification of the intensity attenuation relationship for the Lower Rhine Basin.

[Ahorner et al. \(1986\)](#) state that the layer structure and the vertical velocity structure of the earth's crust are reflected in the observations, causing a concentration or weakening of the seismic shaking at certain focal distances. It has been observed that the decrease in intensity is significantly lower in the distance range between 30 km and 90 km and can be predicted quite good with the available intensity attenuation relationships. In the range smaller than 30 km, the radiation pattern due to the source mechanism plays a major role. At a distance starting around 90 km, depending on the magnitude of the earthquake, the influence of the subsoil conditions begins to have a greater impact and leads to a smaller decrease compared to the prediction of the intensity attenuation relationships.

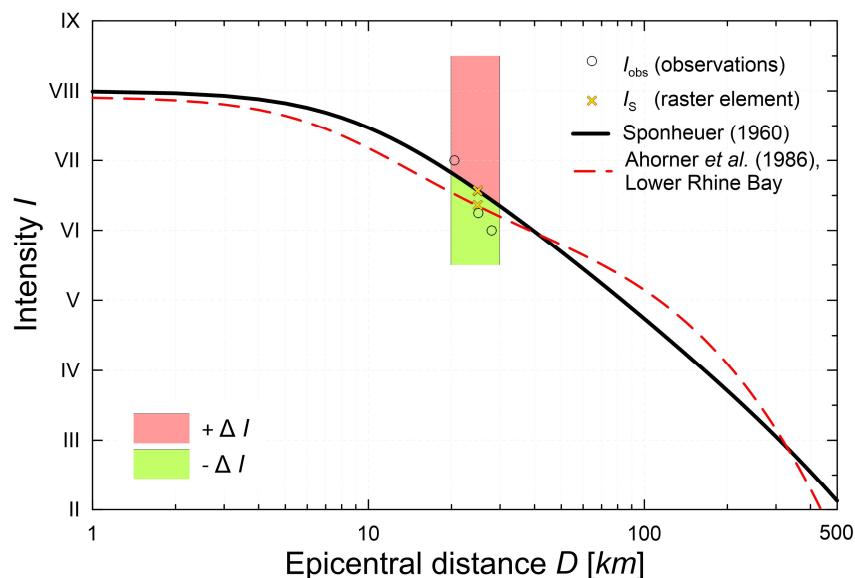


Figure 6-11. Example for the evaluation of a grid element with macroseismic observations for the 1911 Ebingen earthquake of epicentral intensity $I_0 = \text{VIII}$ (8.0) and focal depth $h_0 = 10$ km for the relations according to [Ahorner et al. \(1986\)](#) and [Sponheuer \(1960\)](#).

Table 6-13 summarises the relative intensity increments (intensity increments) ΔI determined by [Ahorner et al. \(1986\)](#) as a function of the geological subsurface. Depending on the type of rock and the thickness of the unconsolidated cover layers, the geological subsoil is divided into seven classes according to the increase in recognizable intensification (G_i , $i = 1$ to 7).

Table 6-13: Relative Intensity increment ΔI ([Ahorner et al., 1986](#); [Bossu et al., 2000](#))

(Ahorner et al., 1986)						German code	(Bossu et al., 2000)		
Subsoil class G_i		N	Results of the analysis				DIN-classes	Age	ΔI
Type i	Description		ΔI_{cal}	σ	ΔI^*	ΔI		in Mio. years [Ma]	(Probability of occurrence)
1	crystalline rock	-	-	-	-	+ 0.0	-	rock	
2	sedimentary hard rock, hard	167	- 0.48	± 0.74	+ 0.00	+ 0.0	A-R	> 1 Ma	0
3	sedimentary hard rock, soft	43	- 0.58	± 0.70	- 0.10	- 0.1	A-R		
4	loose rock 200 m	197	- 0.40	± 0.59	+ 0.08	+ 0.1	C-S	sediments	< 0.05
5	loose rock 50 bis 200 m	37	- 0.30	± 0.54	+ 0.18	+ 0.2	C-S, B-S C-T, B-T	0.75 bis 0.01 Ma	0.6 \pm 0.2 (52%)
6	loose rock 10 bis 50 m	37	+ 0.11	± 0.36	+ 0.59	+ 0.6	C-R, B-R C-T, B-T	0 Ma	0.6 \pm 0.2 (83%)
7	extremely soft loose rock	-	-	-	-	+ 1.0	[not allowed]		

Notes:

- N number of observations
- ΔI_{cal} for results with epicentral distances $D_{epi} < 30$ km
- ΔI^* (G2) relative value in relation to reference subsoil G2 (sedimentary hard rock, hard)

The geological age of the corresponding geologies in million years (Ma) can be correlated with these. The youngest strata (including Holocene sediments, slope debris, backfills) represent the most vulnerable subsoil in terms of amplification. [Medvedev \(1965\)](#), [DIN 4149-1 \(1981\)](#) and [Ahorner et al. \(1986\)](#) also come to this conclusion, as do [Bossu et al. \(2000\)](#) (see Table 6-13). The younger the formation, the higher the probability of an intensity amplification. H/V measurements can be used to assess this.

Depending on the information known about a region of application, the methods described in Figure 6-1 can be applied. In Figure 6-12 various scenarios are shown for an example region. The radial scenario shown in Figure 6-1a shows the application of an intensity attenuation relationship. The elliptical scenario in Figure 6-1b takes into account the orientation of the fault line. Figure 6-1c displays the scenario which takes into account intensity increments ΔI for the epicentral region. The determination of intensity increments for especially low to medium seismic regions give the opportunity not only to use parameters like the $v_{s,30}$ to correct the probable observable intensity, but also apply knowledge from previous events as well as the outcome or site response analysis to reduce the scatter between prediction and observation. A requirement is the application of the EMS-98 as scale for the generated shake-maps to eliminate the influence of the different vulnerabilities of the existing building stock (cf. for general approach in Section 3.2.2).

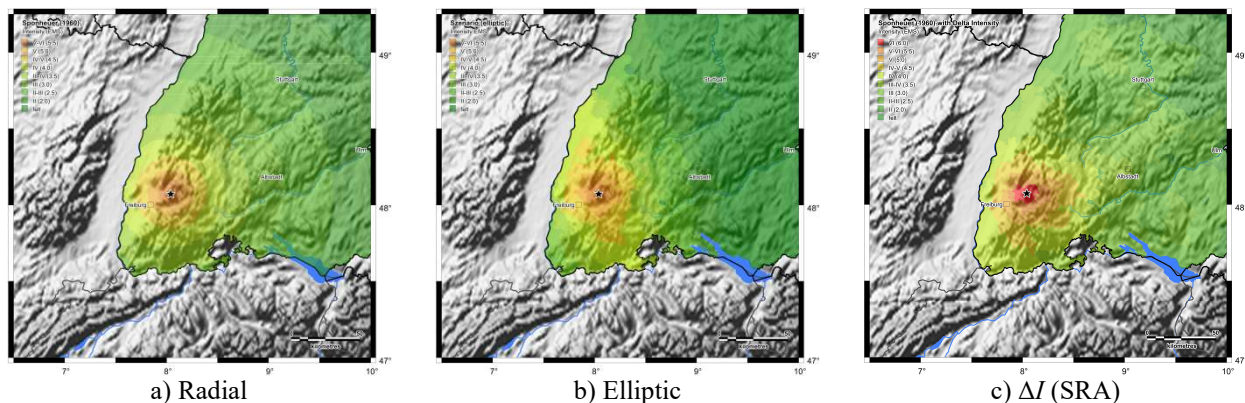


Figure 6-12. Scenarios (Intensity EMS-98) of the Dec. 5, 2004 Waldkirch earthquake (epicentre ★) based on the attenuation model from [Sponheuer \(1960\)](#) for the epicentral intensity $I_0 = VI (6.0)$

6.3 Harmonized Vs30 maps at European level

Felt earthquakes nucleate at hard-rock settings, where sudden fault slip leads to radiation of seismic waves. When these waves reach the Earth's surface, typically their amplitude is increased. Amplification occurs due to the slowing of the seismic waves over soft material near the Earth's surface. Additional amplification may occur due to waves resonating between the Earth's surface and large impedance contrasts close to the surface. The amplification factor AF is frequency-dependent and varies largely per site.

In the absence of direct measurement of the AF at most places, empirical relations are used that predict site amplification. A common predictor for site amplification is Vs30: the harmonically averaged S-wave velocity over the top 30 metres. Another proxy for amplification is a (seismic noise) recording of the horizontal-to-vertical spectral ratio.

In the framework of the new European Seismic Risk Model (ESRM20) (European SERA project: <http://www.sera-eu.org/>), two site characterization models at the European scale were built based on the Vs30 proxy: one using a digital elevation model (DEM) and the other using geological data ([Crowley et al., 2019](#)).

The limitations of DEM-based models described in [Roullé et al. \(2010\)](#) and [Lemoine et al. \(2012\)](#) lead us to prefer the geology-based model. This soil model is based on the correlation between Vs30 and geology, depending on both the lithology and information about its age. This relation was previously developed by [Vilanova et al. \(2018\)](#) for the Portugal region.

For Europe, three complementary geological maps were used: 1) the pan-European geological map of superficial formations at 1:1,000,000 from OneGeologyEurope, available from EGD services (<http://www.europe-geology.eu/>), 2) the pan-European geological map at 1:1,500,000 from the Promine project (<http://promine.gtk.fi/>; [Cassard et al., 2015](#)), and 3) the bedrock geological map of Iceland at 1:600,000, available from the Icelandic Institute of Natural History ([Johannesson, 2014](#)). The resulting geology-based site characterization Vs30 model consisted of three soil classes (A, B, and C), following the EC8 classification.

The following figures provide Vs30 maps for all TB areas, based on the following formats and models:

1. Geology-based model: based on [Vilanova et al. \(2018\)](#); in vector format, where each polygon contains the attributes described in Table 6-14.
2. DEM-based model: based on [Wald and Allen \(2007\)](#); in raster format, where each value corresponds to the Vs30 ranges described in Table 6-15.

Table 6-14. Data fields describing the Vs30 model based on geology.

Shapefile field name	Description
Class_Vill	Soil class following the geology-based model proposed by Vilanova et al., 2018
VS30	Log-average Vs30 value
VS30-sigma	Lower limit of the 68% confidence interval for the Vs30 distribution
VS30+sigma	Upper limit of the 68% confidence interval for the Vs30 distribution

Table 6-15. Raster codes expressed in Vs30 ranges, for the model based on DEM.

Raster code	Vs30 ranges [m/s]
1	< 180
2	180-240
3	240-300
4	300-360
5	360-490
6	490-620
7	620-760
8	> 760
255	No Value

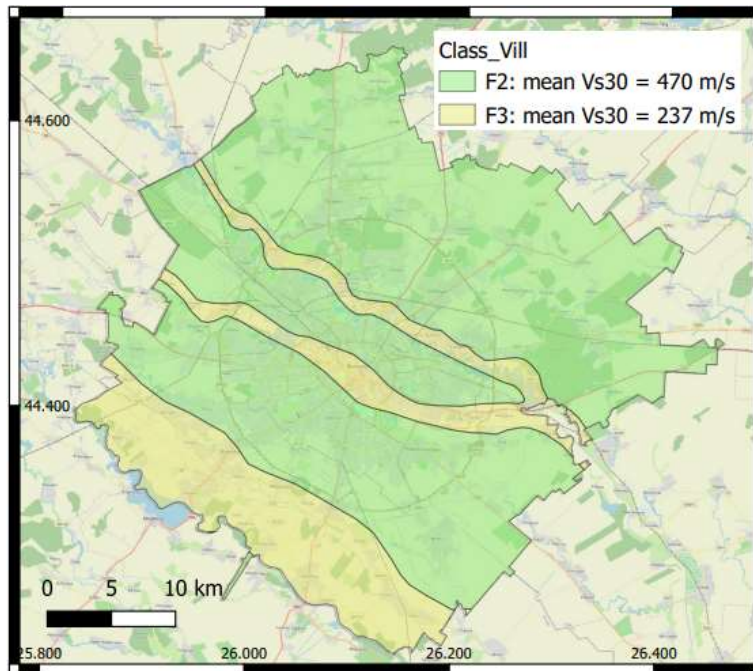


Figure 6-13: Geology-based Vs30 model for TB1.

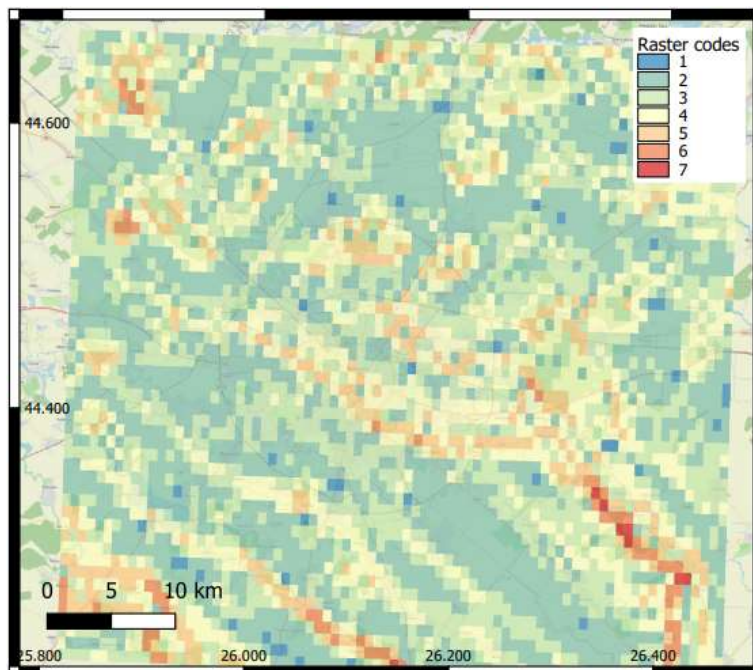


Figure 6-14: DEM-based Vs30 model for TB1.

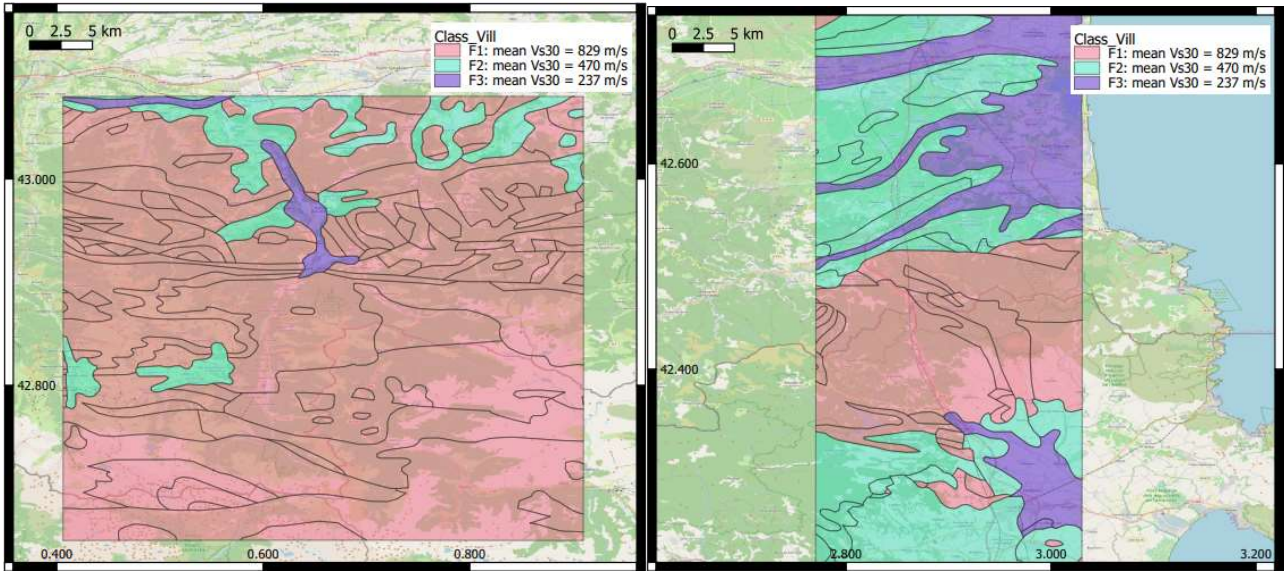


Figure 6-15: Geology-based Vs30 model for TB2 (left: Luchon area; right: Perpignan-Figueras area).

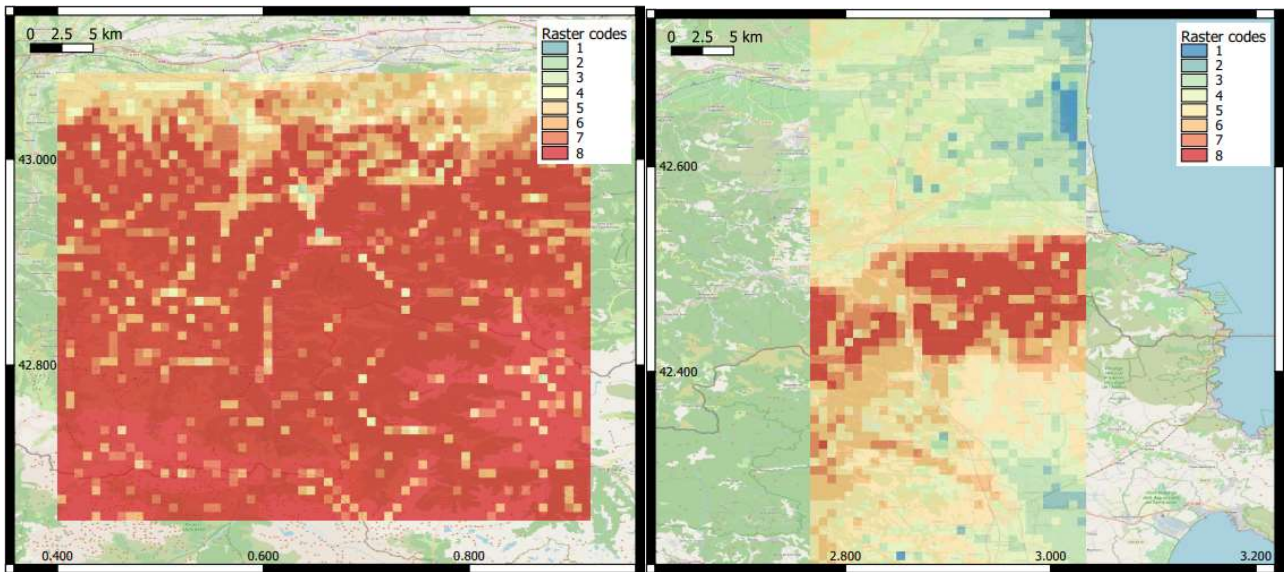


Figure 6-16: DEM-based Vs30 model for TB2 (left: Luchon area; right: Perpignan-Figueras area).

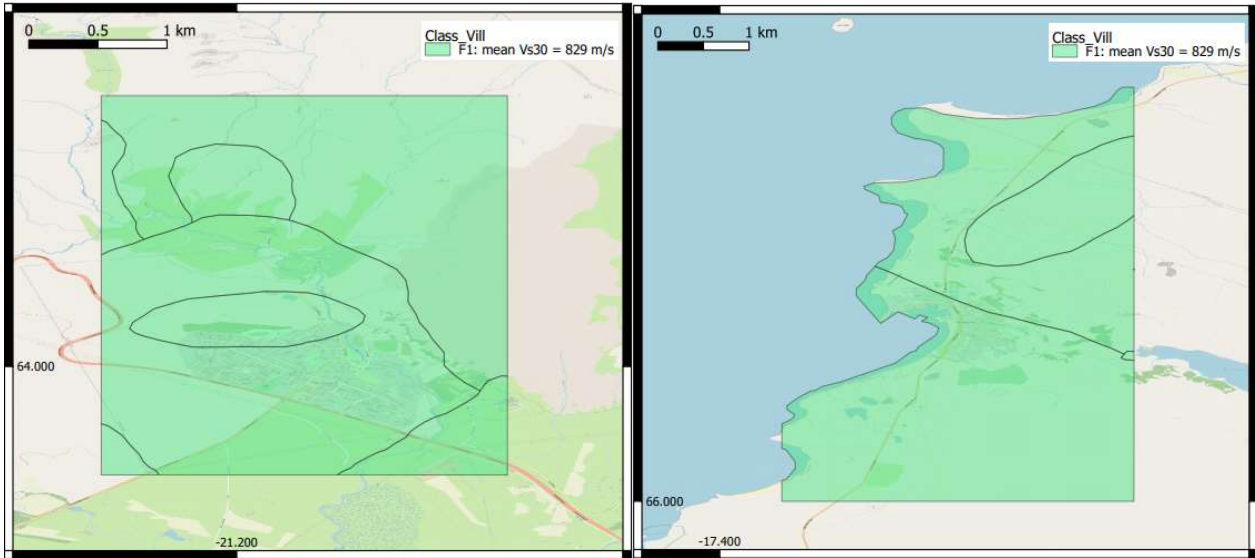


Figure 6-17: Geology-based Vs30 model for TB3 (left: town of Hveragerði; right: town of Húsavík).

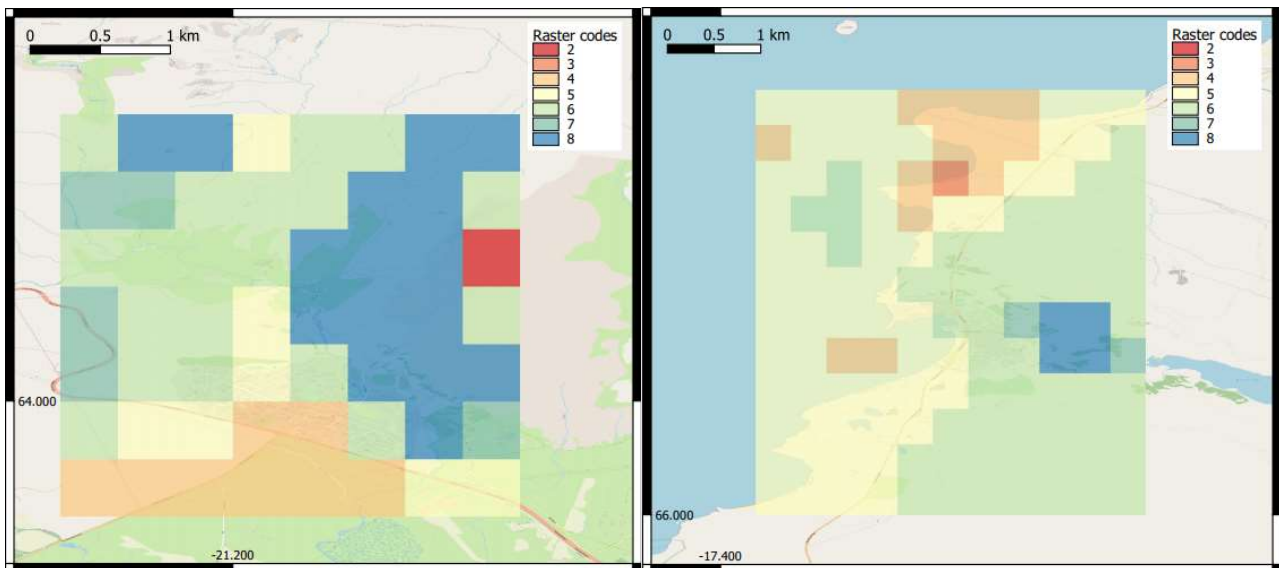


Figure 6-18: DEM-based Vs30 model for TB3 (left: town of Hveragerði; right: town of Húsavík).

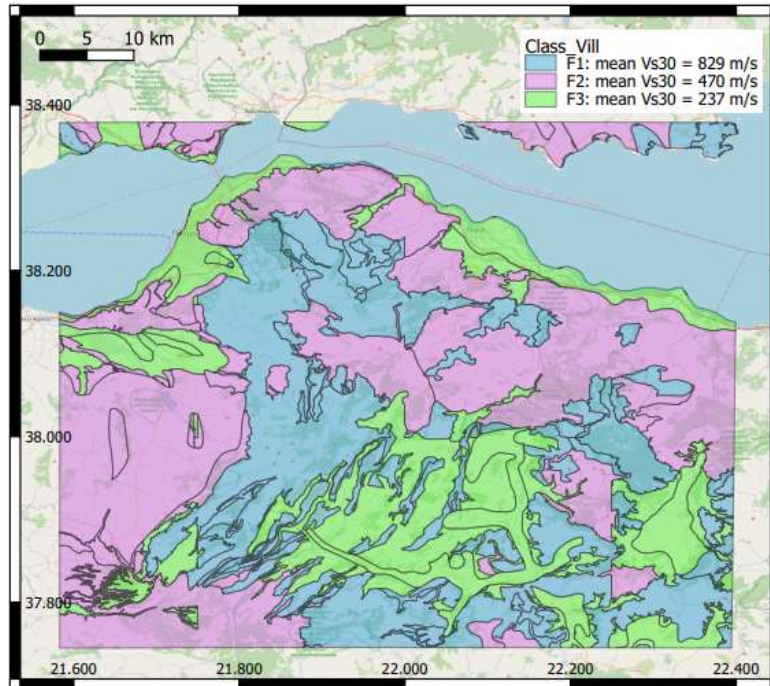


Figure 6-19: Geology-based Vs30 model for TB4.

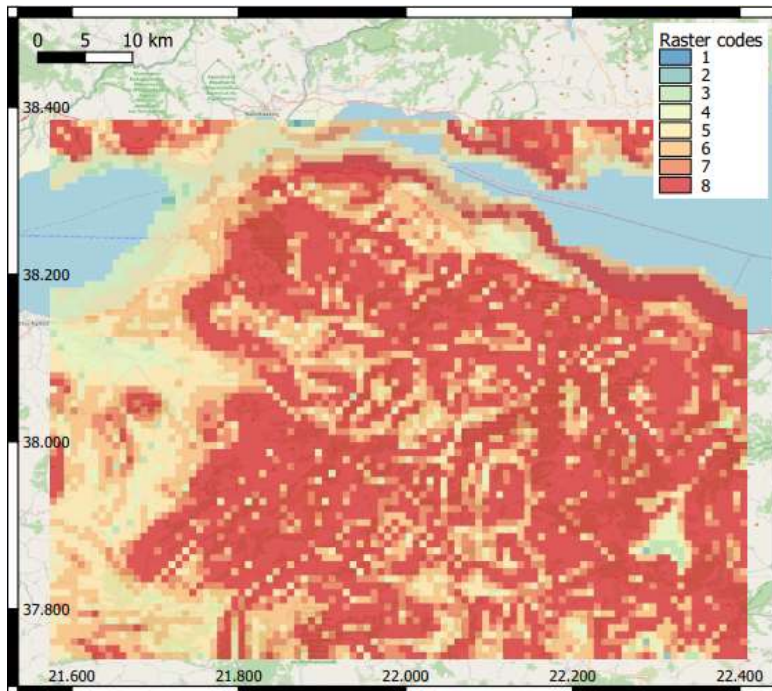


Figure 6-20: DEM-based Vs30 model for TB4.

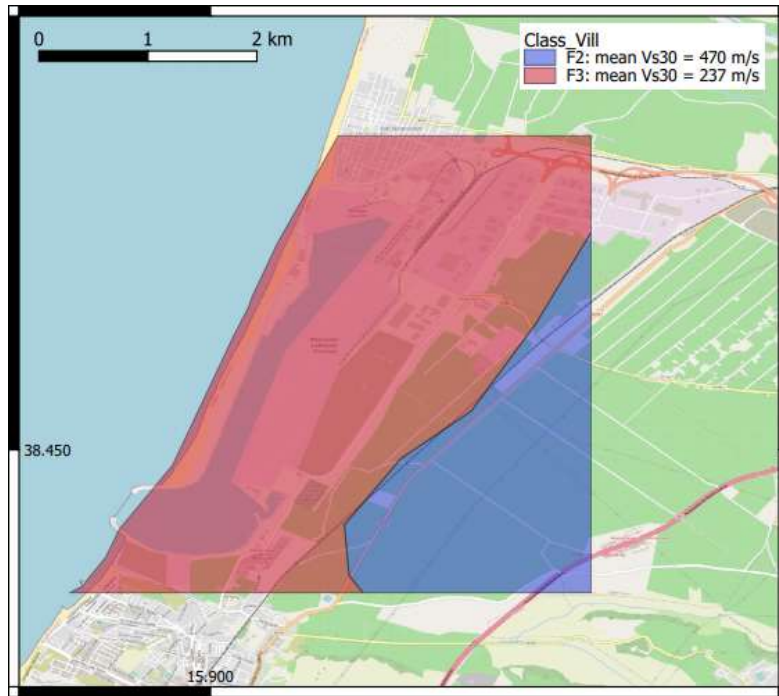


Figure 6-21: Geology-based Vs30 model for TB5.

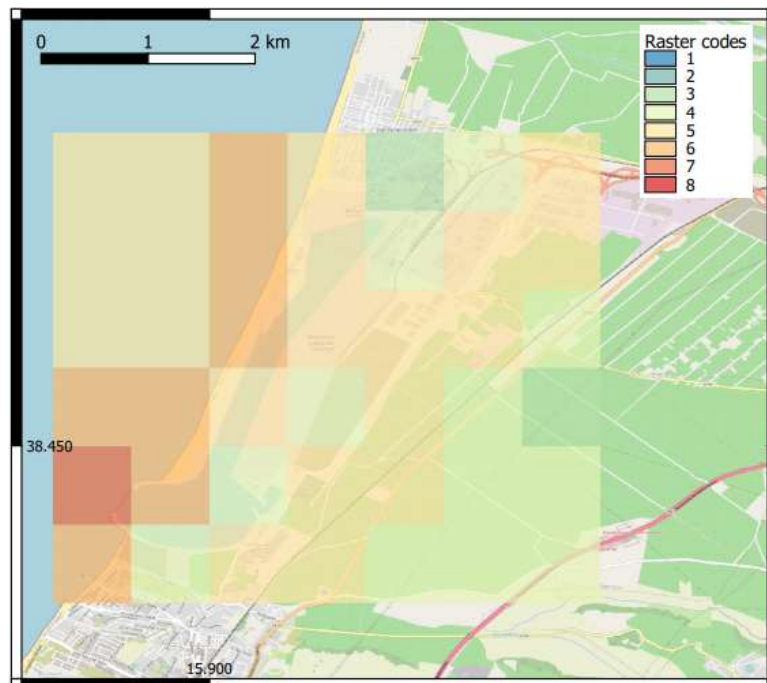


Figure 6-22: DEM-based Vs30 model for TB5.

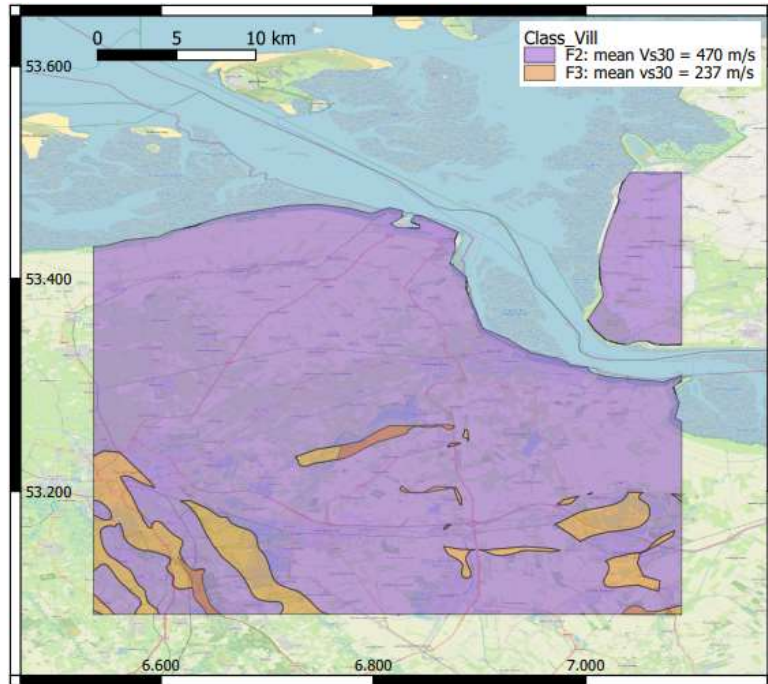


Figure 6-23: Geology-based Vs30 model for TB6.

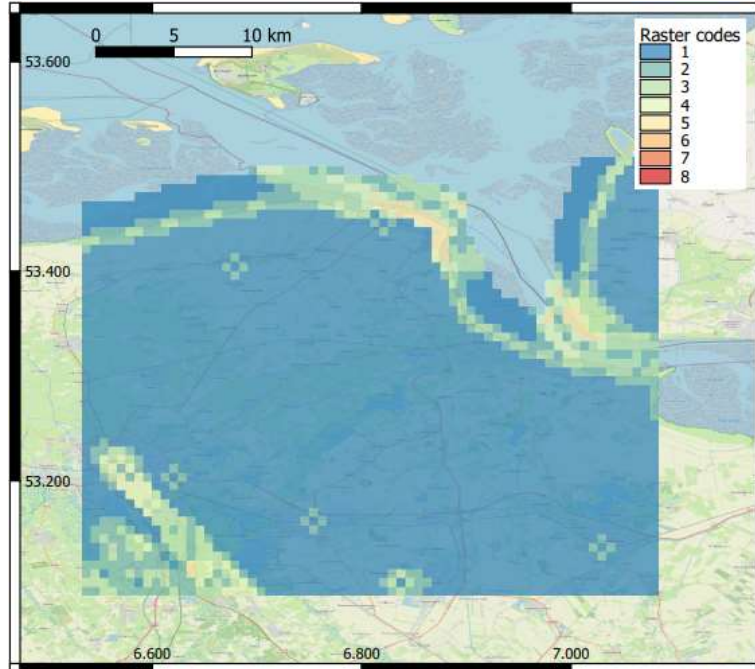


Figure 6-24: DEM-based Vs30 model for TB6.

6.4 Collection of site amplification factors at local level

The following sub-sections detail site amplification maps and models that are available at the local level for each TB. The objective is to identify to availability of specific local models that can applied instead of the European-level amplification models. When possible, the comparison between local and global models is discussed.

6.4.1 TB1: Bucharest, Romania

Bucharest, the capital of Romania (Figure 6-25), with more than 2.5 million inhabitants, is considered the second-most earthquake-endangered metropolis in Europe after Istanbul. It is identified as a natural disaster hotspot by a global study of the World Bank and Columbia University (Dilley et al., 2005).

Four major earthquakes with moment magnitudes between 6.9 and 7.7 hit Bucharest in the last century. The most recent destructive earthquake of 4th March 1977, with a moment magnitude of 7.4, caused about 1.500 casualties in the capital alone. All disastrous earthquakes are generated within a small epicentral area – the Vrancea region – about 160 km northeast of Bucharest (Figure 6-25).

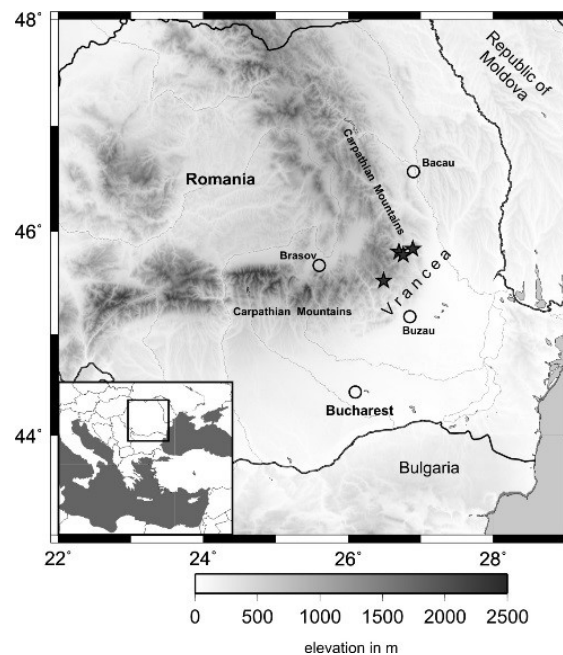


Figure 6-25: Romania map with location of Bucharest and Vrancea (main seismic source).

6.4.1.1 Elements of geology and layout of Bucharest

Bucharest is built on young, partly unconsolidated and water-saturated sediments of the Dâmbovița and Colentina river systems and their surrounding plains. This subsurface is especially prone to strong shaking and even amplification of earthquake waves as shear-waves causing severe destruction including ground liquefaction.

Thus, disaster prevention and mitigation of earthquake effects is an issue of highest priority for Bucharest and its population. Bucharest is located in the central part of Vlăsiei Plain, part of the Romanian Plain, about 165 km away from the epicentral area of Vrancea (Figure 6-25). Vlăsiei Plain is considered by some authors (Mihăilescu, 1924) as a transition zone between the northern piedmont plains and the Danube plain to the south.

In Bucharest, the Dâmbovița valley looks like a long corridor approximately 22 km long, through the city, with variable width from 650 m, to about 4 km at the eastern end of the city. (before being suburbanized in the last century). In the city are also several lakes, in parks. A novelty is the Morii lake, formed by building a dam on the Dâmbovița river in the 20th century. Geological, geotechnical and hydrogeological boreholes in the city are provided information on the succession of subsoil deposits.

The brief presentation above demonstrates the complex environment in which Bucharest is situated and the difficulty of researchers to specify a final model of amplification for the city area.

6.4.1.2 Recent subsoil studies in Bucharest

Several national and international research programs were performed in the past decades to understand the causes for the Vrancea seismicity, to study seismic wave propagation in the region and to assess seismic hazard for Bucharest and other communities.

Next two examples research programs on the subsoil of Bucharest achieved in the 21st century will be presented.

In Bucharest, high-quality seismic data were acquired during the URS (URban Seismology) project from October 2003 to August 2004 (a cooperation between INFP and University of Karlsruhe/ Collaborative Research Centre (CRC461) "Strong Earthquakes"). Within this project, 32 state-of-the-art broadband stations were continuously recording in the metropolitan area of Bucharest (Ritter et al., 2005). This unique dataset provides important information on seismic amplitude variation across the area.

In addition, engineering geology and modelling of wave propagation in near-surface layers (consolidated and non-consolidated material) were addressed. However, it was found that there is an urgent need for a homogeneous dataset of geotechnical parameters of the soils and rocks of the uppermost layers underneath Bucharest. These are partly responsible for local ground motion amplification and thus are important for hazard assessment.

The NATO Science for Peace Project no.981882 (a cooperation between INFP and University of Karlsruhe/ Collaborative Research Centre (CRC461) "Strong Earthquakes") was established undertaken to fill this gap of knowledge.

The main results of this project can be summarized as:

- 10 new boreholes including complete lithological profiles and about 250 recovered core samples for geotechnical analysis,

- 10 downhole measurements for vp and vs profiles,
- 400 geotechnical analyses of samples from 6 Quaternary layers,
- spectral amplification curves,
- improved Vs30 map,
- investigation of seismological measurements across the city.

Improved Vs30 map from project NATO SFP/981882

Within the NATO SFP project 981882, the CRC461, NIEP and UKA projects seismic velocities values were obtained through seismic measurements in boreholes (Bala et al., 2006, 2007a, 2007b), at the surface (von Steht et al., 2008) and by the SCPT (seismic cone penetration test) method (Hannich et al., 2006). These results and previous measurements (e.g. Kienzle et al., 2006) were gathered in order to compute the mean weighted seismic velocity for the first 30 m depth (Vs30) according to Equation (6-10).

The resulting new map of Vs30 is presented in Figure 6-26. It was obtained by interpolation of the velocity values at the different measurement sites. According to this map, Vs30 in Bucharest ranges from 240 m/s to 320 m/s. The north-eastern part of Bucharest is characterised by rather low velocity values, less than 260 m/s, with the exception of Baneasa zone with velocity values of 280 m/s.

The map in Figure 6-26 shows that in the central part of Bucharest, areas with low Vs30 values are neighboured by areas with high Vs30 values. The interfluvial area is characterised by rather high Vs30 values of 290-300 m/s. The southern plain is characterised by medium Vs30 velocities around 280 m/s. More seismic measurements are needed in order to obtain an improved map of this important parameter, which has a great importance for the microzonation map of Bucharest.

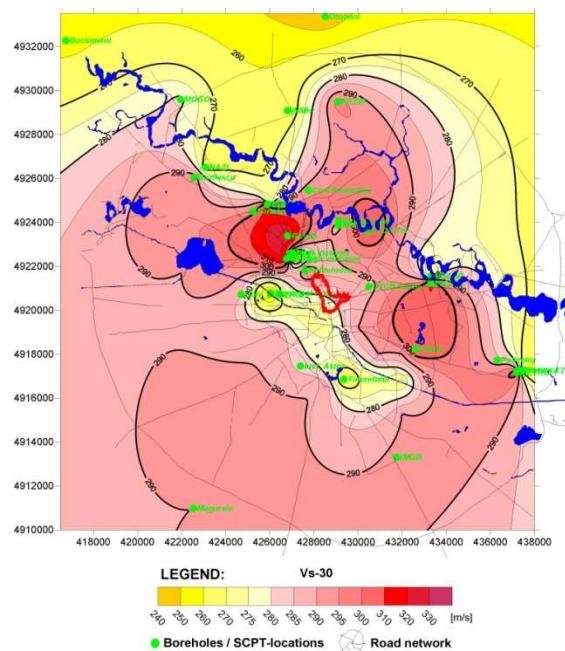


Figure 6-26: Improved Vs30 map for Bucharest City. (Project NATO SFP/981882).

Weighted mean values for Vs30 were computed according to the following equation:

$$\overline{v_s} = \frac{\sum_{i=1}^n h_i}{\sum_{i=1}^n \frac{h_i}{v_{s_i}}} \quad (6-10)$$

where h_i and v_{s_i} denote the thickness (in metres) and the shear-wave velocity (in m/s) of the i -th layer, for a total of n layers (according to the Romanian code for the seismic design of buildings - P100-1/2006).

In the Romanian Code for the seismic design for buildings - P100_1/2006 and EUROCODE 8 the weighted mean values Vs30, computed for at least 30 m depth, determine 4 classes:

1. Class A, rock type : $Vs30 > 800$ m/s;
2. Class B, hard soil : $360 < Vs30 < 800$ m/s;
3. Class C, intermediate soil: $180 < Vs30 < 360$ m/s;
4. Class D, soft soil: $Vs30 < 180$ m/s;

All the Vs30 values in Bucharest belong to type C (intermediate soil) following this classification. Also the Vs50 values in Bucharest fall into the type C category.

A reference paper on the microzonation of Bucharest presenting numerous parameters is “A GIS-based study of earthquake hazard as a tool for the microzonation of Bucharest”, by [Kienzle et al. \(2006\)](#).

6.4.1.3 Spectral amplification factor (local amplification and nonlinear behaviour of soil strata)

A method used for making a connection between seismic hazard, local site effects/local amplifications and nonlinear behaviour is using spectral amplification factors (SAF) ([Mărmureanu et al. 2005](#), [Bălan et al. 2016](#)). This approach applied for areas with thick Quaternary sediments may offer a demonstration of nonlinear dependence of spectral amplification factors on local site conditions for strong magnitudes.

The spectral amplification factor (SAF) is defined as ratio between maximum spectral values of absolute acceleration (S_a), relative velocity (S_v) and displacement (S_d) from response spectra for a fraction of critical damping (ζ %) at its **fundamental period** and peak values of acceleration (a_{max}), velocity (v_{max}) and displacement (d_{max}), respectively, from processed strong motion recordings, : (i.e.: $(SAF)_a = S_a/a_{max}$; $(SAF)_v = S_v/v_{max}$; $(SAF)_d = S_d/d_{max}$.

For illustration of this non-linear seismic propagation, we consider the following stations located within the Bucharest metropolitan area: INCERC, Panduri, Metalurgiei and Branesti.

Table 6-16: Bucharest- INCERC seismic station (Mărmureanu Gh. et al. 2014, Bălan et al. 2016).

Earthquake	a_{max} [cm/s ²] recorded	$S_{a_{max}}^{a}$ [cm/s ²] $\beta=5\%$	(SAF) _a	c	S_{a^*} [cm/s ²] $\beta=5\%$	a^* [cm/s ²]
March 4, 1977, $M_W=7.4$	206.90	650	3.14	1.079	700.98	223.24
August 30, 1986 $M_W=7.1$	96.96	255	2.63	1.292	329.46	125.27
May 30, 1990 $M_W=6.9$	66.21	225	3.39	1.000	225	66.21

Table 6-17: Bucharest- Panduri seismic station (Mărmureanu Gh. et al. 2014, Bălan et al. 2016).

Earthquake	a_{max} [cm/s ²] recorded	$S_{a_{max}}^{a}$ [cm/s ²] $\beta=5\%$	SAF _a	c	S_{a^*} [cm/s ²] $\beta=5\%$	a^* [cm/s ²]
August 30, 1986 $M_W=7.1$	89.4	295	3.30	1.469	446.36	135.26
May 30, 1990 $M_W=6.9$	131.3	590	4.49	1.080	653.78	145.61
May 31, 1990 $M_W=6.4$	33.0	160	4.85	1.000	160.00	33.00

Table 6-18: Bucharest- Metalurgiei seismic station (Mărmureanu Gh. et al. 2014, Bălan et al. 2016).

Earthquake	a_{max} [cm/s ²] recorded	$S_{a_{max}}^{a}$ [cm/s ²] $\beta=5\%$	(SAF) _a	c	S_{a^*} [cm/s ²] $\beta=5\%$	a^* [cm/s ²]
August 30, 1986 $M_W=7.1$	71.07	220	3.09	1.471	323.04	104.54
May 30, 1990 $M_W=6.9$	55.40	220	3.97	1.143	251.39	63.32
May 31, 1990 $M_W=6.4$	12.10	55	4.54	1.000	55	12.10

Table 6-19: Bucharest- Branesti seismic station (Mărmureanu Gh. et al. 2014, Bălan et al. 2016).

Earthquake	a_{max} [cm/s ²] recorded	$S_{a_{max}}^{a}$ [cm/s ²] $\beta=5\%$	(SAF) _a	c	S_{a^*} [cm/s ²] $\beta=5\%$	a^* [cm/s ²]
August 30, 1986 $M_W=7.1$	93.30	295	3.16	1.553	457.87	144.89
May 30, 1990 $M_W=6.9$	142.20	470	3.31	1.483	698.02	210.88
May 31, 1990 $M_W=6.4$	23.80	117	4.91	1.000	117	23.80

In

Table 6-16 to Table 6-19, a_{max} is the maximum recorded acceleration with corresponding spectral acceleration $S_{a_{max}}$, SAF is the spectral amplification factor, c is the ratio of SAF for the May 30 or 31 1990 Vrancea event to the SAF for each stronger earthquake. S_a^* is the maximum spectral acceleration and a^* the maximum acceleration if a linear response at the fundamental frequency at each considered site is assumed. We consider this to be the case for the smallest event, May 30 (or 31), 1990. Multiplying the c coefficient by the maximum recorded acceleration a_{max} for each strong event, one obtains these a^* accelerations, and by multiplying them with the corresponding $(SAF)_a$, the maximum spectral values in the linear response case are computed (S_a^*). As can be seen, the values of a^* are increasing in comparison to corresponding recording values, and c emerges as a measure of nonlinear response of the sites. We observe significant variations between $S_{a_{max}}$ (recorded spectral acceleration) and S_a^* (maximum spectral acceleration if the system would have a linear response) for the same event and location, demonstrating us that strong seismic motions produce nonlinear effects in local soils.

In addition, we observe that spectral amplification factors (SAFs) have a nonlinear dependence on seismic magnitude. This is also visible in Table 6-20, where mean values of spectral amplification factors are presented for three strong earthquakes from the 20th century.

Table 6-20: Mean values of spectral amplification factors for three strong earthquakes from the 20th century (Mărmureanu et al., 1996).

Damping	August 30, 1986; M _w 7.1		May 30, 1990; M _w 6.9		May 31, 1990; M _w 6.4	
$\beta\%$	$(SAF)_a$	$(SAF)_v$	$(SAF)_a$	$(SAF)_v$	$(SAF)_a$	$(SAF)_v$
2%	4.74	3.61	5.58	3.72	6.22	4.84
5%	3.04	2.69	3.98	2.95	4.76	3.48
10%	2.43	2.99	2.56	2.14	2.92	2.69
20%	1.78	1.5	1.82	1.58	2.13	1.86

In Figure 6-27, response spectra are represented for the same site (INCERC-Bucharest) obtained from recordings during the three most destructive earthquakes of the last century (whose spectral amplification factors are presented in Table 6-20). One can observe a tendency of increasing fundamental period with increasing magnitude.

The soft Quaternary sediments under Bucharest could be responsible for the decreasing in wave velocity in these superficial layers and for absorbing high frequencies. Therefore, high fundamental periods throughout the city area are observed. Though these implications

probably are not a direct consequence of the nonlinearity phenomenon, they are important for site evaluation and seismic risk studies.

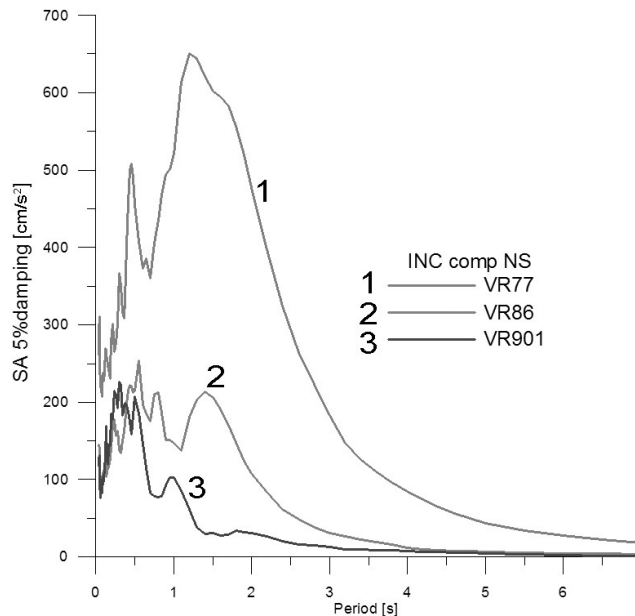


Figure 6-27: Response spectra for the site INCERC-Bucharest obtained from recordings during the three most destructive earthquakes of the last century (Bălan et al. 2016).

LEGEND: VR77- earthquake of 1977 (M=7.4), earthquake of 1986 (M=7.1), earthquake of 1990 (M=6.9).

6.4.1.4 Amplification models for shake-maps

Two shake map systems are currently implemented at INFP:

- INFP shake-map, based on USGS ShakeMap® v.3.5 (atlas2.infp.ro/~shake/shakemap);
- SeisDaRo shake-map, using a custom Matlab code based on USGS ShakeMap® v.3.5 (Toma-Danila et al., 2018).

Both shake-maps are using the amplification model by Wald and Allen (2007). The INFP shake-map is using the GMPE by Sokolov et al. (2008), which does not consider Vs30I and uses regional coefficients. The city of Bucharest is considered a single zone. The SeisDaRo shake-map uses the GMPE by Vacareanu et al. (2014) and Vs30 (for certain points of the city). As seen in the above sub-sections, Vs30 values for Bucharest are available from different papers and projects, but there is no official recognized amplification model for the city currently in use.

6.4.2 TB2: Pyrenees mountain range, France

Within TB-2, the Luchon area (see Figure 6-28) has been studied in detail by Fayjaloun et al. (2021b) in terms of available models for soil amplification and building exposure. Two soil amplification models, at regional and local scales (see Figure 6-29 and Figure 6-30), are compared with the European-level SERA model.

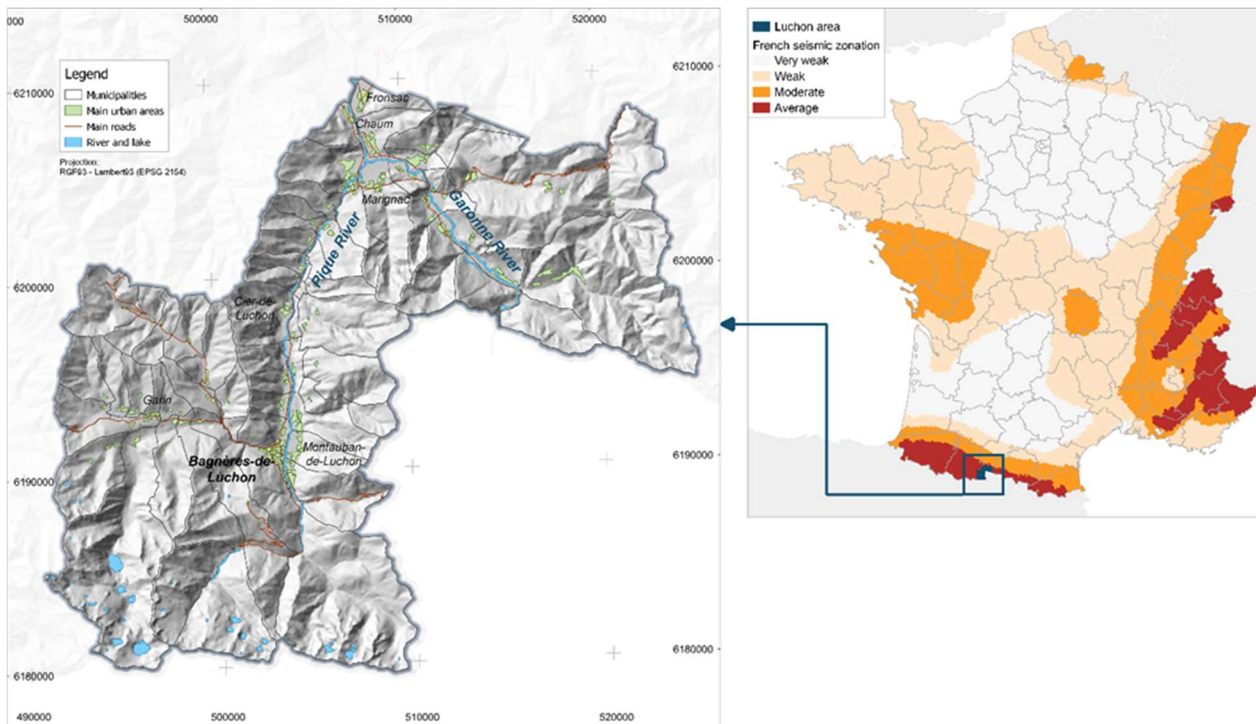


Figure 6-28: Left: map of the Luchon area and the 53 municipalities. Right: location of the Luchon area overlaid with the French seismic zonation map.

In the framework of the European project SISPy, a regional soil characterization map was developed for the Pyrenean range (Colas et al., 2010 & 2012). It is based on data combined from two geological maps describing quaternary deposits and the geological structure of the Pyrenees at 1:400,000 scale, from Courboulex et al. (2008) and Baudin et al. (2008), as well as available borehole data on the two sides of the French-Spanish border. The borehole data were obtained from the following sources:

- French BSS complete database, with geological description and (sometimes) geotechnical information (5258 analysed boreholes);
- Ministerio de Medio Ambiente y Medio Rural y Marino (MARM; IGC, 2011);
- Confederación Hidrográfica del Ebro (CHE) and Agència Catalana de l'Aigua (ACA; IGC, 2011).

Following Colas et al. (2010 & 2012), the resulting soil condition map at the regional scale was built as follows. First, homogeneous geological units were defined from the lithological and geometric information of basement and quaternary deposits. Second, the representative soil column types of the Pyrenean geological context were defined, using information on deposit lithology, thickness, and geo-mechanical characteristics derived from borehole data. Those soil column types and the geological units defined above were then used for geo-mechanical zonation. EC8 soil classes were finally assigned to each of the resulting geo-mechanical zones and a map of EC8 soil classes with a 500 m grid mesh was computed (see Figure 6-29).

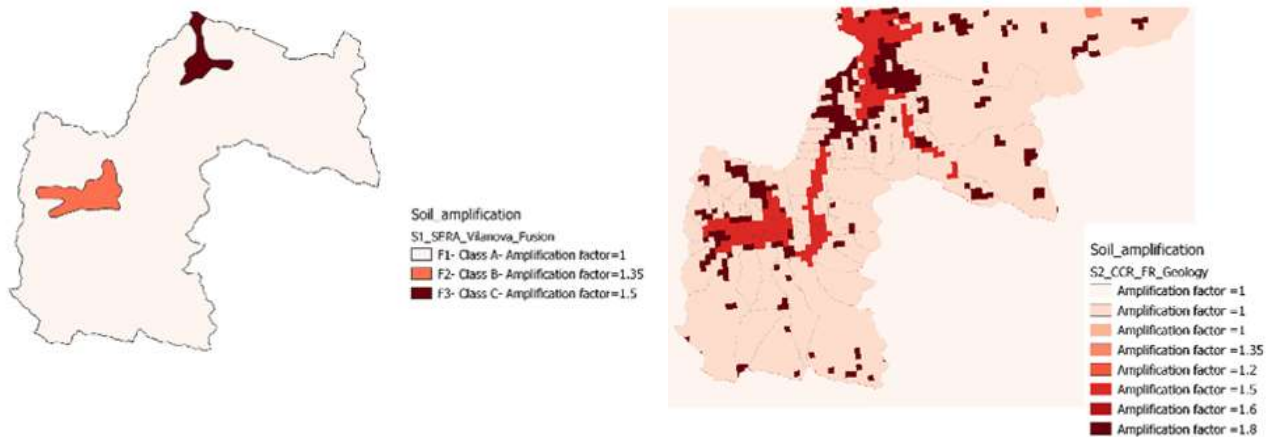


Figure 6-29: Comparison of soil characterization maps at different scales, expressed as amplification factors, for the Luchon area. Left: geology-based model presented in Section 6.2; right: regional model.

BRGM has also developed a local soil condition map of the Luchon valley for the purpose of seismic risk scenarios (Roullé and Colas, 2013). This map is based on:

- a 1:50,000 geological map of the area;
- borehole data (geological and geotechnical data) extracted from the French borehole database;
- additional geophysical data, in order to determine the frequency resonance and V_s profiles on the main superficial deposits of the valley. A campaign of 75 H/V measurements, 21 MASW profiles, and 3 seismic noise array measurements was realized to complement the poor existing geological and geotechnical data in the valley. Special attention was paid to the alluvial deposits of the central valley area (between Marignac and Chaum), which present an unexpected low frequency resonance (around 0.5 Hz), corresponding to a thick layer of soft deposits which could be associated to the alluvial deposits overlying glacial rock deposits.

A combined interpretation of geological, geotechnical, and geophysical data was then used to map zones with homogeneous geology and frequency resonance. Representative 1D soil columns for each zone were defined and classified, in terms of EC8 soil classes. The resulting product was a 1:10,000 microzonation map for the entire Luchon valley with EC8 soil classification (see Figure 6-30).

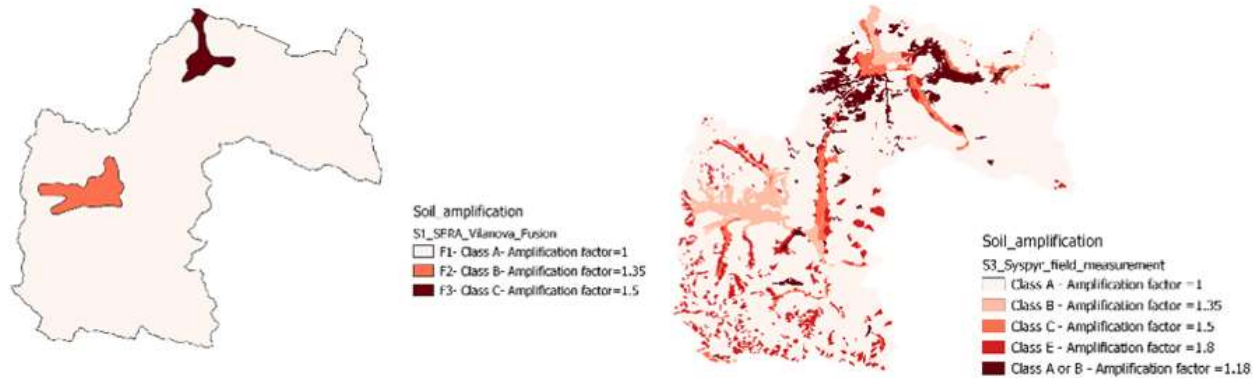


Figure 6-30: Comparison of soil characterization maps at different scales, expressed as amplification factors, for the Luchon area. Left: geology-based model presented in section 6.2; right: local model.

A comparison between soil classes distributions for the urban areas and the three studied scales (Figure 6-29 and Figure 6-30) showed that the extent of the urban areas located on soils prone to site effects (soil classes from B to E) varied strongly with the map scale (see Figure 6-31). This represented 25% of urban areas at the European scale, 56% at the regional scale, and 65–74% for the local scale site map. Therefore, the chosen scale is a key parameter, which can cover (or not) the critical size of the geomorphological object studied (here, the Pique river valley, characterized by a width about 300 m at Cier-de-Luchon and about 1500 m at Montauban-de-Luchon).

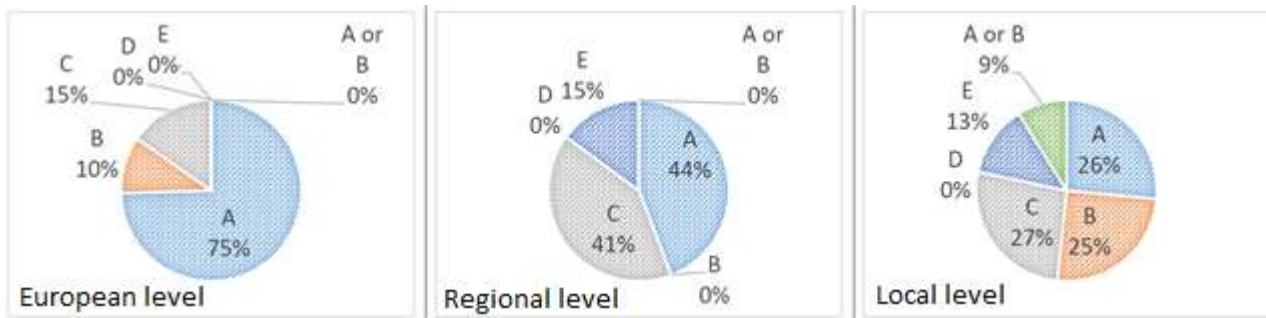


Figure 6-31: Pie charts of the distribution of soil characterization classes in urbanized areas for the three defined scale scenarios.

In our case, a first glance at maps of site classes (Figure 6-29 and Figure 6-30) showed that the European-scale site model missed all the alluvial deposits located in the Pique river valley (from Cier-de-Luchon to Bagnères-de-Luchon, the main city of the valley), where a great part of the urban area (among which the touristic thermal area) and the main road of the valley are located on those deposits.

If we consider only the regional and local scales, the main difference between the two approaches arose from the soil classification itself; in particular, the distinction between classes B and C in the glacial deposits at the South-West (near Garin village) and Northern (Fronsac village) parts of the valley. However, in both cases, the critical geological formations in terms of site effects (alluvial deposits, glacial deposits, alluvial fans) were identified (see Figure 6-28).

6.4.3 TB3: Hveragerði and Húsavík, Iceland

6.4.3.1 Localized site amplification and station terms

The towns of Hveragerði and Húsavík in Iceland have been selected as the urban areas of interest for the TURNkey project in Iceland due to their 1) dense urban strong-motion array instrumentation, datasets, and the corresponding research, 2) complex and different geologies and topographies, and 3) collocation with urban areas, buildings and infrastructures of modern society. Figure 6-32 shows their respective detailed geologies along with the strong-motion array recording sites of ICEARRAY I (Hveragerði) and ICEARRAY II (Húsavík).

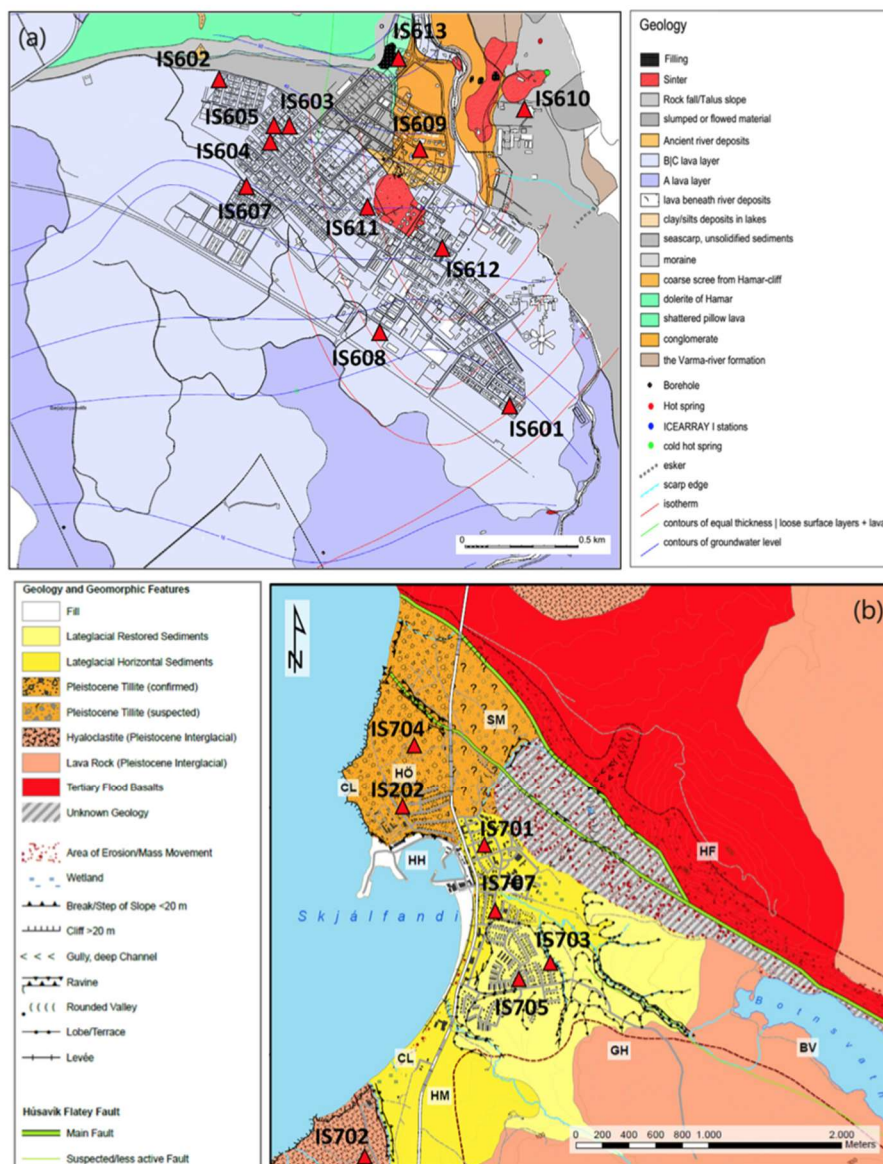


Figure 6-32 Geological maps of the towns of Hveragerði (top) and Húsavík (bottom) in TB3 Iceland that are of the highest detail and spatial resolution, shown along with the recording stations of the Icelandic strong-motion arrays (ICEARRAY I at top, ICEARRAY II at bottom) (Rahpeyma et al. 2019).

The strong-motion datasets for each town have been analysed thoroughly using a Bayesian Hierarchical Model (Rahpeyma et al. 2018, 2019, 2020) that provides the posterior distribution of the individual station terms that effectively quantify the localized site response differences across the array, both for peak ground acceleration (PGA) (Rahpeyma et al. 2019) at Hveragerdi and Husavik, and for pseudo-acceleration spectral response at oscillator periods of engineering interest at Hveragerdi (Rahpeyma et al. 2020). Figure 6-33 shows the effective site factors for horizontal motions of ICEARRAY I stations in Hveragerdi relative to an array station on bedrock, listed in Table 6-21. The amplification seen at 0.1-0.5 s is due to the unique geological structure of intercalated soil layers between the two hard lava-rock layers (purple colours in Figure 6-32).

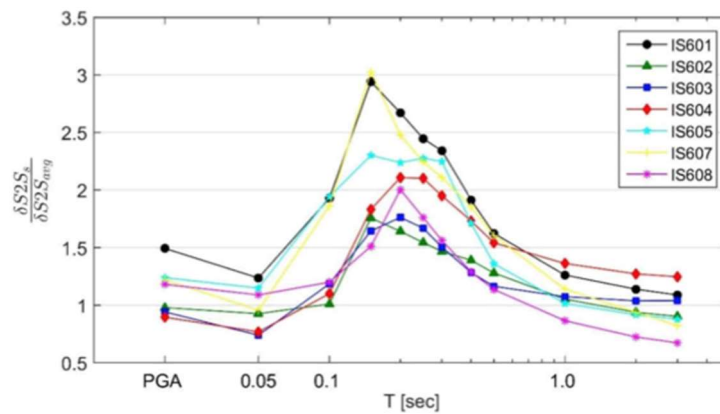


Figure 6-33 Mean station terms at ICEARRAY I stations in Hveragerdi relative to a reference station on bedrock.

Table 6-21. Station terms at ICEARRAY I stations in Hveragerdi relative to a reference station on bedrock

T [sec]	$\frac{\delta S2S_1}{\delta S2S_{avg}^*}$	$\frac{\delta S2S_2}{\delta S2S_{avg}}$	$\frac{\delta S2S_3}{\delta S2S_{avg}}$	$\frac{\delta S2S_4}{\delta S2S_{avg}}$	$\frac{\delta S2S_5}{\delta S2S_{avg}}$	$\frac{\delta S2S_6}{\delta S2S_{avg}}$	$\frac{\delta S2S_7}{\delta S2S_{avg}}$
PGA	1.49	0.98	0.94	0.90	1.24	1.22	1.18
0.05	1.24	0.93	0.74	0.77	1.15	0.96	1.09
0.10	1.93	1.01	1.19	1.10	1.94	1.86	1.20
0.15	2.94	1.76	1.64	1.83	2.30	3.02	1.51
0.20	2.67	1.64	1.76	2.11	2.34	2.48	2.00
0.25	2.45	1.54	1.67	2.10	2.28	2.25	1.76
0.30	2.34	1.47	1.50	1.95	2.25	2.11	1.56
0.40	1.91	1.39	1.28	1.73	1.71	1.85	1.29
0.50	1.62	1.28	1.16	1.54	1.36	1.60	1.14
1.00	1.26	1.05	1.07	1.36	1.02	1.14	0.86
2.00	1.14	0.94	1.04	1.27	0.92	0.94	0.72
3.00	1.09	0.90	1.04	1.25	0.88	0.82	0.67

* $\delta S2S_{avg}^*$ is defined as the average of mean posterior station terms of stations IS609, IS611, IS612

The station terms have been determined for Husavik as well, albeit only for PGA. The posterior distributions of the station terms are shown in Figure 6-34 and their percentiles are listed in Table 6-22 relative to the array average. The site factors can be derived from the posteriors by e.g. using station IS702 as a reference station (Rahpeyma et al. 2019).

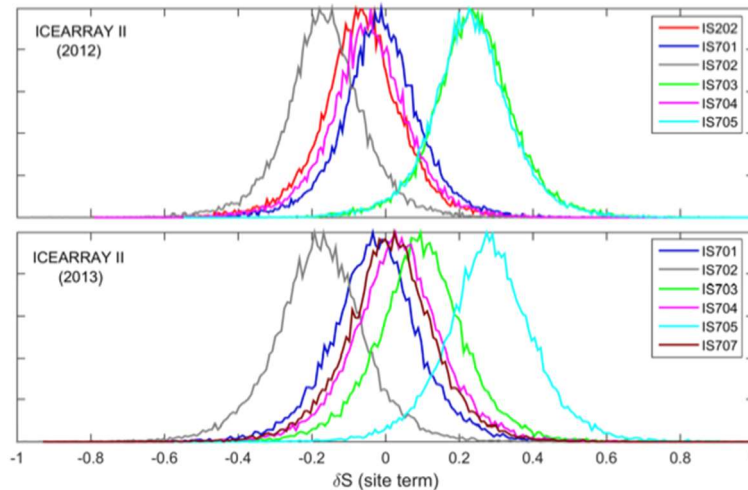


Figure 6-34 Posterior distributions of station terms at ICEARRAY II stations in Husavik relative to the array average.

Table 6-22. Station terms at ICEARRAY II stations in Husavik relative to a reference station on bedrock

stations	IS202	IS701	IS703	IS704	IS705	IS707
$\frac{\delta S_2 S_s}{\delta S_2 S_r}$	$\frac{\delta S_2 S_1}{\delta S_2 S_r}$	$\frac{\delta S_2 S_2}{\delta S_2 S_r}$	$\frac{\delta S_2 S_4}{\delta S_2 S_r}$	$\frac{\delta S_2 S_5}{\delta S_2 S_r}$	$\frac{\delta S_2 S_6}{\delta S_2 S_r}$	$\frac{\delta S_2 S_7}{\delta S_2 S_r}$
ICEARRAY II (swarm 2012)						
PGA	1.25	1.42	2.54	1.32	2.51	-
ICEARRAY II (swarm 2013)						
PGA	-	1.41	1.88	1.63	2.90	1.56

On the basis of this research, shake-maps for the towns of Hveragerdi and Husavik can be that take into account the site effects drawn. In this context, it is imperative to keep in mind that, strictly speaking, the site factors are only valid for the locations of the stations, but expected relative differences in shaking over the array area can be obtained by interpolation. The site factors are not informative for areas outside the array.

6.4.3.2 The geology of Hveragerdi and Husavik, TB3 Iceland

The main subsoil geological characteristics across ICEARRAY I and II are entirely different (Figure 6-32). Across ICEARRAY I, the uppermost lava layer (~5,000 year-old) lies on top of a softer sedimentary layer, which in turn lies on top of another lava rock layer (~10,000 year-old), resulting in a velocity reversal. This profile was derived based on geological and borehole information of the uppermost lava rock layer. As can be seen on the geological map of Hveragerði, the majority of the ICEARRAY I strong-motion stations is located on the stiff lava rock layer. In contrast, local soil conditions across ICEARRAY II are much more complicated in

comparison to ICEARRAY I. Húsavík itself is characterized by several stiff sedimentary layers, which generally overlay the Grjótháls lava rock and hyaloclastite, and vary in softness as well as depth from site to site. The subsoil structure beneath the ICEARRAY II can be clustered into four main geological units: (1) the northernmost part of the town sits on relatively hard tillite, while (2) the geology along the shoreline towards the south is characterized by horizontally layered fluvial sediments. (3) On top of the sediments lies a delta formation of glacial deposits. (4) The oldest sediments are glacial deposits which have over time been altered to solid tillite rock, which underlay parts of Húsavík (Waltl 2013; Waltl et al. 2018, and references therein).

The classification of the geology of the TB-areas may vary by the spatial scale and the size of the region considered. In Figure 6-32, a very detailed spatial resolution is shown and the geology map reflects that. Figure 6-35 shows lower-scale geology maps of the TB3 towns showing a greater region around the array with less spatial resolution.

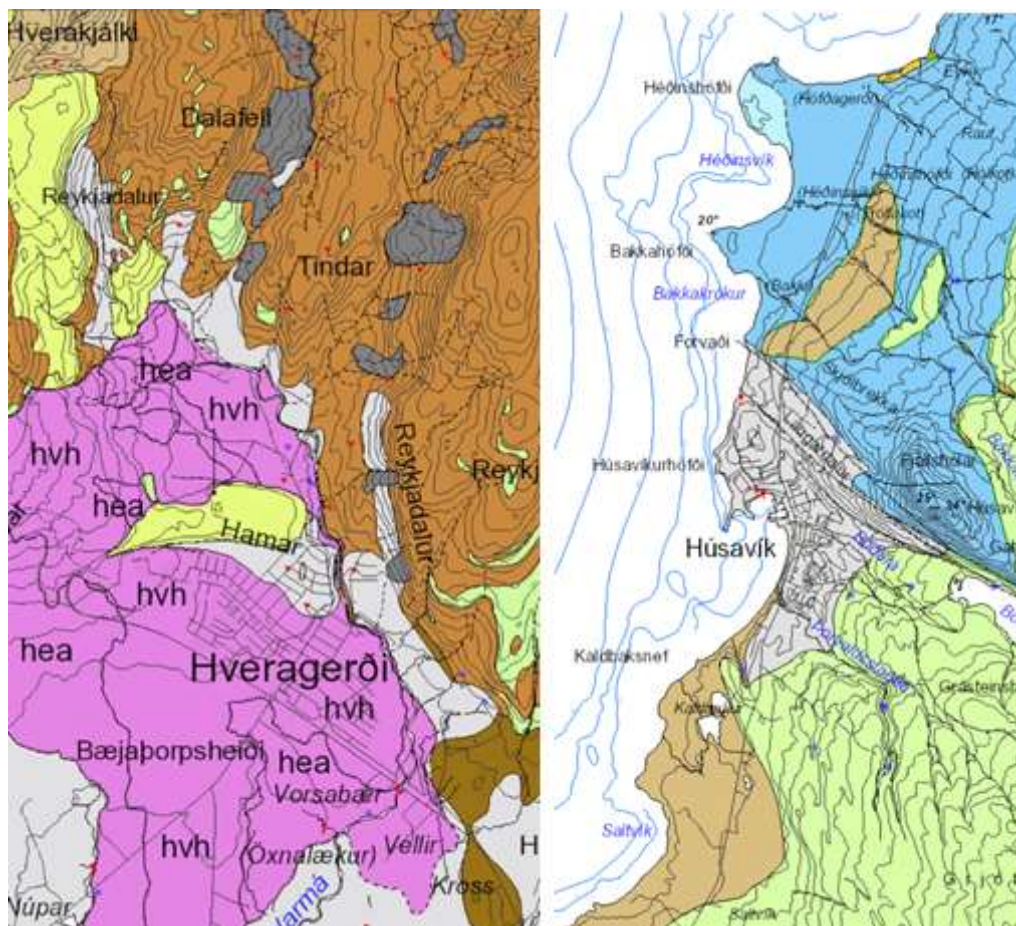


Figure 6-35 Geological maps for TB3-Hveragerdi and TB3-Husavik with lower resolution, obtained from ÍSOR database (<http://jardfraedikort.is/>).

For example, contrasting Figure 6-32 and Figure 6-35, no distinction is made between the different ages of the two lava layers beneath Hveragerdi, and the entire area of Husavik town is classified as one geological unit instead of the multiple ones that have been identified. For an even larger scale of the geological map, the simplifications increase, as shown in Figure 6-36,

where only a distinction of 4 units and 2 units for Hveragerdi and Husavik, respectively, are made.

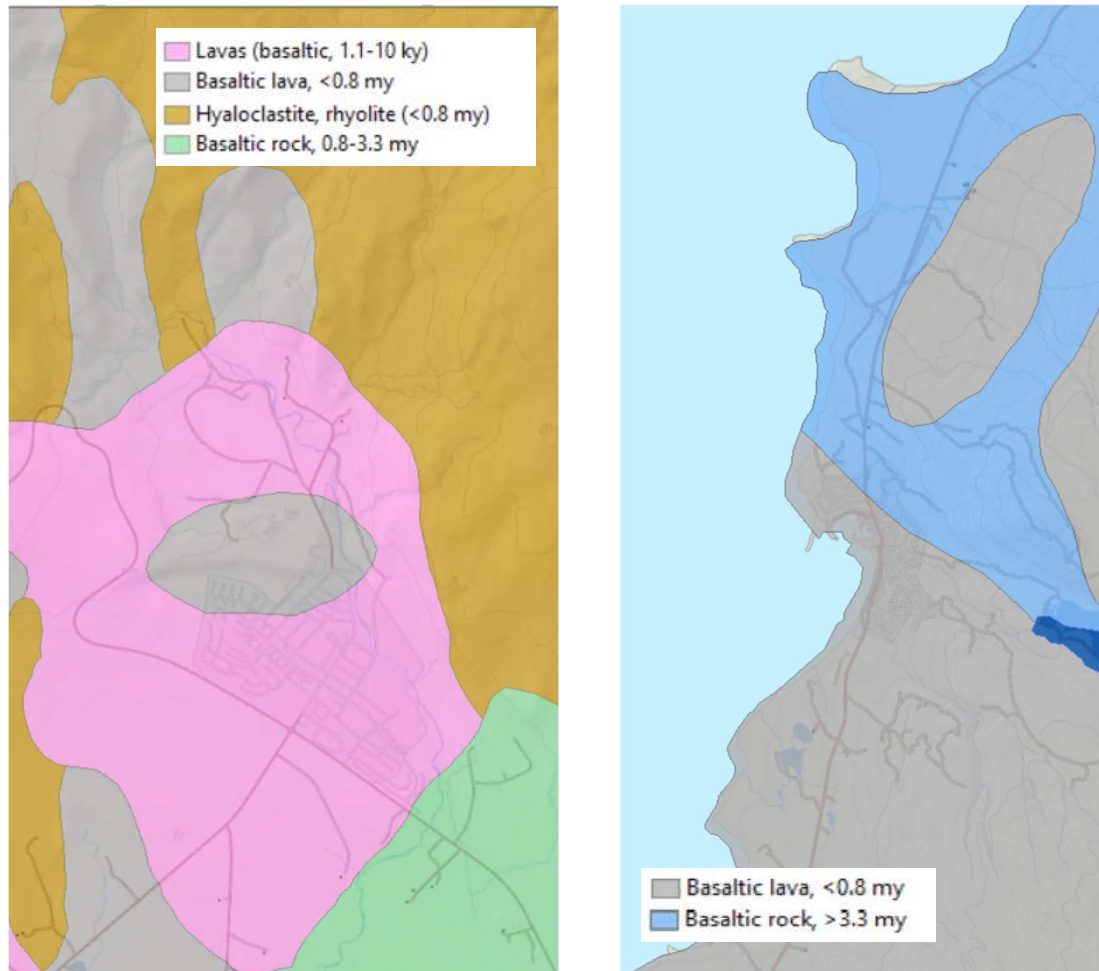
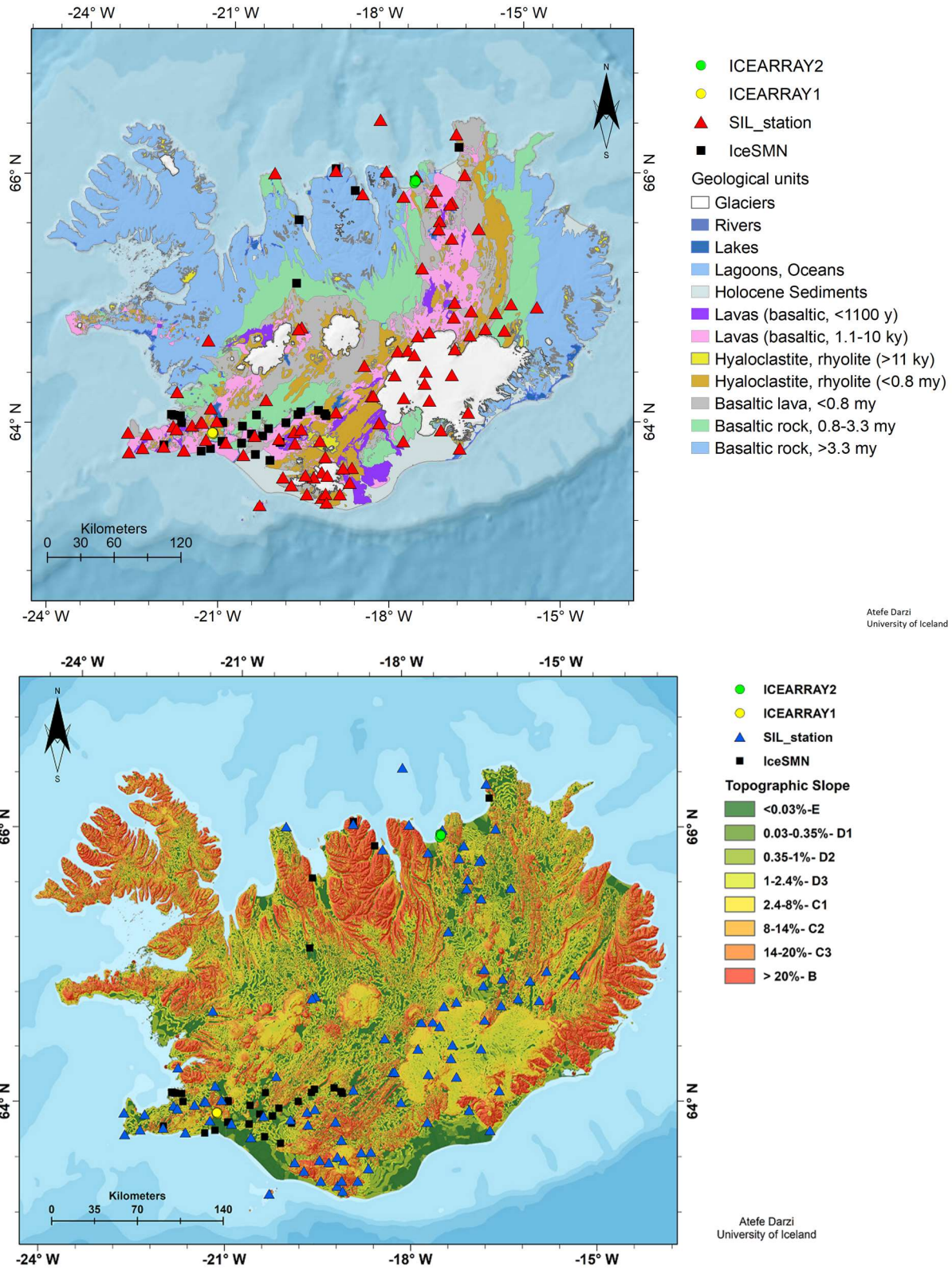


Figure 6-36 Geological maps for TB3-Husavik of yet coarser resolution.

Finally, we present in Figure 6-37 a large-scale geological map of Iceland as a whole along with the corresponding slope maps calculated from a high-resolution DEM. One can identify essentially six main geological units at this coarse spatial scale. The blue and green colours represent the oldest and second oldest bedrock in Iceland, which mainly consists of glacially eroded ancient lava flows, and they are distributed symmetrically around the extensional plate margin that crosses Iceland. On the plate margin itself, the units are associated with recent volcanism (brown, grey and pink). Finally, the light grey areas along the south coast are soft sedimentary deposits.



Atefe Darzi
University of Iceland

Atefe Darzi
University of Iceland

Figure 6-37 Geological and slope maps of Iceland along with the locations of the strong-motion (ICEARRAY I and II and IceSMN) and seismic (SIL) stations.

6.4.3.3 Proxies of site amplification

In the SAFER project, the USGS ShakeMap system was implemented at the Icelandic Meteorological Office (IMO). As a result, an estimation of V_{s30} was required, resulting in the first of such estimates for Iceland, shown in Figure 6-39 and listed in Table 6-23 (from [Vogfjörð et al. 2010](#)). Immediately apparent are the high-velocity values for the geological units, the lowest being 600 m/s for the sedimentary deposits along the coast. For reference, this is close to the value of “generic rock” for California ([Boore and Joyner 1997](#)) and would be classified as NEHRP class C ([BSSC 2004](#)). Lower velocity values generally associated with soil, e.g., “generic soil” of 310 m/s ([Boore and Joyner 1997](#)), and NEHRP classes D and F are nowhere to be found.

Moreover, the velocities are considerably higher than those of the California site-category map constructed in [Wills et al., \(2000\)](#), and near-surface velocities in crustal rocks for seismic hazard analyses ([Chandler et al. 2005](#)). The main reason for this difference is the young and igneous geology of Iceland that has been shaped by repeated glacial erosion. As a result, sedimentary layers are rare (and thin) and significantly metamorphosed rocks are rarely found near the surface. The older Tertiary rocks (coloured green in Figure 6-39) mostly represent glacially eroded lava flows and the younger formations in the rift zones (coloured violet and brown in Figure 6-39) generally consist of newly formed volcanic rocks.

When considering the topographical slope in Figure 6-37, about half of the country has a slope of less than 2° . The basaltic volcanism in Iceland during warm periods, in which glaciers did not cover the country, results in fast-flowing lava flows that cover large areas and are predominantly flat (pink and dark grey colours in Figure 6-37, and violet and brown colours in Figure 6-39). Not surprisingly, therefore, the implementation of a popular model ([Wald and Allen 2007](#)), which uses topographic slope as a proxy for V_{s30} i.e., site amplification, on the Icelandic DEM (see Figure 6-39) predicts V_{s30} values for soils when in fact, the relatively flat ground in Iceland is predominantly glacially eroded bedrock and lava-rock. Therefore, employing topographic slope as a proxy for site effects would be ineffective in improving ground motion prediction.

Focusing again on the towns of Hveragerdi and Husavik, the V_{s30} values that are considered to be realistic for the principal geological units in those micro-scale testbeds are listed in Table 6-24. The values are consistent with the estimates in Table 6-23 and Figure 6-38 and due to the coarse spatial resolution, the values are provided for the coarse geological maps in Figure 6-36. Again, in stark contrast, we show the V_{s30} values from the topographic slope model used above as predicted for the areas of Hveragerdi and Husavik in Figure 6-40. The same information is shown in Figure 6-41 except at a vastly different spatial scale.

Looking at other European efforts on geology-based V_{s30} classes ([Vilanova et al. 2018](#)), we see that both TB3 towns are classified as F1 for which a broad range of V_{s30} values from 523 to 1315 m/s is assigned (see Table 6-25). Again, it is clear that the velocities are in stark contrast with the reality of Icelandic geology.

Thus, the above at least qualitatively demonstrates that V_{s30} values from topographic slope models calibrated to other regions cannot be considered as appropriate or reliable proxies for site amplification in Iceland. Moreover, topographical slope cannot be employed at all for this

purpose in Iceland. In addition, Vs30 values from surface geology models calibrated to other regions cannot be applied to Icelandic geological units.

Table 6-23. Nine different categories used to describe the geological units of Iceland for USGS ShakeMap's implementation at the IMO in association with the SAFER project, along with their corresponding shear-wave velocity estimates. Velocities of underwater geological units (lakes, oceans) are estimated.

Vs (km/s)	Geological Unit
0.60	Sediment, mostly alluvium, thickness greater than 30 m
0.70	Sediment, thickness less than 30 m
0.75	Lakes – unknown basement
0.80	Ocean – unknown basement
1.20	Hyaloclastite and rhyolite
1.30	Holocene lava, less than 25 m thick on top of sediments
1.50	Holocene lave
1.60	Basaltic lava, younger than 0.8 million years
2.00	Basalt, older than 0.8 million years

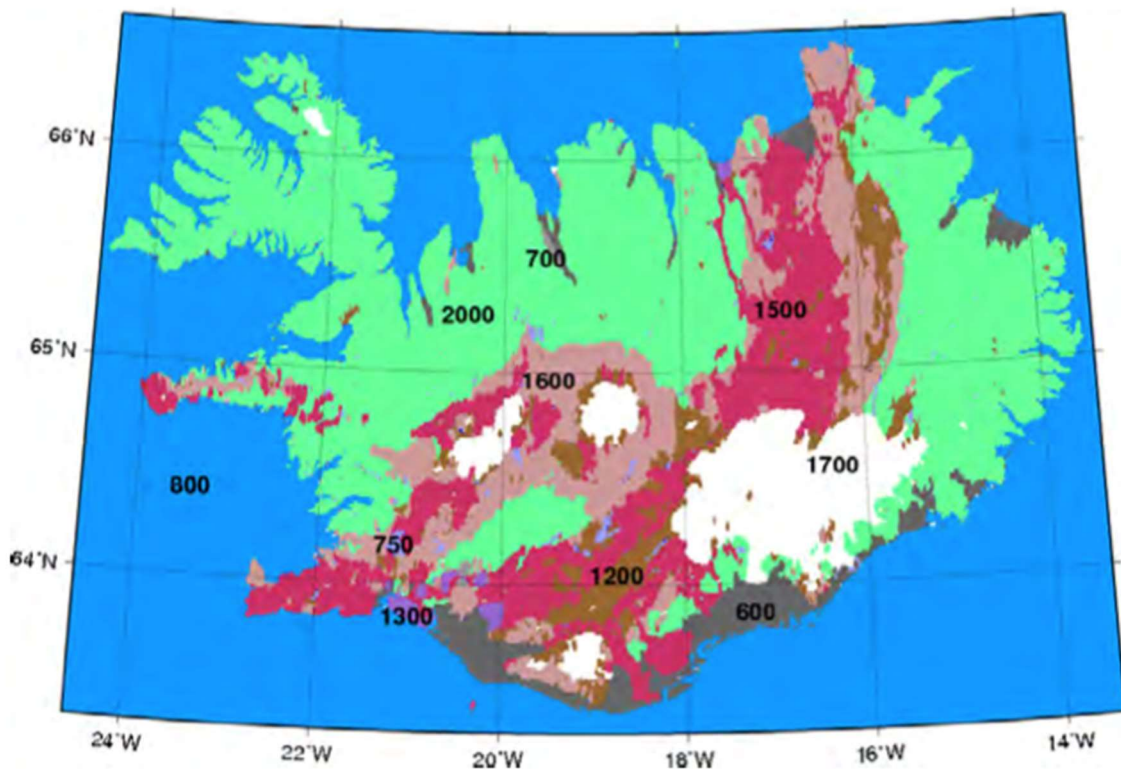


Figure 6-38 Near-surface geology of Iceland showing the categories of estimated Vs30 velocities, listed in Table 6-23.

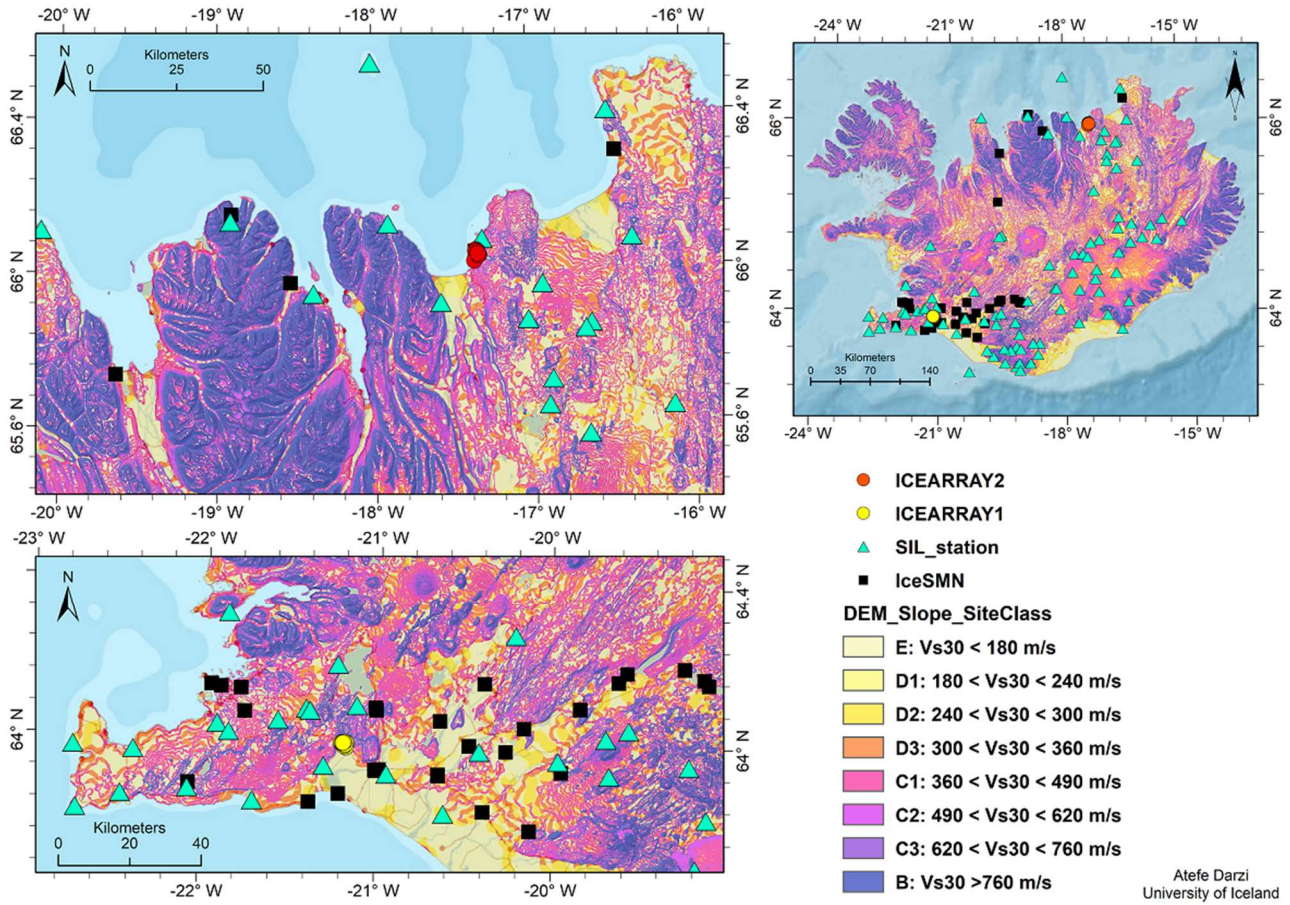


Figure 6-39 Map of V_{S30} -based site classes for Iceland (top right panel), North Iceland (top left panel) and SW-Iceland (bottom left panel), classified by the topographic slope proxy according to slope- V_{S30} ranges proposed by Wald and Allen (2007) for active tectonic regions. DEM 20m-by-20m (2/3 arcsec) resolution is used to generate the inferred V_{S30} map (Darzi et al. 2022)

Table 6-24. Estimates of the average shear-wave velocities of the geological units in Hveragerdi and Husavik

TB3-Hveragerdi geology units	V_{S30}	TB3-Husavik geology units	V_{S30}
Lavas (basaltic, 1.1-10 ky)	1500	Basaltic rock, >3.3 my	2000
Basaltic lava, <0.8 my	1600	Basaltic lava, <0.8 my	1600
Hyaloclastite, rhyolite (<0.8 my)	1200		
Basaltic rock, 0.8-3.3 my	2000		

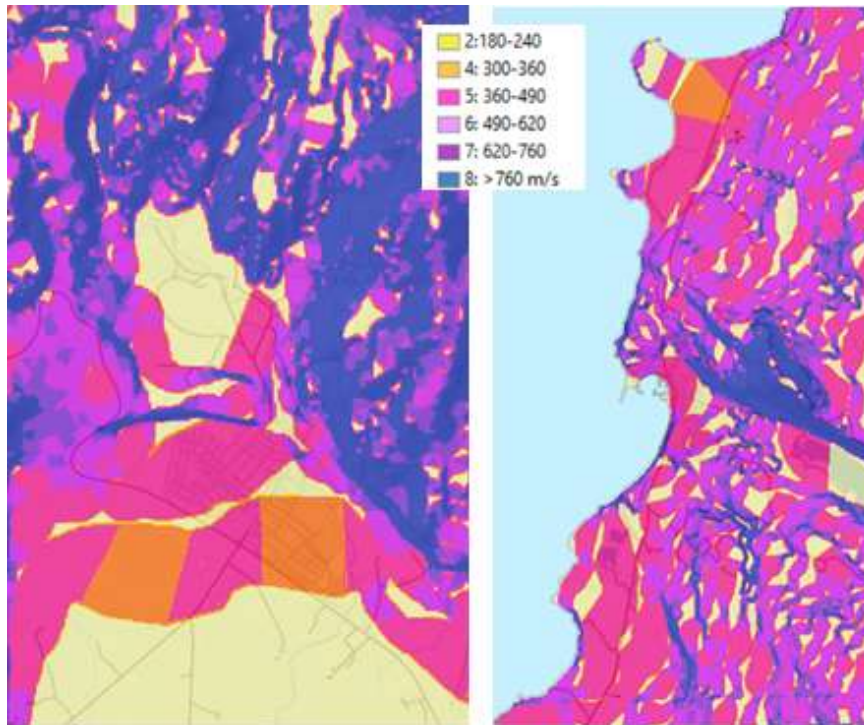


Figure 6-40. Map of V_{S30} -based site classes for TB3-Hveragerdi (left) and TB3-Husavik (right), classified by the topographic slope proxy according to slope- V_{S30} ranges proposed by Wald and Allen (2007) for active tectonic regions. DEM 20m-by-20m (2/3 arcsec) resolution is used to generate the inferred V_{S30} map (Darzi et al., 2022).

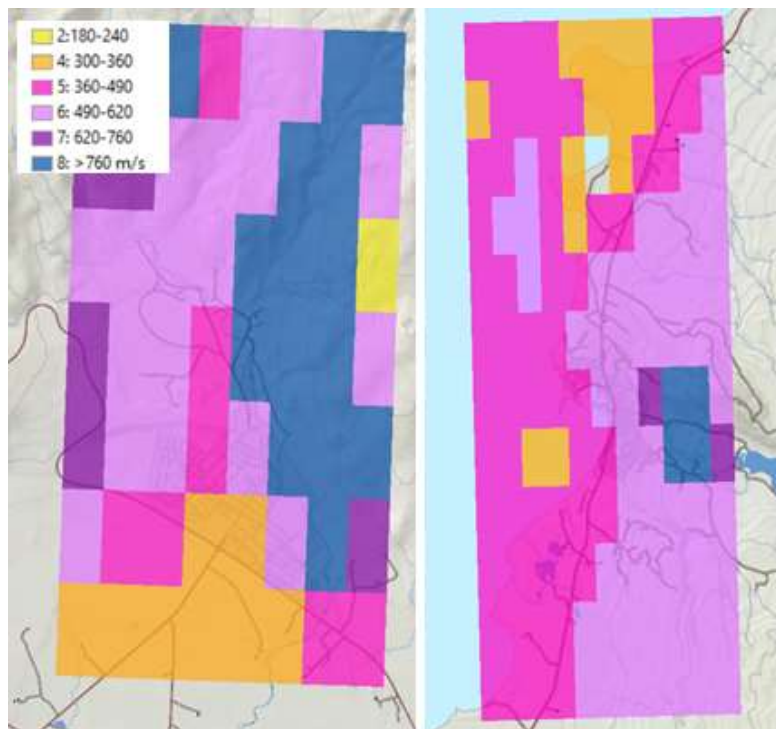


Figure 6-41. European V_{S30} maps based on (left) DEM topographic slope according to Wald and Allen (2007a) based on a 30 arc-second DEM model (~ 1000 m resolution).



Figure 6-42. European geology-based site class model for the Hveragerdi (left) and Husavik (right) testbeds, according to Vilanova et al. (2018).

Table 6-25. Geology-based Vs30 classes (Vilanova et al., 2018)

Name	Geological Unit	<i>N</i>	$\mu_{\log V_{S30}}$	$\sigma_{\log V_{S30}}$	V_{S30} (m/s)*	V_{S30} 68%CI (m/s) [†]
F1	Igneous, metamorphic, and old sedimentary rocks	23	2.91	0.20	829	[523, 1315]
F2	Neogene and Pleistocene formations	55	2.67	0.15	470	[329, 672]
F3	Holocene formations	29	2.38	0.22	237	[144, 392]

*The log-averaged V_{S30} value.

[†]The 68% confidence interval.

6.4.3.4 Predicting site effects in GMMs for Iceland

The inescapable conclusion from the previous sections is that on the basis of the Vs30 estimates for the main geological units in Iceland, empirical ground motion models (GMMs) should be established that can reliably predict the differences in site amplifications between the units. At present, however, this can only be done very approximately in terms of rock vs. stiff soil, using any of the multiple new Bayesian GMMs (Kowsari et al. 2020a) shown in Figure 6-43 for rock. These have been qualitatively associated with Vs30 values of 750 m750m/s and larger for rock and between 360m/s and 750m/s for stiff soil (Sigbjornsson et al., 2014). In particular, the predictions cannot be considered to be reliable for soft site conditions, primarily since no strong-motion stations are located on such soft materials.

In order to apply those GMMs using a binary site classification, the geological maps need to be presented accordingly. But as can be seen in Figure 6-37, the “stiff soil” predictions only apply to very limited coastal areas. The conclusion is, therefore, that the existing empirical GMMs

should be used to predict ground motion parameters on the generic Icelandic rock condition that is associated with V_{s30} values ranging anywhere from 750 m/s to 2000 m/s. This means that any shake-maps generated at present cannot reliably show variations in predicted ground motion levels due to either geological or topographical variations. Further research needs to be completed.

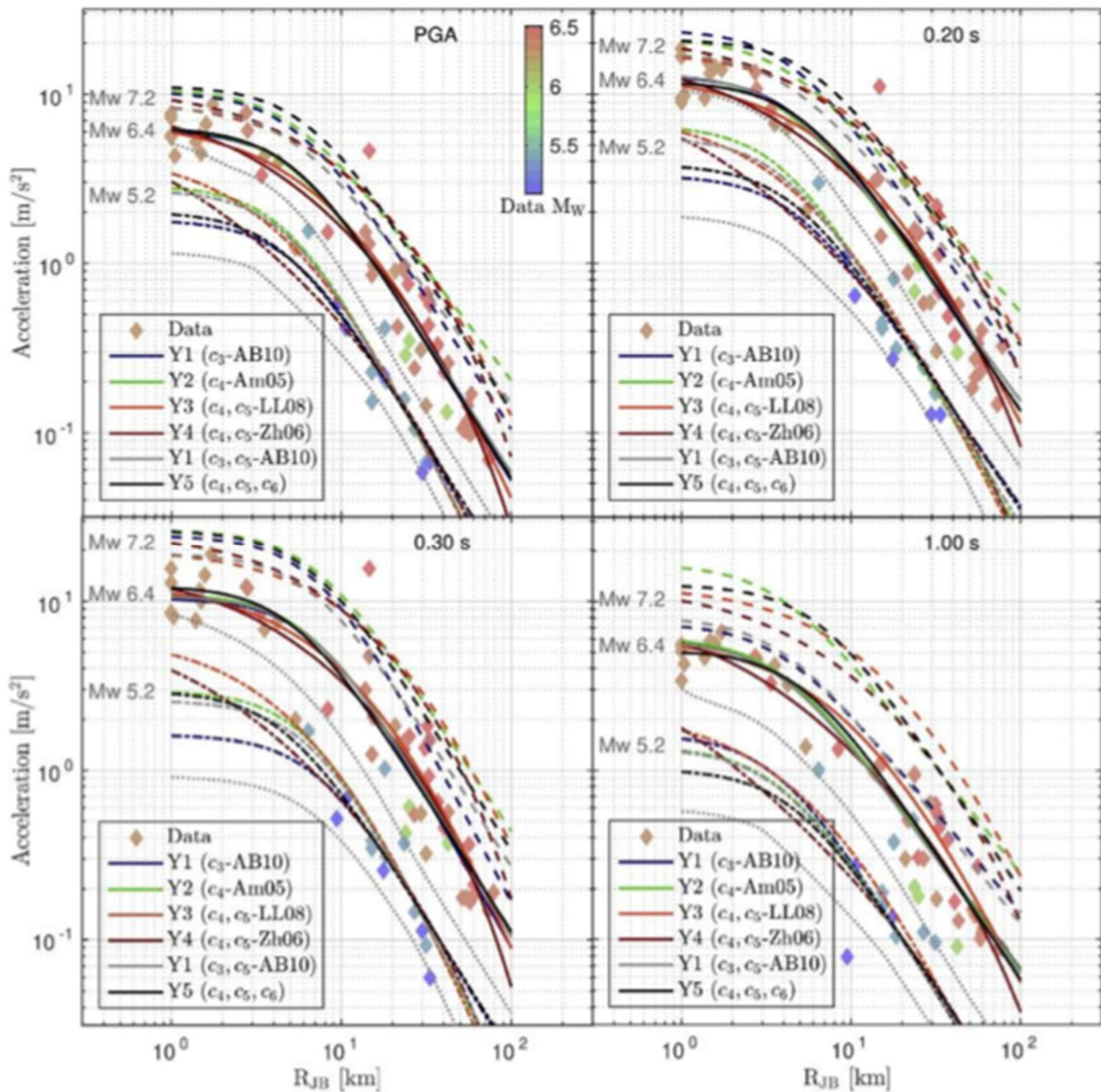


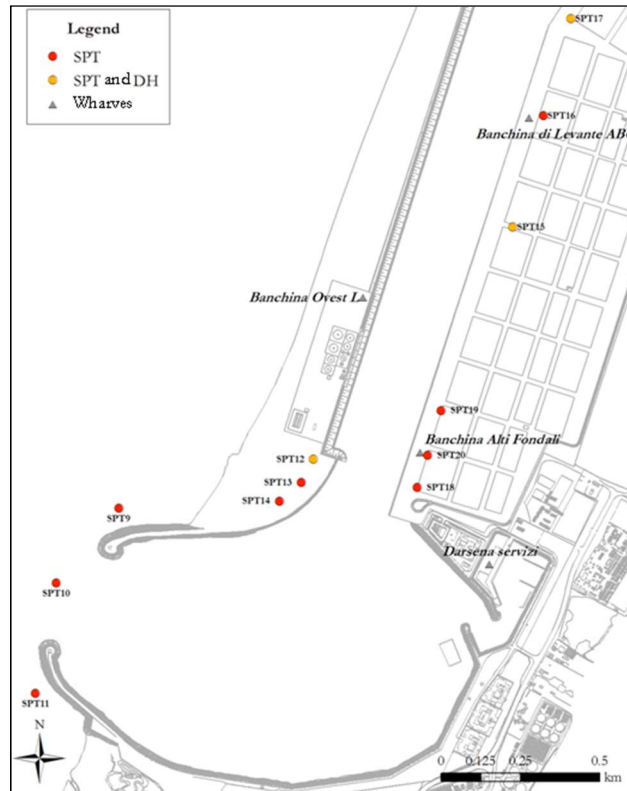
Figure 6-43 The six new Bayesian GMMs for Iceland predicting PGA and PSA vs. oscillator period (Kowsari et al. 2020a).

6.4.4 TB-5: Gioia Tauro port, Italy

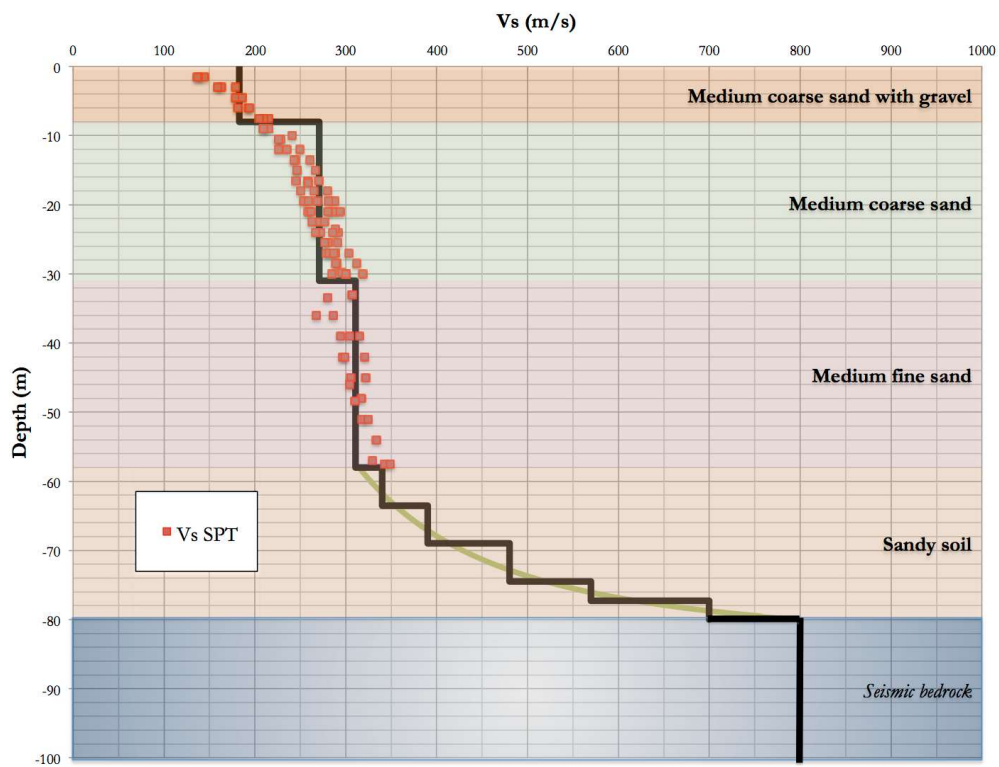
With reference to TB5, ground response analyses have been carried out in the port area of Gioia Tauro. The starting point is represented by a seismo-geotechnical characterization of the Gioia Tauro port area, based on data from in-situ geotechnical and geophysical investigation campaigns provided by the Port Authority and on geological information retrieved from the literature. Proper interpretation of the acquired data led to the definition of two suitable soil geotechnical models, one referred to as northern part of the Gioia Tauro port area and one as southern part, to be used for ground response analyses. Fully stochastic site response analyses were carried out to account for the uncertainty of each soil model parameter as well as the variability of seismic input. The main outcomes of this study are presented hereinafter. For further details, the interested reader can refer to [Bozzoni et al. \(2014\)](#). Within the TURNkey project, starting from the subsoil modelling of the port area, non-linear ground response analysis has been carried out in the framework of Task 3.4.

In order to derive a detailed and complete description of the subsoil conditions at the seaport, geological information was analysed in conjunction with geotechnical and geophysical data. The seismic geotechnical characterization of the soil deposits was based on the findings of various investigation campaigns, performed from 1975 to 2012. 45 boreholes were drilled to different depths, ranging from 6.4 m to 60 m (from the ground level). Various kinds of in situ tests were executed: Standard Penetration Tests (SPT), Cone Penetration Tests (CPT), Dilatometer Marchetti Tests (DMT), Down-Hole tests (DH), Seismic Tomography (TS) and Multi-Channel Analysis of Surface Waves (MASW) measurements. Data on grain size distribution of samples, taken from soil deposits within the harbour area, and their main physical properties (e.g. unit weight of soil particles, dry unit weight) were obtained from laboratory tests. Proper interpretation of the acquired data on soil deposits led to the definition of two suitable geotechnical models, one referred to as northern part of the Gioia Tauro port area and one as southern part, to be used for ground response analyses.

The soil model for the northern part of the Gioia Tauro port is well-characterized from a seismic geotechnical point of view, as shown in Figure 6-44a. As a first approximation, this area was modelled as a sequence plane and parallel layers of constant thickness corresponding to a one-dimensional (1D) soil stratigraphy. Figure 6-44b shows the mean shear-wave velocity (V_s) profile, obtained starting from the direct measurements of V_s (from DH, MASW and TS), and the V_s values computed from the penetration resistances (from SPT and CPT) by using empirical correlation relations available in literature. It was assumed that the seismic bedrock is located at the mean depth of 80 m and has a V_s of 800 m/s. Available data do not allow the definition of the V_s profile for soil deposits deeper than 40 m, thus a hyperbolic law according to Gibson's model was adopted, as shown in Figure 6-44b. A similar approach has been adopted to construct the soil model for the southern part of the Gioia Tauro port, even if only a few field tests are available in this area (

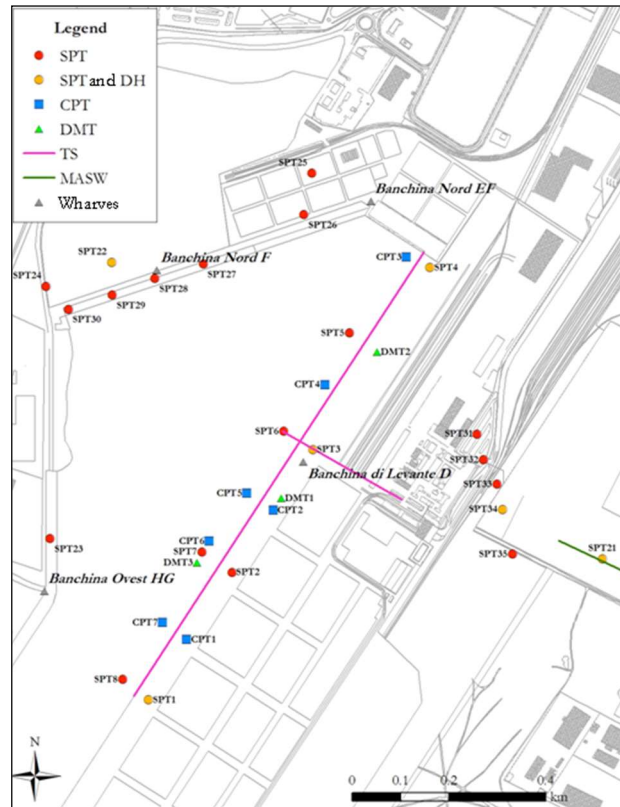


(a)

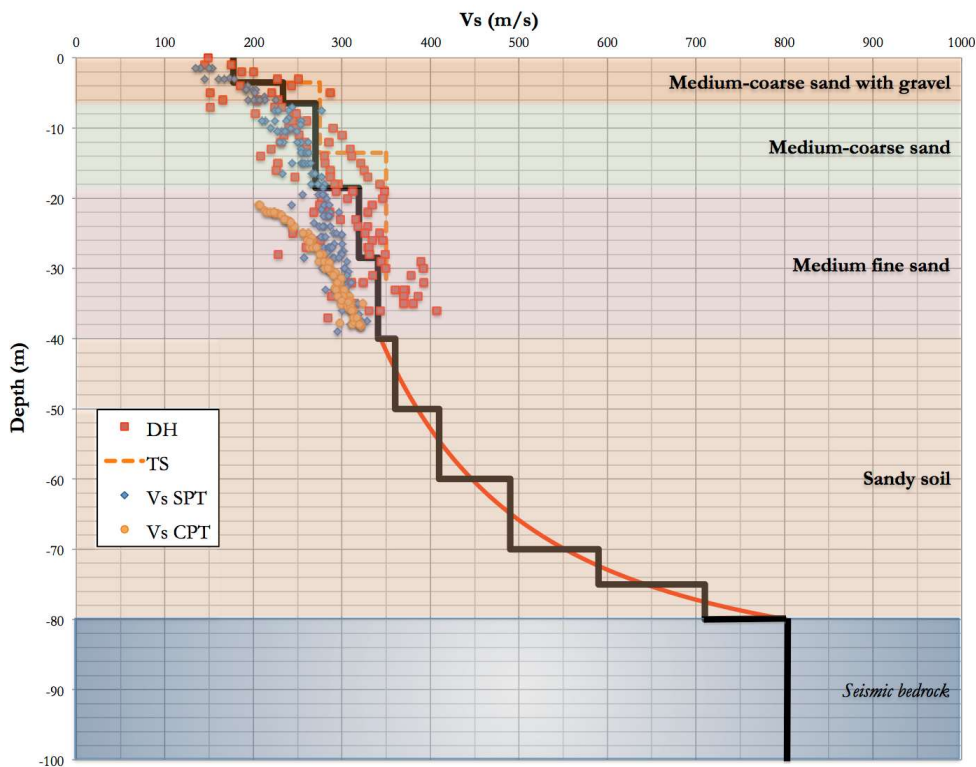


(b)

Figure 6-4545).

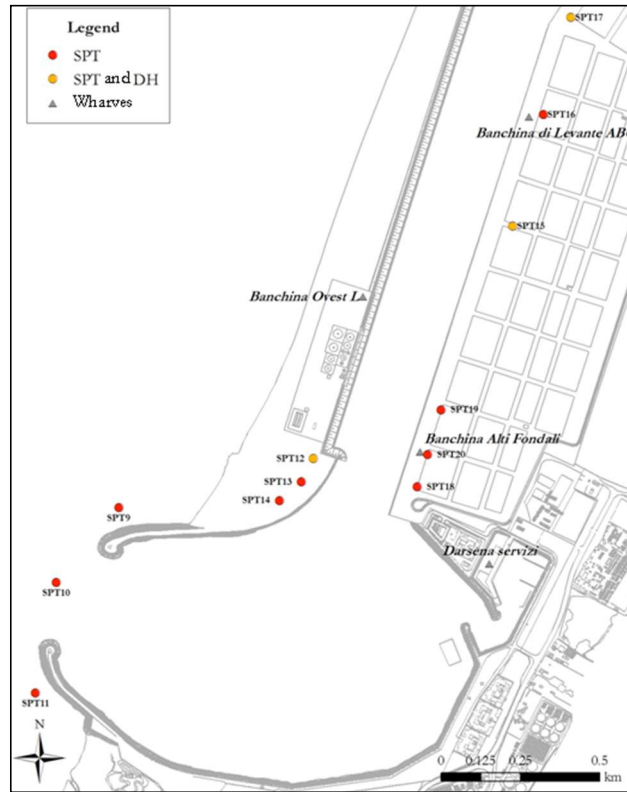


(a)

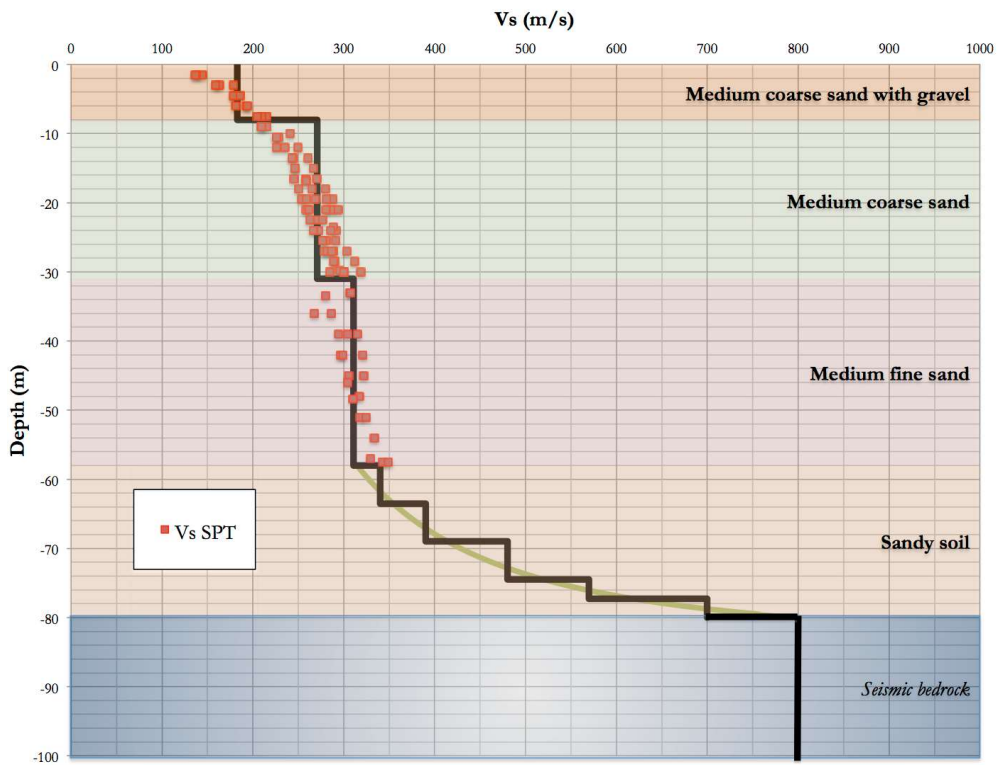


(b)

Figure 6-44: Seismic geotechnical soil modelling for the Northern part of Gioia Tauro port (Bozzoni et al., 2014): a) available data; b) 1D soil stratigraphy.



(a)



(b)

Figure 6-45: Seismic geotechnical soil modelling for the Southern part of Gioia Tauro port (Bozzoni et al., 2014): a) available data; b) 1D soil stratigraphy.

Further information has been acquired within the TURNkey project for better characterizing the position of the seismic bedrock. Indeed, the previous assumptions have been confirmed.

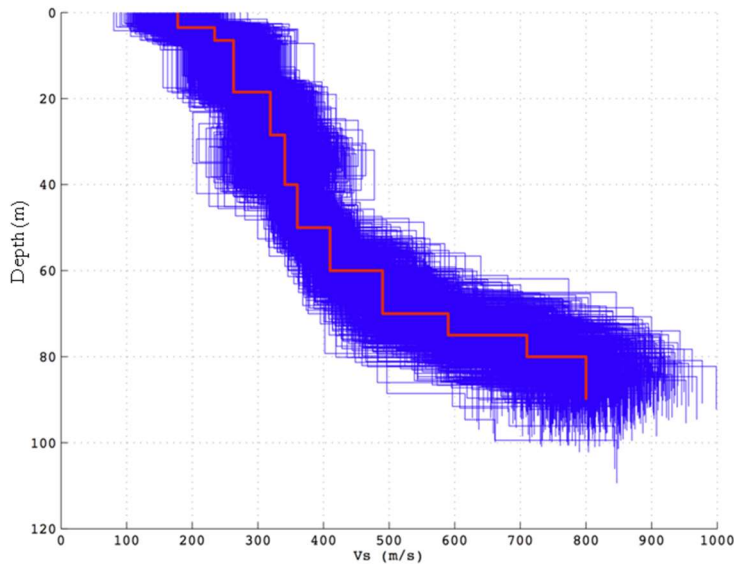
At the Gioia Tauro port, fully stochastic ground response analyses were carried out by [Bozzoni et al. \(2014\)](#) using a code implemented at EUCENTRE, called STOCH-SHAKE (e.g. [Bozzoni et al., 2011](#); [Rota et al., 2011](#); [Bozzoni et al., 2020](#), etc.), which allows uncertainties associated with the geotechnical properties of soil deposits as well as with the seismic input to be accounted for using Monte Carlo simulations.

Table 6-26: Mean values of geotechnical parameters and corresponding uncertainties assumed for the stratigraphic profile of the subsoil for the Northern area of the Gioia Tauro port.

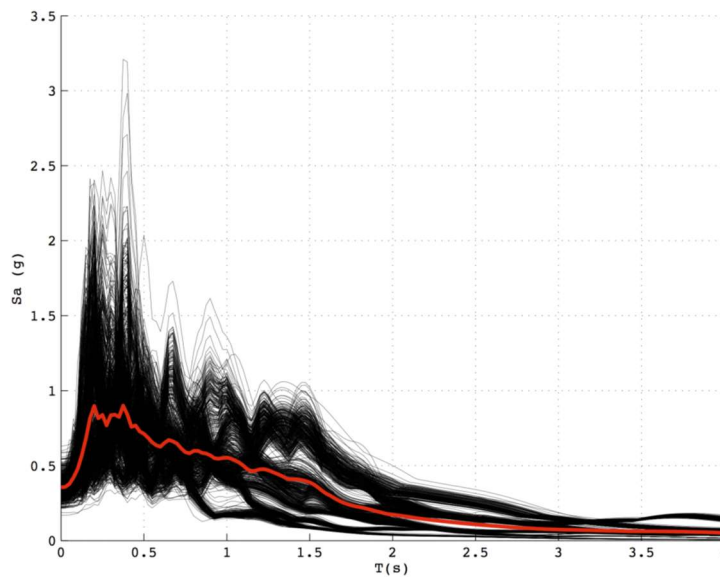
Layer	Soil type	Thickness (m)	CoV (%)	V _s (%)	CoV (%)	γ (%)	CoV (%)
1	medium-coarse sand with gravel	3.5	40%	178	35%	19	6%
2	medium-coarse sand with gravel	3	40%	234	35%	19	6%
3	medium-coarse sand	12	30%	270	25%	20	6%
4	medium-fine sand	10	30%	319	20%	20	6%
5	medium-fine sand	11.5	30%	341	25%	20	6%
6	sandy soil	10	40%	360	10%	20	6%
7	sandy soil	10	40%	410	10%	20	6%
8	sandy soil	10	40%	490	15%	20	6%
9	sandy soil	5	40%	590	10%	20	6%
10	sandy soil	5	40%	710	15%	20	6%
-	<i>seismic bedrock</i>	-	-	800	15%	21	6%

Table 6-26 summarizes, for example, the mean values adopted for the geotechnical parameters used in the stochastic ground response analyses performed for the Northern part of the port and the corresponding uncertainties, expressed in terms of mean value and coefficient of variation (CoV), which represents the rate of standard deviation σ .

The results obtained from ground response analyses are represented in terms of free-surface horizontal acceleration time histories and the corresponding elastic acceleration response spectra. The variability of the soil model used in stochastic analyses for the northern part of Gioia Tauro port is shown in Figure 6-46a, illustrating 1000 shear-wave velocity profiles, corresponding to random realizations of V_s extracted from the statistical distributions of V_s and thicknesses of different layers in the Monte Carlo simulations. The variability of model parameters obviously determines a variability in the results. Figure 6-46b shows the elastic acceleration response spectra computed for each of the 1000 simulations of input parameters overlapped to a mean spectrum for the 475-year return period.



(a)



(b)

Figure 6-46: Stochastic ground response analysis for the Northern part of Gioia Tauro port (475-years return period): a) 1000 random V_s profiles generated by Bozzoni et al. (2014); the red line represents the mean profile; b) acceleration response spectra computed out of 1000 numerical simulations (black lines) and mean spectrum (red line).

Table 6-27: Amplified peak ground acceleration (PGA_{amp}) predicted from stochastic ground response analysis for the Northern and the Southern part of Gioia Tauro harbour and PGA on rock outcropping provided by the current Italian building code.

Return period (years)	PGA (g) on rock outcropping	PGA _{amp} (g) computed from stochastic analysis			
		Northern part of Gioia Tauro harbour		Southern part of Gioia Tauro harbour	
		μ	$\mu+\sigma$	μ	$\mu+\sigma$
100	0.127	0.208	0.241	0.186	0.217
475	0.261	0.355	0.420	0.299	0.359

950	0.348	0.430	0.540	0.365	0.459
-----	-------	-------	-------	-------	-------

Predictions from stochastic ground response analyses, in terms of mean PGA (μ) and its scatter computed as plus/minus one standard deviation (σ), are shown in Table 6-27 for each return period under consideration (i.e. 100, 475 and 950 years) and for the two port areas under investigation. It is worth noting that the litho-stratigraphic amplification turns out to be more significant in the northern part of the port of Gioia Tauro.

The dynamic response of soils is nonlinear even at low to moderate deformation levels. Therefore, [Bozzoni et al. \(2014\)](#) took these manifestations of soil behaviour into account using a linear-equivalent, viscoelastic constitutive model for Gioia Tauro soil deposits. Indeed, standard data from the literature was adopted for the shear modulus and damping ratio degradation curves. This approach of adopting one-constituent, equivalent-linear viscoelastic rheology for the soil is inadequate to correctly reproduce the seismic response of geomaterials exhibiting strong nonlinearities in the hydromechanical behaviour. An example is constituted by liquefiable soils, which require ground response analyses to be more correctly conducted using effective stress-based soil constitutive models.

Recently, non-linear 1D ground response analysis has been performed for the subsurface of the port of Gioia Tauro starting from the previously illustrated subsoil modelling. Figure 6-47 shows, as an example, the comparison among acceleration response spectra (with associated uncertainties) computed for the northern part of the port and the return period of 100 years. It is worth remarking that the findings of this study confirm that results from linear-equivalent analysis are, as first approximation, appropriate.

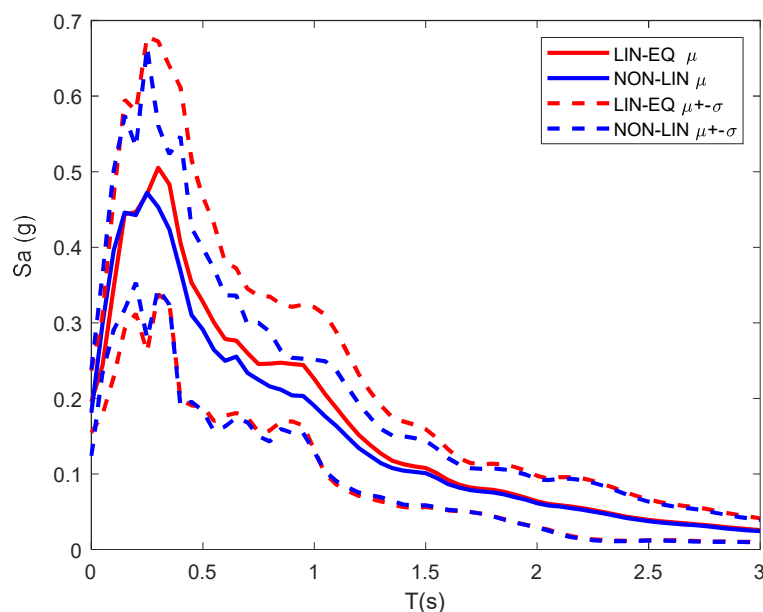


Figure 6-47: Comparison among acceleration response spectra with associated uncertainties ($\mu \pm \sigma$), computed by using linear-equivalent (red lines) and non-linear (blue lines) 1D ground response analysis for the Northern part of the port and the return period of 100 years.

6.4.5 TB6: Groningen area, Netherlands

6.4.5.1 Vs30 for Groningen

The Groningen region is very well characterized by many boreholes, Seismic Cone Penetration Tests (SCPT) and normal Cone Penetration Tests (CPT). This enabled the development of a detailed geological model (Kruiver et al, 2017a) that is one of the inputs to the seismic hazard analysis (Bommer et al., 2017).

The subsurface in Groningen consists of unconsolidated sediments of the North Sea Supergroup up to approximately 800 m depth. Focusing on the top tens of meters, the sediments are of Holocene and Pleistocene age. A wedge of Holocene clays and peats with a maximum of 20 m thins out to the south where Pleistocene sands are present at the surface. Figure 6-48 shows a geological cross-section through the detailed digital geological model GeoTOP for the top 50 m.

A top view of lithoclasses and the position of the cross section is shown in Figure 6-49. The region was divided into approximately 160 zones of similar shallow geology (Kruiver et al 2017a). These zones were used to aggregate Vs30 and amplification values (section 6.4.5.2).

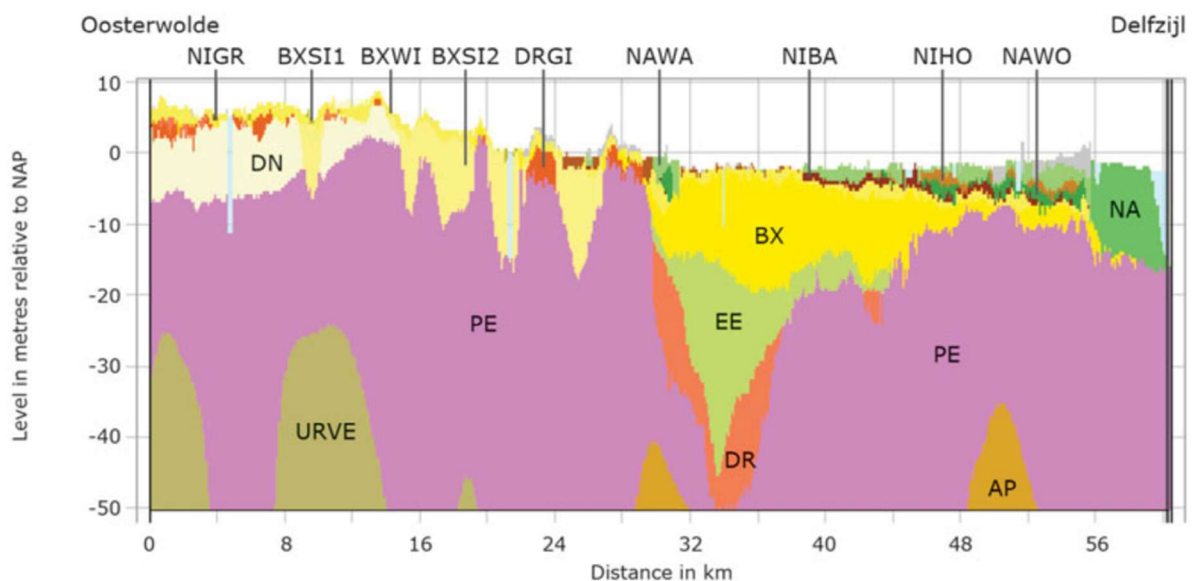


Figure 6-48: Geological cross section from south (left) to north (right). Different colours and codes denote different geological formations. The wedge of Holocene deposits consists of geological formations coded by NA (Naaldwijk), NAWO (Naaldwijk, Wormer Member), NAWA (Naaldwijk, Walcheren member), NIHO (Nieuwkoop, Holland Peat) and NIBA (Nieuwkoop, Basal Peat) (from Kruiver et al., 2017a). The position of the cross-section is shown in Figure 6-49.

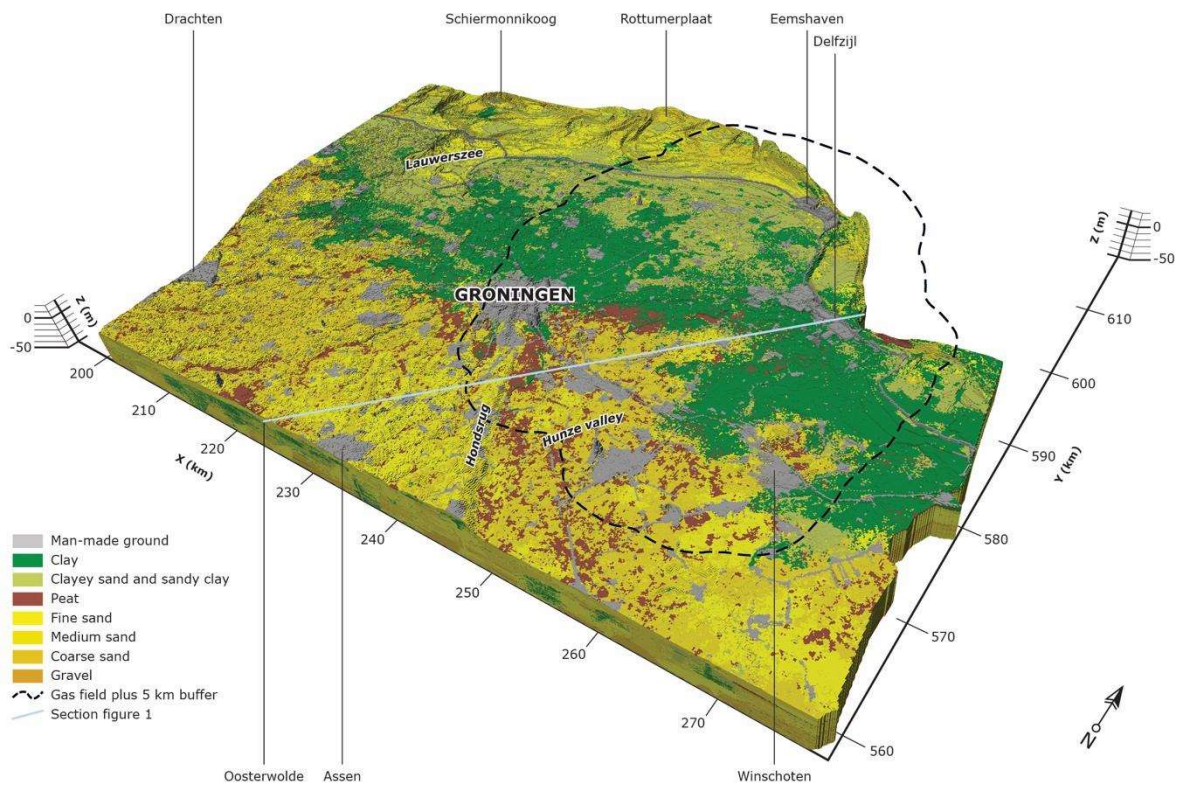


Figure 6-49: GeoTOP lithoclasses, showing a dominant outcropping of clay in the northern part and sand in the southern part (from [Kruiver et al. 2017a](#)). The dashed line shows the outline of the Groningen gas field with a 5 km buffer zone added.

A detailed shear-wave velocity (V_s) model has been derived using the abundant Seismic Cone Penetration Test dataset and the detailed geological model GeoTOP. The integrated V_s model for the region is described in [Kruiver et al \(2017b\)](#). The shallow part, which is relevant for V_{s30} , is summarized here. All V_s observations from a set of 88 SCPTs to a depth of 30 m on average were classified in terms of lithostratigraphy and lithoclass. Next, all data for one combination of lithostratigraphy and lithoclass, referred to as soil type, were converted to $\ln(V_s)$ and plotted versus confining stress. Linear regression resulted in an empirical relation between confining stress and V_s for a particular soil type. An example is shown for clays of the Peelo Formation in **Erreur ! Source du renvoi introuvable.** For the soil types that were present in the SCPT dataset the empirical relations were derived. For those present in the region, but not represented in the SCPT dataset, an equivalent soil type was defined. The confidence intervals allowed a probabilistic approach for deriving V_s profiles. For each 100 m x 100 m grid cell (resolution of the GeoTOP model), a mean V_s profile was calculated. Based on a correlation of 0.5 between successive layers of varying soil type, V_s profiles were sampled. Examples of mean and sampled V_s profiles are shown in Figure 6-51.

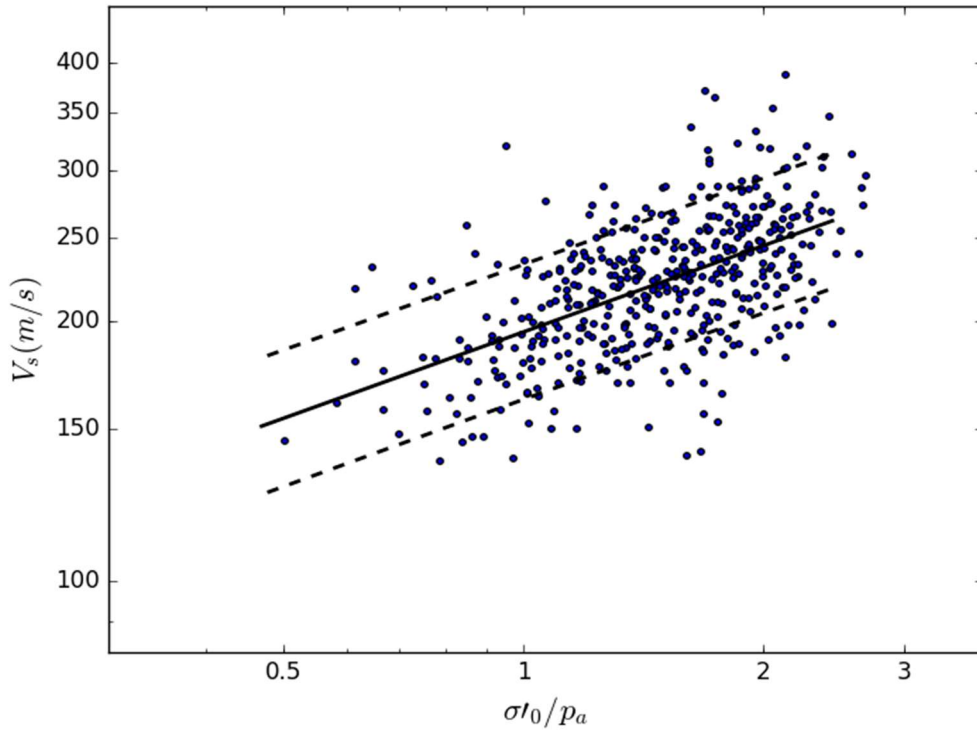


Figure 6-50: Example of V_S observations in the SCPT data set, for clays from the Peelo Formation. The observations of V_S are plotted versus the confining stress σ'_0 normalised by atmospheric pressure p_a . The solid line describes a regression, while dotted lines indicate 95% confidence intervals (from [Kruiver et al., 2017b](#)).

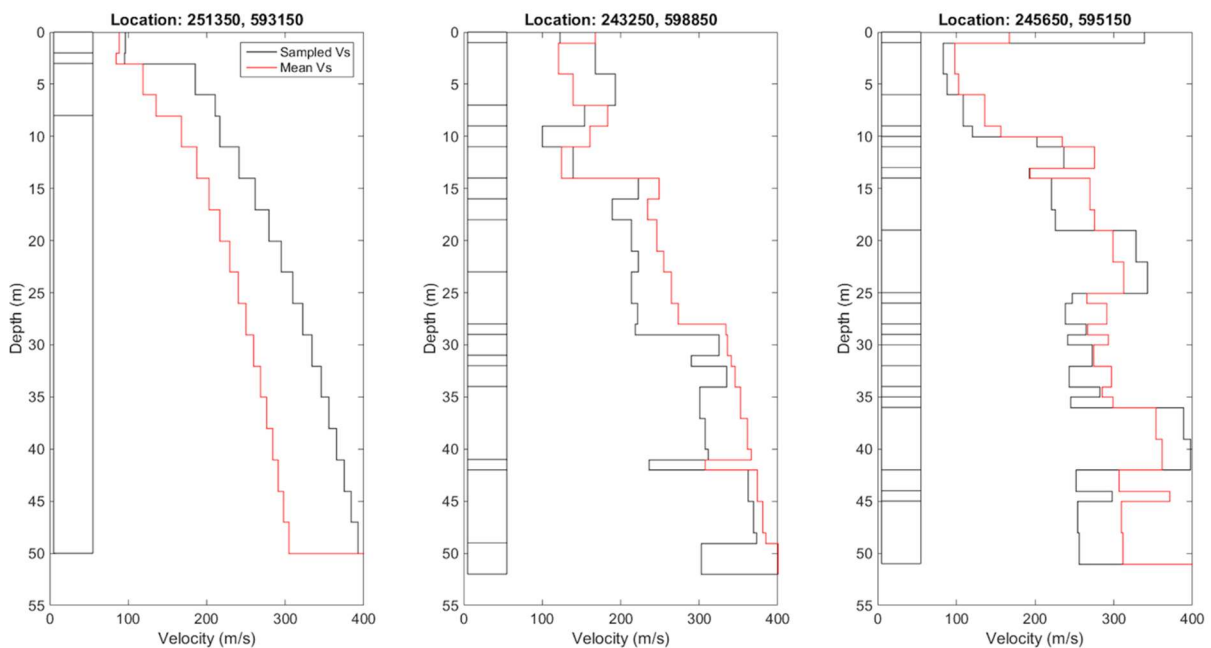


Figure 6-51: Examples of mean V_S profiles (red lines, using the mean regression parameters) and sampled V_S profiles (black lines, using random samples of V_S from the confidence interval and a correlation of 0.5 between successive

layers of varying soil type). The column on the left of each panel shows layers of constant soil type (from [Kruiver et al., 2017b](#)).

In order to calculate V_{s30} at each location, the soil profile was sampled 100 times. V_s profiles were converted to V_{s30} and the average V_{s30} was calculated for each geological zone of the region. The resulting average V_{s30} map and standard deviation map are shown in Figure 6-52 using the original classification in 15 m/s bins. V_{s30} values are very low, varying between 158 and 272 m/s for the geological zones and between 120 and 310 m/s for individual grid cells. Individual layers may possess V_s values significantly lower than 100 m/s.

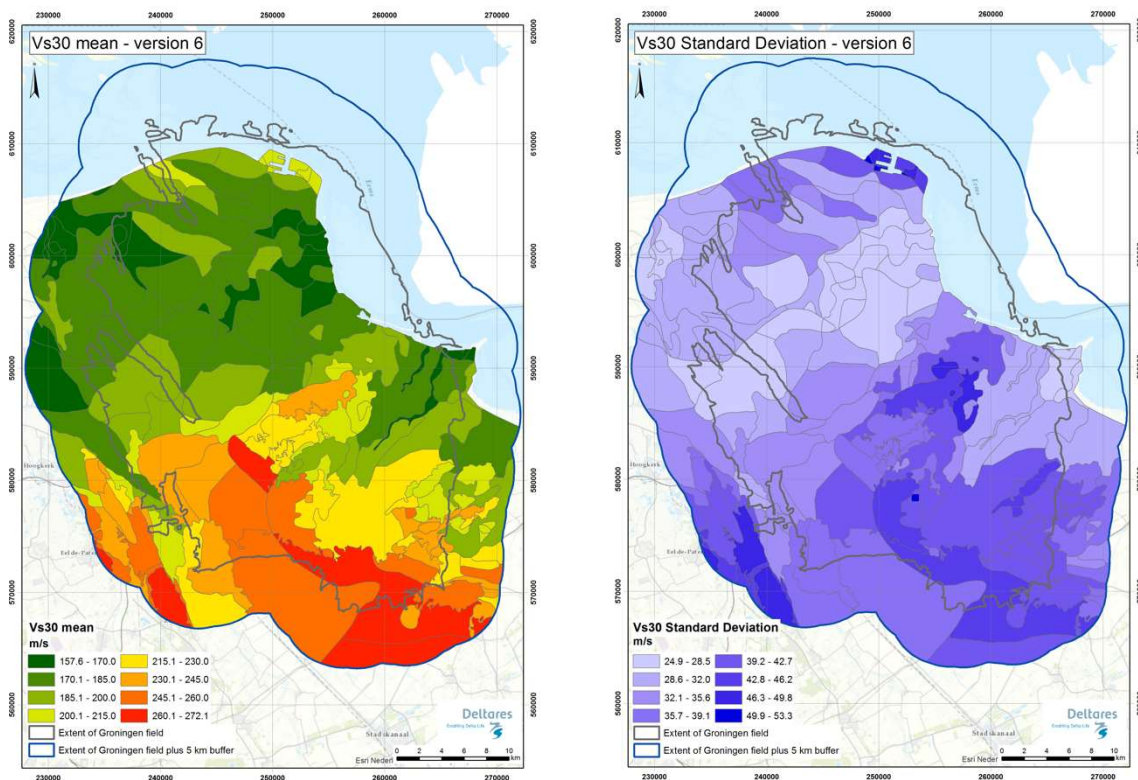


Figure 6-52: Mean (left) and standard deviation (right) of V_{s30} for the Groningen region for the most recent Ground Motion Model version 6 (after [Kruiver et al., 2017b](#)).

Figure 6-53 shows the average V_{s30} using the classification bins from Section 6.3. The Groningen V_{s30} data are shown with the geology-based classification of [Vilanova et al. \(2018\)](#) on the left panel with a mean V_{s30} of 470 m/s for Pleistocene sediments of class F2 and a mean V_{s30} of 237 m/s for the Holocene sediments of class F3. The transition is taken at the log-average between the means of F2 and F3, being 335 m/s. Figure 6-53 (left) shows that the entire region would classify as Holocene based on V_{s30} values. The southern part of the region, however, consists of Pleistocene sediments, but with a lower V_{s30} than the F2 class. The right panel of Figure 6-53 shows the Groningen V_{s30} data using the V_{s30} classes of Table 6-15. Although the region is topographically flat, there are three of the DEM-based classes present. This is an artefact of the coarse DEM grid, which results in the assignment of bathymetric slopes to the onshore area.

Comparing the maps of Figure 6-53 to Figure 6-23 and Figure 6-24 indicates that there is much more detail in the Groningen-specific map relative to the map produced by general rules applied in Section 6.3. Moreover, the Groningen-specific map is based on Vs30 values that are closer to the actual values to be found in the region.

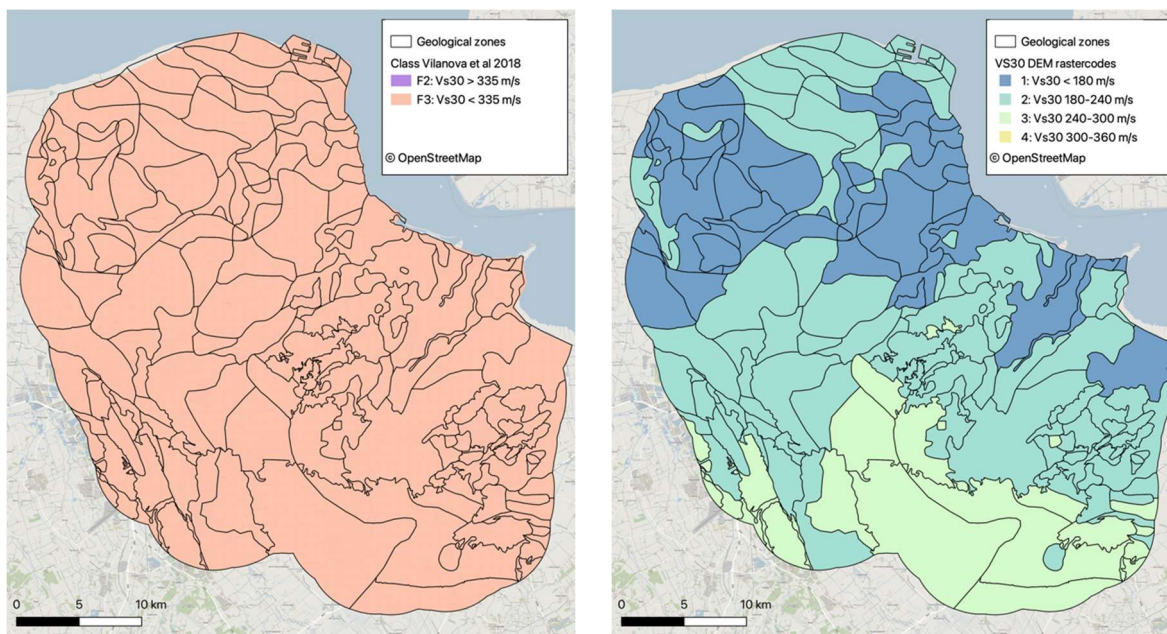


Figure 6-53: Mean Vs30 map of Groningen using the symbology of Section 6.3. Left: classes F2 and F3 from Vilanova et al. (2018). Right: classes using Table 6-15 based on DEM.

6.4.5.2 Amplification model for Groningen

The Ground Motion Model of the Groningen region is based on an amplification model using site response calculations (Bommer et al., 2017, Rodriguez-Marek et al., 2017, Bommer et al., 2019b). No proxies such as Vs30 are used to estimate amplification.

The site response calculations were carried out on a 100 m x 100 m grid, covering ~ 140,000 soil profiles. The 1D equivalent linear site response program STRATA was used for the calculations (Kottke and Rathje, 2008). The reference baserock horizon is situated at the base of the North Sea Supergroup at on average 800 m depth. This level was chosen to include the entire column of unconsolidated sediments. The transition between the North Sea Supergroup and the underlying Chalk Group represents a sharp contrast in Vs from ~ 600 to 1400 m/s, making it a suitable reference level.

Site response calculations require three types of input:

1. Soil profiles with properties such as Vs.
2. Modulus Reduction and Damping (MRD) curves, defining the dynamic behaviour of the soil.
3. Input motions at the reference baserock horizon.

The stratigraphy and lithology were based on a combination of GeoTOP (described in section 6.4.5.1) and scenarios of likely soil profiles (Kruiver et al., 2017a). The construction of V_s profiles is described in Kruiver et al. (2017b).

These profiles are a combination of the SCPT model with GeoTOP (described in section 6.4.5.1), inversion of surface waves from legacy seismic data and the V_p -to- V_s conversion from the PreStack Depth Migration model.

Parameters for the Modulus Reduction and Damping (MRD) curves were estimated from local literature, laboratory tests on local samples and expert judgment (Kruiver et al., 2018). MRD curves for sandy material were based on Menq (2003), for clayey material on Darendeli (2001) and for peat, Groningen-specific curves were derived from laboratory tests (Zwanenburg et al., 2020).

The input motions at the reference baserock horizon consisted of Frequency Amplitude Spectra (FAS), one type of input to STRATA. The input motions were derived from the inversion of recorded ground motions and EXSIM simulations for a larger range of magnitudes (1.5 to 7.5) and an epicentral distance of 3 to 60 km. The motions were sorted into 10 groups of increasing Peak Ground Acceleration (PGA). One motion from each group was used to calculate amplification factors (AF) for each of the soil columns, resulting in 1,400,000 site response calculations.

Spectral AF functions were fitted using linear regression and these functions include estimates of uncertainty. The parameters describing the AF functions for the latest Ground Motion Model (version 6) can be found in Bommer et al. (2019b). In order to calculate the hazard at the surface, the hazard at the reference bedrock horizon is combined probabilistically with the AFs.

The AFs are shown for several key structural periods in Figure 6-54. The amplification model is a combination of the input motion at reference depth (~ 800 m in this case), the damping model (significantly more damping than laboratory-based Modulus Reduction and Damping curves) and non-linear soil behaviour. The AF values shown on the map are calculated for a specific choice of magnitude and distance, e.g. in Rodriguez-Marek et al. (2017), with other choices for levels of input motions and damping showed different values for the AF. Generally, the patterns in AF show good correspondence to the geology of the region.

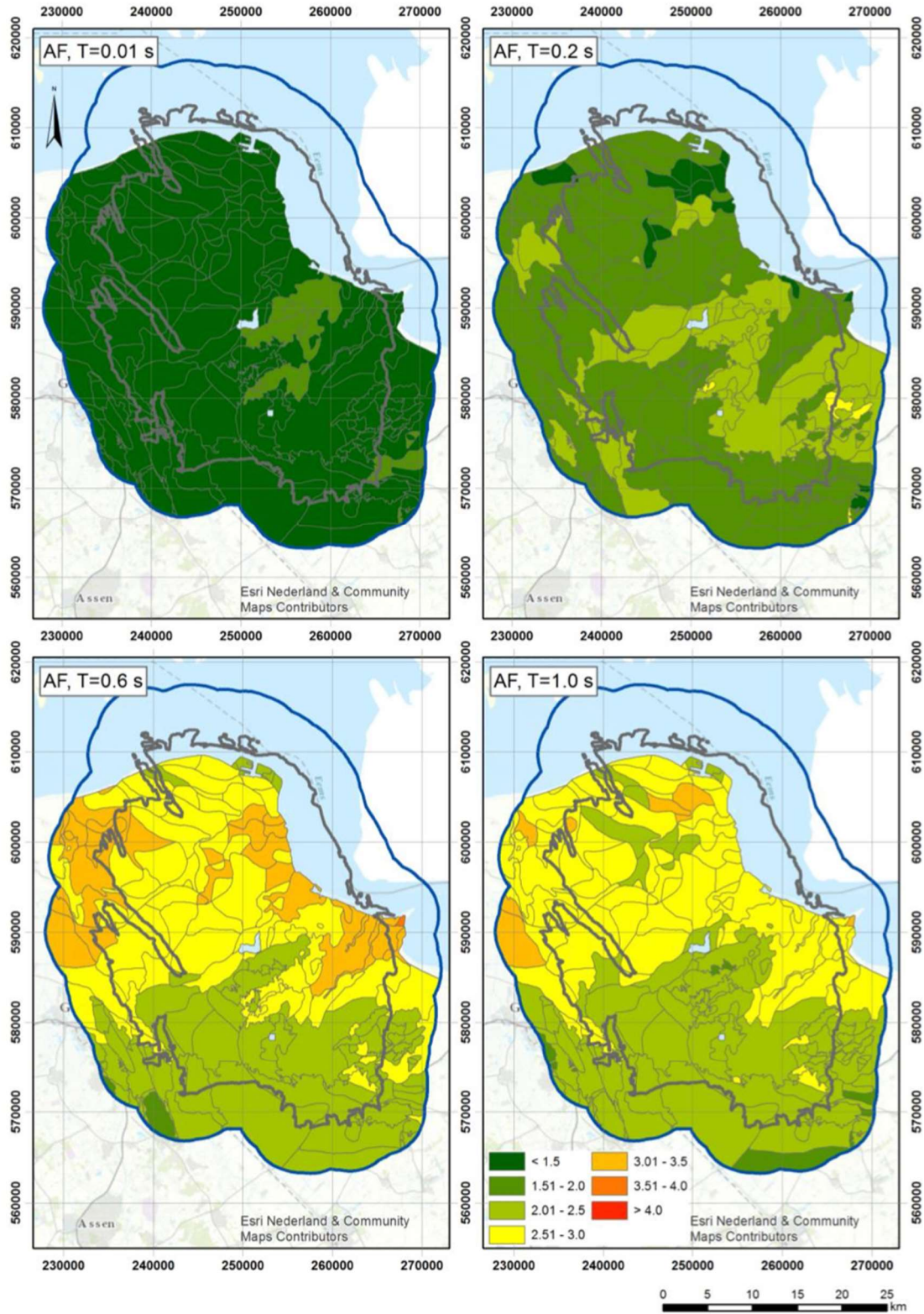


Figure 6-54: Weak motion AFs for the zones in the Groningen region. The AFs are shown for an M 4.5, R 5 km scenario and selected periods (from Bommer et al., 2019b).

6.4.5.3 Testing site-amplification proxies

In this section, we test different proxies for site amplification that have an average velocity as an intermediate step. For Groningen, both V_{s30} and horizontal-to-vertical spectral ratios are available (van Ginkel et al., 2019). At the surface, the up- and down-going waves interfere constructively to double the amplitude in addition. This free-surface effect is left out of the AF.

In TB6, an extensive borehole network (the G-network, Dost et al., 2017) is installed with sensors at 0, 50, 100, 150 and 200 m depth. Moreover, a large number of local events with a maximum magnitude of $M=3.4$ have been detected. This has provided direct recordings of AFs between various depth levels and the Earth's surface. For each of the proxies, an empirical relation is fitted between the measured AF and their proxy. A comparison of the coefficient of determination yields insights into which proxy is the most effective in this soft-sedimentary setting.

Measuring amplification

For measuring amplification, we select all local events within 15 km distance and with local magnitudes ranging from 1.8 to 3.4 for each station. The earthquake responses are bandpass-filtered between 1 and 10 Hz. In this band, almost all the S-wave energy resides. Subsequently, the largest absolute amplitude is taken of the transverse component, both at 200 m and 0 m depth. An example of the resulting AFs for one station is shown in Figure 6-55. The left panel shows that all observed motions can be fitted well by a straight line, indicating that the amplification is still in the linear regime.

The ratio between the amplitudes, with the free-surface effect removed, yields the local amplification, with a reference horizon placed at 200 m. The interface between consolidated and unconsolidated sediments is at about 800 m depth. Because of this, within the GMM (section 6.4.5.2), the reference horizon has been chosen at 800 m depth. Still, the amplifications between the two methods can be more or less compared, because a significant part of the soil amplification occurs in the top ~ 100 m.

Site calculations using STRATA (Section 6.4.5.2) have shown that notable PGA amplification starts at varying depths, between 10 and 70 m below the surface depending on the soil column.

Typically, it is the direct S-wave that yields the largest amplitude at both depth levels. Surface waves were not yet observed for the Groningen induced events. For each G-network station (G01-G70), records of at least 10 events are available. Possible outliers are removed by rejecting all data points that are outside of the 68% confidence zone. Figure 6-55 (right) shows the remaining AF distribution after this rejection stage. In the following, only the mean AF from this distribution is used.

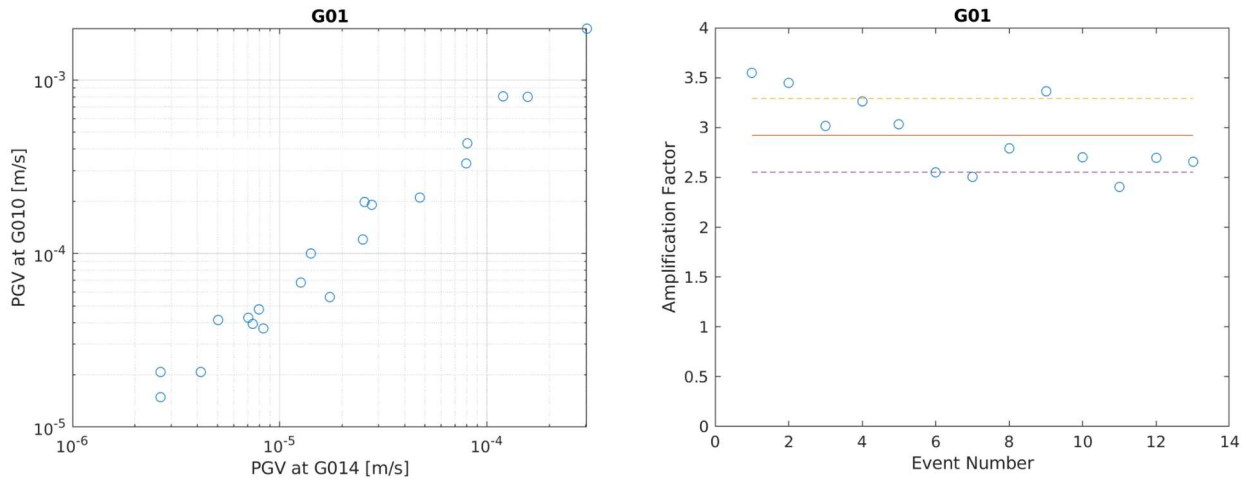


Figure 6-55: (Left) cross-plot of the largest Peak Ground Velocity (PGV) being observed at 200 m depth (x-axis) and at 0 m depth (y-axis), for borehole station G01. (Right) a distribution of extracted amplification factors (circles), their mean (solid line) and 68% confidence zone delimited with the dashed lines.

Fitting amplification

If the subsurface consists of a smooth impedance gradient from 200 to 0 m depth, the resulting gradient amplification can be written as

$$AF_{grad} = \sqrt{\rho_{200}V_{200} / \rho_0V_0} \quad (6-11)$$

where ρ_{200} and V_{200} are the density and velocity at 200 m depth and ρ_0 and V_0 are the values near the Earth's surface.

In the actual subsurface, the amplification is more complex due to layering, 3D effects and anelastic losses. For fitting amplification to an amplification proxy (often V_{s30}), we use a functional form similar to equation (6-11):

$$AF_{fit} = x_0 + \sqrt{x_1 / V_{s30}} \quad (6-12)$$

where x_0 and x_1 are the fitting parameters. The more complex amplification effects are lumped into x_0 .

The above model yields an estimate of AF_{fit} with the V_{s30} proxy. To determine how well the measured AF is approximated by the model, we determine the coefficient of determination R^2 :

$$R^2 = 1 - SS_{res} / SS_{tot} \quad (6-13)$$

in which SS_{res} is the residual sum of squares over n data points:

$$SS_{res} = \sum_{i=1}^n AF_i - AF_{fit,i} \quad (6-14)$$

which is normalized by the total sum of squares:

$$SS_{tot} = \sum_{i=1}^n AF_i - \overline{AF} \quad (6-15)$$

where the last term is the mean over the measured AFs. If $R^2=0$, the mean amplification provides a prediction of the local amplification that is as good as the model. If $R^2=1$, all amplification values are perfectly predicted by the model.

Vilanova Vs30

The first proxy we consider is based on the approach taken in [Vilanova et al. \(2018\)](#). As described in section 6.3, an estimate of Vs30 is obtained from a European-wide geological map. The different sites are divided into 3 soil classes: F1, igneous, metamorphic, and old sedimentary rocks (mean Vs30 = 829 m/s); F2, Neogene and Pleistocene formations (mean Vs30 = 470 m/s); F3, Holocene formations (mean Vs30 = 237 m/s). F2 and F3 exist in the Groningen region (Figure 6-23). The lower value of 237 m/s is attributed to only 3 borehole stations. All other available stations (58) obtain a Vs30 estimate of 470 m/s. Figure 6-56 shows the fitted relation between Vilanova Vs30 and amplification. The Vilanova Vs30 proxy has no predictive power for AF ($R^2=0$).

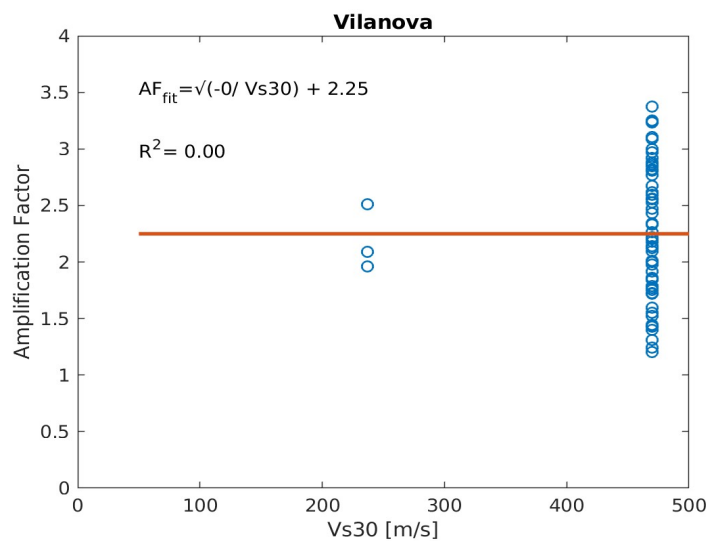


Figure 6-56: A plot of Vilanova Vs30 versus measured AF data points at 61 stations of the G-network and the fitted function through the data points using Equation (6-2).

DEM Vs30

The second proxy we consider is a Vs30 estimate that is derived from the digital elevation model (DEM). From that model the topographic gradient is taken and mapped to a Vs30 value ([Wald and Allen, 2007](#)). More details are described in section 6.3.

The Vs30 values are gridded to so-called raster codes ranging from 1 to 8. Figure 6-24 shows these raster codes for Groningen and Table 6-15 lists the corresponding Vs30 ranges. Most of the Groningen is topographically flat. Exceptions are local dwelling mounds and a glacial feature, the Hondrug, at the southwestern edge of the region. In addition, the shallow waterbodies in the area, the Wadden Sea and the Eems-Dollar, show a modest bathymetric

slope. Due to the coarse DEM resolution, some of this bathymetric slope is assigned to the onshore area.

The G-network stations are located in raster codes 1 to 4. For raster code 1, a mean V_{s30} of 150 m/s is taken. Raster codes 2-4 correspond to mean V_{s30} values of 210, 270 and 330 m/s, respectively (Table 6-15). We take these mean V_{s30} values at all available borehole stations (61) and use equation (6-12) to fit V_{s30} with the measured AF. The result is shown in Figure 6-57. With $R^2=0.03$, the DEM proxy performs only marginally better than the Vilanova proxy.

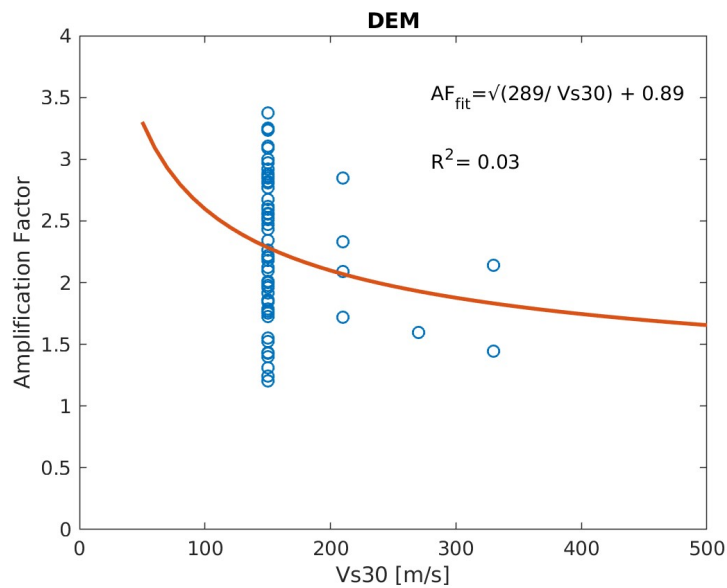


Figure 6-57: A plot of DEM V_{s30} versus measured AF data points at 61 stations of the G-network and the fitted function through the data points using Equation (6-12).

GeoTOP V_{s30}

In section 6.4.5.1, the approach for deriving a V_{s30} model from a local digital geological model (called GeoTOP) has been described. At the G-stations, the lowest (mean) V_{s30} is 166 m/s (at station G19) and the highest value is 283 m/s (at G59). In Figure 6-47, these GeoTOP V_{s30} values are plotted against the measured AFs and an empirical function is fitted. Using this proxy based on detailed local information, a better predictive power is achieved ($R^2=0.14$) than with the previous two pan-European models. The predictive power, however, is still low.

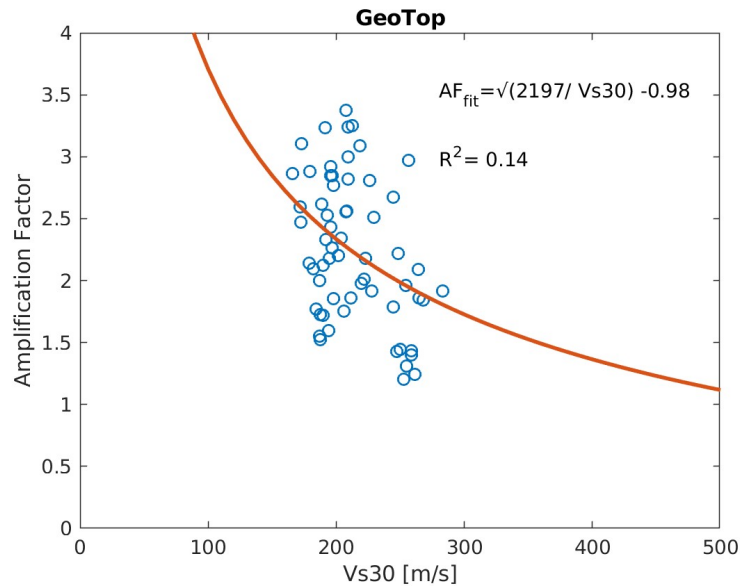


Figure 6-58: A plot of GeoTOP Vs30 versus measured AF data points at 61 stations of the G-network and the fitted function through the data points using Equation (6-12).

SCPT Vs

In the previous tests, Vs30 proxies and measured AFs were available at 61 of the 69 G-network stations. For the development of version 7 of the GMM for the Groningen gas field, an additional set of seismic cone penetration tests (SCPTs) has been performed at, or very close to, the borehole stations. From the 61 sites, there are 51 stations with an SCPT. From these measurements, Vs30 is derived and plotted versus the measured AFs (Figure 6-59). As with the previous Vs30 proxy (the GeoTOP proxy), $R^2=0.14$. Hence, measuring the detailed layering of Vs by SCPT has little use when it is harmonically averaged again to a Vs30 value. Information from the detailed Vs profile is lost by condensing it into one value. This analysis shows that the predictive power of Vs30 for AF remains limited, even if detailed and reliable values for Vs30 are known.

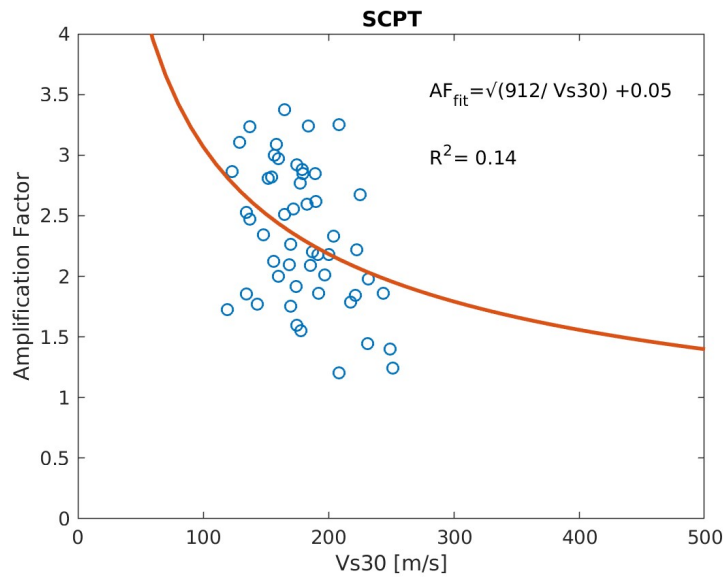


Figure 6-59: A plot of SCPT Vs30 versus measured AF data points at 51 stations of the G-network and the fitted function through the data points using Equation (6-12).

The coefficient of determination increases when instead of V_{s30} , the average is computed over a shallower section of the subsurface. When taking only the top 3 metres into account (Figure 6-60), referred to as V_{s3} , $R^2=0.19$ is obtained. Thus, the average velocity over the top 3 metres provides more information on the AF than the average velocity over the top 30 metres. This observation likely only holds for a Groningen-type setting, where very slow S-wave velocities exist in the top soil with correspondingly very short wavelengths.

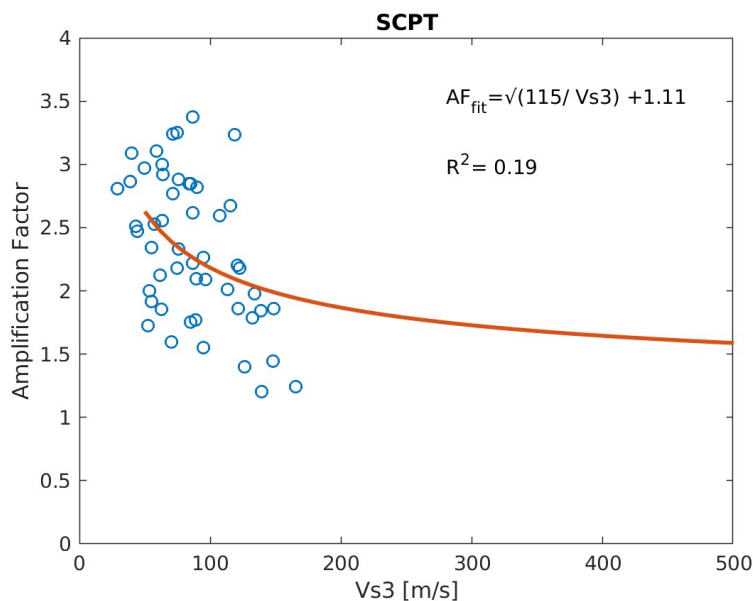


Figure 6-60: A plot of SCPT Vs30 versus measured AF data points at 51 stations of the G-network and the fitted function through the data points using Equation (6-12).

Finally, we demonstrate that that the predictive power of V_{s3} can be significantly improved when considering a different frequency band. Using AFs measured in the 1-4 Hz frequency band (instead of 1-10Hz) results in a larger R^2 of 0.44 (Figure 6-61). Comparing Figure 6-60 and Figure 6-61 shows that the fit for the latter is much better. This can be explained by the fact that anelastic losses, fine-scale layering and 3D scattering play less of a role at these low frequencies.

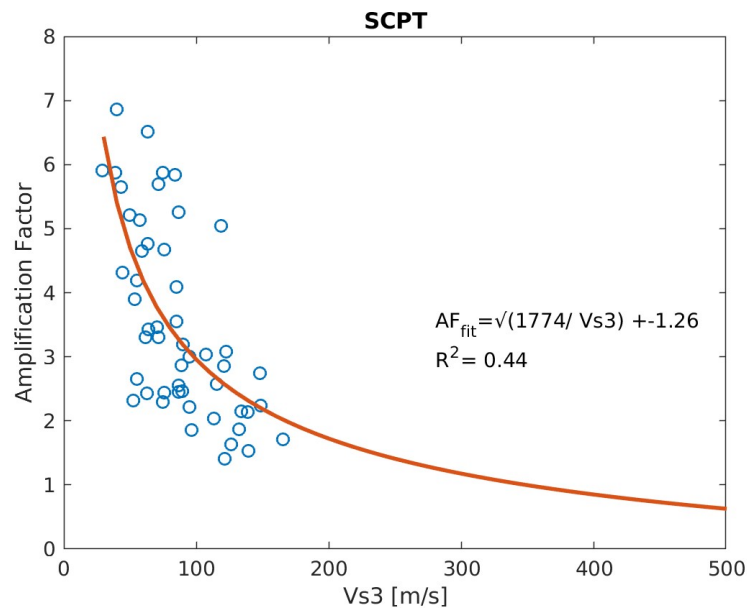


Figure 6-61: A plot of SCPT V_{s30} versus measured AF data points at 51 stations of the G-network and the fitted function through the data points using Equation (6-12). The AF is determined in the 1-4 Hz frequency band, whereas the previous figures plot AFs in the 1-10 Hz band.

In general, amplification cannot be predicted well employing (a proxy for) an average V_s velocity. For a good prediction of AF, more of the physical processes (actual layering, anelastic losses, 3D scattering) need to be included in the computation. Only the local AF model (section 6.4.5.2) takes these processes into account.

6.5 Recommendations for TBs

Based on the data models collected in each TB, recommendations on which soil amplification model to apply are summarized in Table 6-28.

Table 6-28: Summary of local site condition maps in each TB

TB	Method	Scale / Resolution	Source	Output	Limitations	Recommendations for use
all	Trans-european Geological maps (EGDI + Promine)+ Icelandic geological map + Vs30-geology correlation of Vilanova et al., (2018)	Europe (except Iceland): 1/1,000,000 to 1/1,500,000 Iceland: 1/600,000	SERA project	$v_{s,30}$ classes shapefile	$v_{s,30}$ -geology built in a moderate seismicity area (Portugal). Extrapolation to other areas, especially active seismic ones, would benefit from further validation and calibration.	When no other information is available
all	DEM GEBCO_2014 + Vs30-slope correlations of Wald and Allen (2007)	30-sec data	SERA project	Vs30 classes raster	Not suitable for some specific geological context (e.g. flat volcanic plateaus, glaciated terrains)	When no other information is available
TB1	Vp and Vs in 7 geological strata	30-sec data	Marmureanu et al., (2010)	raster	General use	-Use SERA data; -There are a lot of data (V_{s30} , H/V, inversions, etc.) referring to different points in the city, all this should be assembled in a model in the future.
TB2	Geological maps and boreholes + geotechnical data	1/400,000	SISPy project Colas et al. (2010, 2012)	EC8 classes raster		Usable for regional damage scenarios and shake-maps (near-real

TB	Method	Scale / Resolution	Source	Output	Limitations	Recommendations for use
						time for crisis management).
TB2	Geological maps and boreholes + geotechnical and geophysical data	1/10,000	SISPy project Roullé and Colas (2013)	EC8 classes shapefile		Usable for land use planning at local scale (long term risk analysis). The study by Fayjaloun et al. (2021b) has shown that damage scenarios using either the 1/400,000 or the 1/10,000 scale maps provide comparable results.
TB3	Simplified Geology map		SAFER project	$v_{s,30}$ map	$v_{s,30}$ assigned to large scale geology units	Usable for analyses at regional scale.
TB3	Topographical slope based on high resolution DEM	10m x 10m cells across Iceland	TURNkey	NEHRP classes raster file	The map has not been verified with measured Vs30 due to its inexistence in Iceland	
TB3	Station term relative to a reference station on bedrock	Local scale (Húsavík)	RANNIS Icelandic Research Fund	Site factor across Husavik, North Iceland TB	PGA and PSA at periods of engineering interest	Preferred to uncertain Vs30
TB3	Station term relative to a reference station on bedrock	Local scale (Hveragerði)	RANNIS Icelandic Research Fund	Site factor across Hveragerdi, South Iceland TB	Applicable to PGA	Preferred to uncertain Vs30
TB5	Ground response analysis (GRA) carried out at EUC for the port area based on subsoil model(s) built from geological	local scale (port area)	Subsoil modelling and stochastic linear-equivalent GRA results from Bozzoni et al. (2014) . Non-linear GRA carried out within	Outcomes from GRA (peak values, response spectra, etc.)	Results computed at free surface, i.e. by neglecting soil-structure interaction. One-dimensional (1D) subsoil modelling.	Site-specific

TB	Method	Scale / Resolution	Source	Output	Limitations	Recommendations for use
	information and data from several geophysical and geotechnical investigation campaigns		TURNkey project.			
TB6	Ground Motion Model includes Amplification Functions	1/10,000	Rodriguez-Marek et al (2017) and Bommer et al (2019)	Shapefile with zonation and functions with coefficients	Relative to a reference baserock horizon at a depth of ± 800 m	Preferred option instead of Vs30
TB6	Vs30 map for the region	1/10,000	Kruiver et al. (2017b)	Shapefile with mean, median and standard deviation of Vs30 for 160 geological zones	Based on geology and Seismic Cone Penetration Tests	High confidence Vs30 map, but not indicative parameter for soil amplification in this region (see section 6.4.5.3).

7 SOCIAL SENSORS AS SOURCES OF OBSERVATION

7.1 Felt reports

7.1.1 Introduction

Felt reports are crowdsourced by the EMSC from eyewitnesses through a set of 12 cartoons depicting different shaking and damage level on its websites and its LastQuake app. Felt reports are generally collected in large numbers for earthquakes in Europe and surrounding regions as well as the USA, where hundreds and sometimes thousands reports are collected within tens of minutes of the earthquake's occurrence. In other regions, the numbers are generally lower. Rather than macroseismic data, we prefer the denomination of "felt reports" as no information concerning the vulnerability of buildings –essential in macroseismic surveys– is taken into account. There is an important consequence in terms of mapping shaking distributions. Collected felt reports for damaging level (intensity greater than 8) reflect at least in part building vulnerability rather than shaking level per se. The second important requirement, which is shared with all macroseismic data, is to consider them from a statistical point of view. In other words, individual felt reports are affected by intrinsic variability to be exploited and only clustered information should be integrated in shaking distribution estimates. This chapter provides an overview on the current state of felt report exploitation for shaking estimates.

7.1.2 A rapid data collection

Felt reports are collected at global scale and high speed after a felt earthquake (Figure 7-1). This information flow can put major stress on EMSC IT infrastructure and generate significant service delays and disruptions (an issue that is being addressed).

The Petrinja (Croatia) earthquake was probably the worst-case scenario, since it struck an area where EMSC communication tools were highly popular because of the previous earthquake, which struck the capital city of Zagreb in March 2020. In this example, about 2 000 felt reports were collected in 8 mins before service disruption started. Still, what it shows is that felt reports are collected sufficiently fast to be ingested in rapid shaking estimates of global earthquakes and, in turn, in rapid impact assessments.

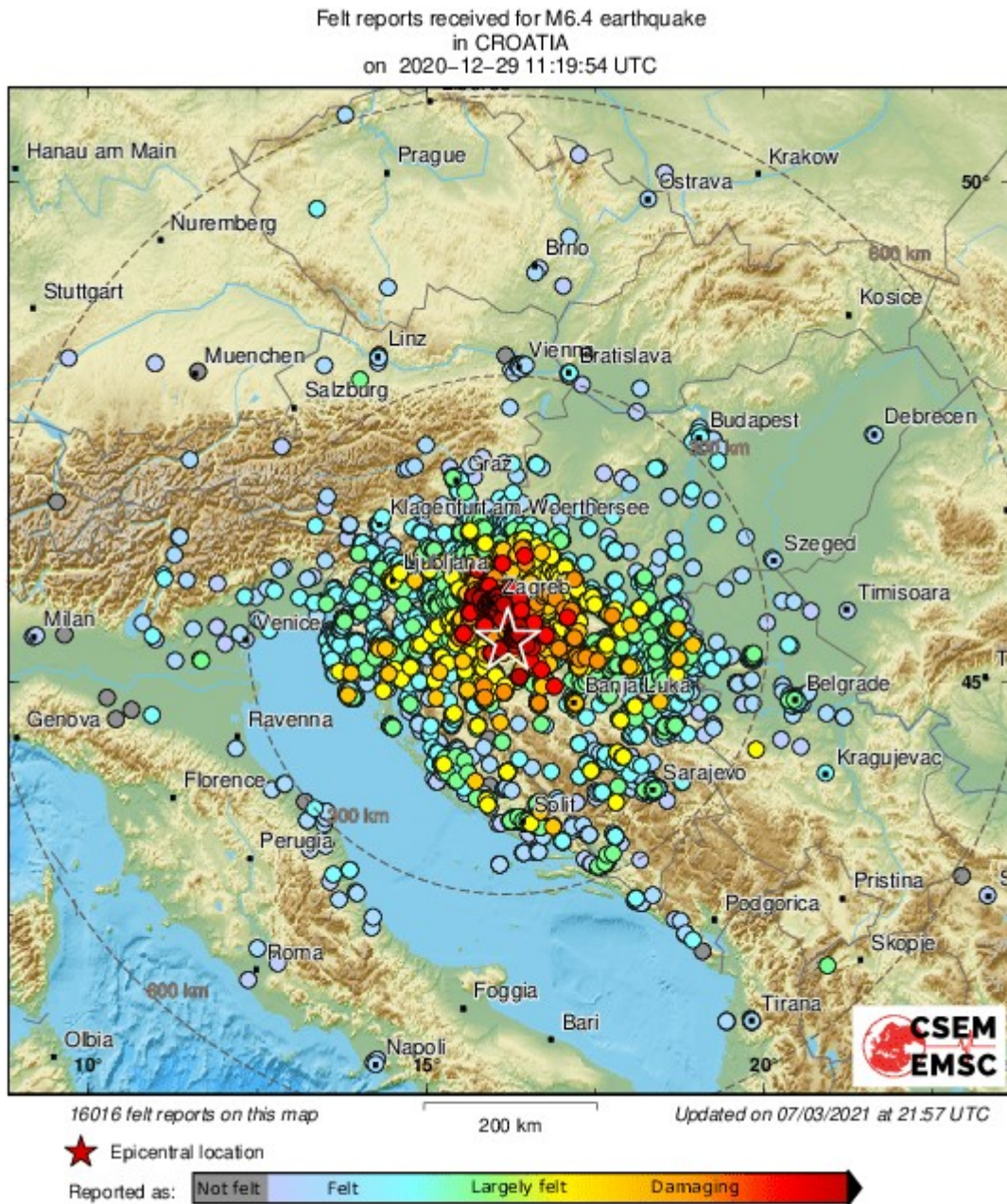
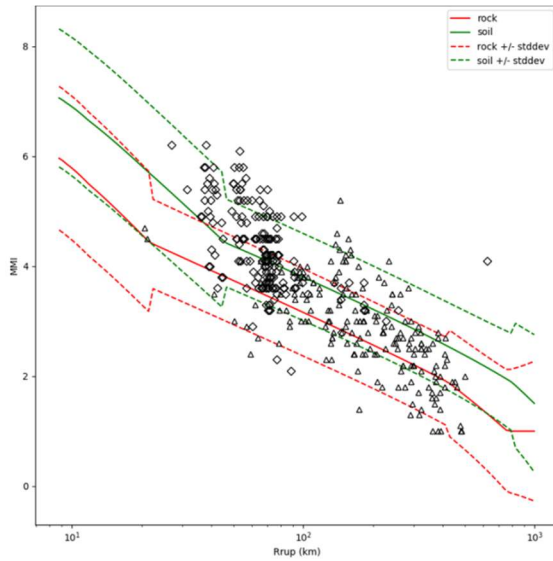


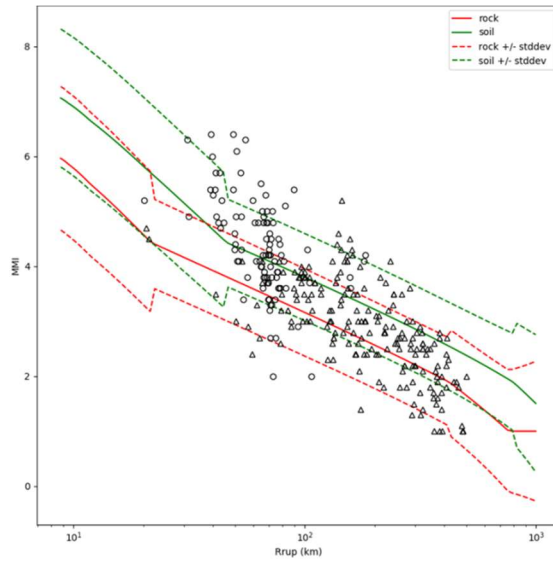
Figure 7-1: Map of felt reports for M6.4 Petrinja Croatia Dec. 29th 2020 earthquake through the app, website for mobile devices and website for desktop.

7.1.3 Felt reports and shaking estimates

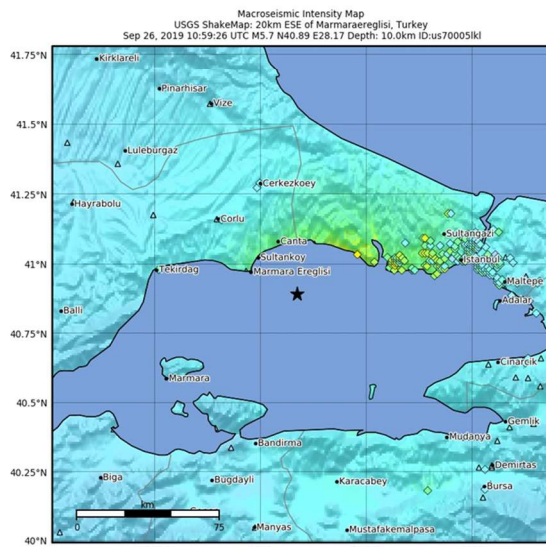
A first study showed good agreement in terms of intensity between EMSC felt reports and USGS DYFI data (Bossu et al., 2017). Knowing that DYFI data are routinely ingested in USGS ShakeMaps for global earthquakes, it opens the way to a similar exploitation of felt reports. An exploratory work was initiated with the USGS (Quitoriano and Wald, 2020) to evaluate this possibility (Figure 7-2).



2008 Felt reports vs 184 stations

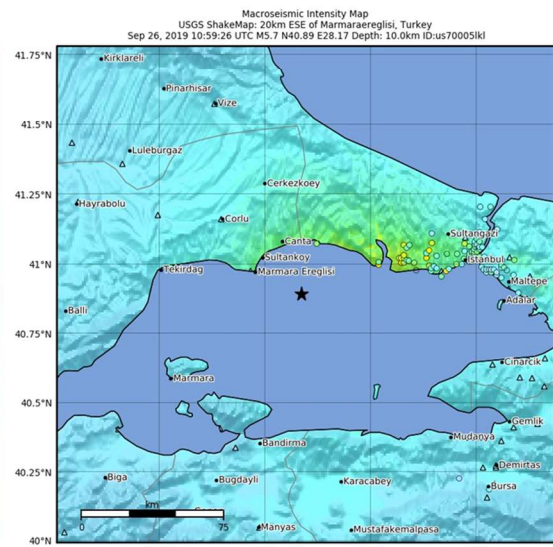


981 DYFI vs 184 stations



SHAKING	Not felt	Weak	Light	Moderate	Strong	Very strong	Severe	Violent	Extreme
DAMAGE	None	None	None	Very light	Light	Moderate	Moderate/heavy	Heavy	Very heavy
PGA(%g)	<0.05	0.3	2.76	6.2	11.5	21.5	40.1	74.7	>139
PGV(cm/s)	<0.02	0.13	1.41	4.65	9.64	20	41.4	85.8	>178
INTENSITY	I	II-III	IV	V	VI	VII	VIII	IX	X

2008 Felt reports + 184 stations

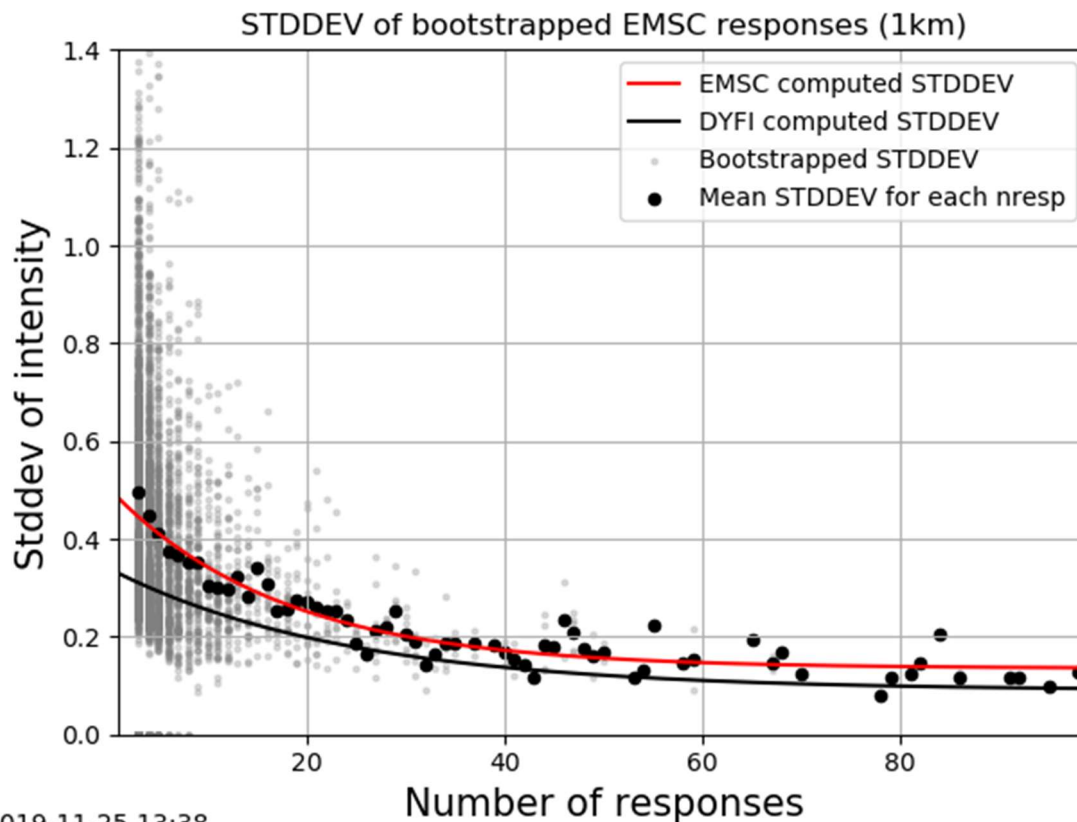


SHAKING	Not felt	Weak	Light	Moderate	Strong	Very strong	Severe	Violent	Extreme
DAMAGE	None	None	None	Very light	Light	Moderate	Moderate/heavy	Heavy	Very heavy
PGA(%g)	<0.05	0.3	2.76	6.2	11.5	21.5	40.1	74.7	>139
PGV(cm/s)	<0.02	0.13	1.41	4.65	9.64	20	41.4	85.8	>178
INTENSITY	I	II-III	IV	V	VI	VII	VIII	IX	X

981 DYFI + 184 stations

Figure 7-2: Comparison between intensity vs distance (top) and shake-map with EMSC felt reports (left) and DYFI data (right) for the M5.7 Western Turkey earthquake of Sept. 26th 2019.

An initial comparison, which applied the same methodology for EMSC felt reports and USGS DYFI, showed good consistency and even a higher density of felt reports (Bossu et al., 2017). However, there is a major difference between the two datasets. While individual DYFI values are derived from about 15 questions, felt reports result from user-assigned values, and one can expect the variability of the latter to be significantly higher. Obviously, standard deviation is an important input for reliable shaking estimates. A bootstrapping approach confirmed that the felt report's variability was higher (Figure 7-3).



2019-11-25 13:38

Figure 7-3: Estimated standard deviation for EMSC felt reports (red curve) and DYFI data (black curve) as a function of the number of observations in 1km² grid cells.

7.1.4 Spatial clustering of felt reports

Geographical clustering is needed to extract meaningful measurements from individual crowdsourced intensity data. The USGS uses fixed grid cells of 1 and 10 km. The limitation of these approach is firstly, they do not take into account the actual density of reports and secondly, the larger the epicentral distance is, the smaller are the intensity variations. In other words, a small grid cell makes sense at close epicentral distances if the density of observation is sufficient. At larger distances, larger grid cells are acceptable since intensity variations are small. In order to optimize the use of felt reports in ground shaking estimates, EMSC have initiated an adaptive grid method (Figure 7-4). The work is ongoing in collaboration with the USGS, who is potentially interested in adapting it to their own DYFI data.

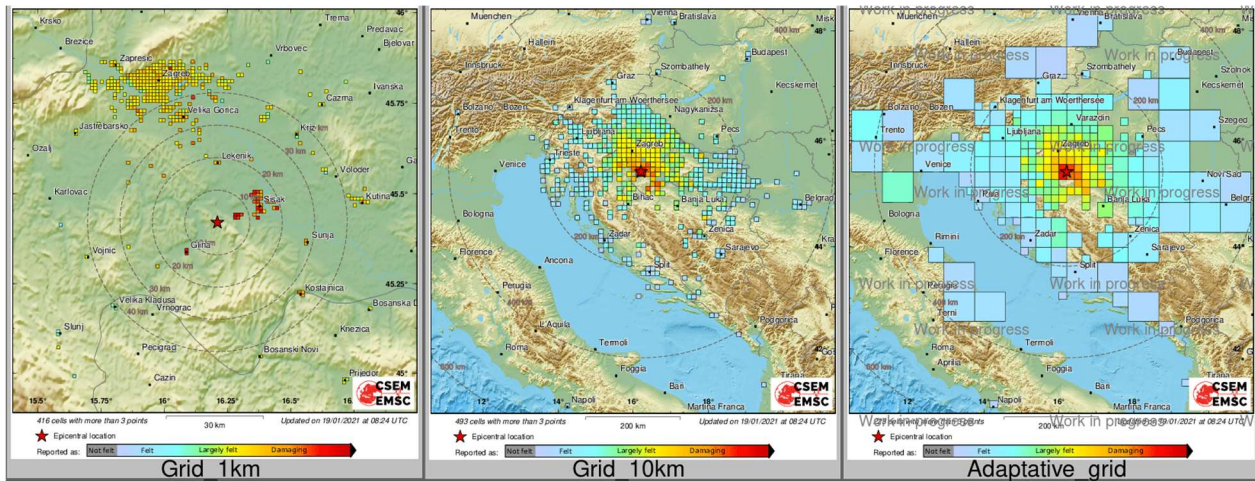


Figure 7-4: Examples of felt reports spatially averaged into different grid cells.

7.1.5 Current and future developments

Work is ongoing with the USGS to finalize the methodology to automatically ingest EMSC felt reports in their global shake-maps. This step will be decisive, since the USGS ShakeMap algorithm is implemented in many institutes around the world opening the way for straightforward integration for any national or regional institute. In parallel, we are working with GEMPA in TURNkey WP6 to develop a real-time exchange protocol of felt reports with identified end-users. If successful, this represents a lasting contribution of the TURNkey project.

7.2 Information from social media (Twitter)

7.2.1 A global social network to monitor earthquakes around the world

Social media broadcast data from millions of connected social sensors that share events online on a daily basis (Goodchild, 2007). When a natural disaster occurs, social media platforms allow testimonies to be shared spontaneously and quickly. These mainly come from those citizens that are affected by the event (Comunello et al., 2016): these 'local citizens' tend to exchange information related to their own perception of ground-motions or of visible impacts (Grace et al., 2017), while people not present in the affected area tend to relay this information or to express their empathy (Olteanu et al., 2015). However, when the risk becomes very high, the amount of information coming from the 'local citizens' affected by the event decreases sharply because of an opportune self-protection behaviour (Comunello et al., 2016; Bossu et al., 2017). Twitter had over 321 million active users in 2020 (TIZ, 2020) and comprises practical features such as short messages publication in real time and free streaming Application Programming Interfaces (APIs), which make it possible to automate monitoring tasks, the ability to attach pictures and to share GPS geolocation and so forth. Researchers have observed a strong and immediate spread of tweets when a significant earthquake occurs (Kryvasheyev et al., 2016; Comunello et al. 2016). Twitter is now considered as a social sensor for natural hazards, by allowing shared access to live data streams (Fayjaloun et al., 2021a).

Nonetheless, continuous monitoring of Twitter addresses important challenges. First, we need to set up and maintain a robust IT infrastructure connected to Twitter's servers through the free public API. Second, we need to retrieve the tweets satisfying specific search criteria, usually via keywords, taking into account the constraints associated with free language. Targeted queries should be defined to be sufficiently generic to capture a maximum of tweets dealing with the subject, while remaining specific enough to not “pollute” the data with off-topic messages (Auclair et al., 2019). Yet, Twitter does not give free access to the totality of messages exchanged at a given time via its streaming API. In addition, Twitter delivers only a portion of the total messages with “black-boxed” sampling rules and thresholds. This is not critical, since we are not seeking to obtain the entire message flow; however, it can have a significant impact when aiming at quantitatively describing the dataset. After being retrieved, the tweets have to undergo a first post-processing step to eliminate duplicates or messages sent by “robots”, which contain no information. Although potentially cumbersome, the implementation and maintenance of this type of architecture has become relatively common, and it does not present any major difficulties. Finally, the main challenge resides in the fine-grained extraction of relevant information from each tweet and its metadata.

The most crucial information needed to map the intensity distribution from the earthquake is the geolocation of the tweets. However, since the development of Twitter in 2006, the number of tweets that are natively geotagged (i.e. sharing the user's location via their GPS geographic coordinates by the users or twitter) consists in less than 1% of the tweets (Cheng et al., 2010; Graham et al., 2014). Twitter also recently announced plans to further remove this functionality (Twitter, 2019). Alternatively, a common way to find the location of the tweets is to use Named Entity Recognition (NER) techniques to identify references to places in the text of the tweets, and to retrieve the corresponding geographic coordinates via specialized web-services (e.g. OpenStreetMap). Additionally, another data processing step is needed to remove disambiguities in geolocation of the events: for example, if an earthquake occurs in California, it is more likely that a tweet from a witness mentioning the city of “Dublin” evokes the Californian locality rather than the capital of Ireland. These techniques allow a significant and relatively robust enrichment at the municipal scale (Kropivnitskaya et al. 2017a; Auclair et al., 2019). More complex approaches have recently been proposed, consisting of grouping tweets mentioning the same toponyms to improve their location (de Bruijn et al., 2018), or jointly predicting location and other thematic attributes via semi-supervised approaches (Ouaret et al., 2019). In addition to the geolocation of the event, tweets contain information that helps better identify the extent of the earthquake shaking, such as the identification of witnesses (Starbird et al., 2012; Zahra et al.; 2020), the detection of damage (Resch et al. 2018), the description of the level of intensity of the shaking (Arapostathis et al., 2016), and the reporting of victims (Communello et al., 2016) and so forth, which are worth extracting using Natural Language Processing (NLP) and other topic modelling approaches.

By constantly monitoring tweets, earthquakes can be detected automatically and quickly (Sakaki et al., 2010; Earle et al., 2010 and 2011). Earthquakes are not predictable and can happen at any time and only last a few seconds: this kinetic behaviour is translated to the tweets' activity. When an earthquake strikes, Twitter activity is marked by a very rapid rise of the number of related tweets, which peaks within few minutes, and then decreases gradually within a period that depends on the size of the earthquake (Communello et al., 2016; Francalanci et al., 2017). Boccia Artieri et al. (2012) explained that this observation of rapid increase of Twitter activity followed by a gradual decrease are caused by the “witnessing” activity of the

users, followed by other activities related to information research, to expression of empathy and to commentary in the upcoming minutes to hours. Thus, the main peak of activity is generated almost exclusively by people who have personally felt the earthquake. Several studies have been carried out in recent years to analyse the tweets exchanged during the first minutes after an earthquake to be able to deduce information related to the intensity of the earthquakes, and thus contribute to the rapid calculation of shake-maps. These studies are based on two main approaches to extract the intensity information from the tweets.

The first approach consists of generating empirical equations relating the number of tweets relative to the population density of a community to the macroseismic intensity (Kropivnitskaya et al., 2017a,b). This approach is easy to implement and independent from the language used for the tweets, and it generally shows satisfactory performance. Nevertheless, the main limitation of this work is that it strongly depends on the number of current Twitter users for developing the empirical equations. However, the number of users is different from one country (or region) to another, and it also changes with time: while the number of Twitter users grows in some countries, it stagnates in others. Consequently, these relationships might not be adapted to different regions, or no longer be valid already a few months after their publication.

The second approach consists in developing predictive models via machine learning approaches to evaluate the maximum intensity of the earthquake (Cresci et al., 2014) or to map the local intensity (Burks et al., 2014 and Mendoza et al., 2018 and 2019) or via the development of lexicons to different degrees of macroseismic intensities (Arapostathis et al., 2016). This approach relies on a tweet-by-tweet analysis taking into account the content of each message individually, and it is therefore more durable and robust. However, these methods are more complex to implement and they necessitate a periodic validation and adaptation to the changes made by Twitter itself, like the maximum number of characters per tweet that was increased in 2017 from 140 to 280 characters, as well as the continuous evolution of the behaviour of the Twitter users, like the tendency to use fewer hashtags (Auclair et al., 2019). Furthermore, many of these approaches require large datasets to calibrate the models, which are not always available due to the significant return periods of earthquakes. Indeed, many regions of the world with moderate seismicity have not experienced significant earthquakes since the appearance of Twitter in 2006, and therefore have very partial datasets for calibration.

Alternatively, Resch et al. (2018) proposed to combine machine-learning topic models with spatiotemporal clustering to deduce the extent of the area experiencing damage. Accordingly, macroseismic intensity greater than or equal to 6 or 7 on the EMS-98 and MM intensity scales can be assigned to the area of damage, depending on the mean level of vulnerability of the buildings in the study area.

7.2.2 Analysis of Twitter feeds with agnostic extraction of the raw felt area

In 2019, 58% of the French population is an active user of social media (WeAreSocial, 2019), among which Twitter ranks sixth behind Facebook, YouTube, Instagram, WhatsApp and Snapchat. Based on the geotagged tweets (i.e. with GPS coordinates in their metadata) as an approximation of the location of Twitter users, Auclair et al. (2019) showed that the most active users on Twitter correspond to the most densely populated areas, with the highest concentration in Paris. Consequently, Twitter is more likely to provide data to calibrate

macroseismic intensities inside urban areas rather than in rural ones. It should be noted that the characteristics of the buildings in these urban areas may present specific characteristics to be taken into account when attributing intensities based on the tweets (e.g. ground-motions generally better felt in high-rise buildings).

Resch et al. (2018) proposed the topic-modeling procedure to identify “hot-spots” of geolocated tweets classified as “earthquake-related”: the clusters thus identified correlate with relatively strong ground-motions and they correspond to what the authors call the “earthquake footprint”. Alternatively, Mendoza et al. (2019) proposed identifying an “area of interest” grouping together the “municipalities affected by the earthquake” via a supervised binary classification of tweets aggregated at the municipal level.

Here, we propose another clustering approach for the geolocated tweets that does not require calibration of any predictive algorithm based on the analysis of the textual content, nor the knowledge of the characteristics of the earthquake, and is easy to implement in any study area. The spatio-temporal clustering approach is based on the ST-DBSCAN algorithm (Birant and Kut, 2007) i.e. Density-Based Spatial Clustering of Applications with Noise (DB-SCAN; Ester et al., 1996) extended to the time domain. This approach was successfully applied to identify, in the areas impacted evolving with time, other fast kinetics phenomena such as forest fires (Zhong et al., 2016). Contrary to other clustering approaches, DB-SCAN algorithms have the ability to discover clusters of arbitrary shape; they can easily process large amounts of data (Zhou et al., 2000); additionally, they integrate relevant authoritative demographic and environmental information, such as population density (Zhong et al., 2016); and finally, DB-SCAN algorithms do not require a predetermination of the number of clusters.

Practically, Twitter users posting earthquake-related tweets (i.e. using lexical field of earthquakes) within a short time period mentioning places geographically close to the original epicentre, imply the occurrence of a new event and allow for the detection of message clusters. Our DB-SCAN algorithm requires the determination of two parameters within a specific period: (1) the “size” parameter describing the minimum number of neighbouring tweets to declare a cluster, and (2) the “proximity” parameters in space and time describing the minimum distance and duration between the tweets to be assigned to the same cluster.

We limit the analysis to the direct tweets posted during the first ten minutes after the earthquake, excluding the “retweets”: the peak of the activity of users on Twitter generally occurs during the first 10 minutes after the earthquake, and those users are commonly direct witnesses of the earthquake (Boccia Artieri et al., 2012; Burks et al., 2014; Communello et al., 2016; Kropivnitskaya et al., 2017a). Limiting the collection of tweets to 10 minutes makes it possible to produce a first shake-map very quickly to respond to the first questions from the civil protection services and to execute rapid response systems such as PAGER (Wald, 2010).

We consider that there is a “temporal proximity” between tweets when they have been sent less than 10 minutes apart. This temporal dimension can be modified for other usage. This temporal dimension parameter is, however, interesting to keep, in particular with a perspective of continuous monitoring of Twitter, and can for example allow to detect clusters corresponding to aftershocks occurring shortly after the main shock. Regarding the “spatial proximity”, we introduce a site-specific parameter instead of a fixed value, defined by the radius in which the residential population is greater than or equal to 2,500,000 inhabitants. We compute this parameter on the fly from the grid of the French population delivered by the French Institute of Statistics (INSEE) with a resolution of 200 metres. Therefore, the spatial

proximity parameter is larger in the countryside than in cities. So far, this approach has only been tested on the French territory.

The parameter describing the minimum number of points (e.g. georeferenced tweets) necessary to declare a cluster may however differ depending on the regional density of Twitter users and must therefore be tuned specifically to the study area. The main effect of changing this parameter is to significantly modify the number of clusters detected by the algorithm, which has no impact on our method, since we only consider the main cluster. In France, we fix a minimum number of points of 5 as a criterion to define a cluster.

Spatio-temporal clustering within 10 minutes, therefore, acts as a natural “agnostic” filter allowing first-order identification of the felt area without any knowledge of the earthquake or any analysis of the content of tweets other than the detection of place references. Furthermore, the absence of tweets from certain large municipalities with more than 50,000 inhabitants indicates that the intensity of the ground-motions was very low, insufficient to arouse the “testimony” reflex from Twitter users. These locations are subsequently classified as “unfelt”.

Another important observation is the “truncated” form of felt-areas extracted from clusters in areas where no tweets are available: along borders (e.g. no tweets collected in Italy due to the fact that we collect messages in French language only), at sea and within uninhabited areas. This well-known bias in macroseismicity related to missing data must be taken into account when assigning the intensity level.

7.2.3 Generation of Twitter-enhanced shake-maps

The principle of shake-maps relies on the combination of a priori GMPE estimates with field observations in order to constrain uncertainties of the ground-motion field generated by an earthquake. This section details the algorithm used to integrate tweets as observation for the generation of shake-maps (Fayjaloun et al., 2021a).

The limit between intensity grades 2 and 3 remains tricky to distinguish on the sole basis of individual data, which makes it difficult to assess the actual proportion of the population of a given locality having felt the tremors. However, although a few tweets may come from areas of intensity 2 quickly after an earthquake - especially in large cities where populations are concentrated - we make the hypothesis that, if people mention the earthquake right after its occurrence in localities close to each other (i.e. clusters), there are high chances that they have felt it with an intensity greater than or equal to 3, corresponding to weakly felt shaking according to the EMS-98 macroseismic scale (Grünthal, 1998). Therefore, we consider that the “felt area” deduced from Twitter data may be translated into macroseismic observations points, assigning an intensity value equal to 3 or above (i.e. $MI \in [3 ; 12]$) to each grid point with the cluster. This assumption represents the minimum information that can be extracted from tweets about the intensity level, while respecting the problem of missing data.

In the same way, the “unfelt locations” are translated into macroseismic observations points, assigning intensity values ranging from 1 (unfelt shaking) to 2 (rarely noticeable shaking) - (i.e. $MI \in [1 ; 2]$). It follows the hypothesis that if people do not mention the earthquake at a given densely populated location, the chance is high that they have not felt it.

Such information about the minimum intensity corresponds to soft evidence, while our current Bayesian Network (BN) approach only accepts hard evidence or fixed values (i.e., no option of inequality or larger than). A possible way to integrate such data is to decompose the posterior shake-map distribution over all possible values of macroseismic intensities, given the “tweet

observation". Let us define $P(Y_i|T)$ as the conditional distribution at a grid point, given Twitter evidence at a given point. It may then be expressed as:

$$P(Y_i|T) = \int_{-\infty}^{+\infty} P(Y_i|Z_{obs}) \cdot P(Z_{obs}|T) \cdot dZ_{obs} \quad (7-1)$$

where Z_{obs} is the MI at the location of the Twitter evidence. $P(Z_{obs}|T)$ represents the conditional probability of observing the value Z_{obs} given the tweet: it is proposed to estimate this probability by using the a priori distribution of the MI (i.e., the expected value of the intensity, given the earthquake parameters), and by truncating the distribution according to the aforementioned assumptions: $P(Z_{obs} < 3 | T) = 0$ and $P(Z_{obs} > 2 | T) = 0$, respectively, for the unfelt and felt locations. Moreover, the bounded nature of the EMS-98 macroseismic scale is taken into account by assigning a zero probability to intensities less than 1 and greater than 12: $P(Z_{obs} < 1 | T) = 0$ & $P(Z_{obs} > 12 | T) = 0$. Therefore, equation (9-1) is transformed as follows:

$$P(Y_i|T) = \int_3^{12} P(Y_i|Z_{obs}) \cdot P_{trunc,prior}(Z_{obs}) \cdot dZ_{obs} \quad (7-2)$$

where $P_{trunc,prior}(Z_{obs})$ is the truncated prior distribution of Z_{obs} as illustrated in Figure 7-5, for the case that the observation is within a "felt area". A similar expression is assembled for the "unfelt locations", with the integration bounds ranging from 1 to 2. In the end, it can be seen that the addition of Twitter data provides a very loose type of information (i.e., lower and upper bounds on the MI).

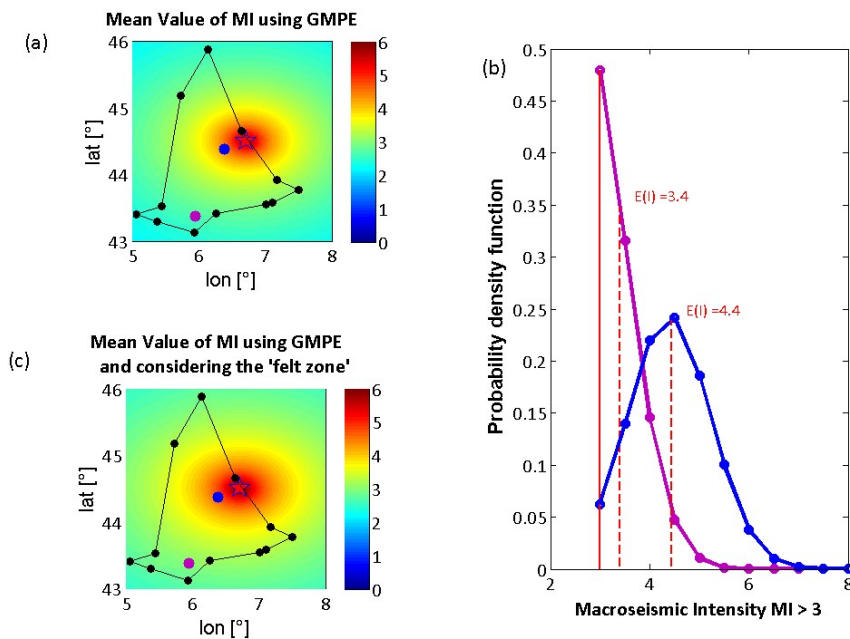


Figure 7-5: (a) A priori estimation of the MI and the contour lines defining the "felt area" from Twitter data, example of a location inside the felt area; (b) Truncated normal distribution of the macroseismic intensities at two locations shown in (a) by purple and blue dots, after considering the information from the felt area, and the expected values to be entered as evidence observations (red dotted vertical lines) and implemented to generate map (c). (c) A posteriori estimation of the MI when considering the "felt area" from Twitter data. Coordinate of epicenter in (a) and (b) are from RéNaSS (example from the M5.2 Barcelonette earthquake in 2014).

The main issue with the framework presented in equation (7-2) is the computational cost, since many instances of shake-maps would have to be computed (for each possible value of Z_{obs}) in order to integrate the evidence. Moreover, the problem becomes increasingly more complex when additional “tweet observations” are added (i.e., generation of multiple integrals). Therefore, a first-order approximation is adopted here: instead of integrating over the possible range of Z_{obs} , the expected value estimated over the truncated distribution is directly used as an input to the shake-map (Figure 7-5).

In the following, we detail the steps to define the value of the soft evidence at each point within the “felt area” and at the “unfelt locations”. The whole process is illustrated by the flowchart in Figure 7-6.

At each grid point inside the contour defined by the Twitter felt area, we estimate the mean value and the corresponding standard deviation of the intensity using a GMPE and a GMICE without any observation as an a priori estimate (Figure 7-5a).

Then, at each of these grid points, we generate a truncated normal distribution of intensities (using the mean and standard-deviation computed in the previous step), within the range of [3 – 12] or [1 – 2] (Figure 7-5).

In addition, at each point, we compute the expected value of the intensity for the probability distribution defined above, by summing the values of the intensity on the range [3 – 12] (or [1 – 2]) weighted by the corresponding probability. This soft evidence is then assumed to be equal to the expected value of the intensity. Finally, these approximate observations are entered in the BN as additional evidence to complement the instrumental observations.

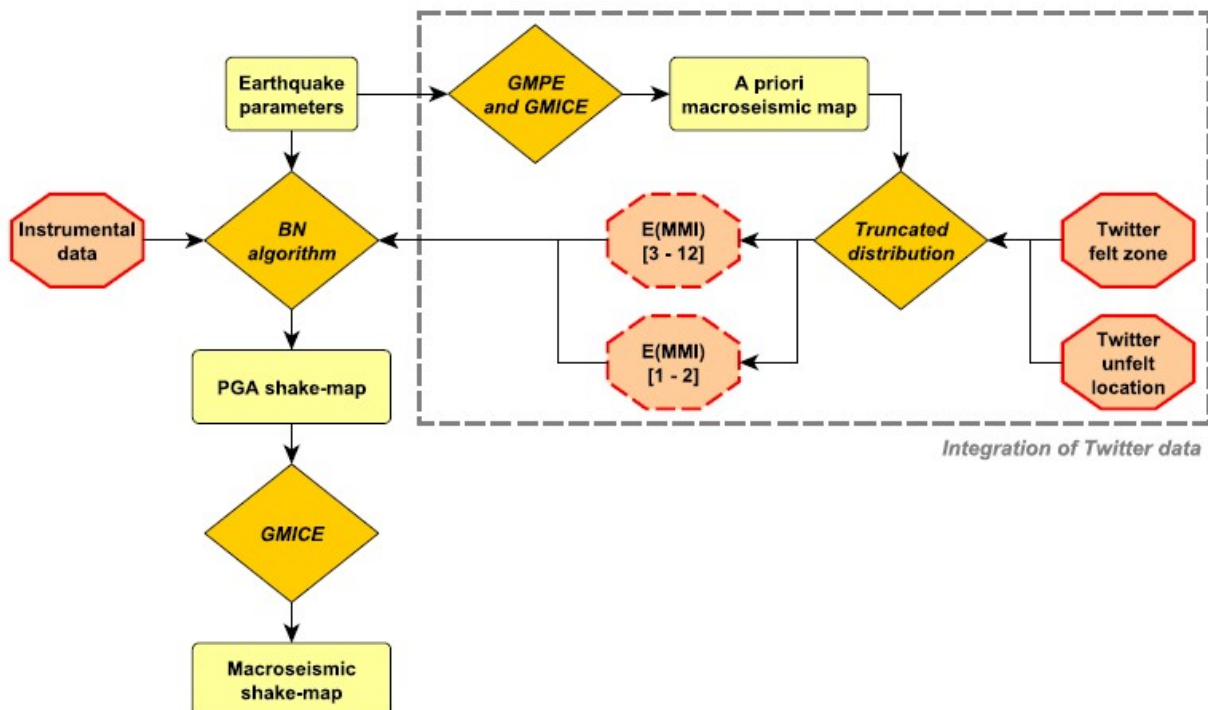


Figure 7-6: Successive steps and datasets involved in the generation of shake-maps that include Twitter data. GMPE stands for Ground-Motion Prediction Equation, GMICE for Ground-Motion Intensity Conversion Equation, BN for Bayesian Network, E(MMI) for the expected value of macroseismic intensity.

Two earthquakes of magnitude 5.2 that occurred recently in France, the Barcelonnette earthquake in 2014 (Figure 7-7) and the Le Teil earthquake in 2019 (Figure 7-8), are studied in [Fayjaloun et al. \(2021a\)](#). In this paper, we used two types of observations available immediately after the occurrence of an earthquake, the instrumental measurements of PGA on one hand, and the messages posted on Twitter on the other hand (where we translate the tweets into 'felt' or 'unfelt' observations with $MI \geq 3$ and $MI < 3$, respectively). The combination of the felt and unfelt areas with ground-motion recordings enhanced the prediction of the distribution of macroseismic intensity. In doing so, we answer the need to inform authorities about the potential impact of the earthquake within 10 minutes of the occurrence of the event, via direct communication of shake-maps in terms of macroseismic intensity (MI) or via rapid loss assessment based on these shake-maps.

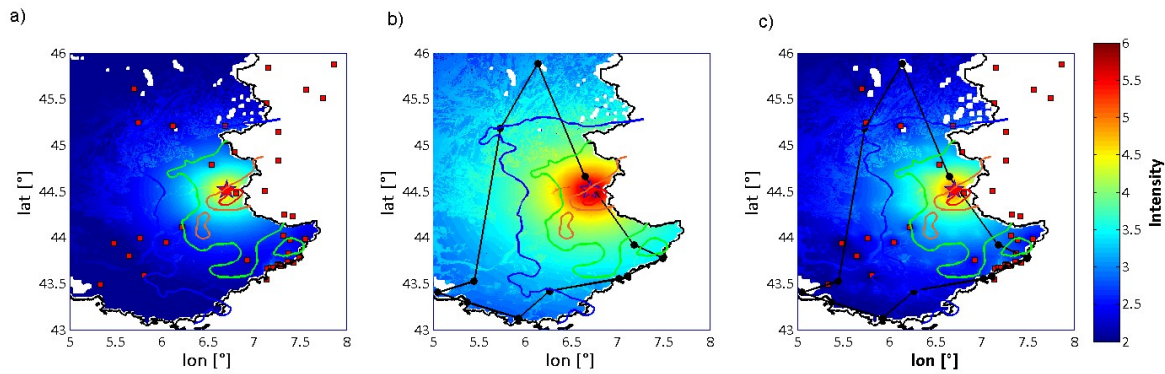


Figure 7-7. Shake-maps for the Barcelonnette earthquake, taking into account the information from: (a) the seismic stations recording PGA (shown as red squares), (b) the Twitter data (the felt zone is bordered by black lines), and (c) both seismic stations and Twitter data. The contour lines represent the reference isoseismal areas defined by the French Central Seismological Office (BCSF).

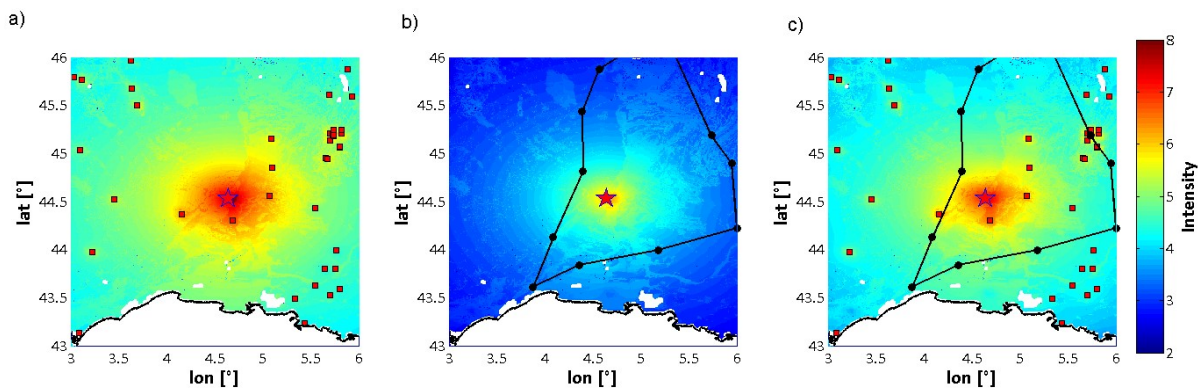


Figure 7-8: Same as Figure 7-7, for the Le Teil earthquake.

PGA measurements recorded far from the epicentre (beyond a hundred kilometres for earthquakes of moderate magnitude) tend to underestimate the entire macroseismic field because of very low PGA values. It is important to note that the shake-maps are initially and mainly controlled by the selected GMPE. The observations modify the shake-map locally (through the updating of the intra-event error term) and globally (through the updating of the inter-event error term), but they do not modify the geometrical decay of the ground motion imposed by the GMPE. Thus, future work should investigate updating of the spatial decay of intensity, for instance through the GMPE coefficient related to the source-to-site distance term.

8 CONCLUDING REMARKS

This report began by detailing current approaches for the derivation of shake-maps. In terms of shake-map algorithms, the version 4.0 of ShakeMap® offers substantial improvements over the version 3.5. The weighted interpolation algorithm, which is based on the definition of “radii of influence” that are difficult to quantify in practice, is replaced by a matrix-based procedure that relies on the multi-variate normal (MVN) distribution. The latter approach presents the benefit of generating exact solutions of the updated ground-motion field, with an accurate uncertainty structure (Worden et al., 2018). Moreover, this approach is able to consider multiple types of IMs, for instance by accounting for the statistical cross-correlation between spectral ordinates at various periods: this feature is especially useful when dealing with interconnected exposed assets that are susceptible to various types of IMs (i.e., loss assessment of infrastructure systems). In parallel, the Bayesian updating approach by Gehl et al. (2017) is based on the theory of spatially correlated Gaussian fields in order to update the ground-motion field by various types of observations. The Bayesian approach is based on the same mathematical concepts as the procedure by Worden et al. (2018), such that the results are identical when the same assumptions are used. It is also able to handle cross-correlation between different IMs, although at the cost of longer computation times. Regardless of the approach used, it should be noted that these two recommended procedures provide an accurate description of the uncertainties associated with the updated ground-motion field, so that these uncertainties should ideally be propagated to the loss assessment step.

The choice of the GMMs to be used in the shake-maps may have a major influence on the final results. A solution presented here is to directly update GMM coefficients from recorded strong motions of the event in order to obtain a specific updated GMM for a given earthquake: thus, such a calibrated model may be used to derive a more accurate shake-map of this specific event, and it may even be helpful for estimating the shaking in case of subsequent aftershocks. In parallel, the Bayesian framework for the derivation of shake-maps has been modified in order to account for uncertain GMM coefficients (i.e., prior distribution): as a result, the algorithm provides posterior distributions of ground shaking estimates (i.e., the shake-map) and of GMM coefficients. Current results require further investigation before an actual implementation.

Another major source of uncertainty lies in the characterization of site amplification factors: by default, most shake-map systems use the Wald and Allen (2007) model based on topographic slope. While this is better than no amplification map at all, and while the influence of amplification factors on the result decreases with increasing ground-motion and/or intensity, there is no guarantee that it provides accurate results for the area of interest. Therefore, regional maps should be used when available, to complement or replace estimated Vs30 values from topographic data, using the method of Heath et al. (2020) for instance. Moreover, a proper characterization of the sites where ground motions are recorded is crucial, since inaccurate amplification factors may propagate errors when devolving the observations to rock conditions and, in turn, they may alter the whole shake-map field (this is a less important problem in ShakeMap® v4, in which the observations are not converted to rock condition before interpolation). Therefore, recent efforts carried out in the SERA project for a better characterization of site conditions in Europe should be integrated in the upcoming developments: specific local models, however, should always be preferred, as recommended in section 6.

Finally, the integration of macroseismic testimonies is not systematic in all shake-map systems, with various ways of collecting and interpreting the data (i.e., different types of online forms). The duration required to collect meaningful data and to translate them into macroseismic intensities constitutes a challenge for their use in near real-time applications. Less conventional sources of social data, such as the use of the mobile applications (LastQuake; Earthquake Network) or data mining of social media (e.g., Twitter feeds – [Fayjaloun et al., 2021a](#)), have proven to be very efficient thanks to the reactivity of users right after an earthquake (i.e., a few seconds to a few minutes). Their use as additional data inputs for shake-maps is worth investigating in order to cover the time gap before the determination of more accurate macroseismic intensities (i.e., after several minutes).

9 REFERENCES

- Abrahamson, N., & Youngs, R. (1992). A stable algorithm for regression analyses using the random effects model. *Bulletin of the Seismological Society of America*, 82(1), 505–510.
- Abrahamson, N., Silva, W., & Kamai, R. (2014). Summary of the ASK14 ground motion relation for active crustal regions. *Earthquake Spectra*, 30(3), 1025–1055.
- Abrahamson, N., Gregor, N., & Addo, K. (2016). BC Hydro Ground Motion Prediction Equations for Subduction Earthquakes. *Earthquake Spectra*, 32, 23-44. doi:10.1193/051712EQS188MR
- Ahorner, L. (1983a). *Makroseismische Magnituden-Bestimmung*.
- Ahorner, L. (1983b). Seismicity and neotectonic structural activity of the Rhine Graben system in Central Europe. In: A. R. Ritsema & A. Gürpınar eds. *NATO Advanced Research Workshop on the Seismicity and Seismic Risk in the Offshore North Sea Area, The Netherlands, June 1 - 4, 1982*. Dordrecht/Holland, pp101–111.
- Ahorner, L., Budny, M. (1985). Seismische Bestimmung der bodendynamischen Kennwerte von oberflächennahen Schichten in Erdbebengebieten der Niederrheinischen Bucht. In: K.-H. Heitfeld ed. *Ingenieurgeologische Probleme im Grenzbereich zwischen Locker- und Festgesteinen*. Berlin, Heidelberg, Springer, pp560–582.
- Ahorner, L., Rosenhauer, W., Budny, M. (1986). Methoden zur Erdbebengefährdungsanalyse - Regionale Erdbebengefährdung. In: Institut für Bautechnik ed. *Realistische seismische Lastannahmen für Bauwerke*. Stuttgart, pV/1-V/45, (*Abschlussbericht im Auftrag des Instituts für Bautechnik, Berlin*).
- Ahorner, L., Rosenhauer, W. (1986). Realistische seismische Lastannahmen für Bauwerke - Kap. 9: Regionale Erdbebengefährdung. *Frankfurt/Main. II. Abschlussbericht im Auftrag des Instituts für Bautechnik, Berlin*.
- Ahorner, L., Rosenhauer, W. (1993). 3.3 Seismische Risikoanalyse. In: G. Klein ed. *Bestandsaufnahme des Erdbebenwissens: DGEB - Publikation No. 6*. DGEB - Publikation. Weinheim, VCH Verlagsgesellschaft mbH, (*Kenntnisse und Kenntnislücken zum Naturereignis Erdbeben nach dem Stand 1990 koordiniert von der Deutschen Gesellschaft für Erdbeben-Ingenieurwesen und Baudynamik für das Deutsche IDNDR-Komitee*).
- Ahorner, L. (1993). Gemessene Bodenbeschleunigungen beim Roermonder Erdbeben am 13. April 1992. *Bauingenieur*, 68 (5), pp201–205.
- Akkar, S., & Bommer, J. (2010). Empirical Equations for the Prediction of PGA, PGV, and Spectral Accelerations in Europe, the Mediterranean Region, and the Middle East. *Seismological Research Letters*, 81, 195-206. doi:10.1785/gssrl.81.2.195

Akkar, S., Sandikkaya, M., & Bommer, J. (2014). Empirical ground-motion models for point- and extended-source crustal earthquake scenarios in Europe and the Middle East. *Bulletin of Earthquake Engineering*, 12(1), 359–387.

Akkar, S., Douglas, J., Di Alessandro, C., Campbell, K., Somerville, P., Cotton, F., Silva, W., & Baker, J. (2012). *Defining a consistent strategy to model ground motion parameters for the GEM-PEER Global GMPEs Project*. 10p.

Allen, T., & Wald, D. (2007). Topographic Slope as a Proxy for Seismic Site-Conditions (VS30) and Amplification around the globe. *U.S. Geological Survey Open-File Report 2007-1357*, 69 p.

Allen, T. I., & Wald, D. J. (2009). On the use of high-resolution topographic data as a proxy for seismic site conditions (VS 30). *Bulletin of the Seismological Society of America*, 99(2A), 935-943.

Ambraseys, N.N. (1975). The correlation of intensity with ground motion. In: *XIV General Ass. ESC 1974 in Trieste*. Potsdam, Nationalkomitee für Geodäsie und Geophysik, Akademie der Wissenschaften der DDR, pp335–341.

Ambraseys, N. (1985). Intensity-attenuation and magnitude-intensity relationships for northwest european earthquakes. *Earthquake Engineering & Structural Dynamics*, 13 (6), pp733–778. doi: 10.1002/eqe.4290130604.

Ameri, G., Drouet, S., Traversa, P., Bindi, D., & Cotton, F. (2017). Toward an empirical ground motion prediction equation for France: accounting for regional differences in the source stress parameter. *Bulletin of Earthquake Engineering*, 15(11), 4681–4717.

Arapostathis, S. G., Isaak, P., Emmanuel, S., George, D., & Ioannis, K. (2016). A method for developing seismic intensity maps from twitter data. *Journal of Civil Engineering and Architecture*, 10, 839-852.

Arroyo, D., Ordaz, M., & Rueda, R. (2014). On the selection of ground-motion prediction equations for probabilistic seismic-hazard analysis. *Bulletin of the Seismological Society of America*.

Atkinson, G. (2015). Ground-Motion Prediction Equation for Small-to-Moderate Events at Short Hypocentral Distances, with Application to Induced-Seismicity Hazards. *Bulletin of the Seismological Society of America*, 105(2A), 981–992.

Atkinson, G.M., Wald, D.J. (2007). "Did You Feel It?" Intensity Data: A Surprisingly Good Measure of Earthquake Ground Motion. *Seismol. Res. Lett.*, 78 (3), pp362–368.

Auclair, S., Boulahya, F., Birregah, B., Quique, R., Ouaret, R., & Soulier, E. (2019). SURICATE-Nat: Innovative citizen centered platform for Twitter based natural disaster monitoring. In *2019 International Conference on Information and Communication Technologies for Disaster Management (ICT-DM)* (pp. 1-8). IEEE.

Bakun, W.H., Scotti, O. (2006). Regional intensity attenuation models for France and the estimation of magnitude and location of historical earthquakes. *Geophysical Journal International*, **164** (3), pp596–610. doi: 10.1111/j.1365-246X.2005.02808.x.

Bala A., Raileanu V., Zihan I., Ciugudean V., Grecu B. (2006). Physical and dynamic properties of the shallow sedimentary rocks in the Bucharest Metropolitan Area. *Romanian Reports in Physics*, Vol. 58, no. 2, 221-250.

Bala A., Ritter J.R.R., Hannich D., Balan S.F., Arion C. (2007a). Local site effects based on in situ measurements in Bucharest City, Romania. *Proceedings of the International symposium on Seismic Risk Reduction*, ISSRR-2007, Bucharest, 367-374.

Bala A., Zihan I., Ciugudean V., Raileanu V., Grecu B. (2007b). Physical and dynamic properties of the Quaternary sedimentary layers in and around Bucharest City. *Proceedings of the International symposium on Seismic Risk Reduction*, ISSRR-2007, Bucharest, 359-366.

Bălan S.F., Apostol B.F., (2016). The Necessity of Considering Nonlinear Seismology in Site Evaluation. *Conference Proceedings SGEM 2016*, p: 663-670.

Baudin, T., Barnolas, A., Gil, I., Martin-Alfageme., S. (2008). Carte géologique des Pyrénées à 1/400 000 (Socle). *BRGM - ITGE, Orléans*: Editions BRGM.

Beauval, C., Cotton, F., Abrahamson, N., Theodulidis, N., Delavaud, E., Scherbaum, F., Haendel, A. (2012). Regional differences in subduction ground motions. *arXiv preprint arXiv:1212.3287*.

Beinersdorf, S. (2016). *Intensitätsbasierte Bewertung der Verletzbarkeit allgemeiner Hochbauten in deutschen Erdbebengebieten*. Weimar, Bauhaus-Universität, Univ.-Verl. Schriftenreihe des Institutes für Konstruktiven Ingenieurbau, Heft 029. (Dissertation).

Beinersdorf, S., Schwarz, J. (2011). Reinterpretation der Schütterwirkungen des „Mitteleuropäischen Erdbebens“ vom 16. November 1911. In: *C. Könke ed. 12. D-A-CH Tagung – Erdbeben und Baudynamik*, Hannover, Deutschland, 15.–16. September 2011. Hannover, pp1–12.

Benn, N., Stange, S., Brüstle, W., Henk, A., Stribrny, B. (2006). Das Beben von Waldkirch am 5.12.2004. In: *Dt. geophys. Ges.*, 66. J.-Tag. Bremen, pp400–401.

Bindi, D., Massa, M., Luzi, L., Ameri, G., Pacor, F., Puglia, R., & Augliera, P. (2014). Pan-European ground-motion prediction equations for the average horizontal component of PGA, PGV, and 5 %-damped PSA at spectral periods up to 3.0 s using the RESORCE dataset. *Bulletin of Earthquake Engineering*, 12(1), 391–430.

Bindi, D., Pacor, F., Luzi, L., Puglia, R., Massa, M., Ameri, G., & Paolucci, R. (2011). Ground motion prediction equations derived from the Italian strong motion database. *Bulletin of Earthquake Engineering*, 9(6), 1899–1920.

Birant, D., & Kut, A. (2007). ST-DBSCAN: An algorithm for clustering spatial–temporal data. *Data & Knowledge Engineering*, 60(1), 208-221.

Bertil D., Roviro J., Jara J.A., Susagna T., Nus E., Goula X., Colas B., Dumont G., Cabanas L., Anton R., Calvet M. (2012). ShakeMap implementation for Pyrénées in France-Spain border: regional adaptation and earthquake rapid response process. In: *15th World Conference on Earthquake Engineering*.

Bommer, J., Douglas, J., Scherbaum, F., Cotton, F., Bungum, H., & Fäh, D. (2010). On the selection of ground-motion prediction equations for seismic hazard analysis. *Seismological Research Letters*.

Bommer, J.J., P.J. Stafford, B. Edwards, B. Dost, E. van Dedem, A. Rodriguez-Marek, P. Kruiver, J. van Elk, D. Doornhof & M. Ntinalexis (2017). Framework for a ground-motion model for induced seismic hazard and risk analysis in the Groningen gas field, The Netherlands. *Earthquake Spectra* 33(2), 481-498.

Bommer, J., Stafford, P., & Ntinalexis, M. (2019a). *Updated Empirical GMPEs for PGV from Groningen Earthquakes* – March 2019.

Bommer, JJ, B Edwards, PP Kruiver, A Rodriguez-Marek, PJ Stafford, B Dost, M Ntinalexis, E Ruigrok and J Spetzler (2019b). *V6 Ground-Motion Model (GMM) for Induced Seismicity in the Groningen Field - With Assurance Letter*. A report prepared for NAM. Available from: <https://nam-onderzoeksrapporten.data-app.nl/reports/download/groningen/en/b66dd73e-9ff9-4be8-9302-5a2b514414bd>.

Boccia Artieri, G., Giglietto, F., & Rossi, L. (2012). *terremoto! l'uso di Twitter durante il terremoto tra testimonianza, propagazione e commenti*.

Boore, D. (2010). Orientation-independent, nongeometric-mean measures of seismic intensity from two horizontal components of motion. *Bulletin of the Seismological Society of America*, 100(4), 1830–1835.

Boore, D., & Atkinson, G. (2008). Ground-Motion Prediction Equations for the Average Horizontal Component of PGA, PGV, and 5%Damped PSA at Spectral Periods between 0.01 s and 10.0 s. *Earthquake Spectra*, 24. doi:10.1193/1.2830434.

Boore, D., Stewart, J., Seyhan, E., & Atkinson, G. (2014). NGA-West2 equations for predicting PGA, PGV, and 5% damped PSA for shallow crustal earthquakes. *Earthquake Spectra*.

Boore, D., Stewart, J., Skarlatoudis, A., Seyhan, E., Margaris, B., Theodoulidis, N., Scordilis, E., Kalogeras, I., Klimis, N., & Melis, N. (2021). A Ground-Motion Prediction Model for Shallow Crustal Earthquakes in Greece. *Bulletin of the Seismological Society of America* 111 (2): 857–874.

Boore DM, Joyner WB (1997). Site amplifications for generic rock sites. *Bulletin of the Seismological Society of America* 87:327–341

Boore, D., Joyner, W., & Thomas, E. (1997). Equations for Estimating Horizontal Response Spectra and Peak Acceleration from Western North American Earthquakes: A Summary of Recent Work. *Seismological Research Letters*, 68 (1), 128–153.

Borcherdt, R. (1994). Estimates of site-dependent response spectra for design (methodology and justification). *Earthquake Spectra* (doi: 10. 1193/1.1585791.).

Bosco F., Deschamps A., Auclair S. (2019). Rapid Assessment of Seismic Impact in Western Alpine Area: Development in Italy and French Cross-Border Project (ALCOTRA RISVAL). 38 ° *Convegno Nazionale GNGTS (Roma, 12-14 Novembre 2019)*.

Bossu, R., Scotti, O., Cotton, F., Cushing, M., Levret, A. (2000). Determination of geomechanical site effects in France from macroseismic intensities and reliability of macroseismic magnitude of historical events. *Tectonophysics*, 324, pp81–110.

Bossu, R., Landès, M., Roussel, F., Steed, R., Mazet-Roux, G., Martin, S. S., & Hough, S. (2017). Thumbnail-based questionnaires for the rapid and efficient collection of macroseismic data from global earthquakes. *Seismological Research Letters*, 88(1), 72-81.

Bozzoni, F., Ozcebe, A.G., Balia, A., Lai, C.G., Borzi, B., Nascimbene, R., Khairy, D., Gabbianelli, G., Ippoliti, L., Berardi, S., Trombetti, M., Moroni, C. (2020) Seismic ground response analyses at an international airport in northern Italy by using a stochastic-based approach, *Journal of Theoretical and Applied Mechanics*, 58, 2, 499-511. DOI: 10.15632/jtam-pl/119017.

Bozzoni F., Scandella L., Lai C.G., Corigliano M. (2011). Assessment of the seismic damage of maritime ports by using GIS technology: the case study of the port of Salerno (in Italian), *Prog. Sismica*, 1(1), 117-137.

de Bruijn, J. A., de Moel, H., Jongman, B., Wagemaker, J., & Aerts, J. C. (2018). TAGGS: Grouping tweets to improve global geoparsing for disaster response. *Journal of Geovisualization and Spatial Analysis*, 2(1), 2.

Brüstle, W., Stange, S. (1999). *Geologische Untergrundklassen zum Entwurf von Normspektren für DIN 4149 (neu)*. Freiburg/Breisgau, Landesamt für Geologie, Rohstoffe und Bergbau. Vorstudie. p50.

Building Seismic Safety Council. (2004). *NEHRP recommended provisions for seismic regulations for new buildings and other structures*. Washington, D.C: FEMA 450.

Burks, L., Miller, M., & Zadeh, R. (2014). Rapid estimate of ground shaking intensity by combining simple earthquake characteristics with tweets. In *10th US Nat. Conf. Earthquake Eng., Front. Earthquake Eng.*, Anchorage, AK, USA, Jul. 21Y25.

Campbell, K., & Bozorgnia, Y. (2014). NGA-West2 Ground Motion Model for the Average Horizontal Components of PGA, PGV, and 5% Damped Linear Acceleration Response Spectra. *Earthquake Spectra*, 30, 1087–1115.

Campbell, K., & Bozorgnia, Y. (2008). NGA ground motion model for the geometric mean horizontal component of PGA, PGV, PGD and 5% damped linear elastic response spectra for periods ranging from 0.01 to 10 s. *Earthquake Spectra*, 24, 139-171.

Caprio, M., Tarigan, B., Worden, C.B., Wiemer, S., Wald, D.J. (2015). Ground Motion to Intensity Conversion Equations (GMICEs): A Global Relationship and Evaluation of Regional Dependency. *Bulletin of the Seismological Society of America*. doi: 10.1785/0120140286.

Cassard, D., Bertrand, G., Billa, M., Serrano, J.J., Tourlière, B., Angel, J.M., & Gaál, G. (2015). ProMine mineral databases: new tools to assess primary and secondary mineral resources in Europe. In *3D, 4D and Predictive Modelling of Major Mineral Belts in Europe* (pp. 9-58). Springer, Cham.

Cauzzi, C., Faccioli, E., Vanini, M., & Bianchini, A. (2015). Updated predictive equations for broadband (0.01–10 s) horizontal response spectra and peak ground motions, based on a global dataset of digital acceleration records. *Bulletin of Earthquake Engineering*, 13(6), 1587–1612.

CEN (2003). EuroCode 8: design of structures for earthquake resistance—part 1: general rules, seismic actions and rules for buildings. European Committee for Standardization, Bruxelles.

Chandler AM, Lam NTK, Tsang HH (2005). Shear wave velocity modelling in crustal rock for seismic hazard analysis. *Soil Dynamics and Earthquake Engineering* 25:167–185. <https://doi.org/10.1016/j.soildyn.2004.08.005>

Cheng, Z., Caverlee, J., & Lee, K. (2010). You are where you tweet: a content-based approach to geo-locating twitter users. In *Proceedings of the 19th ACM international conference on Information and knowledge management* (pp. 759-768).

Chiou, B., & Youngs, R. (2014). Update of the Chiou and Youngs NGA Model for the Average Horizontal Component of Peak Ground Motion and Response Spectra. *Earthquake Spectra*, 30, 1117–1153.

Choi, Y., & Stewart, J. (2005). Nonlinear Site Amplification as Function of 30 m Shear Wave Velocity. *Earthquake Spectra*, 21, 1-30. doi:<https://doi.org/10.1193/1.1856535>

Colas, B., Goula, X., Roullé, A., Garcia, I., Buxo, P., Roviro, I., Dewez, T., & Nus, E. (2010). *SISPyrr report R10*. Action 4.1: Shake-Map - Site effect corrections.

Colas, B., García, I., Buxó, P., Roullé, A. & Goula, X. (2012). Geological based seismic microzonation for Pyrenees. In *7th European Congress on REgional GEOscientific cartography and Information systems: 7th EUROGEO*.

Comunello, F., Parisi, L., Lauciani, V., Magnoni, F., & Casarotti, E. (2016). Tweeting after an earthquake: user localization and communication patterns during the 2012 Emilia seismic sequence. *Annals of Geophysics*, 59(5), 0537.

Costanzo A., Shaking maps based on cumulative absolute velocity and arias intensity: the cases of the two strongest earthquakes of the 2016-2017 central Italy seismic sequence. *ISPRS Int. J. Geo-Inf.* 7 (7) (2018), <https://doi.org/10.3390/ijgi7070244>.

Cotton, F., Scherbaum, F., Bommer, J., & Bungum, H. (2006). Criteria for selecting and adjusting ground-motion models for specific target regions: Application to central Europe and rock sites. *Journal of Seismology*, 10(2), 137–156.

Courboux, S., Barnolas, A., Calvet, M., Martin-Alfageme, S. (2008). Carte géologique du Quaternaire des Pyrénées à 1/400 000. *BRGM - ITGE, Orléans* : Editions BRGM.

Cremen, G., Werner, M., & Baptie, B. (2020). A new procedure for evaluating ground-motion models, with application to hydraulic-fracture-induced seismicity in the United Kingdom. *Bulletin of the Seismological Society of America*, 110(5), 2380–2397.

Cresci, S., La Polla, M., Marchetti, A., Meletti, C., & Tesconi, M. (2014). Towards a timely prediction of earthquake intensity with social media. *IIT TR-12/2014 Technical report*, IIT: Istituto di Informatica e Telematica, CNR.

Crowley, H., Weatherill, G., Riga, E., Pitilakis, K., Roullé, A., Tourlière, B., Lemoine, A., Gracianne Hidalgo, C. (2019). *Deliverable SERA : D26.4 Methods for Estimating Site Effects in Risk Assessments*.

Darendeli, M. (2001). *Development of a new family of normalized modulus reduction and material damping curves*. Ph.D. Thesis, Dept. of Civil Eng., University of Texas, Austin, TX.

Darzi, A., Zolfaghari, M., Cauzzi, C., & Donat, F. (2019). An Empirical Ground-Motion Model for Horizontal PGV, PGA, and 5% Damped Elastic Response Spectra (0.01–10 s) in Iran An Empirical Ground-Motion Model. *Bulletin of the Seismological Society of America*.

Delavaud, E., Cotton, F., Akkar, S., Scherbaum, F., Danciu, L., Beauval, C., Drouet, S., Douglas, J., Basili, R., Sandikkaya, M., & et al. (2012). Toward a ground-motion logic tree for probabilistic seismic hazard assessment in Europe. *Journal of Seismology*.

De Matteis R, Convertito V (2015). Near-real-time ground-motion updating for earthquake shaking prediction. *Bulletin of the Seismological Society of America*, 105(1): 400-408.

Derras, B., Bard, P., & Cotton, F. (2014). Towards fully data driven ground-motion prediction models for Europe. *Bulletin of Earthquake Engineering*, 12(1), 495–516.

Di Capua, G., Peppoloni, S., Amanti, M., Cipolloni, C., & Conte, G. (2016). Site classification map of Italy based on surface geology. *Geological Society, London, Engineering Geology Special Publications*, 27(1), 147-158.

DIN 4149-1 (1981). *Bauten in deutschen Erdbebengebieten - Lastannahmen, Bemessung und Ausführung üblicher Hochbauten*. Berlin [u.a.]. Deutsche Normen.

DIN 4149:2005. (2005). *Buildings in German earthquake regions – Design loads, analysis, and structural design of buildings*. Normenausschuss Bauwesen (NABau) im Deutschen Institut für Normung.

Dilley, M., Chen, R.S., Deichmann, U., Lerner-Lam, A.L. and Arnold, M. with Agwe, J., Buys, P., Kjekstad, O. , Bradfield Lyon, B. And Gregory Yetman, G. (2005). *Natural disaster hotspots: A global risk analysis, synthesis report*.

Dost, B., Eck, T., & Haak, H. (2004). Scaling of peak ground acceleration and peak ground velocity recorded in the Netherlands. *Bollettino Di Geofisica Teorica Ed Applicata*, 45, 153–168.

Dost, B., Ruigrok, E., & Spetzler, J. (2017). Development of seismicity and probabilistic hazard assessment for the Groningen gas field. *Netherlands Journal of Geosciences*, 96(5), s235-s245.

Douglas, J., & Edwards, B. (2016). Recent and future developments in earthquake ground motion estimation. *Earth-Science Reviews*, 160, 203–219.

Douglas, J., Edwards, B., Convertito, V., Sharma, N., Tramelli, A., Kraaijpoel, D., Cabrera, B., Maercklin, N., & Troise, C. (2013). Predicting Ground Motion from Induced Earthquakes in Geothermal Areas. *Bulletin of the Seismological Society of America*, 103(3), 1875–1897.

Douglas J., Inferred ground motions on Guadeloupe during the 2004 Les Saintes earthquake, *Bull. Earthq. Eng.* 5 (3) (2007) 363–376.

Earle, P., Guy, M., Buckmaster, R., Ostrum, C., Horvath, S., & Vaughan, A. (2010). OMG earthquake! Can Twitter improve earthquake response?. *Seismological Research Letters*, 81(2), 246-251.

Earle, P. S., Bowden, D. C., & Guy, M. (2011). Twitter earthquake detection: earthquake monitoring in a social world. *Annals of Geophysics*, 54(6).

Ester, M., Kriegel, H. P., Sander, J., & Xu, X. (1996). A density-based algorithm for discovering clusters in large spatial databases with noise. In *Kdd* (Vol. 96, No. 34, pp. 226-231).

Esteva, E. (1964). Espectros de temblores a distancias moderadas y grandes. *Bol. Soc.Mex. Inge. Sismica*, 2, 1–18.

European Committee for Standardization (2004). *Design of structures for earthquake resistance – Part 1: General rules, seismic actions and rules for buildings*. Brussels.

European Committee for Standardization. (2021). *Eurocode 8: Earthquake resistance design of structures (Draft) (1 ed.)*. Portugal: CEN.

Faenza, L., Michellini, A. (2010). Regression analysis of MCS intensity and ground motion parameters in Italy and its application in ShakeMap. *Geophys. J. Int.*, 180 (3), pp1138–1152.

Faenza, L., Michellini, A. (2011): Regression analysis of MCS intensity and ground motion spectral accelerations (SAs) in Italy. *Geophys. J. Int.*, 186 (3), pp1415–1430.

Farajpour, Z., Pezeshk, S., & Zare, M. (2019). A New Empirical Ground-Motion Model for Iran. *Bulletin of the Seismological Society of America*. doi:10.1785/0120180139

Fayjaloun, R., Gehl, P., Auclair, S., Boulahya, F., Guérin-Marthe, S., & Roulle, A. (2021a). Integrating strong-motion recordings and Twitter data for a rapid shakemap of macroseismic intensity. *International Journal of Disaster Risk Reduction*, 101927.

Fayjaloun, R., Negulescu, C., Roullé, A., Auclair, S., Gehl, P., & Faravelli, M. (2021b). Sensitivity of Earthquake Damage Estimation to the Input Data (Soil Characterization Maps and Building Exposure): Case Study in the Luchon Valley, France. *Geosciences*.

Francalanci, C., Guglielmino, P., Montalcini, M., Scalia, G., & Pernici, B. (2017). IMEXT: A method and system to extract geolocated images from Tweets—Analysis of a case study. In *11th International Conference on Research Challenges in Information Science (RCIS)* (pp. 382-390). IEEE.

Gehl P., Douglas J., D’Ayala D., Inferring earthquake ground-motion fields with Bayesian Networks, *Bull. Seismol. Soc. Am.* 107 (6) (2017).

Gibbs, J., Fumal, T., Boore, D., & Joyner, W. (1992). *Seismic velocities and geologic logs from borehole measurements at seven strong-motion stations that recorded the Loma Prieta earthquake*. US Geological Survey Report.

Gneiting, T., & Raftery, A. (2007). Strictly proper scoring rules, prediction, and estimation. *Journal of the American Statistical Association*.

Goodchild, M. F. (2007). Citizens as sensors: the world of volunteered geography. *GeoJournal*, 69(4), 211-221.

Grace, R., Kropczynski, J., Pezanowski, S., Halse, S. E., Umar, P., & Tapia, A. H. (2017). Social Triangulation: A new method to identify local citizens using social media and their local information curation behaviors. In *ISCRAM*.

Graham, M., Hale, S. A., & Gaffney, D. (2014). Where in the world are you? Geolocation and language identification in Twitter. *The Professional Geographer*, 66(4), 568-578.

Grünthal, G., Musson, R.M.W., Schwarz, J., Stucchi, M. (1993). European macroseismic scale 1992 (updated MSK scale). G. Grünthal ed. Luxembourg. *Cahiers du Centre européen de géodynamique et de séismologie* v. 7.

Grünthal, G., Musson, R.M.W., Schwarz, J., Stucchi, M. (1998). European Macroseismic Scale 1998. G. Grünthal ed. Luxembourg. *Cahiers du Centre Européen de Géodynamique et de Séismologie* 15.

Guérin-Marthe S., Gehl P., Fayjaloun R., Negulescu C., & Auclair S. (2021). Rapid earthquake response: the state-of-the art and recommendations with a focus on European systems. *International Journal of Disaster Risk Reduction*, 101958.

Gutenberg, B., Richter, C.F. (1956). Earthquake magnitude, intensity, energy, and acceleration: (Second paper). *Bull. Seismol. Soc. Am.*, 46 (2), pp105–145.

Hannich D., Huber G., Ehret D., Hoetzl H., Balan S., Bala A., Bretotean M., Ciugudean V. (2006). SCPTU Techniques Used for shallow geologic/hydrogeologic Site Characterization in Bucharest, Romania. *3-rd International Symposium on the Effects of Surface Geology on Seismic Motion*, Grenoble, France, 30 Aug. - 1 Sept. 2006, paper 71

Hinzen, K.-G., Oemisch, M. (2001). Location and Magnitude from Seismic Intensity Data of Recent and Historic Earthquakes in the Northern Rhine Area, Central Europe. *Bulletin of the Seismological Society of America*, 91 (1), pp40–56.

Heath D.C., Wald D.J., Worden C.B., Thompson E.M., Smoczyk G.M. (2020). A global hybrid VS30 map with a topographic slope-based default and regional map insets. *Earthq. Spectra*, <https://doi.org/10.1177/8755293020911137>.

Hosser, D. (1987). Realistische seismische Lastannahmen für Bauwerke. *Bauing*, 62, pp567–574.

Huang, C., & Galasso, C. (2019). Ground-motion intensity measure correlations observed in Italian strong-motion records. *Earthquake Engineering & Structural Dynamics*, 48.

Jayaram N., Baker J.W. (2009). Correlation model for spatially distributed ground-motion intensities. *Earthq. Eng. Struct. Dynam.* 38 (15), 1687–1708.

Johannesson, H. (2014). *Geological map of Iceland – 1/600 000 – Bedrock geology*, Icelandic Institute of Natural History.

Joyner, W., & Boore, D. (1993). Methods for regression analysis of strong-motion data. *Bulletin of the Seismological Society of America*, 83(2), 469–487.

Joyner, W., & Boore, D. (1981). Peak horizontal acceleration and velocity from strong-motion records including records from the 1979 Imperial Valley, California, earthquake. (T. S. America, Ed.) *Bulletin of the seismological Society of America*, 71, 2011--2038.

Kaka, S.I., Atkinson, G.M. (2004). Relationships between Instrumental Ground-Motion Parameters and Modified Mercalli Intensity in Eastern North America. *Bulletin of the Seismological Society of America*, 94 (5), pp1728–1736. doi: 10.1785/012003228.

Kaklamanos, J., Baise, L., & Boore, D. (2011). Estimating unknown input parameters when implementing the NGA ground-motion prediction equations in engineering practice. *Earthquake Spectra*, 27(4), 1219–1235.

Kale, Ö., Akkar, S., Ansari, A., & Hamzehloo, H. (2015). A Ground-Motion Predictive Model for Iran and Turkey for Horizontal PGA, PGV, and 5% Damped Response Spectrum: Investigation of Possible Regional Effects. *Bulletin of the Seismological Society of America*, 105, 693-980. doi:10.1785/0120140134

Kienzle A., Hannich D., Wirth W., Ehret D., Rohn J., Ciugudean V., Czurda K. (2006). A GIS-based study of earthquake hazard as a tool for the microzonation of Bucharest. *Engineering Geology* 87, 13–32.

King S.A., Hortacsu A., Hart G.C.(2004). Post-earthquake estimation of site-specific strong ground motion. In: *13th World Conference on Earthquake Engineering*.

Kottke, A.R. & E.M. Rathje (2008). *Technical Manual for STRATA. PEER Report 2008/10*. Pacific Earthquake Engineering Research Center, University of California at Berkeley, February, 84 pp.

Kövesligethy, R. v. (1907). Seismischer Stärkegrad und Intensität der Beben. *Gerlands Beiträge zu Geophysik*, 8, pp363–366 (org. publ. 1906).

Kowsari, M., Halldorsson, B., Hrafinkelsson, B., Snæbjörnsson, J. Þ., & Jónsson, S. (2019). Calibration of ground motion models to Icelandic peak ground acceleration data using Bayesian Markov Chain Monte Carlo simulation. *Bulletin of Earthquake Engineering*, 17(6), 2841-2870.

Kowsari, M., Sonnemann, T., Halldorsson, B., Hrafinkelsson, B., Snæbjörnsson, J. Þ., & Jonsson, S. (2020). Bayesian inference of empirical ground motion models to pseudo-spectral accelerations of south Iceland seismic zone earthquakes based on informative priors. *Soil Dynamics and Earthquake Engineering*, 132, 106075.

Kropivnitskaya, Y., Tiampo, K. F., Qin, J., & Bauer, M. A. (2017a). Real-Time Earthquake Intensity Estimation Using Streaming Data Analysis of Social and Physical Sensors. *Pure & Applied Geophysics*, 174(6), 2331.

Kropivnitskaya, Y., Tiampo, K. F., Qin, J., & Bauer, M. A. (2017b). The predictive relationship between earthquake intensity and tweets rate for real-time ground-motion estimation. *Seismological research letters*, 88(3), 840-850.

Kruiver PP, Wiersma A, Kloosterman F, de Lange G, Korff M, Stafleu J, Busschers FS, Harting R, Gunnink JL, Green RA, van Elk J, Doornhof D (2017a). Characterisation of the Groningen

subsurface for seismic hazard and risk modelling. *Netherlands Journal of Geosciences*, 96(5), S215-S233. <https://doi.org/10.1017/njg.2017.11>

Kruiver PP, van Dedem E, Romijn R, de Lange G, Korff M, Stafleu J, Gunnink JL, Rodriguez-Marek A, Bommer JJ, van Elk J & Doornhof D (2017b). An integrated shear-wave velocity model for the Groningen gas field, The Netherlands. *Bulletin of Earthquake Engineering* 15 (9): 3555–3580. <https://doi.org/10.1007/s10518-017-0105-y>

Kruiver PP, de Lange G, Korff, M, Wiersma A, Harting R, Kloosterman FH, Stafleu J, Gunnink JL, van Elk J & Doornhof D (2018). Parameterization of Geological Models for Regional Site Response and Liquefaction Potential Indicators (Extended Abstract, 12 pp). *16th European Conference on Earthquake Engineering*, June 18 – 21, 2018, Thessaloniki, Greece.

Kryvasheyev, Y., Chen, H., Obradovich, N., Moro, E., Van Hentenryck, P., Fowler, J., & Cebrian, M. (2016). Rapid assessment of disaster damage using social media activity. *Science advances*, 2(3), e1500779.

Kuehn, N., & Scherbaum, F. (2015). Ground-motion prediction model building: a multilevel approach. *Bulletin of Earthquake Engineering*, 13(9), 2481–2491.

Landesamt für Geologie Rohstoffe und Bergbau Baden-Württemberg (1998). *Geowissenschaftliche Übersichtskarten Baden-Württemberg 1:350.000 - 20 landesweite Karten für Planung, Wirtschaft und Umwelt*. Freiburg. (CD-ROM).

Lang, D.H. (2004). *Schadenspotential seismischer Bodenbewegung unter Berücksichtigung lokaler Standorteffekte*. Bauhaus-Universität Weimar. (Dissertation).

Lang, D.H., Schwarz, J. (2006). Instrumental subsoil classification of Californian strong motion sites based on single-station measurements. In: *8th U.S. National Conference on Earthquake Engineering, April 18-21, 2006*. San Francisco, California, p10, (Paper No. 120).

Lanzano G., P. (2018). *Engineering Strong Motion Database (ESM) flatfile [Data set]*. Istituto Nazionale di Geofisica e Vulcanologia (INGV).

Lanzano, G., Luzi, L., D'Amico, V., Pacor, F., Meletti, C., Marzocchi, W., Rotondi, R., & Varini, E. (2020). Ground motion models for the new seismic hazard model of Italy (MPS19): selection for active shallow crustal regions and subduction zones. *Bulletin of Earthquake Engineering*, 18(8), 3487–3516.

Lanzano, G., Luzi, L., Pacor, F., Felicetta, C., Puglia, R., Sgobba, S., & D'Amico, M. (2019). A Revised Ground-Motion Prediction Model for Shallow Crustal Earthquakes in Italy. *Bulletin of the Seismological Society of America*, 109(2), 525–540.

Lee, C. T., & Tsai, B. R. (2008). Mapping Vs30 in Taiwan. *TAO: Terrestrial, Atmospheric and Oceanic Sciences*, 19(6), 6.

Lee, W.H.K. (2009): A Glossary for Rotational Seismology. *Bulletin of the Seismological Society of America*, **99** (2B), pp1082–1090. doi: 10.1785/0120080342.

Lemoine A., Douglas J., Cotton F. (2012). Testing the applicability of correlations between topographic slope and $V_s/30$ for Europe. *Bull. Seismol. Soc. Am.* 102 (6) (2012) 2585–2599.

Li, X., Zhai, C., Wen, W., & Xie, L. (2020). Ground Motion Prediction Model for Horizontal PGA, 5% Damped Response Spectrum in Sichuan-Yunnan Region of China. *Journal of Earthquake Engineering*, 24, 1829-1866. doi:10.1080/13632469.2018.1485600

Mărmureanu Gh., Mișicu M., Cioflan C., Bălan F.S., Apostol B.F. (2005). Nonlinear Seismology-The Seismology of the XXI Century. In: *Lecture Notes of Earth Sciences, Perspective in Modern Seismology*, vol.105, Springer Verlag, Heidelberg, Germany, pp 47-67.

Mărmureanu Gh., Mărmureanu Al., Cioflan C.O., Manea E.F. (2014) The Real Evidence of Effects from Source to free Field as base for Nonlinear Seismology. *EGU General Assembly* April 27-May 02, Austria.

Marmureanu Gh., Moldoveanu C., Cioflan C. (1996). The dependence of the spectral amplification factors of Vrancea earthquake magnitudes. *Revue Roumaine des Sciences Techniques, série Mécanique Appliquée*, Romania, Tome 41, No.5-6, pp 487-491.

McPherson, A., & Hall, L. (2013). Site classification for earthquake hazard and risk assessment in Australia. *Bulletin of the Seismological Society of America*, 103(2A), 1085-1102.

Medvedev, S.V. (1965). *Engineering Seismology*. Jerusalem, Israel program for Scientific Translation.

Medvedev, S.W., Sponheuer, W., Kárník, V. (1965). Seismische Intensitätsskala MSK-1964. In: Bericht über die Weiterentwicklung der seismischen Skala. *Veröffentlichungen des Instituts für Geodynamik*, Jena. Berlin, pp12–17, (Progress Report on Seismic Scale).

Medvedev, S.V., Sponheuer, W. (1969). Scale of seismic intensity. In: *World Conf. Earthquake Engr. Santiago, Chile*, pp143–153, (A-2).

Mendoza, M., Poblete, B., & Valderrama, I. (2018). Early tracking of people's reaction in Twitter for fast reporting of damages in the Mercalli scale. In: *International Conference on Social Computing and Social Media* (pp. 247-257). Springer, Cham.

Mendoza, M., Poblete, B., & Valderrama, I. (2019). Nowcasting earthquake damages with Twitter. *EPJ Data Science*, 8(1), 3.

Menq, F.Y. (2003). *Dynamic Properties of Sandy and Gravelly Soils*. PhD Thesis, Department of Civil Engineering, University of Texas, Austin, TX.

Mihăilescu V. (1924). *Vlășia and Mostiștea* / BSRG, Romania, vol.: XLIII.

- Montalva, G. (2010). *Site-specific seismic hazard analyses*. Washington State University.
- Murphy, K. P. (2002). *Dynamic Bayesian networks: representation, inference and learning*. Ph.D. Dissertation, University of California, Berkeley.
- Murphy, J., O'Brien, L. (1977). The correlation of peak ground acceleration amplitude with seismic intensity and other physical parameters. *Bull. Seismol. Soc. Am.*, 67 (3), pp877–915.
- Musson, R.M.W. (2002). Effective Peak Acceleration As A Parameter For Seismic Hazard Studies. In: *12th European Conference on Earthquake Engineering, 9. - 13. September 2002*. London, UK, p9.
- Olteanu, A., Vieweg, S., & Castillo, C. (2015). What to expect when the unexpected happens: Social media communications across crises. In: *Proceedings of the 18th ACM conference on computer supported cooperative work & social computing* (pp. 994-1009).
- Ouaret, R., Birregah, B., Soulier, E., Auclair, S., & Boulahya, F. (2019). Random Forest location prediction from social networks during disaster events. In *2019 Sixth International Conference on Social Networks Analysis, Management and Security (SNAMS)* (pp. 535-540). IEEE.
- Park, D., & Hashash, Y. (2004). Soil damping formulation in nonlinear time domain site response analysis. *Journal of Earthquake Engineering*, 8, 249-274. doi:10.1142/S1363246904001420
- Phung, V.-B., Loh, C., Chao, S., & Abrahamson, N. (2020). Ground motion prediction equation for Taiwan subduction zone earthquakes. *Earthquake Spectra*, 36, 1331-1358. doi:10.1177/8755293020906829
- Project NATO Science for Peace Project/981882 a cooperation between INFP and University of Karlsruhe/ Collaborative Research Centre (CRC461). "*Strong Earthquakes*" (2005-2007).
- Rahpeyma S, Halldorsson B, Hrafinkelsson B, et al (2019). Site effect estimation on two Icelandic strong-motion arrays using a Bayesian hierarchical model for the spatial distribution of earthquake peak ground acceleration. *Soil Dynamics and Earthquake Engineering* 120:369–385. <https://doi.org/10.1016/j.soildyn.2019.02.007>
- Rahpeyma S, Halldorsson B, Hrafinkelsson B, Jónsson S (2018). Bayesian hierarchical model for variations in earthquake peak ground acceleration within small-aperture arrays. *Environmetrics* 29:e2497. <https://doi.org/10.1002/env.2497>
- Rahpeyma S, Halldorsson B, Hrafinkelsson B, Jonsson S (2020). Frequency dependent site factors for the Icelandic strong-motion array from a Bayesian hierarchical model of the spatial distribution of spectral accelerations. *Earthquake Spectra* (in review).
- Resch, B., Usländer, F., & Havas, C. (2018). Combining machine-learning topic models and spatiotemporal analysis of social media data for disaster footprint and damage assessment. *Cartography and Geographic Information Science*, 45(4), 362-376.

Ritter J.R.R., Balan, S., Bonjer, K.-P., Diehl, T., Forbriger, T., Marmureanu, G., Wenzel F. and Wirth, W. (2005). Broadband urban seismology in the Bucharest metropolitan area. *Seism. Res. Lett.*, 76, 573-579.

Rodríguez-Marek, A., & Bray, J. (1997). Geotechnical site categories. *Proceedings of the First PEERPG&E Workshop on Seismic Reliability of Utility Lifelines*.

Rodríguez-Marek, A., Bray, J., & Abrahamson, N. (2001). An empirical geotechnical seismic site response procedure. *Earthquake spectra*, 17, 65--87.

Rodríguez-Marek, A., P.P. Kruiver, P. Meijers, J.J. Bommer, B. Dost, J. van Elk & D. Doornhof (2017). A regional site-response model for the Groningen gas field. *Bulletin of the Seismological Society of America* 107(5), 2067-2077. <https://doi.org/10.1785/0120160123>

Roselli, P., Marzocchi, W., & Faenza, L. (2016). Toward a new probabilistic framework to score and merge ground-motion prediction equations: The case of the Italian Region. *Bulletin of the Seismological Society of America*.

Rosenhauer, W., Ahorner, L. (1994). Seismic hazard assessment for the Lower Rhine Embayment before and after the 1992 Roermond earthquake. *Geologie en Mijnbouw*, 73, pp415–424.

Rosenhauer, W. (1999). Benutzungs-Anleitung für das Programm PSSAEL zur probabilistischen seismischen Standort-Analyse. *Rösrath, Bericht im Auftrag des VGB*. p42.

Rosenhauer, W. (2005). Zuordnung individueller Intensitäten in PSSAEL. *Rösrath*. p38. (*Bericht - Im Auftrag der VGB-PowerTech Service GmbH, Essen*).

Rota, M., Lai, C.G., Strobbia, C., (2011). Stochastic 1D site response analysis at a site in central Italy. *Soil Dyn. Earthq. Eng.* 31 (4), 626-639. DOI: 10.1016/j.soildyn.2010.11.009.

Roullé A., Auclair S., Dewez T., Hohmann A., Lemoine A., Rey J. (2010). Cartographie automatique des classes de sol à l'échelle régionale à partir d'un modèle numérique de terrain ou de surface. *Rapport final. BRGM/RP-58853-FR* (in French).

Roullé, A., & Colas, B. (2013). *SISPy report R12b. Action 4.2: Microzonage sismique de la vallée de Luchon (France)*.

Ruigrok, E., & Dost, B. (2020). *Advice on the computation of peak- ground-velocity confidence regions for events in gas fields other than the Groningen gas field*.

Sakaki, T., Okazaki, M., & Matsuo, Y. (2010). Earthquake shakes Twitter users: real-time event detection by social sensors. In: *Proceedings of the 19th international conference on World wide web* (pp. 851-860).

Scherbaum, F., Delavaud, E., & Riggelsen, C. (2009). Model selection in seismic hazard analysis: An information-theoretic perspective. *Bulletin of the Seismological Society of America*.

Schmitt, T. (2012). *Zusammenhänge zwischen makroseismischen Intensitäten und Antwortspektren, Erdbebendauer und Bauwerksvulnerabilität*. Aachen, Mainz. (Dissertation).

Schnabel, P., Lysmer, J., & Seed, H. (1972). *A computer program for earthquake response analysis of horizontally layered sites*. University of California Berkeley.

Schwarz, J., Abrahamczyk, L., Amstein, S., Kaufmann, C., Langhammer, T. (2006a). Das Waldkirch-Erdbeben (Baden-Württemberg) vom 5. Dezember 2004. *Bautechnik*, 83 (3), pp202–208.

Schwarz, J., Langhammer, T., Kaufmann, C. (2006b). Quantifizierung der Schadenspotentiale infolge Erdbeben - Teil 2: Modellstudie Baden-Württemberg. *Bautechnik*, 83 (12), pp827–841.

Schwarz, J., Lang, D.H., Kaufmann, C., Ende, C. (2007). Empirical ground-motion relations for Californian strong-motion data based on instrumental subsoil classification. In: *9th Canadian Conference on Earthquake Engineering*. Ottawa, Ontario, Canada, pp489–500, (paper 1359). https://edac.biz/fileadmin/pdf/1359_EJ.pdf [Accessed 08-04-14].

Schwarz, J., Beinersdorf, S., Kaufmann, C., Langhammer, T. (2008a). Damage scenarios for Central Europe - Reinterpretation of historical earthquakes. In: T. Camelbeeck, H. Degée, G. Degrande, & A. Sabbe eds. *Seismic Risk 2008 - Earthquakes in North-Western Europe*. Liège, pp311–320.

Schwarz, J., Beinersdorf, S., Swain, T., Langhammer, T., Leipold, M. (2008b). Vulnerability of masonry structures - experience from recent damaging earthquakes in Central Europe. In: T. Camelbeeck, H. Degée, G. Degrande, & A. Sabbe eds. *Seismic Risk 2008 - Earthquakes in North-Western Europe*. Liège, pp209–216. doi: 10.13140/2.1.5031.4248.

Schwarz, J., Beinersdorf, S., Kaufmann, C., Langhammer, T. (2008). Damage scenarios for Central Europe - Reinterpretation of historical earthquakes. In: T. Camelbeeck, H. Degée, G. Degrande, & A. Sabbe eds. *Seismic Risk 2008 - Earthquakes in North-Western Europe*. Liège, pp311–320.

Schwarz, J., Beinersdorf, S., Swain, T., Langhammer, T., Leipold, M. (2008). Vulnerability of masonry structures - experience from recent damaging earthquakes in Central Europe. In: T. Camelbeeck, H. Degée, G. Degrande, & A. Sabbe eds. *Seismic Risk 2008 - Earthquakes in North-Western Europe*. Liège, pp209–216.

Schwarz, J., Beinersdorf, S., Golbs, C. (2014). Auswertung der in PSSAEL implementierten Intensitäts-Zuordnungsbeziehung (IZB) und Ergebnisse der Variation der Koeffizientenfestlegung; Vergleich der Modellannahmen mit den regionalen makroeismischen Befunden nach EK DAG. Weimar. (*Unveröffentlichtes Arbeitsmaterial*)

Schwarz, J., Beinersdorf, S., Golbs, C., Kaufmann, C. (2015). Simulation von Erdbebenbibliotheken für risikoorientierte und verhaltensbasierte Bemessungskonzepte. *SIA 0255, Erdbeben und bestehende Bauten*, pp31–38.

Schwarz, J., Beinersdorf, S., Kaufmann, C., Langhammer, T. (2016). SHAKEMaps – effiziente Tools für die Reinterpretation und Prognose von Erdbebenschäden. *Bautechnik*, 93 (4), pp230–242.

Schwarz, J. (2018). *Background document for EN 1998-1 produced by SC8T1 (Project Team 1). Proposed modifications of section 3.2.2 basic representation of seismic action*. Weimar: Bauhaus-Universität Weimar.

Schwarz, J., Beinersdorf, S., Meidow, H. (2019a). *Magnitudenorientierter Erdbebenkatalog für deutsche und angrenzende Gebiete – EK DAG*. Bauhaus-Universität Weimar, Fakultät Bauingenieurwesen, Zentrum für die Ingenieuranalyse von Erdbebenschäden (Erdbebenzentrum) am Institut für Konstruktiven Ingenieurbau ed. Weimar, Bauhaus-Universitätsverlag als Imprint von arts + science weimar GmbH.

Schwarz, J., Kaufmann, C., Golbs, C., Beinersdorf, S. (2019b). Gefährdungsanalysen und Einwirkungsmodelle für Gebiete mit vorwiegend induzierter Seismizität. *Bautechnik*, 96 (3), pp269–282. doi: [10.1002/bate.201800013](https://doi.org/10.1002/bate.201800013).

Schwarz, J., Abrahamczyk, L., Hadidian, N., Haweyou, M., Kaufmann, Ch. (2021). Report on Knowledge-based exposure modelling framework depending on the accuracy and completeness of available data. *Deliverable D4.1. TURNkey project. H2020-SC5-2018*.

Sieberg, A. (1918). Material zum Süddeutschen Erdbeben vom 16. November 1911. (*unveröffentlicht - Manuskript*).

Sieberg, A. (1923). *Geologische, physikalische und angewandte Erdbebenkunde*. Jena, Fischer.

Sieberg, A. (1937). Qualitative Versuche über Erdbebenstöße und ihre zerstörende Wirkung auf Ziegelmauerwerk - Beiträge zur erdbebenkundlichen Bautechnik und Bodenmechanik. Leipzig & Berlin. *Veröffentlichungen der Reichsanstalt für Erdbebenforschung Jena* 29.

Sedaghati, F., & Pezeshk, S. (2017). Partially Nonergodic Empirical Ground-Motion Models for Predicting Horizontal and Vertical PGV, PGA, and 5% Damped Linear Acceleration Response Spectra Using Data from the Iranian Plateau. *Bulletin of the Seismological Society of America*, 107, 934–948. doi:10.1785/0120160205

Shabestari K.T., Yamazaki F. (2001). A proposal of instrumental seismic intensity scale compatible with MMI evaluated from three-component acceleration records. *Earthq. Spectra* 17 (4), 711–723.

Sokolov, V., Bonjer, K., Wenzel, F., Grecu, B., & Radulian, M. (2008). Ground-motion prediction equations for the intermediate depth Vrancea (Romania) earthquakes. *Bulletin of Earthquake Engineering*, 6(3), 367–388.

Sponheuer, W. (1960). Methoden zur Herdtiefenbestimmung in der Makroseismik. Berlin. *Veröffentlichungen des Instituts für Bodendynamik und Erdbebenforschung in Jena*.

Spudich, P., Rowshandel, B., Shahi, S., Baker, J., & Chiou, B.J. (2014). Comparison of NGA-West2 directivity models. *Earthquake Spectra*, 30(3), 1199–1221.

Stafford P.J. (2012). Evaluation of structural performance in the immediate aftermath of an earthquake: a case study of the 2011 Christchurch earthquake. *Int. J. Forensic Eng.* 1(1), 58–77.

Stafford, P. J. (2019). Continuous integration of data into ground-motion models using Bayesian updating. *Journal of Seismology*, 23(1), 39-57.

Starbird, K., Muzny, G., & Palen, L. (2012). Learning from the crowd: collaborative filtering techniques for identifying on-the-ground Twitterers during mass disruptions. In: *Proceedings of 9th International Conference on Information Systems for Crisis Response and Management, ISCRAM* (pp. 1-10).

Stewart, J. P., Afshari, K., & Hashash, Y. M. (2014). *Guidelines for performing hazard-consistent one-dimensional ground response analysis for ground motion prediction*. PEER Report, 16, 117.

Stewart, J., Choi, Y., & Liu, A. (2001). Amplification factors for spectral acceleration in active regions. *Bulletin of the Seismological Society of America*.

Stewart, J.P., Zimmaro, P., Lanzo, G., Mazzoni, S., Ausilio, E., Aversa, S., Bozzoni, F., Cairo, R., Capatti, M.C., Castiglia, M., Chiabrando, F., Chiaradonna, A., d’Onofrio, A., Dashti, S., De Risi R., de Silva, F., della Pasqua, F., Dezi, F., Di Domenica, A., Di Sarno, L., Durante, M.G., Falcucci, E., Foti, S., Franke, K.W., Galadini, F., Giallini, S., Gori, S., Kayen, R.E., Kishida, T., Lingua, A., Lingwall, B., Mucciacciaro, M., Pagliaroli, A., Passeri, F., Pelekis, P., Pizzi, A., Reimschiessel, B., Santo, A., Santucci de Magistris F., Scasserra, G., Sextos, A., Sica, S., Silvestri, F., Simonelli, A.L., Spanò, A., Tommasi P., Tropeano G. (2018). Reconnaissance of 2016 Central Italy Earthquake Sequence. *Earthquake Spectra*, Vol. 34, No. 4, pp. 1547-1555, November 2018.

Stewart, J., Klimis, N., Savvaidis, A., Theodoulidis, N., Zargli, E., Athanasopoulos, G., . . . Margaris, B. (2014). Compilation of a Local VS Profile Database and Its Application for Inference of VS30 from Geologic- and Terrain-Based Proxies. *Bulletin of the Seismological Society of America*, 104. doi:10.1785/0120130331

Stromeyer, D., Grünthal, G. (2009). Attenuation Relationship of Macroseismic Intensities in Central Europe. *Bull. Seismol. Soc. Am.*, 99 (2A), pp554–565.

Tapia, M. (2006). *Desarrollo y aplicación de métodos avanzados para la caracterización de la respuesta sísmica del suelo a escala regional y local*. Tesis Doctoral. Universitat Politècnica de Catalunya. (Doctoral dissertation).

Toma-Danila D., Ciaflan C.O., Ionescu C., Tigianescu A., The near real-time system for estimating the seismic damage in Romania (SeisDaRo). Recent upgrades and results, in: 16th European Conference on Earthquake Engineering, 2018.

Tselentis, G.-A., Danciu, L. (2008): Empirical Relationships between Modified Mercalli Intensity and Engineering Ground-Motion Parameters in Greece. *Bulletin of the Seismological Society of America*, **98** (4), pp1863–1875. doi: <https://doi.org/10.1785/0120070172>.

Trifunac, M.D., Brady, A.G. (1975): On correlation of seismoscope response with earthquake magnitude and Modified Mercalli Intensity. *Bull. Seismol. Soc. Am.*, 65 (2), pp307–321.

Tusa, G., Horst, L., & Raffaele, A. (2020). Localizing ground motion models in volcanic terranes: Shallow events at Mt. Etna, Italy, revisited. *Bulletin of the Seismological Society of America*. doi:10.1785/0120190325

van Ginkel, J., Ruigrok, E., & Herber, R. (2019). Assessing soil amplifications in Groningen, the Netherlands. *First Break*, 37(10), 33-38.

Vanmarcke E., *Random Fields, Analysis and Synthesis*, The MIT Press, 1983.

Văcăreanu R., Radulian M., Iancovici M., Pavel F. (2014). Fore-arc and back-arc ground motion prediction model for Vrancea intermediate depth seismic source. In: *The 2nd European Conference on Earthquake Engineering and Seismology*, Istanbul, Turkey.

Vilanova SP, Narciso J, Carvalho JP, et al (2018). Developing a Geologically Based Vs30 Site-Condition Model for Portugal: Methodology and Assessment of the Performance of Proxies Developing a Geologically Based VS30 Site-Condition Model for Portugal. *Bulletin of the Seismological Society of America* 108:322–337. <https://doi.org/10.1785/0120170213>

Vogfjörd KS, Kjartansson E, Slunga R, et al (2010). *Development and Implementation of Seismic Early Warning Processes in South-West Iceland*. SAFER EU-Project Report no. VÍ 2010-012, Icelandic Meteorological Office.

Wald, D.J., Quitoriano, V., Heaton, T.H., Kanamori, H. (1999a). Relationships between Peak Ground Acceleration, Peak Ground Velocity, and Modified Mercalli Intensity in California. *Earthq. Spectra*, 15 (3), pp557–564.

Wald D., Quitoriano V., Heaton T.H., Kanamori H., Scrivner C.W., Worden C.B. (1999b). TriNet 'ShakeMaps': rapid generation of peak ground-motion and intensity maps for earthquakes in Southern California. *Earthq. Spectra* 15 (3) 537–556.

Wald, D.J., Wald, L., Dewey, J., Quitoriano, V., Adams, E. (2001). *Did You Feel It?: Community-made Earthquake Shaking Maps*. US Geological Survey. <http://geopubs.wr.usgs.gov/factsheet/fs030-01/>.

Wald D., Allen T. (2007). Topographic slope as a proxy for seismic site conditions and amplification. *Bull. Seismol. Soc. Am.* 97 (5) 1379–1395.

Wald, D. J (2010). PAGER-Rapid Assessment of an Earthquakes Impact. In: *Encyclopedia of solid Earth Geophysics*, Harsh Gupta(Ed.), Springer, Part 5, 243-245.

- Wald D.J., Worden C.B., Quitariano V., Pankow K.L. (2006). *ShakeMap® Manual, Technical Manual, Users Guide, and Software Guide*.
- Wald D.J., Jaiswal K.S., Marano K.D., Bausch D. (2011). Earthquake impact scale. *Nat. Hazards Rev.* 12 (3), [https://doi.org/10.1061/\(ASCE\)NH.1527-6996.0000040](https://doi.org/10.1061/(ASCE)NH.1527-6996.0000040).
- Wald D.J., Quitariano V., Worden B., Hopper M., Dewey J.W. (2011). USGS “Did You Feel It?” internet-based macroseismic intensity maps. *Ann. Geophys.* 54 (6).
- Walling, M., Silva, W., & Abrahamson, N. (2008). Nonlinear Site Amplification Factors for Constraining the NGA Models. *Earthquake Spectra*, 24, 243-255. doi:<https://doi.org/10.1193/1.2934350>.
- Waltl P (2013). *Geomorphology and Building Stock of Húsavík, North Iceland: A Uniform GIS Database for Application in Hazard and Risk Modeling*. Master's Thesis, University of Natural Resources and Life Sciences. Department of Civil Engineering and Natural Hazards, Vienna, Austria.
- Waltl P, Halldorsson B, Pétursson HG, Fiebig M (2018). Geomorphic assessment of the urban setting of Húsavík, North Iceland, in the context of earthquake hazard. *Jökull* 68:27–46.
- Wieck, J., Schneider, G. (1980). Herdnahe Messungen während der Erdbebenserie im Herbst 1978 auf der westlichen Schwäbischen Alb. *Mitteilungen Inst. Für Bautech.*, 11 (1), pp1–3.
- Wills, C. J., & Clahan, K. B. (2006). Developing a map of geologically defined site-condition categories for California. *Bulletin of the Seismological Society of America*, 96(4A), 1483-1501.
- Wills CJ, Petersen M, Bryant WA, et al (2000). A site-conditions map for California based on geology and shear-wave velocity. *Bulletin of the Seismological Society of America* 90:S187–S208
- Wood, H.O., Neumann, F. (1931). Modified Mercalli intensity scale of 1931. *Bulletin of the Seismological Society of America*, 21, pp277–283.
- Worden C.B., Wald D., Allen T., Lin K.W., Garcia D., Cua G. (2010). A revised ground-motion and intensity interpolation scheme for ShakeMap. *Bull. Seismol. Soc. Am.* 100 (6), 3083–3096.
- Worden C.B., Thompson E.M., Baker J.W., Bradley B.A., Luco N., Wald D. (2018). Spatial and spectral interpolation of ground-motion intensity measure observations. *Bull. Seismol. Soc. Am.* 108 (2), 866–875.
- Worden, C.B., Thompson, E.M., Hearne, M.G., Wald, D.J. (2020). *ShakeMap Manual Online: technical manual, user's guide, and software guide*. USGS ed. (*ShakeMap Vers. 4*; <http://usgs.github.io/shakemap/>). <https://doi.org/10.5066/F7D21VPQ>.

Zahra, K., Imran, M., & Ostermann, F. O. (2020). Automatic identification of eyewitness messages on twitter during disasters. *Information processing & management*, 57(1), 102107.

Zalachoris, G., & Rathje, E. (2019). Ground Motion Model for Small-to-Moderate Earthquakes in Texas, Oklahoma, and Kansas. *Earthquake Spectra*, 35, 1–20.

Zechar, J., & Zhuang, J. (2014). A parimutuel gambling perspective to compare probabilistic seismicity forecasts. *Geophysical Journal International*.

Zhong, X., Duckham, M., Chong, D., & Tolhurst, K. (2016). Real-time estimation of wildfire perimeters from curated crowdsourcing. *Scientific reports*, 6, 24206.

Zhou, A., Zhou, S., Cao, J., Fan, Y., & Hu, Y. (2000). Approaches for scaling DBSCAN algorithm to large spatial databases. *Journal of computer science and technology*, 15(6), 509-526.

Zwanenburg, C., Konstadinou, M., Meijers, P., Goudarzy, M., König, D., Dyvik, R., Carlton, B., van Elk, J., Doornhof, D. & Korff, M. (2020). Assessment of the Dynamic Properties of Holocene Peat. *Journal of Geotechnical and Geoenvironmental Engineering*, 146(7), 04020049. DOI: 10.1061/(ASCE)GT.1943-5606.0002259

Web-references:

CEMSD (2011): Map of Strong Motion Stations for Mineral Virginia Earthquake of 23 Aug 2011 [Internet]. http://strongmotioncenter.org/cgi-bin/CESMD/iqrStationMap.pl?ID=MineralVirginia_23Aug2011_usse082311a [Accessed 06-08-13].

DTK - Deutsches Talsperrenkomitee Talsperren in Deutschland [Internet]. http://www.talsperrenkomitee.de/talsperren_in_deutschland/talsperren_in_deutschland.htm [Accessed 05-01-16].

Dost, B., Haak, H.W., Koninklijk Nederlands Meteorologisch Instituut (1997): Macroseismische waarnemingen Roswinkel 19-2-1997. De Bilt, Ministerie van Verkeer en Waterstaat, Koninklijk Nederlands Meteorologisch Instituut. Technical reports.

Dost, B., Kraaijpoel, D. (2013): The August 16, 2012 earthquake near Huizinge (Groningen). *KNMI Scientific report*. [http://c.knmi2.nl/knmi-library/knmipubmiscellaneousreport/The_August16_2012_earthquake_near_Huizinge_\(Groningen\).pdf](http://c.knmi2.nl/knmi-library/knmipubmiscellaneousreport/The_August16_2012_earthquake_near_Huizinge_(Groningen).pdf) [Last access 13-11-2015].

EMSC (2020): Earthquake, Magnitude 6.4 - CROATIA - 2020 December 29, 11:19:54 UTC [Internet]. <https://www.emsc-csem.org/Earthquake/earthquake.php?id=933701> [Accessed 29-01-2021].

Esri Deutschland Open Data Portal (2015a): OSM DE Medi: Standorte der Krankenhäuser, Kliniken, Ärzten und Apotheken in Deutschland. <http://opendata.esri->

de.opendata.arcgis.com/datasets/1b7d13c04158407a9c79718dfb5afe4d_0 [Accessed 19-01-16].

Esri Deutschland Open Data Portal (2015b): OSM DE Schulen: Standorte der Schulen in Deutschland. http://opendata.esri.de.opendata.arcgis.com/datasets/7904a95feda94f16b077553953e4ee25_0 [Accessed 19-01-16].

Esri Deutschland Open Data Portal (2015c): OSM DE Sicherheitseinrichtungen. http://opendata.esri.de.opendata.arcgis.com/datasets/59711f4ee839438299c90164115f129b_0 [Accessed 15-12-15].

Landesamt für Geologie Rohstoffe und Bergbau Baden-Württemberg (1998): Geowissenschaftliche Übersichtskarten Baden-Württemberg 1:350.000 - 20 landesweite Karten für Planung, Wirtschaft und Umwelt. Freiburg. (CD-ROM).

Landeserdbebendienst Baden-Württemberg (LED) (2005): Regierungspräsidium Freiburg - Abt. 9 LGRB - Landeserdbebendienst - Aktuelle Erdbeben [Internet], (Jahr 2004). http://www.lgrb.uni-freiburg.de/led_pool/led_2_1.htm [Accessed 21-01-14].

Landeserdbebendienst Baden-Württemberg (LED) (2013): Regierungspräsidium Freiburg - Abt. 9 LGRB - Landeserdbebendienst - Aktuelle Erdbeben [Internet], (Jahr 2013). http://www.lgrb.uni-freiburg.de/led_pool/led_2_1.htm [Accessed 21-01-14].

RAP, Institut National des Sciences de l'Univers (2005): BDsis: 2004-12-05 01:52:39 [Internet], (Réseau Accélérométrique Permanent - RA 1995 - 2008 (données validées)). <http://f1.obs.ujf-grenoble.fr/BDsis/servlet/SacOrSeedEvents?content=html&dbcourante=rap> [Accessed 17-02-14].

Statistische Ämter des Bundes und der Länder (2013): ZENSUS2011 - Ergebnisse des Zensus 2011 [Internet]. <https://www.zensus2011.de/SharedDocs/Aktuelles/Ergebnisse/DemografischeGrunddaten.html?nn=3065474> [Accessed 06-06-14].

Umweltbundesamt (2013): Datenbank 'Kraftwerke in Deutschland' [Internet]. <http://www.umweltbundesamt.de/dokument/datenbank-kraftwerke-in-deutschland> [Accessed 16-12-15].

VCI Online (2013): Chemieparks: Zahlen, Daten und Standortinfos [Internet]. <https://www.vci.de/vci/downloads-vci/bilder/standortkarte-zahlen-300dpi.jpg> [Accessed 17-12-15].

TIZ - Active Twitter users: <https://www.tiz.fr/utilisateurs-reseaux-sociaux-france-monde/>, last access in July 2020.

Tweet from Twitter about modification of geotagging options:
<https://twitter.com/TwitterSupport/status/1141039841993355264>.

USGS (2011): M5.8 – Virginia: Raw data collected by the Did You Feel It? (*Data received from J.Dewey (USGS Emeritus), V.Quitoriano, and D.Wald*).
<http://earthquake.usgs.gov/earthquakes/dyfi/> [Last access 03-07-2013]

USGS (2014): ShakeMaps [Internet]. <http://earthquake.usgs.gov/earthquakes/shakemap/> [Accessed 23-01-14].

USGS. (2020). Vs30 Models and Data. Retrieved 2021, from <https://earthquake.usgs.gov/data/vs30/>

WeAreSocial - Use of social media in France: <https://wearesocial.com/fr/digital-2019-france>, last access in July 2020.

10 APPENDIX I

Table 10-1: Recordings from the Norcia earthquake: coordinates of the stations (Long, Lat), Vs30, distance from the source (Rjb) and PGA and SA at 1s (in m/s²), as the maximum of the two horizontal components and corrected for site effects following [Kotha et al. \(2020\)](#) amplification factors based on Vs30.

Long	Lat	Vs30	Rjb [km]	PGA [m/s ²]	SA(1s) [m/s ²]
12.6308	43.4723	415.56	71.35	1.68816177	4.14014247
12.2488	43.4621	335.7	89.591	1.74430954	5.06876671
12.5127	43.5873	503.99	87.172	1.32585178	2.8122467
12.264	43.5462	577.3	95.395	0.29258904	0.75102906
12.341	43.3041	395.26	72.537	2.45615169	5.64056656
13.242	42.696	623.9	2.188	50.9796876	155.805295
13.4125	42.7713	660.29	9.159	29.3661019	12.8293328
13.2866	42.6325	672.91	10.131	70.6126552	85.5595878
13.5074	43.5922	553.46	77.041	4.33811974	11.7243489
13.0786	42.4182	598.79	33.286	4.24689582	9.41331145
13.3393	42.3755	473.84	38.047	3.54660609	5.71336709
13.3547	42.3807	510.98	37.889	4.62950891	10.4797605
13.337	42.3737	473.84	38.184	5.17439321	9.22709318
13.4009	42.345	325.67	42.939	4.80396879	7.10182859
13.3439	42.3771	446.74	37.99	6.47914617	12.3196395
13.6479	42.848	427.22	30.188	12.9745396	14.609122
13.4259	42.0274	244.68	77.248	1.46160146	2.53899996
12.188	43.7068	552.27	112.973	1.05822748	2.54148625
11.9912	43.8895	615.3	138.718	0.35360496	0.87616835
13.5902	42.3243	677.21	52.15	6.87315202	9.84129391
13.8453	42.1917	735.48	75.737	1.78247435	5.67780471
13.5431	41.9983	206.2	83.121	2.60619837	3.26888689
12.611	42.9323	351.8	35.866	6.60900395	9.845768
13.4685	42.337	360.66	46.106	3.12135826	7.7786263
12.2346	43.3683	284.63	83.723	1.67605768	3.0081468
14.1994	42.0033	715.25	110.404	1.07126481	1.82771061
13.1632	42.5942	422.6	12.555	33.1837037	58.9333622
12.9204	43.0367	300.26	17.769	9.60137028	25.6270082
13.5207	42.0852	639.44	73.419	0.81640351	1.74705523
13.206	42.8294	359.4	0	42.517602	91.2801442
14.6524	41.5628	645.27	172.057	0.20859579	0.24379672
13.1528	42.8944	694.37	0	53.7554606	132.576722
13.7583	42.2716	762.48	64.343	2.32861012	5.64764315
11.9805	43.2678	533.19	95.762	0.29945038	0.81739263
12.5906	43.008	304.68	39.031	5.29454998	12.5108357
13.0122	42.719	374.78	12.865	13.5941764	27.7140857
12.0035	42.754	596.32	87.17	2.23553385	5.50404083
12.2414	44.137	412.07	151.074	0.80013755	2.98485407



13.088	42.1009	679.17	67.573	2.21646315	6.89122792
13.8231	41.4858	602.45	144.579	0.32564938	0.7323853
12.9477	42.3884	546.33	40.815	6.78378574	21.5805667
12.7358	43.955	270.47	116.694	1.39554219	3.15590807
12.2233	43.4919	315.96	93.366	1.35653085	2.5577295
11.2822	42.9941	649.25	144.495	0.13457614	0.22370331
14.4565	41.6611	669.4	153.31	0.77046713	1.18122063
11.8907	44.298	760	180.572	0.50816013	1.16639329
12.9119	43.3436	312.32	47.952	7.53090237	14.0824409
11.2944	43.8072	646.37	173.831	0.10182203	0.21412459
13.3254	41.8933	826.08	90.506	0.81533751	1.30219069
13.1172	42.268	836.11	48.859	2.90906612	7.70593936
12.8965	43.0263	425.91	18.13	34.6355044	132.526814
12.7031	42.9697	352.51	29.064	10.3514604	11.6312504
12.8351	43.0146	442.42	21.116	7.42289679	20.3773186
13.255	41.6926	637.94	112.321	0.79627997	2.28072052
12.8101	43.6905	659.9	86.883	1.80067659	3.15402247
12.5726	43.3553	303.01	63.058	0.96124707	2.67002442
12.5894	43.3138	410.35	58.616	4.08846985	8.56760603
12.5702	42.8038	771.62	40.796	5.02469921	14.1714383
13.3169	41.8134	842.63	99.263	0.79683049	2.21184854
13.5194	42.4207	462	39.957	5.1755671	14.849609
12.9072	41.4723	760	138.899	1.03404395	1.79240917
14.1826	42.0392	548.24	106.507	0.93648025	3.32701331
12.9689	42.5582	566.96	25.13	4.79633342	8.80983198
12.4475	43.7998	593.64	110.318	1.68070319	5.11508919
12.1067	43.9937	577.26	142.746	0.37891786	1.31773501
13.0013	42.9934	504.29	10.224	30.3935098	26.5379903
13.3268	42.8993	648.84	9.786	23.1892395	42.0015973
12.7483	42.2492	641.25	62.828	2.11376328	8.1545747
13.1844	43.0596	667.65	12.54	14.2219445	43.5542636
11.1827	43.1396	593.05	154.282	0.0708824	0.17092827
13.3508	42.5268	678.27	22.959	9.27753056	36.0407204
13.3509	42.5267	678.27	22.973	9.65766073	37.5275599
13.0083	43.2494	449.56	35.324	7.4231324	13.5045756
12.257	42.9619	561.11	64.929	0.92687507	2.45976829
12.7845	43.1115	509.64	31.275	17.3806612	23.5484213
13.0924	42.7924	323.54	3.153	30.9924599	58.4865526
13.0964	42.7925	323.54	2.862	40.9512931	141.226661
12.5194	42.5155	749.67	59.187	1.58982114	6.21983025
13.6423	41.9536	344.36	90.749	0.83185345	1.67486331
13.338	42.558	654.11	19.415	16.2931228	32.0144246
13.5394	42.3229	764.9	50.28	9.15918119	14.0364521
12.2628	43.8181	514.88	119.554	1.523972	5.46724779
13.0334	42.8793	702.1	2.648	31.0269779	59.9743761



12.3251	43.111	548.8	63.196	0.66547205	1.21782108
13.7892	41.812	449.18	110.125	0.42424161	0.69251044
13.657	43.0665	723.76	42.344	5.15935741	14.6978337
12.4485	43.4273	616.17	75.617	1.95395915	6.31073197
13.3262	42.4356	504.24	31.36	5.8931768	10.1039766
12.829	42.4302	269.87	43.22	4.68096877	12.5852785
13.1055	41.9132	761.14	88.118	0.90027378	1.40877591
13.8604	42.9338	466	49.911	4.83901789	17.9631712
13.5577	42.2897	779.02	54.24	3.49443668	8.54089229
14.9644	41.6845	692.34	180.56	0.21288809	0.84145577
12.7408	43.3308	584.81	53.28	4.12193801	8.63244356
13.2261	43.6855	470.26	82.013	5.31109592	14.4902883
12.554	42.632	558.78	50.326	4.34164268	10.9836867
12.4493	43.9343	592.29	123.323	0.85092126	1.25238186
13.3041	43.0371	417.5	15.799	7.45918048	13.478402
12.1312	43.5735	330.43	105.022	1.14787748	1.72635122
13.6136	41.7203	317.38	114.281	0.84088237	1.42671792
13.371	42.5151	677.94	24.897	7.93994219	14.7117952
12.7512	42.7232	642.7	31.269	10.6162411	19.3533678
12.7363	42.7344	731.86	31.72	11.790173	18.8741966
13.6193	43.5179	385.89	73.71	2.52685612	5.45315836
11.8768	42.8746	553.01	95.819	0.34389033	0.82883819
12.154	43.5715	373.52	103.558	0.50563869	1.4086984
11.7944	43.9081	550.81	150.601	0.17472812	0.5166767
13.9343	42.0895	969.62	89.252	1.55678652	2.31958498
13.9166	42.0734	628.04	89.898	3.09495676	6.51169469
13.909	42.068	578.44	90.052	2.24696416	4.9932135
13.9274	42.085	491.54	89.335	3.17400997	8.65982829
13.6895	42.6565	688.54	32.867	9.6717016	13.8901557
13.2584	43.2159	709.55	30.866	13.8040818	60.6705168
12.3873	42.7381	708.97	57.293	2.87080574	8.06117279
12.7358	42.8765	306.31	25.815	10.1164254	21.167355
12.9323	42.4613	793.19	34.922	10.7650477	25.7021046
12.6461	42.5582	324.73	47.793	1.64403716	3.42616349
11.8696	42.4226	542.09	110.684	0.79870319	1.60915468
12.7732	41.893	525.12	96.748	2.01454836	5.90468274
12.2556	43.2544	614.2	75.224	1.13143835	3.86021317
12.6017	43.1593	457.62	45.943	6.30931792	18.3173201
11.8947	43.1427	284.56	97.64	1.17303727	3.0546914
14.0501	41.4805	303.27	152.768	0.80404423	0.71280752
12.9046	43.0049	279.74	15.99	4.44636069	1.27243496
13.43116	42.85635	573.46	14.928	7.90193285	12.9111913
13.409	42.53578	526.36	24.385	3.27068438	7.43789541
13.21452	42.50898	669.63	21.581	15.0178362	34.741891
12.58676	42.608486	685.25	49.277	3.70207146	3.80627137



13.9138	42.8081	638.14	50.187	4.75471298	5.46562992
13.469252	43.137378	598.99	33.258	10.3637066	16.0650728
12.9973	43.44183	647.33	56.139	3.16162706	5.83130002
13.58379	42.26573	678.82	57.608	4.58541972	5.11532923
12.94153	43.49807	650.26	63.312	3.09655612	2.21353997
13.6095	43.37783	408.03	60.436	4.71463919	11.6784739
13.602	43.55017	577.7	76.115	2.17169544	2.44627849
12.50993	42.23696	591.66	77.075	0.70930942	1.48829458
13.776334	42.22944	609.66	69.046	2.86675969	7.14458235
12.26801	43.33419	567.7	79.281	4.62049592	5.08227395
12.74222	42.0228	560.43	84.608	1.27299416	0.94085059
13.53233	43.60768	627.92	79.402	4.81809956	13.6648791
13.40057	42.02193	641.34	77.375	0.52467311	1.60341782
12.40663	43.38211	583.1	74.226	2.33993761	2.98192101
12.77707	43.69309	417.89	88.044	3.90965258	4.21576381
12.7103	41.76039	529.65	112.369	3.80116187	3.163041
13.31229	41.7945	601.24	101.319	2.30036305	1.38101602
13.62324	41.86965	668.64	98.82	2.88811303	1.52967432
11.6765	42.77861	464.49	113.108	0.79129548	0.47854376
14.1832	42.0468	548.24	105.918	2.43837282	2.99391797
12.70492	41.811928	379.07	107.218	1.75230732	1.8721951
12.770183	41.750225	483.94	111.741	0.48887276	1.64359621
12.5923	41.7805	574.64	114.246	0.92241041	0.83146897
14.347	42.2273	585.63	103.052	1.90777234	2.66908997
11.95167	43.61888	580	119.085	0.42409069	0.91829034
13.58658	41.64709	665.9	121.478	3.0004896	1.16619104
10.90265	43.11478	760	176.48	0.11071238	0.251555
14.1524	41.70328	632.4	135.116	0.75973798	1.45904221
12.445128	43.937695	609.01	123.813	2.35576322	2.06720144
11.29017	43.47311	579.88	156.16	0.12037115	0.22111611
11.7893	43.7967	580	142.076	0.24298736	0.50950018
11.15622	43.20972	760	157.795	0.18233553	0.40394297
11.1309	42.42828	760	166.004	0.08060638	0.18110429
10.8652	42.7908	760	178.964	0.05426364	0.14447502
15.51	42.123	760	194	0.19362528	0.60534012
11.707267	44.07746	580	169.317	0.46524092	0.64491881
11.35855	44.05428	580	186.892	1.93078155	1.53004316
12.08023	44.28418	760	171.653	0.48206017	1.02370507
14.90502	41.65418	385.87	179.156	0.15543416	0.68955305
12.5715	43.3666	571.85	64.105	1.20559771	3.36534583
12.457	43.4807	580.01	79.807	1.67056493	4.31492908
12.3536	43.1979	663.71	65.191	0.85833141	3.12454961
11.7666	44.2245	760	179.268	0.3182981	0.73067093
12.2336	43.4584	286.92	90.214	0.91003138	2.08439193
14.0183	41.5978	772.96	140.001	0.44721298	0.98342766



13.670091	43.305297	415.64	57.823	2.44522828	4.64785911
10.9795	43.7956	760	194.623	0.07975662	0.20726805
11.2551	43.7744	311.23	174.441	0.17993382	0.40484215
13.0674	43.2381	548.22	32.81	18.3950169	74.9255967
14.910201	41.513145	596.39	190.494	0.26210447	0.37221837
11.74248	44.35955	760	192.704	0.37110499	0.7133135
12.69864	41.67747	543.99	121.334	1.14087466	2.53454647
13.1427	43.1927	567.15	27.05	9.75442764	22.6475207
15.127	41.7059	646.56	189.46	0.54465536	1.19394477
12.11214	42.91263	798.71	76.505	1.67814416	5.81905707
14.25402	41.64188	878.8	145.355	0.62023121	1.0991984
12.535	43.53567	775.69	81.318	2.55394058	8.58974271
14.17989	41.200001	760	185.512	0.16691834	0.2687848
13.71202	41.71743	721.65	117.241	0.57399911	0.79574268
11.90967	42.84906	546.88	93.311	0.68015253	1.42433117
13.176956	43.228783	442.66	31.117	3.78030728	5.14179885
13.2508	42.6573	493.25	6.302	34.0217041	60.7796815
12.855145	42.532852	575.31	34.316	6.37116079	8.24077448
13.044636	42.751556	532.8	8.78	28.472275	51.2937264
13.125775	42.724918	528.4	4.426	80.5491765	139.079408
13.208697	42.759537	736.45	0	72.2109764	202.476319
12.868511	42.80188	816.98	18.612	9.46816104	13.7869528
13.019	42.890667	533.11	3.057	26.9617338	57.2856652
12.931333	42.711902	786.02	19.028	13.6776806	22.5230476
13.00473	43.05583	573.82	16.155	16.3847822	58.7812612
13.08894	43.11018	619.02	18.59	26.0810569	47.7000224
13.29779	42.75697	591.34	0.032	30.5047947	64.7427977
13.282205	42.634223	672.91	9.789	51.65047	89.2344518
13.60393	42.62279	650.46	27.879	10.2595327	12.8352731
13.312848	43.311198	450.6	42.289	7.82468218	16.986213
14.2342	41.4154	760	166.376	0.31259253	0.57790008
13.352786	42.977404	438.84	15.853	25.8331402	17.8389686
13.405	42.354	471.13	42.145	4.41305234	9.6640493
13.29381	42.673895	529.39	6.387	65.5645616	270.112581
13.286562	42.63254	672.91	10.126	61.1562627	132.062314
13.232048	42.70367	636.67	1.048	41.2308648	150.084048
13.29985	42.625117	574.12	11.373	33.5949964	105.982737
13.307648	42.66291	771.93	8.003	20.6980179	50.1602727
13.357295	42.6254	754.99	13.615	26.517579	21.6988786
13.206917	42.64109	717.62	6.893	42.7522141	132.891934
13.288519	42.655239	562.38	7.994	106.52597	218.107661
13.296578	42.612412	564.3	12.481	21.2462917	57.1202976
13.2925	42.6304	699.59	10.569	80.0398212	164.157614
13.29058	42.626432	608.85	10.879	50.0806965	165.942825
13.218	42.598	574.1	11.731	28.5941781	66.1546919

13.285578	42.637948	672.91	9.56	71.1269187	166.338029
13.314377	42.634324	515.96	11.051	31.9734993	100.295538
13.323448	42.629805	534.3	11.85	24.865492	83.7488367

Table 10-2: Recordings from the Lourdes earthquake: coordinates of the stations (Long, Lat), distance from the source (Rjb), amplification factor based on EC8 classes, and corrected PGA on rock conditions (in m/s²).

Long	Lat	Rjb [km]	Ampl. factor	PGA (m/s ²)
-0.700	43.086	43.5	1	0.02485
0.818	42.708	94.6	1	0.00335
1.254	42.599	131.5	1	0.00235
1.133	42.374	137.3	1	0.00281
0.772	42.322	120.5	1	0.00198
-1.507	43.220	108.3	1	0.00360
-1.580	42.773	122.2	1	0.00399
0.195	42.665	62.3	1	0.02745
0.415	43.062	48.4	1	0.00338
-0.426	43.098	21.6	1.5	0.14653
0.797	43.012	80.0	1	0.00232
0.149	43.059	27.9	1	0.04167
-0.048	43.098	11.8	1	0.03288
-0.009	42.860	35.5	1.8	0.02189
0.798	42.703	93.5	1.8	0.00312
-1.190	42.648	100.5	1	0.00348
-1.147	42.455	111.5	1	0.01442